



N°d'ordre NNT : 2017LYSEI127

THESE de DOCTORAT DE L'UNIVERSITE DE LYON
Opérée au sein de
L'INSTITUT NATIONAL DES SCIENCES APPLIQUEES DE LYON

Ecole Doctorale ED162
Mécanique, Energétique, Génie Civil, Acoustique

Spécialité de doctorat
Génie Mécanique

Soutenue publiquement le 08/12/2017, par :

Bérengère GUILBERT

Ingénieur INSA de Lyon

**Hybrid modular models for the dynamic
study of high-speed thin –rimmed/–
webbed gears**

Devant le jury composé de :

Tanguy, Anne	Professeur, INSA de Lyon	Présidente
Desmet, Wim	Professeur, KU Leuven	Rapporteur
Stahl, Karsten	Professeur, Technische Universität München	Rapporteur
Serra, Roger	Maître de Conférences – HDR, INSA CVL	Examineur
Cutuli, Philippe	Ingénieur, SAFRAN Helicopter Engines	Examineur
Velex, Philippe	Professeur, INSA de Lyon	Directeur de thèse
Dureisseix, David	Professeur, INSA de Lyon	Invité

Département FEDORA – INSA Lyon - Ecoles Doctorales – Quinquennal 2016-2020

SIGLE	ECOLE DOCTORALE	NOM ET COORDONNEES DU RESPONSABLE
CHIMIE	<p>CHIMIE DE LYON http://www.edchimie-lyon.fr</p> <p>Sec : Renée EL MELHEM Bat Blaise Pascal 3^e étage secretariat@edchimie-lyon.fr Insa : R. GOURDON</p>	<p>M. Stéphane DANIELE Institut de Recherches sur la Catalyse et l'Environnement de Lyon IRCELYON-UMR 5256 Équipe CDFA 2 avenue Albert Einstein 69626 Villeurbanne cedex directeur@edchimie-lyon.fr</p>
E.E.A.	<p>ELECTRONIQUE, ELECTROTECHNIQUE, AUTOMATIQUE http://edeea.ec-lyon.fr</p> <p>Sec : M.C. HAVGOUDOUKIAN Ecole-Doctorale.eea@ec-lyon.fr</p>	<p>M. Gérard SCORLETTI Ecole Centrale de Lyon 36 avenue Guy de Collongue 69134 ECULLY Tél : 04.72.18 60.97 Fax : 04 78 43 37 17 Gerard.scorletti@ec-lyon.fr</p>
E2M2	<p>EVOLUTION, ECOSYSTEME, MICROBIOLOGIE, MODELISATION http://e2m2.universite-lyon.fr</p> <p>Sec : Sylvie ROBERJOT Bât Atrium - UCB Lyon 1 04.72.44.83.62 Insa : H. CHARLES secretariat.e2m2@univ-lyon1.fr</p>	<p>M. Fabrice CORDEY CNRS UMR 5276 Lab. de géologie de Lyon Université Claude Bernard Lyon 1 Bât Géode 2 rue Raphaël Dubois 69622 VILLEURBANNE Cédex Tél : 06.07.53.89.13 cordey@univ-lyon1.fr</p>
EDISS	<p>INTERDISCIPLINAIRE SCIENCES-SANTE http://www.ediss-lyon.fr</p> <p>Sec : Sylvie ROBERJOT Bât Atrium - UCB Lyon 1 04.72.44.83.62 Insa : M. LAGARDE secretariat.ediss@univ-lyon1.fr</p>	<p>Mme Emmanuelle CANET-SOULAS INSERM U1060, CarMeN lab, Univ. Lyon 1 Bâtiment IMBL 11 avenue Jean Capelle INSA de Lyon 696621 Villeurbanne Tél : 04.72.68.49.09 Fax : 04 72 68 49 16 Emmanuelle.canet@univ-lyon1.fr</p>
INFOMATHS	<p>INFORMATIQUE ET MATHEMATIQUES http://edinfomaths.universite-lyon.fr</p> <p>Sec : Renée EL MELHEM Bat Blaise Pascal, 3^e étage Tél : 04.72. 43. 80. 46 Fax : 04.72.43.16.87 infomaths@univ-lyon1.fr</p>	<p>M. Luca ZAMBONI Bâtiment Braconnier 43 Boulevard du 11 novembre 1918 69622 VILLEURBANNE Cedex Tél : 04 26 23 45 52 zamboni@maths.univ-lyon1.fr</p>
Matériaux	<p>MATERIAUX DE LYON http://ed34.universite-lyon.fr</p> <p>Sec : Marion COMBE Tél:04-72-43-71-70 –Fax : 87.12 Bat. Direction ed.materiaux@insa-lyon.fr</p>	<p>M. Jean-Yves BUFFIERE INSA de Lyon MATEIS Bâtiment Saint Exupéry 7 avenue Jean Capelle 69621 VILLEURBANNE Cedex Tél : 04.72.43 71.70 Fax 04 72 43 85 28 Ed.materiaux@insa-lyon.fr</p>
MEGA	<p>MECANIQUE, ENERGETIQUE, GENIE CIVIL, ACOUSTIQUE http://edmega.universite-lyon.fr/</p> <p>Sec : Marion COMBE Tél:04-72-43-71-70 –Fax : 87.12 Bat. Direction mega@insa-lyon.fr</p>	<p>M. Philippe BOISSE INSA de Lyon Laboratoire LAMCOS Bâtiment Jacquard 25 bis avenue Jean Capelle 69621 VILLEURBANNE Cedex Tél : 04.72 .43.71.70 Fax : 04 72 43 72 37 Philippe.boisse@insa-lyon.fr</p>
ScSo	<p>ScSo* http://ed483.univ-lyon2.fr/ Sec : Viviane POLSINELLI Brigitte DUBOIS Insa : J.Y. TOUSSAINT Tél : 04 78 69 72 76 viviane.polsinelli@univ-lyon2.fr</p>	<p>M. Christian MONTES Université Lyon 2 86 rue Pasteur 69365 LYON Cedex 07 Christian.montes@univ-lyon2.fr</p>

*ScSo : Histoire, Géographie, Aménagement, Urbanisme, Archéologie, Science politique, Sociologie, Anthropologie

Acknowledgements

This PhD research work has been successfully conducted thanks to the (ANRT, 2014/1067) via a CIFRE grant. It is the result of the partnership between SAFRAN Helicopter Engines (ex-Turbomeca) and the Contact and Structure Laboratory (LaMCoS, UMR CNRS 5259) of INSA de Lyon, directed by Daniel Nelias.

I would like first to express my gratitude toward Philippe Velex, Professor at INSA de Lyon for his constant support over these PhD years. It was a real honour and pleasure to be able to learn from his extensive knowledge and experience, both in general mechanics and specific gear dynamics, without forgetting his very helpful English support. None of this work could have been achieved without his accurate guidance.

I also want to thank my collaborators at SAFRAN HE for welcoming me in the Transmissions Department. I would especially like to thank Philippe Cutuli for his guidance, Lionel Renault and Patricio Almeida for their help every time I needed it, despite their own work loads and Antoine Mounetou for his supervision and his warm welcome to SAFRAN HE.

I want to express my gratitude to Wim Desmet and to Karsten Stahl for the time they spent reviewing this work. I am also grateful at Anne Tanguy and Roger Serra for accepting to be members of this jury.

I very much want to thank Jérôme Bruyère for his help and guidance for the beginning of my journey into the gearing world and his availability over the years. Many thanks also to David Dureisseix, for his positive support during these years, as well as his very substantial technical contribution and his agreement be part of this jury.

I would also like to thank Siobhan Wegeler, for checking through my English. An amical thought too for Fabrice Ville for his participation in the construction of this project and his much appreciated friendly support.

I am not forgetting my first research companions, Matthieu, Mouhamad and Nina, who welcomed me in the laboratory.

To my later friends Cyril and Charlotte, Marine and Eleanor for their patience and tolerance over the years, especially during the writing of this thesis. Thanks too to all my lab colleagues.

I would like to address my final thanks to my family, especially to my parents whose love (and much needed calm) supported me during those years, as well as my brother and uncle for attending my PhD defence.

Abstract

The research work presented in this manuscript was conducted in the Contact and Structural Mechanics Laboratory (LaMCoS) at INSA Lyon, in partnership with SAFRAN Helicopter Engines (formerly-Turbomeca).

In helicopters, the power from the turboshaft is transmitted to the rotor and the various accessories (pumps, starters etc...) via transmission gearboxes. In the context of high-speed, light-weight aeronautical applications, mechanical parts such as gears have to meet somehow contradictory design requirements in terms of reliability and mass reduction thus justifying precise dynamic simulations.

The present work focuses on the definition of modular gear dynamic models, capable of integrating both the local phenomena associated with the instant contact conditions between the tooth flanks and the more global aspects related to shafts, bearings and particularly the contributions of light thin-rimmed /-webbed gear bodies. The proposed models rely on combinations of condensed sub-structures, lumped parameter and beam elements to simulate a pinion-gear pair, shafts, bearings and housing. Mesh elasticity is time-varying, possibly non-linear and is accounted for by Winkler foundations derived from a classic thin-slice model. The contact lines in the base plane are therefore discretised into elemental segments which are all attributed a mesh stiffness function and a normal deviation which are updated depending on the pinion and gear angular positions. The main originality in this PhD consists in inserting condensed finite elements models to simulate flexible gear bodies while keeping the simple and faster rigid-body approach for solid gears. To this end, a specific interface has been developed to connect the discretised tooth contact lines to the continuous finite element gear body models and avoid numerical spikes in the tooth load distributions for example.

A number of comparisons with numerical and experimental results show that the proposed modelling is sound and can capture most of the quasi-static and dynamic behaviour of single stage reduction units with thin-webbed gears and/or pinions.

The model is then applied to the analysis of academic and industrial gears with the objective of analysing the contributions of thin, flexible bodies. Results are presented which highlight the role of centrifugal effects and tooth shape modifications at high speeds. Finally, the possibility to further improve gear web design with regard to mass reduction is investigated and commented upon.

Résumé

Ces travaux de thèse ont été réalisés grâce à une collaboration entre SAFRAN Helicopter Engines (anciennement Turbomeca) et le Laboratoire de Mécanique des Contacts et des Structures (LaMCoS) de l'INSA de Lyon (UMR CNRS 5259).

Les boîtes de transmission par engrenages des moteurs d'hélicoptères convoient la puissance mécanique du turbomoteur aux accessoires (pompes, démarreur) et au rotor. Leur conception dépend des nécessités des équipements embarqués, en particulier l'allègement pour réduire la consommation en carburant. Les engrenages haute-vitesse de la transmission sont allégés grâce à des enlèvements de matière dans les corps sous la denture, les voiles-minces.

Un modèle dynamique d'engrenages a été développé pendant ce projet de recherche. Son approche modulaire permet l'inclusion conjointe des sollicitations dues aux vibrations de l'engrenage et de la nouvelle flexibilité des voiles-minces. Il dérive d'un modèle à paramètres concentrés, comprenant des arbres en poutre, des paliers et carters sous forme de raideurs additionnelles et un élément d'engrenage rigide inclus par son nœud central. Hypothèse est faite que tous les contacts sont situés sur les lignes de contact du plan d'action. Ces lignes sont discrétisées selon des tranches-minces dans les dents et la déviation normale des cellules est recalculée à chaque pas de temps selon la déflexion de la denture. Le nouveau modèle remplace l'engrenage rigide par une modélisation EF du pignon et/ou de la roue condensée sur les nœuds de jante. Une interface lie les raideurs du plan d'action discrétisé aux éléments finis du corps d'engrenage. L'élément prend donc en compte à la fois les sollicitations de l'engrenage et le comportement statique et modal des corps flexibles en dynamique.

Des comparaisons sont faites avec des données numériques et expérimentales. Elles attestent de la capacité du nouveau modèle à prédire le comportement dynamique des engrenages flexibles à hauts régimes de rotation. Ces résultats intègrent entre autres des données locales et globales en dynamique.

Finalement, le modèle est utilisé sur les deux cas académiques validés pour visualiser les effets des corps flexibles plus en détail. Les résultats mettent en avant le rôle des effets centrifuges et des modifications de forme à haute-vitesse. Enfin, l'optimisation massique de l'engrenage grâce au design du voile est examiné et commenté.

Table of Contents

Acknowledgements	5
Abstract	7
Résumé.....	9
Table of Contents.....	11
List of Figures	15
List of Tables	20
Nomenclature	21
General Introduction.....	23
Chapter I Literature Review	25
1. Research Context	28
2. Geared Transmission Process	30
2.1. Mesh Excitations, Origins of Vibrations.....	30
2.1.1. <i>Time-Varying Mesh Stiffness</i>	30
2.1.2. <i>Shape Deviation</i>	33
2.1.3. <i>Mounting Deviations</i>	35
2.2. Main Response Parameters	36
2.2.1. <i>Transmission Errors</i>	36
2.2.2. <i>Dynamic Factors</i>	38
2.3. Tooth Modifications – Influence on Dynamic Response.....	39
2.3.1. <i>Type of Modifications</i>	39
2.3.2. <i>Optimisation of Tooth Modifications</i>	40
3. Usual lumped Parameter Gear Dynamic Models	42
3.1. Models depending on meshing stiffness description	42
3.2. Full Contact Description Models	44
4. Flexibility Inclusion.....	45
4.1. Dynamic Hybrid Models.....	46

4.2. Full Finite Elements Models	48
5. Thesis Objectives	53
Chapter II Numerical Model Presentation	55
1. Modular Gear Model Elements.....	58
1.1. Classical Gear Model Elements	58
1.2. Flexible Body Integration – FE Condensation.....	59
1.3. Gear Element Presentation – Modular Model	65
2. Hybrid Model – Tooth Model Development	69
2.1. Introduction.....	69
2.2. Two-point Connection	70
2.3. Mortar Based Interface for Virtual Compatibility	73
2.4. Shape Functions for Node Coincidence – Final Link.....	77
3. Building the Dynamic Model	80
3.1. Equation of motions – Introduction of Damping.....	80
3.2. Centrifugal Effects	82
3.3. Algorithm.....	83
4. Conclusion	84
Chapter III Elements of Validation	85
1. Accessory Gear – Numerical Validation	88
1.1. Straight Webbed Spur Gear – Quasi-Static Validation.....	88
1.1.1. Spur Gear Presentation.....	88
1.1.2. Static/Quasi-Static Numerical Validation	89
1.2. Model for Gear Optimisation.....	91
1.2.1. Profile Modification Definition	91
1.2.2. MasterCurve Fitting	93
1.3. Dynamic Study.....	94
1.3.1. Numerical Validation of the Spur Gear.....	94
1.3.2. Introduction of a Flexible Gear.....	96
2. Power Transmission – Numerical Validation.....	98
2.1. Validation for Rigid Body Gears	98
2.1.1. Helical Gear Data	98
2.1.2. Quasi-Static Load.....	99
2.1.3. Dynamic Effects.....	100
2.2. Flexible Web Influence.....	101

2.2.1.	<i>Effect of wheel static deformation</i>	101
2.2.2.	<i>Modal Inclusion of the Condensed Wheel</i>	103
2.2.3.	<i>High Speed Investigations</i>	107
3.	Industrial Power Transmission	111
3.1.	Model Presentation – Numerical Validation	111
3.1.1.	<i>Gearbox Presentation</i>	111
3.1.2.	<i>Numerical Validation with Respect to FE Industrial Model</i>	114
3.1.3.	<i>Modal Behaviour</i>	117
3.2.	Data Acquisition Process	120
3.2.1.	<i>Experimental Device</i>	120
3.2.2.	<i>Dynamic Model</i>	124
3.3.	Validation – Experimental Comparison	127
3.3.1.	<i>Results Analysis at Significant Speed Steps</i>	127
3.3.2.	<i>Validation – Experimental Comparison</i>	129
4.	Conclusion	131
Chapter IV Influence of Gear Flexibility on Transmission Design		133
1.	Static Deflection Influence – Accessory Gearbox	136
1.1.	Gear Design – Tooth Optimisation	136
1.1.1.	<i>Helix Angle Inclusion Effect – Web Adequacy</i>	136
1.1.2.	<i>Quasi-Static Optimisation of Transmission Error</i>	137
1.2.	Case of Actual Gears – Tooth Profile Deviations	139
1.2.1.	<i>Definition - Local Effects</i>	139
1.2.2.	<i>Influence of Modifications</i>	141
1.3.	Webbed Pinion	144
2.	Dynamic Contributions of Rotating Webs – Power Transmission Gears	147
2.1.	Transmission Modal Behaviour – Effect of Modes	147
2.2.	Wheel Mode Study	151
2.3.	Design Effect – Hollow Web and High Rotational Speed	157
2.4.	Tooth Design Constraints Regarding Flexible Wheels	160
3.	Flexibility for Fully Webbed Power Transmission Case	164
3.1.	Webbed Pinion Integration	164
3.1.1.	<i>Pinion Web – Influence on Meshing</i>	164
3.1.2.	<i>Dynamic Analysis</i>	165
3.2.	Dynamic Optimisation of Lightweight Gear	168
3.2.1.	<i>Web Optimisation – Load Distribution</i>	168
3.2.2.	<i>Modification Optimisation</i>	172

4. Conclusion	176
General Conclusion	177
References.....	179
Annexes.....	193
1. Shaft Element – Beam Matrices	193
2. Newmark Integration Scheme	195
Résumé Etendu en Français	197
1. Introduction.....	197
2. Revue Bibliographique	197
2.1. Paramètres Principaux de Réponse des Engrenages	197
2.2. Modèles de Dynamique des Engrenages	199
2.3. Cas des Engrenages à Voiles-minces.....	199
3. Présentation du Modèle Hybride d’Engrènement.....	200
3.1. Modèle de Dynamique d’Engrenage.....	200
3.2. Modèle Hybride : Lien d’Interface	202
3.3. Intégration des Effets Dynamiques	206
4. Eléments de Validation Numérique et Expérimentale.....	206
4.1. Boite Accessoire – Validation Numérique	207
4.2. Transmission de Puissance – Validation Numérique.....	209
4.3. Transmission de Puissance – Validation Expérimentale	211
5. Résultats – Cas des Engrenages Flexibles	213
5.1. Influence de la Déformation Statique – Optimisation de Denture.....	213
5.2. Etude de la Dynamique de la Roue en Rotation	215
5.3. Allègement d’une Transmission Complète.....	217
6. Conclusion	219
Scientific Contributions	221

List of Figures

Fig. I-1: Re-composition of the gears in the Antikythera mechanism from Archimedes [LEW93]	28
Fig. I-2: Turboshaft from SAFRAN Helicopter Engines (ex-Turbomeca) [MOU14]	29
Fig. I-3: Meshing process for gears with one or two teeth in contact during meshing [VEL88]	30
Fig. I-4: Hertz pressure.....	30
Fig. I-5: Tooth parameter definition for stiffness calculation [WEB53].....	32
Fig. I-6: Profile deviation definition [HEN78].....	33
Fig. I-7: Lead deviation definition [HEN78].....	34
Fig. I-8: Pitch deviation definition [HEN78]	34
Fig. I-9: Cumulated pitch deviations [HEN78]	35
Fig. I-10: Inclination and deviation due to mounting deviations [SUZ86]	35
Fig. I-11: Harris map [HAR58].....	36
Fig. I-12: Typical no-load transmission error signal, acc. to Munro [MUN89].....	37
Fig. I-13: Comparison between Kubo's experimental results [KUB72] and numerical predictions, acc. to Ozguven and Houser [OZG88.b]	38
Fig. I-14: Tip and root relief [ISO21771].....	39
Fig. I-15: Helix modification definition: (a) helix crowning and (b) helix relief [ISO21771].....	40
Fig. I-16: Analytical MasterCurve [BRU13].....	41
Fig. I-17: Dynamic tooth load factor versus speed – Influence of profile modifications (--: without profile modification) [BRU15].....	41
Fig. I-18: First spring-mass model from Tuplin [OZG88.a]	42
Fig. I-19: (a) Two-degree-of-freedom torsional model of a gear pair and (b) its equivalent single degree-of-freedom system (acc. to Özgüven and Houser [OZG88.a]).....	43
Fig. I-20: Schematic representation of a finite element model of a geared rotor system, acc. to Kahraman et al. [KAH92]	44
Fig. I-21: Definition of shape deviations on the base plane, acc. to Vlex and Maatar [VEL96].....	44
Fig. I-22: Finite element model of a realistic housing geometry, acc. to Zhou et al. [ZHO14]	45
Fig. I-23: Finite element model of a spur gear pair, acc. to Parker et al. [PAR00.a]	46
Fig. I-24: Contact zone with analytical solution for inner part and finite element solution for outer part [PAR00.a].....	46
Fig. I-25: Rotating ring scheme with space-fixed discrete stiffness [COO14].....	47
Fig. I-26: Eigenvalues of a rotating ring on elastic foundation (a) alone and (b) with a single discrete stiffness element for varying rotating speed [COO14].....	47
Fig. I-27: Dynamic ratio versus increasing rotation speed for both solid and thin-rimmed gears [BET07].....	48
Fig. I-28: Example of mode shape for a large rim, thin-webbed wheel found by FEM [MOU14].....	49
Fig. I-29: Calculated (vertical line) and measured Eigen frequencies [MOU14].....	49
Fig. I-30: FEM model wheel for (a) mesh load and (b) centrifugal analysis [LI02.a-08.a]	50
Fig. I-31: Tooth contact stresses for two types of webs at 0 min^{-1} [LI13].....	50
Fig. I-32: Tooth contact stresses for quasi-static analysis with centrifugal effect at $40\,000 \text{ min}^{-1}$ [LI13]	51
Fig. I-33: Wheel geometry for the hollow web study [HEI15]	52
Fig. I-34: Instantaneous mesh stiffness for axisymmetric lightweight wheel (steady), and lightweight gear with holes (varying) [HEI15]	52

Fig. II-1: Shaft element	58
Fig. II-2: Gear body for (a) rigid gear with single node and (b) beam type gear body, with $k = 1, 2$ depending on pinion or wheel	59
Fig. II-3: Finite Element model of a gear flexible wheel	60
Fig. II-4: Dhatt's brick Finite Elements [DHA81].....	60
Fig. II-5: Simple example of a beam with a single interface node [WEN98]	61
Fig. II-6: First ($x_b = 1, \varphi_b = 0$) and second ($x_b = 0, \varphi_b = 1$) constraint (static) modes [WEN98]....	62
Fig. II-7: First dynamic mode [WEN98].....	62
Fig. II-8: First ($F_b = 1$) and 2 nd ($M_b = 1$) flexibility modes [WEN98].....	62
Fig. II-9: First Dynamic mode [WEN98].....	62
Fig. II-10: Sub-structure master nodes ($k = 1, 2$ depending on pinion or wheel)	64
Fig. II-11: Initial gear element with rigid body approach	65
Fig. II-12: Discretised base plane of the gear.....	65
Fig. II-13: Base place with initial tooth gap distribution on contact lines [VEL11]	66
Fig. II-14: Modular model with (a) only flexible gear and (b) flexible pinion and gear.....	67
Fig. II-15: Rigid plate tooth model.....	69
Fig. II-16: Tooth rotation inclusion on a thin slice for tooth root displacement	70
Fig. II-17: Two-point connection for tooth width (only point $(M_{p_2})_{ij}$ is displayed for simplicity sake)	73
Fig. II-18: Projection of discretised segment on FE mesh	74
Fig. II-19: Different discretisation for the segment, from c for discrete line of contact to q for the quadrating FE matching segment	74
Fig. II-20: New node place on mesh after mortar.....	76
Fig. II-21: Patch test problem with discrete elements (DE) and finite element (FE)	77
Fig. II-22: Displacement along the interface for collocation and mortar interface	77
Fig. II-23: Node repartition for brick element surface	78
Fig. II-24: Scheme of interface summary.....	79
Fig. II-25: Simulation algorithm [VEL96]	83
Fig. III-1: Gear element coordinate system.....	88
Fig. III-2: Geometry for (a) pinion and (b) wheel of the spur test case.....	89
Fig. III-3: (a) Local load on contact line and (b) maximum local load for different modular models in case of rigid gear	90
Fig. III-4: Local load maximum for hybrid models webbed wheel.....	91
Fig. III-5: Profile relief parameter on tooth [GHR13].....	91
Fig. III-6: Profile relief parameters in the profile direction (or line of action direction) [BRU14].....	92
Fig. III-7: Analytical MasterCurve comparison with numerical sweep from the initial model [VEL96] and genetic algorithm [GHR12]	93
Fig. III-8: Quasi-static transmission error depending on wheel flexibility (rigid and flexible condensed wheel with model H1: one node pinion and condensed wheel)	93
Fig. III-9: Comparison with rigid body Master Curve for (a) 2 nd hybrid model H2 with rigid bodies and (b) 1 st hybrid model H1 with flexible wheel.....	94
Fig. III-10: Comparison with modal dependent damping – Rigidified gear body	95
Fig. III-11: 2nd hybrid model H2 comparison to initial depending on Rayleigh damping definition with (a) D1: $a_R = 25.0 \text{ s}^{-1}, b_R = 2.5 \times 10^{-6} \text{ s}$ and D2: $a_R = 40.0 \text{ s}^{-1}, b_R = 4.0 \times 10^{-6} \text{ s}$	96
Fig. III-12: Comparison between model with flexible wheel in both hybrid models for (a) modal dependant damping and (b) Rayleigh damping D1 with $a_R = 25.0 \text{ s}^{-1}, b_R = 2.5 \times 10^{-6} \text{ s}$	97

Fig. III-13: Number of mode choice in the condensed wheel influence on the dynamic ratio.....	97
Fig. III-14: Power transmission wheel geometry, including the web.....	99
Fig. III-15: Dynamic ratio comparison for (a) modal dependent damping and (b) Rayleigh damping	101
Fig. III-16: Local load over a tooth for various web arrangements [LI02.b]	102
Fig. III-17: Load distribution for (a) flexible web and (b) when compared to rigid and initial model maximum contact line load when passing through the base plane	103
Fig. III-18: Typical web flexion mode, characterised as 0 nodal circle and 3 nodal diameters (displayed on wheel + shaft).....	104
Fig. III-19: Modal comparison between the gear analysis (H1) and full FE model of wheel alone ...	104
Fig. III-20: Modes distribution for (a) FE wheel studied (b) plain circular disc [SCH97].....	105
Fig. III-21: Example of 3 rd nodal diameter theoretical shape for $\cos(3\theta)$ [JAC97].....	106
Fig. III-22: Circular plate mode shape for (a) no and (b) 1 nodal diameter mode [JAC97].....	106
Fig. III-23: Dynamic ratio in case of the flexible wheel for (a) modal dependant damping and (b) Rayleigh damping.....	107
Fig. III-24: Comparison for centrifugal effect influence with (a) modal dependant damping and (b) Rayleigh damping for clarity.....	108
Fig. III-25: Rim pressure (a) without and (b) with centrifugal effects (id. for both hybrid model)	109
Fig. III-26: FE wheel model deformation (norm and direction) or (a) full wheel and (b) rim cut	109
Fig. III-27: Scheme of rim expansion effect on gear key parameters	110
Fig. III-28: Test Transmission Architecture (Interest: drive and intermediate gear).....	111
Fig. III-29: FE intermediate train (HST wheel + LST pinion) prepared for condensation process.....	112
Fig. III-30: Industrial FE model of the HST.....	113
Fig. III-31: Intermediate pinion tooth boundary condition.....	113
Fig. III-32: Tooth Flank analysis with quasi-static FE model (centrifugal load for $\Omega_w = 8820 \text{ rpm}$)	114
Fig. III-33: Line of contact pressure on base plane	115
Fig. III-34: Meshing pressure of the hybrid model H1 on dynamic run for (a) above material and (b) above a hole meshing conditions.....	116
Fig. III-35: FE wheel modal comparison to interferometry test (starting to the 2 nd nodal diameter (ND) mode for each circle family (NC))	117
Fig. III-36: 9 th diameter mode as example: Rim mode of interest.....	118
Fig. III-37: Campbell diagrams depending on the chosen frame of expression.....	120
Fig. III-38: Angular position of Displacement Probes (DP) for Numerical model / Experiment comparison	121
Fig. III-39: Radial and axial position of Displacement Probes (DP) devices for rim radial displacement measure.....	121
Fig. III-40: (a) Experimental results and (b) extracted scheme for each DP	122
Fig. III-41: Contribution of Rayleigh damping parameters depending on frequency ω_i	124
Fig. III-42: Numerical data gathering scheme: Rim Node (RN).....	125
Fig. III-43: Rim Node response over a full wheel revolution	125
Fig. III-44: Fast Fourier Transform of the Rim Node response over a full revolution versus tooth number (127 being meshing order)	126
Fig. III-45: Campbell diagram drawn with the RN, (0 NC corresponding to the 8 th , 9 th and 10 th nodal diameters of the family)	126
Fig. III-46: Identification of the speeds of interest.....	127
Fig. III-47: Full frequency analysis with FFT for case A and B	128

Fig. III-48: Frequency analysis for the case C	128
Fig. III-49: Frequency analysis for the case D	129
Fig. III-50: Sum of all nodal diameter signals.....	130
Fig. IV-1: Load at contact for (a) $\beta_b = 10^\circ$ and (b) $\beta_b = 20^\circ$ helix angle.....	136
Fig. IV-2: Optimisation with regards to the Master Curve for (a) $\beta_b = 10^\circ$ and (b) $\beta_b = 20^\circ$	137
Fig. IV-3: Quasi-static load distribution on contact line for (a) original gear (b) gear modified with tip relief thanks to the Master Curve	138
Fig. IV-4: Tip Relief impact on dynamic ratio for (a) modal dependant damping and (b) Rayleigh damping.....	138
Fig. IV-5: Definition of machining deviations of gears [LI07].....	139
Fig. IV-6: Profile deviation $e(M_{ij})$ for a line of contact through the base plane.....	140
Fig. IV-7: Contact line load for (a) Aeronautic ISO standard and (b) lower quality gear.....	140
Fig. IV-8: Dynamic ratio comparison for deviated gears	141
Fig. IV-9: Parabolic profile modification definition	142
Fig. IV-10: Profile modification and deviation definition.....	142
Fig. IV-11: Quasi-static load distribution with parabolic modifications and profile deviations	143
Fig. IV-12: Profile deviation influence on dynamic ratio	143
Fig. IV-13: Webbed pinion geometry	144
Fig. IV-14: Dynamic ratio calculation for webbed pinion influence with (a) modal dependent damping and (b) Rayleigh damping	145
Fig. IV-15: Quasi-static transmission error depending on pinion model and rigidity	146
Fig. IV-16: Profile optimisation for model with flexible bodies	146
Fig. IV-17: Dynamic ratio for the three dynamic conditions	148
Fig. IV-18: Web node definition for web displacement.....	148
Fig. IV-19: Web node response for Ω_1 , wheel mode	149
Fig. IV-20: Web node response for Ω_2 pinion mode and standard response Ω_3	149
Fig. IV-21: Several Wheel Node radial response for Ω_1	150
Fig. IV-22: StopBand filter to eliminate wheel rotation frequency in WN signal	151
Fig. IV-23: Web response phasing after post-processing.....	151
Fig. IV-24: Frequency analysis of the web displacement	152
Fig. IV-25: Mode shape of full FE model modal analysis	153
Fig. IV-26: Campbell diagram for modes present at the studied speeds (Ω_1 , Ω_4 and Ω_5)	154
Fig. IV-27: Mode shape for spotted web modes with $dt = \frac{1}{16} Tm$	155
Fig. IV-28: Hollow web geometry with regard to wheel rim.....	157
Fig. IV-29: Test Case C: Test Case B + secondary holes.....	157
Fig. IV-30: FFT analysis of Ω_1 for the different web geometries.....	158
Fig. IV-31: Dynamic ratio response depending on test case for Ω_3	159
Fig. IV-32: Meshing pressure depending on speed for tooth spot over hollow web for case study B	161
Fig. IV-33: Linear modification along lead.....	162
Fig. IV-34: Effect of a 10 μm linear lead modification on pressure	163
Fig. IV-35: Webbed pinion geometry	164
Fig. IV-36: Pressure distribution on (a) plain and (b) webbed pinion	164
Fig. IV-37: Pinion modal data	165
Fig. IV-38: Dynamic ratio comparison for webbed pinion inclusion.....	166
Fig. IV-39: Pressure distribution at $\Omega_p = 3000 \text{ rad} / s$ for webbed pinion.....	167
Fig. IV-40: Centrifugal effect FE calculation for $\Omega_p = 3000 \text{ rad} / s$	167

Fig. IV-41: Web thickness influence on wheel modal behaviour – FE analysis.....	169
Fig. IV-42: Flexion mode example: 2 circles, 3 diameters (17 922 Hz for Case O).....	169
Fig. IV-43: Effect of the web on quasi-static load distribution for (a) maximum contact line load and (b) maximum pressure.....	170
Fig. IV-44: Maximum pressure over a meshing period for the three test cases at $\Omega_p = 3000 \text{ rad} / s$	171
Fig. IV-45: Meshing pressure comparison for both thinner web cases at $\Omega_p = 3000 \text{ rad} / s$	171
Fig. IV-46: Crowning definition in lead direction.....	172
Fig. IV-47: Crowning influence on dynamic pressure distribution.....	172
Fig. IV-48: Dynamic ratio for original gear O with various crowning at $\Omega_p = 3000 \text{ rad} / s$	173
Fig. IV-49: Maximum load over a passage through the base plane comparison for various crowning values at $\Omega_p = 3000 \text{ rad} / s$	174
Fig. IV-50: Test Case E: meshing pressure distribution depending on crowning at $\Omega_p = 3000 \text{ rad} / s$	175

List of Tables

Tab. III-1: Accessory gear train: tooth geometry data.....	88
Tab. III-2: Pinion bearing displacements in static conditions for $k_b = 1 \times 10^9 N/m$ bearing radial stiffness.....	89
Tab. III-3: Gear bearing displacements under static load.....	90
Tab. III-4: RMS value of quasi-static transmission error comparison for all models	94
Tab. III-5: Helical gear geometry	98
Tab. III-6: Load Comparison on Pinion Bearings	99
Tab. III-7: Load Comparison for the Wheel Bearings.....	99
Tab. III-8: Wheel bearing load for flexible web for H1 model	102
Tab. III-9: Industrial case geometry	111
Tab. III-10: Bearing load comparison with FE model with wrench inclusion for LST influence.....	116
Tab. III-11: Rotating frame frequency order ($Z_2 = 127$) for the wheel flexion modes	120
Tab. III-12: Speed for each mode apparition.....	123
Tab. IV-1: Display of the several speeds for rotational wheel analysis	147
Tab. IV-2: Conditions at various speeds	147
Tab. IV-3: Speeds for the wheel frequency modes	151
Tab. IV-4: Wave speed.....	156
Tab. IV-5: Mass variation depending on hollow web disposition.....	158
Tab. IV-6: modification for the test cases at Ω_1	158
Tab. IV-7: Case study for hollow web effect	160
Tab. IV-8: Energy comparison for principal response modes depending on pinion: rigid or webbed	166
Tab. IV-9: Wheel web geometry thickness modification.....	168

Nomenclature

Definition frames

$\mathbf{S}, \mathbf{T}, \mathbf{Z}$	Pinion / Wheel centre frame
$\mathbf{X}, \mathbf{Y}, \mathbf{Z}$	Gear base plane frame

Gear parameters

α_t	Apparent pressure angle
β_b	Base helix angle
δ	Normal approach
δ_0	Initial tooth gap
Δ	Normal deflection
ε_α	Profile contact ratio
Γ	Normalized extent of tooth modification
m	Module
η	Cell coordinate on the contact line
τ	Normalized time
b	Tooth width
e	Sum of deviations
E	Depth of modification
i	Line of contact
j	Tooth segment
k	Local stiffness of a contact cell
L	Potential length of contact
L_c	Length of tooth modification
M	Potential point of contact on base plane
$O_{1,2}$	Pinion or wheel central node
$P_{1,2}$	Contact line coordinate in the base plane
P_{bt}	Base pitch
$R_{b1,2}$	Base radius
T_n	Nominal torque
\mathbf{V}	Structure vector
\mathbf{V}^*	Structure vector after tooth interface design
$Z_{1,2}$	Tooth number

System definition

α_i	Calculated damping factor
ξ	Modal damping factor
φ, ψ, θ	Rotational DOFs
ω	Rotational displacement
$\Omega_{p,w}$	Pinion or wheel rotation speed
Ω	Rotational DOF vector
a_R, b_R	Rayleigh damping coefficients
C	Damping matrix
e	Energy in a mode
F	Force vector
F_c	Centrifugal load
H	Transfer matrix
K	Stiffness matrix
M	Mass Matrix
n	Normal
R	Dynamic ratio
R	Matrix for tooth rotation
t	Time
u, v, w	Translational DOFs
u	Translational displacement
U	Translational DOF vector
X	DOFs vector

Disk Theory

δ_t	Total displacement
δ_c^n, δ_s^n	Fast Fourier Transform components
n	Nodal diameter

Subscript

b	Boundary DOFs
h	Full structure
i	Interior DOFs
n	Modal DOFs
p	Tooth root
ss	Sub-structure

Superscripts

T	Matrix transposed
-----	-------------------

General Introduction

Gears have been used for centuries to transmit power between rotating axes in heavy duty machinery but also precision mechanisms such as clepsydrae and clocks. An archetypal example of the latter is the famous Antikytera machine built by Archimedes which was capable of giving the positions of the sun, the moon and other planets in the solar system.

Nowadays, gears are widely used in all kinds of applications ranging from car gearboxes, precision watches and high-technology aeronautical transmissions. SAFRAN Helicopter Engines (formerly-Turbomeca) is one of the world leaders for turboshaft development and production in the field of aeronautics. The gears in helicopters have two distinct roles: a) transmit the power from the main motor shaft to the helicopter rotor and, b) operate the various accessories (starter, pumps, etc.). The prime movers can rotate up to 60 000 rpm and mass reduction constraints often lead to light-weight, thin-rimmed or thin-webbed gears to reduce fuel consumption.

In this particular context of light-weight gears at high rotational speeds, a research partnership has been established between SAFRAN HE and the Contact and Structural Mechanics Laboratory (LaMCoS) of INSA Lyon with the objective of developing specific gear dynamic models adapted to helicopter transmissions.

In this memoir, Chapter I synthesises the research works on gear dynamics found in the open literature covering the definition of the major parameters and modelling strategies which, most of the time, rely on lumped parameter models of a pinion-gear pair. Some recent extensions towards the simulation of flexible gear bodies in statics and dynamics are also presented.

An original modular dynamic hybrid model is introduced in Chapter II which combines lumped parameter, shaft and 3D finite elements and makes it possible to account for thin-rimmed/web gears with minimum computational cost.

Chapter III presents some elements of model validation based on simulation results but also experimental measurements on actual helicopter transmissions. Satisfactory agreements are observed which, to a large extent, validate the theoretical and numerical developments in Chapter II.

Finally, Chapter IV focuses on the influence of web flexibility on the static and dynamic behaviour of helicopter gears. The impact on the definition of profile modifications and the

contributions of gear body compliance to the critical speeds are examined in detail. Finally, the possibility of further mass reductions by modifying web designs is investigated.

Chapter I

Literature Review

1. Research Context
2. Geared Transmission Process
3. Usual lumped Parameter Gear Dynamic Models
4. Flexibility Inclusion
5. Thesis Objectives

This PhD work focuses on the dynamic behaviour of thin webbed-rimmed gears such as those used in high-speed mechanical transmissions. The literature on the topic is sparse as most of the research effort has been directed towards the quasi-static and dynamic analysis of solid gears whereas the influence of gear body flexibility has received far less attention. This chapter presents a survey of the research works on gear dynamics with emphasis being placed on the contributions concerning light-weight, thin-rimmed gears. The phenomena at the root of gear vibrations are described and the classic models in gear dynamics are presented. Finally, the specific modelling efforts for thin-rimmed gears are described and commented upon.

1. Research Context

The first gears defined as toothed wheels capable of transmitting power while changing speed, torque and direction of rotation were developed by the Greeks in Alexandria during the 3rd century BC mostly in the following two areas:

- The strength of classic gear arrangements for heavy duty machines, required in mills and for irrigation.
- Accurate smaller gears used in clocks.

A typical example of heavy duty work machinery is known as “Saqiya”, which was originally developed in Egypt and very popular in the 5th century AD [LEW93]. It was made of a horizontal gear driven by an animal operating a vertical gear lifting up buckets of water.

The main application on early clocks can be illustrated by the works of Archimedes of Syracuse (287-212 BC). Later, more sophisticated mechanisms were set up in order to predict the positions of the sun, the moon and planets.

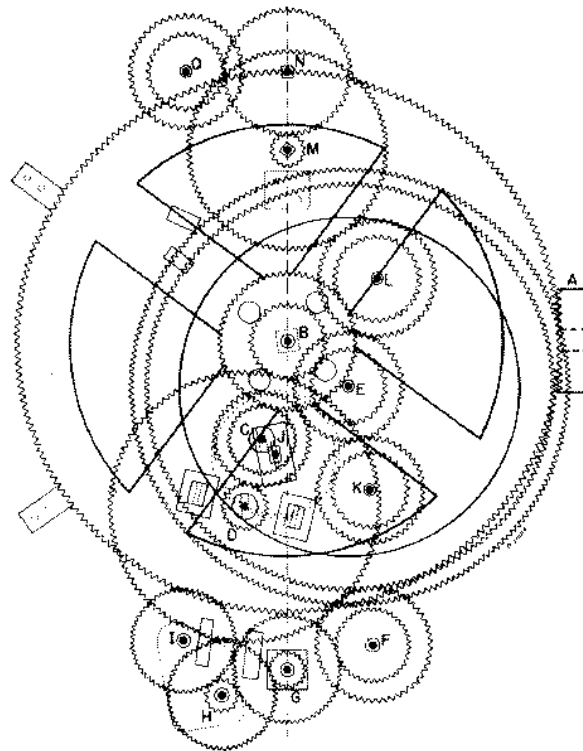


Fig. I-1: Re-composition of the gears in the Antikythera mechanism from Archimedes [LEW93]

The most famous mechanism of this era is probably the Antikythera machine [LEW93-FIE85] whose size was that of a shoe box and comprised 30 gears (Fig. I-1). It was used in Celestial Mechanics and is one of the oldest known differential systems [LEW93].

These advanced technologies were in use in the Roman and Byzantine empires and then in Western Europe where true mechanical clocks were developed in the 13th and 14th centuries.

With the help of missionaries, clocks were produced as of the beginning of the 17th century in Japan and it has been found that, even if there was no evidence of tooth profile theory at the time, Japanese clocks circa 1688 had some tooth crowning and were characterised by fairly good vibration and noise levels [UED17].

The 19th century Industrial Revolution fostered the development of both heavy duty and precision gears in order to meet the needs for higher load carrying capacities in heavy machinery particularly in the transport industry: trains, automobiles and aircrafts. In particular, gears play a prominent role in the development of helicopter industry with the invention of the first helicopter turboshaft in 1948 by the French firm Turbomeca and its founder Joseph Szydlowski [SAY08].

The turboshaft, shown in Fig. I-2 is composed of a compressor and a turbine mounted on either sides of the combustion chamber which convert the gas kinetic energy into mechanical energy on the main shaft. This mechanical power is then transferred to the helicopter rotors and accessories (pump, generators, etc.) via geared transmissions. Such mechanical transmissions are characterized by high rotational speeds and light-weight components (gears in particular) of complex architectures which are the main subject of this research work.

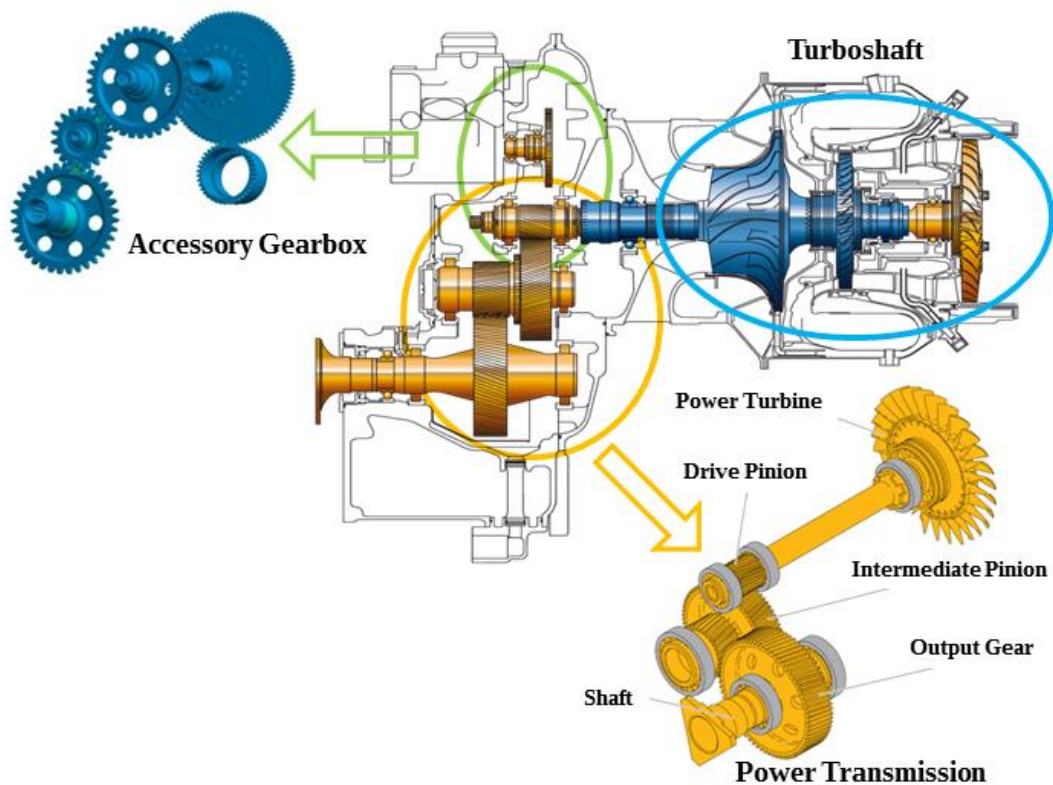


Fig. I-2: Turboshaft from SAFRAN Helicopter Engines (ex-Turbomeca) [MOU14]

2. Geared Transmission Process

2.1. Mesh Excitations, Origins of Vibrations

2.1.1. Time-Varying Mesh Stiffness

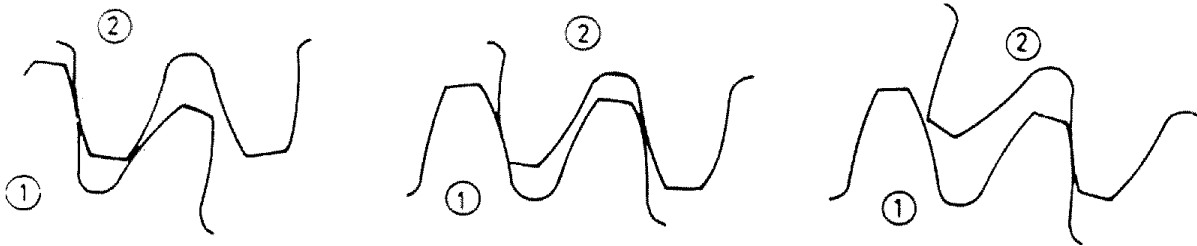


Fig. I-3: Meshing process for gears with one or two teeth in contact during meshing [VEL88]

One of the principal sources of excitation in gears is the meshing process itself as the mesh stiffness varies with time (Fig. I-3) depending on the number of teeth in contact. The simplest model is to consider a constant mesh stiffness per unit contact length as is the case in the ISO standard [ISO6336] so that the global mesh stiffness functions is directly proportional to the time-varying length of contact. More realistic models have been set up including that of Weber & Banaschek [WEB53] in which a pair of mating teeth is assimilated to two cantilevers fixed to an elastic half-plane and connected by a Hertzian contact stiffness function.

a. Contact stiffness

The contact stiffness expression is based on the classic 2D Hertzian contact model as illustrated in Fig. I-4.

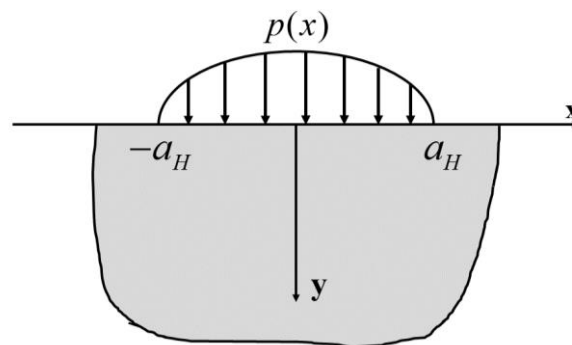


Fig. I-4: Hertz pressure

This representation assumes that the contact effects remain localised close to the contact zone. In order to eliminate the singularity in the displacement field, the authors supposed that

the contact displacement is nil at the tooth neutral fibre thus leading to the following equation for the contact deflection:

$$\delta_c = 4 \frac{F}{b} \frac{(1-\nu^2)}{\pi E} \left(\ln \frac{2\sqrt{d_1 d_2}}{a_H} - \frac{\nu}{2(1-\nu)} \right) \quad (1.1)$$

With:

F/b : load per unit face width, with b tooth width

$d_i, i=1,2$: distances between point of contact and tooth centre line, i standing for pinion and wheel (Fig. I-5)

$$a_H = \sqrt{8 \frac{F}{b} \rho_{eq} \frac{1-\nu^2}{\pi}} : \text{half-width of the contact area}$$

$$\rho_{eq} = \frac{\rho_1 \rho_2}{\rho_1 + \rho_2} : \text{equivalent radius of curvature at contact point, with } \rho_i, i=1,2 \text{ for the}$$

pinion and gear respectively

E, ν : Young's modulus and Poisson's ratio of the material

Lundberg [LUN39] proposed an alternative 3D approach by considering a band of pressure at the surface of a half elastic space and determining the normal displacement at the centre of the pressure band (contact area).

b. Tooth bending

The tooth bending component is found by assimilating a tooth to a cantilever of variable cross-section [WEB53] submitted to a lumped force F in the line of action direction (Fig. I-5). After equating the external load work and the cantilever strain energy, the deflection in the force direction at points on the neutral fibre can be derived as:

$$\delta_b = \frac{F}{b} \frac{1}{E} \cos^2(\alpha_p) \left[10.92 \int_0^{u_w} \frac{(u_w - y)^2}{d(y)^3} dy + 3.1(1 + 0.294tg^2(\alpha_p)) \int_0^{u_w} \frac{1}{d(y)} dy \right] \quad (1.2)$$

With:

F/b : load per unit face width, with b tooth face width

α_p : pressure angle

$d(y)$: tooth thickness depending on the y - coordinate

u_w : contact point distance to tooth root

E, ν : Young's modulus and Poisson's ratio

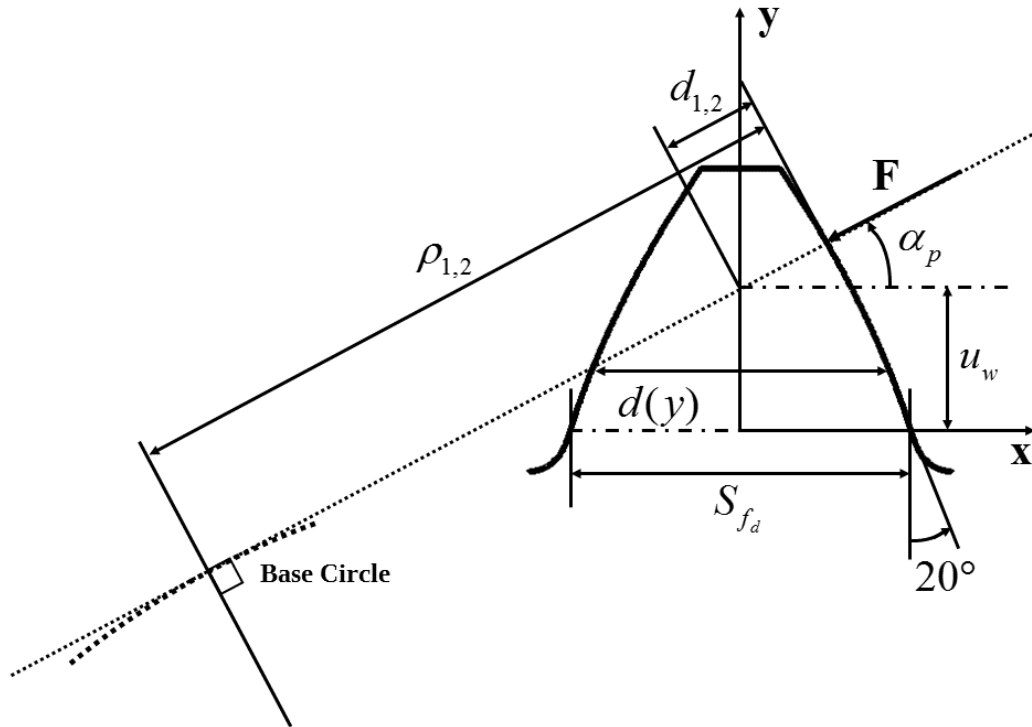


Fig. I-5: Tooth parameter definition for stiffness calculation [WEB53]

c. Elastic foundation

In reality, the connection between the teeth and gear bodies cannot be simulated by built-in-edge conditions and an additional displacement needs to be added to account for gear body compliance. Weber [WEB49] and Weber & Banascheck [WEB53] considered the tooth to be rooted in an elastic half-plane by introducing normal and shear stress distributions at the surface of the half-plane deduced from tooth loading. The general form of the additional deflection brought by body compliance can be expressed under the form:

$$\delta_{fd} = \frac{F}{b} \frac{1}{E} \cos^2(\alpha_p) \left[L \left(\frac{u_w}{S_{fd}} \right)^2 + M \left(\frac{u_w}{S_{fd}} \right) + P \left(1 + Q \cdot \tan^2(\alpha_p) \right) \right] \quad (1.3)$$

With:

S_{fd} : Tooth thickness at critical section

L, M, P and Q: constants depending mostly on the Poisson's ratio (for $\nu = 0.3$, $L = 5.2$, $P = 1.4$ and $Q = 0.3$ [WBE53]), they also differ depending on the author [ANK16]

Velex and Sainsot [SAI04] expanded the previous modelling strategy by considering that gear bodies could be simulated as elastic rings rather than half-planes.

$$X(h, \theta_f) = \frac{A_i}{\theta_f^2} + B_i h^2 + \frac{C_i h}{\theta_f} + \frac{D_i}{\theta_f} + E_i h + F_i \quad (1.4)$$

With

θ_f angle between the tooth centre line and tooth flank intersection with root circle

$h = \frac{R_f}{R_a}$, R_f and R_a respectively outer and inner ring radius

A_i, B_i, C_i, D_i, E_i and F_i constant that can be found in [SAI04]

2.1.2. Shape Deviation

Other sources of excitation arise directly from the manufacturing and finishing processes. Gear teeth are cut and often heat treated and may finally be finished [HEN79]; all these operations inevitably induce shape distortions and errors with respect to the ideal geometry even after grinding or superfinishing.

a. Profile and lead deviations

Profile and lead deviations appear on tooth flanks. Profile deviations represent the difference between the theoretical and actual tooth profiles in the direction normal to the tooth trace as illustrated in Fig. I-6.

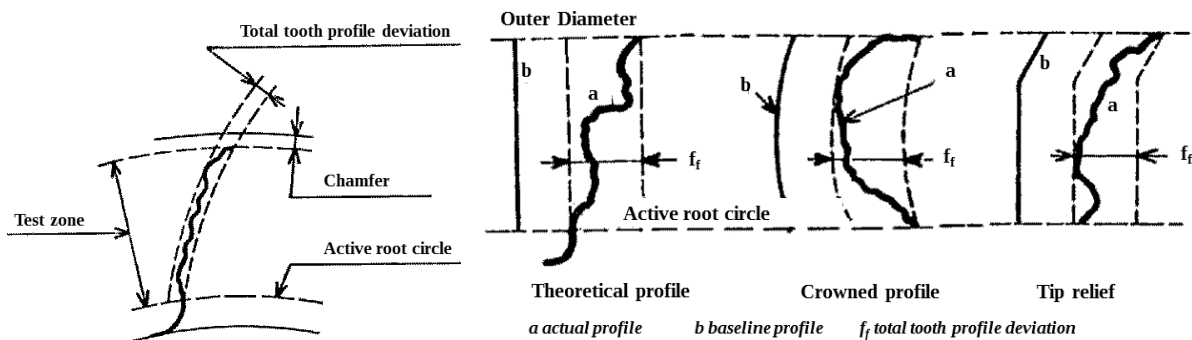


Fig. I-6: Profile deviation definition [HEN78]

On the other hand, lead deviations account for geometry errors in the axial direction as shown in Fig. I-7, they may alter the contact lines in the base plane and therefore modify the meshing process [WEI11-GUI05].

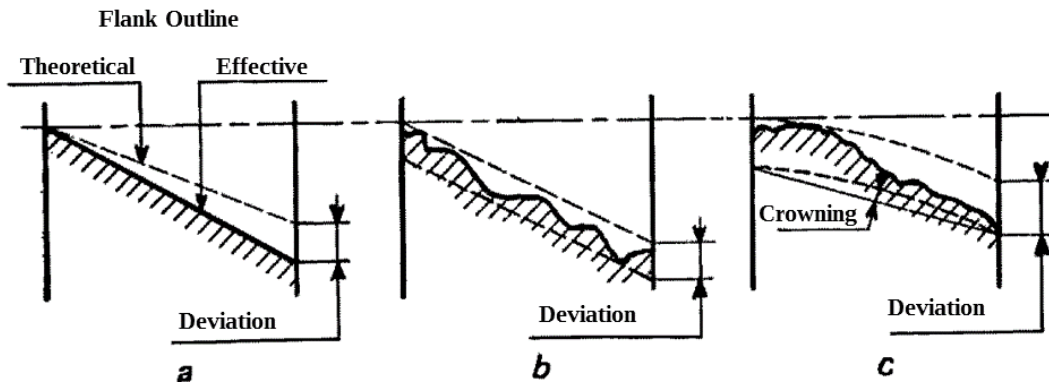


Fig. I-7: Lead deviation definition [HEN78]

b. Pitch deviations

Pitch deviations account for the spacing deviations between successive teeth (Fig. I-8) and might change the meshing conditions by inducing premature or delayed engagements for instance.

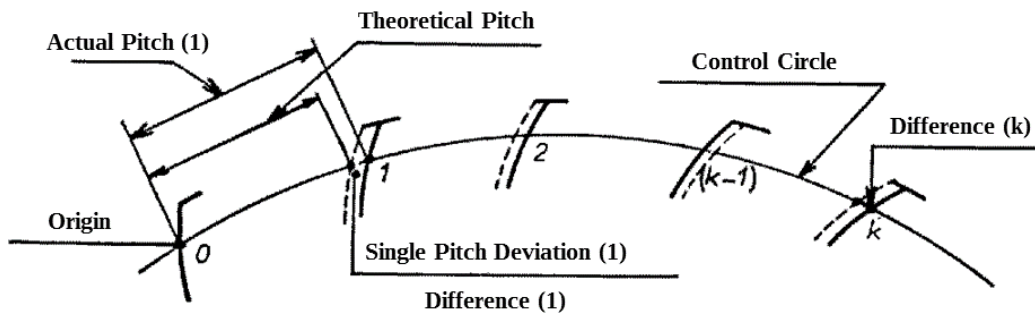


Fig. I-8: Pitch deviation definition [HEN78]

Pitch deviations are measured for each individual tooth (Fig. I-9) but they are often represented as cumulative pitch deviations over a complete revolution on the pinion and the gear.

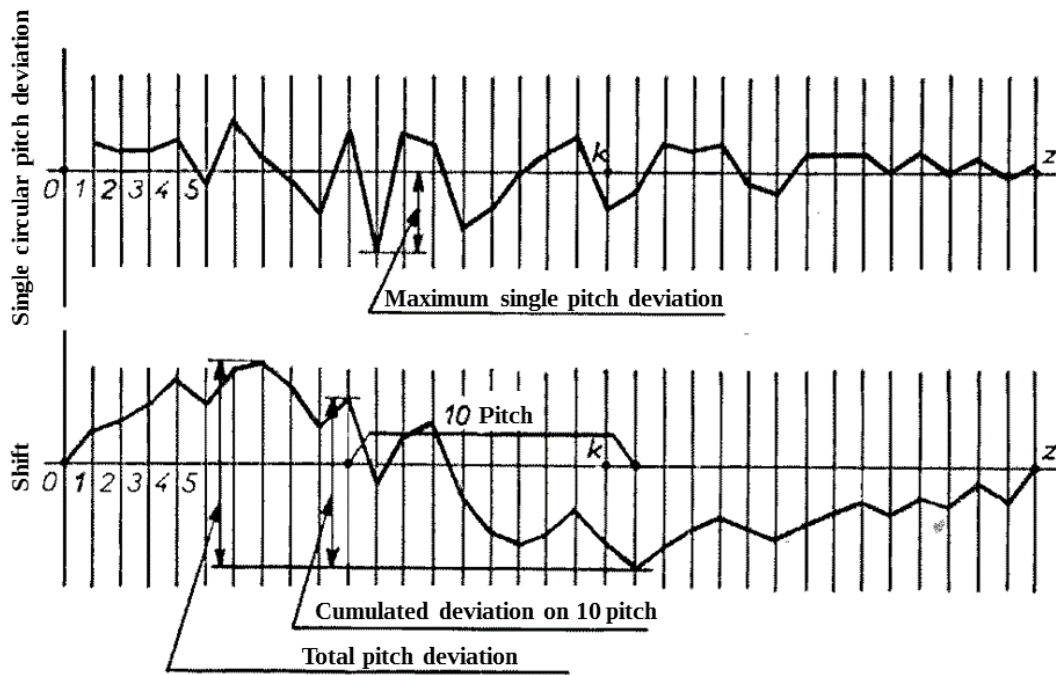


Fig. I-9: Cumulated pitch deviations [HEN78]

2.1.3. Mounting Deviations

Mounting deviations exist when gears are not well positioned with respect to the shafts, bearings and housings. Amongst the most common mounting deviations, misalignments are crucial since they can generate significant pressure peaks on tooth flanks. One usually distinguishes between inclination and deviation which correspond to angular errors (θ_d and θ_i in Fig. I-10) with respect to two perpendicular planes.

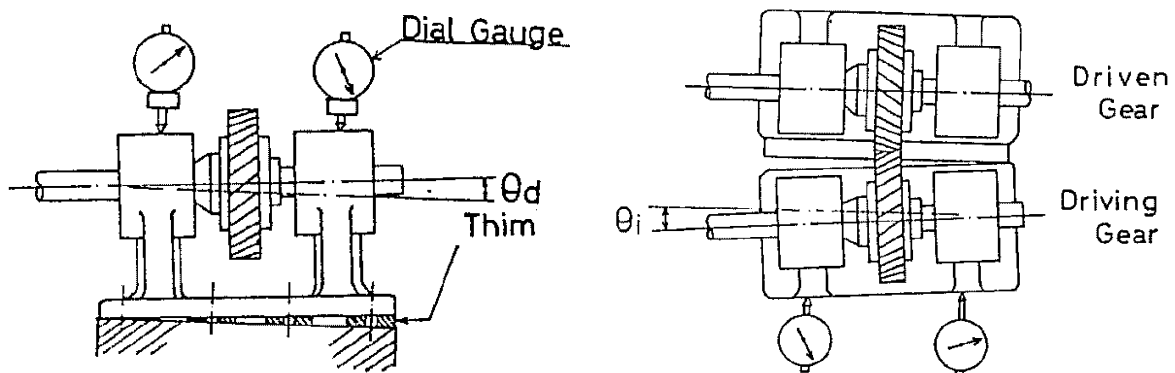


Fig. I-10: Inclination and deviation due to mounting deviations [SUZ86]

Other classic errors comprise eccentricities which occur when the polar axis of inertia of the gear does not coincide with the axis of rotation thus generating speed transfer modulations between the pinion and the gear along with imbalances and synchronous excitations.

2.2. Main Response Parameters

2.2.1. Transmission Errors

The concept of transmission error was first introduced by Harris in 1958 [HAR58] who suggested that the variations in relative displacements between gears at low speeds were at the root of vibrations developed at higher speeds. This was confirmed by a number of experiments and it has been proved theoretically that, as long as linear behaviour prevails, the time-variations of quasi-static transmission errors (TEs) under load are representative of mesh excitations for a pinion-gear pair [VEL06-07] but also multi-mesh systems [VEL16]. The classic definition of transmission error is “for any instantaneous angular position of one gear, the angular displacement of the mating gear from the position it would occupy if the teeth were rigid and unmodified” [GRE63]. Transmission error can be expressed as an angular deviation but it is also often expressed as a distance by projection on the base plane. No-load and quasi-static transmission errors are frequently used to characterize mesh excitations and the influence of shape and mounting errors whereas dynamic transmission errors and dynamic factors are metrics to quantify gear dynamic response.

In the context of defining optimum tooth profile modification, Harris introduced the notion of design load which corresponds to that particular load or torque for which TEs is theoretically constant, i.e., mesh excitations are minimal. By plotting for one given gear, the transmission error curves at different loads on the same graph, the author generated the so-called Harris maps which provide a clear overview of the system behaviour in terms of profile modifications and load (cf. Fig. I-12).

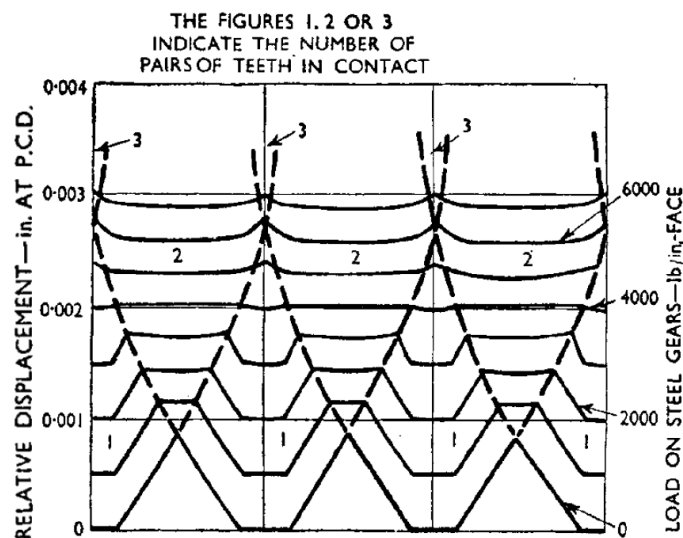


Fig. I-11: Harris map [HAR58]

a. No-load transmission error

No-load transmission error, also referred to as kinematic transmission error, accounts for assembly and geometrical errors along with tooth shape modifications. In the absence of errors and if tooth flanks are unmodified (perfect involute profile), the no-load transmission error is nil. If the profile and lead are modified no-load transmission error is generally not nil and varies with a period equal to that of meshing. On the other hand, pitch errors, run out generate a no-load transmission error function whose period is the least common multiple of the pinion and gear rotational periods. A typical no-load transmission error signal is shown in Fig. I-12.

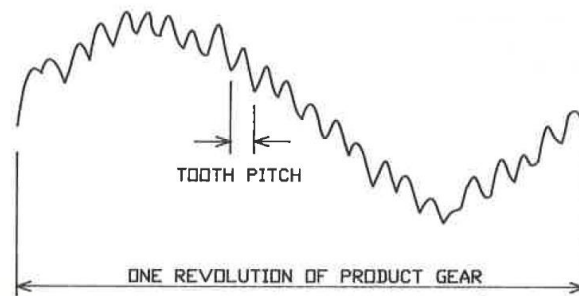


Fig. I-12: Typical no-load transmission error signal, acc. to Munro [MUN89]

b. Quasi-static transmission error

The departure from perfect motion caused by deflections and shape deviations at low speed is captured by quasi-static transmission error. It has been experimentally verified that the time-variation amplitudes of TEs correlate well with gear noise and vibrations [HOU94] thus defining a reliable indicator of mesh excitations and gear noise. TEs is therefore frequently used as design criterion for tooth modifications in order to reduce dynamic tooth loads and noise. [OZG88.b-MUN99-VEL11-BON08]. Based on different mesh stiffness formulations, Bruyère *et al.* have recently proposed a set of analytical formulae to predict optimum profile modifications with regards to transmission error fluctuations for both spur and helical gears. The authors introduced the concept of Master Curve defining the set of optimum linear symmetric tip reliefs [VEL11-BRU13-15].

c. Dynamic transmission error

Dynamic transmission error is the quasi-static transmission error extension for higher rotational speeds when dynamic effects emerge. It is often used to characterize the vibratory and acoustic behaviour. Measurement of dynamic transmission error can be performed by

accelerometers mounted tangentially on the gear wheel [BLA95-KAN12] or by optical means or encoders [GRE63-REM98-GOS00]. Another indicator of gear transmissions dynamic behaviour is the evolution of dynamic tooth loads. These loads are often related to the dynamic factors, presented in the following part.

2.2.2. Dynamic Factors

Dynamic effects can lead to overloads on tooth flanks which are crucial for wear [DIN07], contact and root stresses which, to a large extent, control tooth failures [WAN80-LI11] [OSM10-OSM12]. In this context, the concept of dynamic factor initially introduced by Walker in 1868 is used to quantify dynamic overloads and is defined as the ratio of the maximum dynamic to static tooth load. Depending on the authors, its expression can be based on:

- the global inter-mesh force,
- the force acting on one tooth of the pinion / wheel,
- the stress at the root of one tooth of the pinion / wheel.

The dynamic factor is therefore relevant to characterise overall dynamic tooth loads only and not for tooth load distribution analyses.

Experimentally, dynamic factors are correlated with the dynamic stresses measured by strain gauges cemented at the root of the teeth. As an example, the dynamic root strains recorded experimentally by Kubo on a spur gear set [KUB72] have been extensively used for dynamic models validation [OZG88.b-KAH90-VEL96] (cf. Fig. I-13). However, such measurements are often difficult to obtain and require the use of slip rings or telemetry to transfer the measured signal from the rotary to the stationary system.

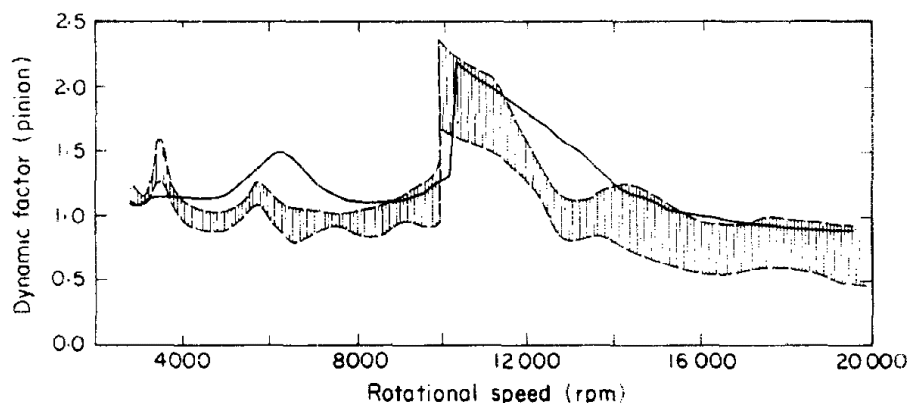


Fig. I-13: Comparison between Kubo's experimental results [KUB72] and numerical predictions, acc. to Ozguven and Houser [OZG88.b]

Dynamic transmission error measurements are usually easier. It explains why some authors have considered the possibility to establish a direct correlation between dynamic transmission error and dynamic factors [TAM07-HOT13]. Vexex proved that a linear dependency can be theoretically found for systems for which torsion is prevalent [VEL09] while Sainte-Marie *et al.* [STM17] showed that this is no longer the case when bending effects cannot be neglected.

2.3. Tooth Modifications – Influence on Dynamic Response

2.3.1. Type of Modifications

As seen before, gear dynamics is influenced by errors and shape deviations which can modify local load distributions and generate corner contacts [HOU06]. Profile and helix modifications are usually introduced to avoid shocks at engagements and improve the load distributions on tooth flanks. They can be introduced separately or merged as topological modifications [ISO21771] where the tooth flank surface is modified so as to give the proper load distribution during the meshing process [CON71-73-LIT91-92]. Profile modifications, for example tip and tooth relief (Fig. I-14), are often used to reduce overloads at engagement [MAA97].

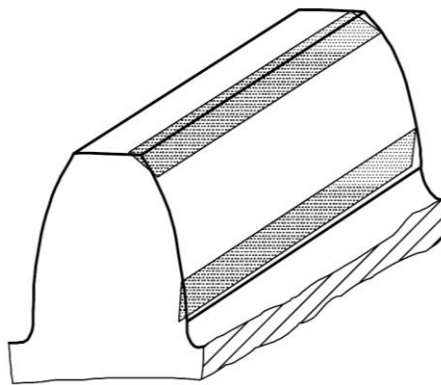


Fig. I-14: Tip and root relief [ISO21771]

The tooth flank can also be modified in the helix direction, commonly, crowning and helix relief at both ends are used (Fig. I-15).

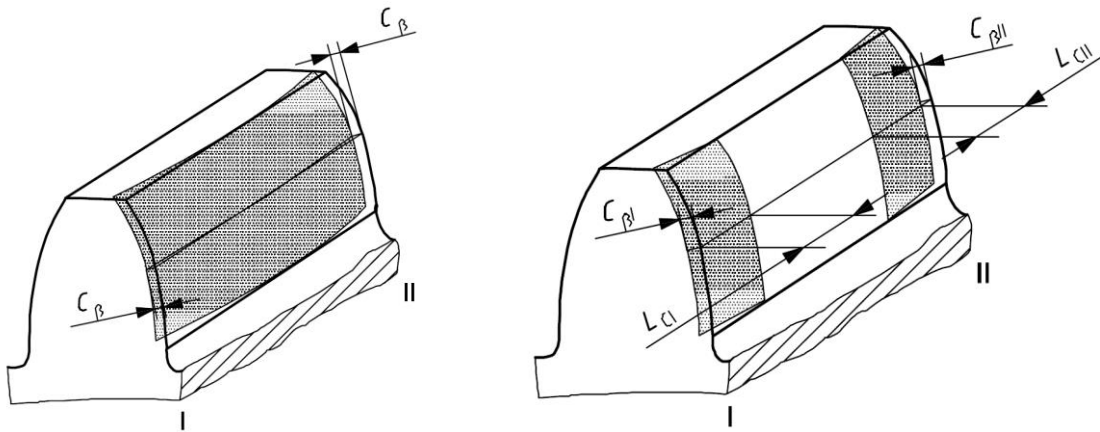


Fig. I-15: Helix modification definition: (a) helix crowning and (b) helix relief [ISO21771]

They are usually used to eliminate the overloads at the edge of tooth flanks, possibly created by misalignment [HOT08].

2.3.2. Optimisation of Tooth Modifications

Tooth modifications are also used to improve gear dynamic behaviour and a number of research works have been conducted on the definition of optimum tooth modifications with regard to the time variations of transmission errors.

Tavakoli and Houser [TAV86] presented a numerical model to calculate static transmission error under load including an algorithm to minimize the amplitudes of the various TE harmonics. Bahk and Parker [BAH13] developed an analytical method based on a perturbation method to study the influence of tooth modifications spur planetary gear. The authors found that the best modifications obtained when considering the whole system were different from those derived when considering individual meshes isolated from the rest of the mechanical system. Bruyère and Vexé [VEL11-BRU13-15] employed an analytical approach to the definition of optimum profile relief and proposed a so-called Master Curve (Fig. I-16) in the depth versus extent of relief plane which gives the families of symmetric linear relief minimising transmission error variations for spur and helical gears transmitting a range of loads. It has been confirmed by numerical simulations that the relief on the Master Curve improves the dynamic response of gears as illustrated in Fig. I-17.

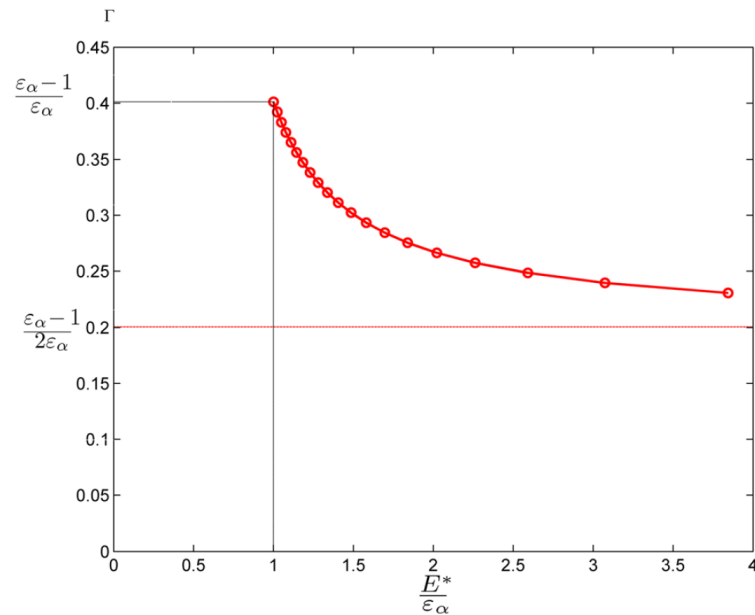


Fig. I-16: Analytical MasterCurve [BRU13]

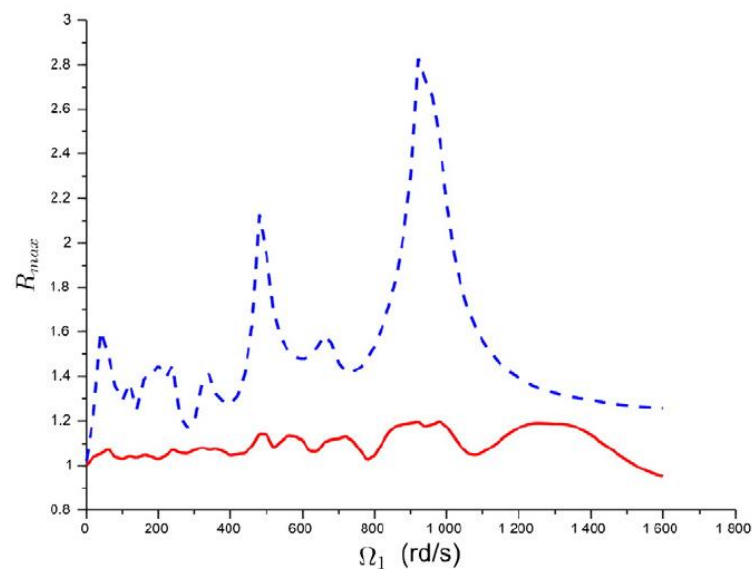


Fig. I-17: Dynamic tooth load factor versus speed – Influence of profile modifications (–: without profile modification) [BRU15]

Much work has also been conducted on the superposition of profile and helix modifications. Carbonelli and Perret-Liaudet [CAR11] used both tip relief and crowning modification for the optimisation of a multi-mesh truck transmission in terms of quasi-static transmission error. The experimental tests [CAR13-14] on an actual truck train proved that significant gain (1dB) can be obtained on the noise radiated by the entire engine. There also on-going research on topological measurements and optimisations with regards to tooth contact patterns [AMI98-ART11]. However, in what follows, the analyses will be limited to profile

relief and lead relief / crowning which represent a large percentage of the tooth modifications used in practice. Another objective is to compare the numerical findings from sophisticated 3D models such as those presented in the following chapter with the analytical indications derived from Master Curves in the context of thin-rimmed gears (as opposed to solid gears).

3. Usual lumped Parameter Gear Dynamic Models

3.1. Models depending on meshing stiffness description

Following the presentation by Özgüven and Houser [OZG88], the simplest models are limited to rigid-solids (usually the pinion and the gear) connected by a mesh stiffness function whereas the flexibility of the surrounding elements (shafts, bearings, etc.) is discarded. The first mathematical models date back to the 1950's, Tuplin [TUP50] introduced the first spring-mass model, based on an equivalent constant mesh stiffness function and wedges of various shapes were introduced at the base of the spring to simulate gear errors (Fig. I-18). The model was used for transient excitations, without taking its periodicity into account and therefore could only estimate the dynamic ratio below any resonance.

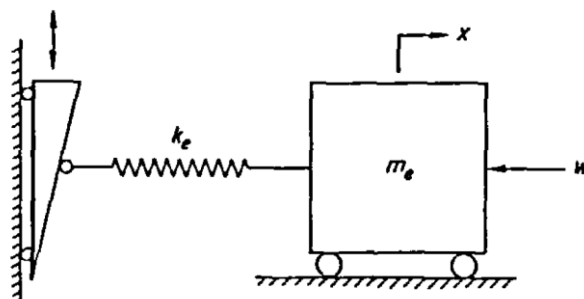


Fig. I-18: First spring-mass model from Tuplin [OZG88.a]

These models were then enhanced to account for time-varying mesh stiffness leading to a second order parametrically-excited linear differential equations. They were referred to as linear time-varying formulations by Blankenship and Singh [BLA92]. Their solutions can only be approximated by numerical time-integration algorithms. Harris [HAR58] proposed a benchmark single degree of freedom model based on the transmission error notion. It incorporated three internal sources of excitation (manufacturing deviations, tooth stiffness variations and linearity due to contact loss). Gregory *et al.* extended Harris' work and developed a torsional model able to predict tooth contact losses [GRE63]. The influence of load and

damping on the occurrence of amplitude jumps in the vicinity of critical speed was demonstrated experimentally (see Fig. I-13). In parallel, models with constant mesh stiffness k_m were still used in which mesh excitations were simulated via quasi-static transmission errors as forcing terms considered as input data [JOH58-KOH59-WOO59-OZG88.a], [KAH90]. The vast majority of these early models were reduced to one-DOF torsional models as illustrated in Fig. I-19 and, in spite of their simplicity, their results compare well with experimental evidence [GRE63-KUB78] essentially because the majority of the test rigs were designed so that torsion was prevalent and the test rigs meet the hypotheses of the mathematical modelling. The vibration couplings between the transmission elements cannot be discarded for real applications. In the late 1960s, it was realized that for more general models, accounting for shaft and bearing flexibilities was necessary.

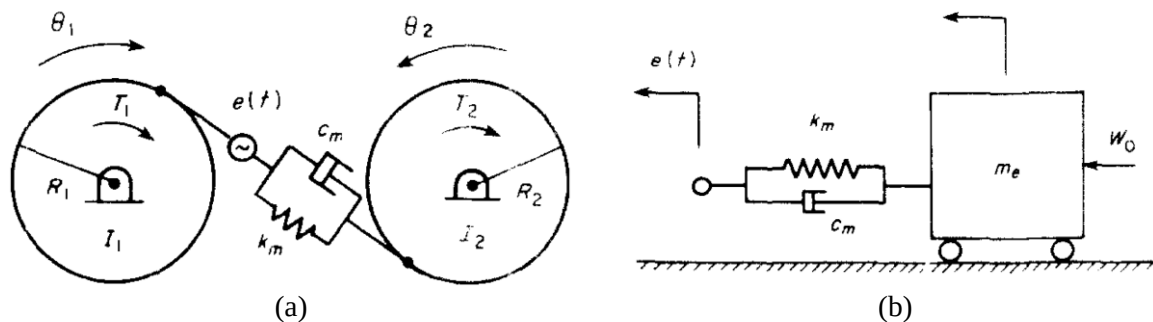


Fig. I-19: (a) Two-degree-of-freedom torsional model of a gear pair and (b) its equivalent single degree-of-freedom system (acc. to Özgüven and Houser [OZG88.a])

Gear dynamic models were then extended to multiple DOFs systems. In 1970, Kohler *et al.* presented a helical gear 6-DOF torsional model [KOH70] with constant mesh stiffness and forcing terms based on transmission error. Fukuma *et al.*, [FUK73], introduced shaft and bearing flexibility in a 3D lumped parameter model and compared their results with measurements. Later, Velez and Berthe [VEL89], Kahraman *et al.* [KAH92] presented models based on a finite element discretization of the gear shafts with time-varying and constant mesh stiffness functions.

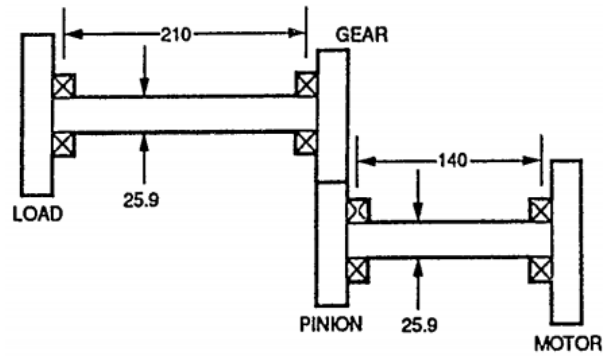


Fig. I-20: Schematic representation of a finite element model of a geared rotor system, acc. to Kahraman et al. [KAH92]

3.2. Full Contact Description Models

Velex *et al.* combined the solution to the contact problem and the equations of motion making it possible to deduced mesh excitations independently of the notion of transmission errors which become results of the numerical process rather than input data [VEL96-BAU02-AJM05]. To this end, the contact problem is solved at each time step and is coupled to a time-step integration scheme. The contact lines in the base plane are discretized in elementary cells which are all attributed an individual mesh stiffness and a normal deviation with respect to perfect tooth geometry (cf. Fig. I-21). A similar approach was recently proposed by Eritenel and Parker [ERI12].

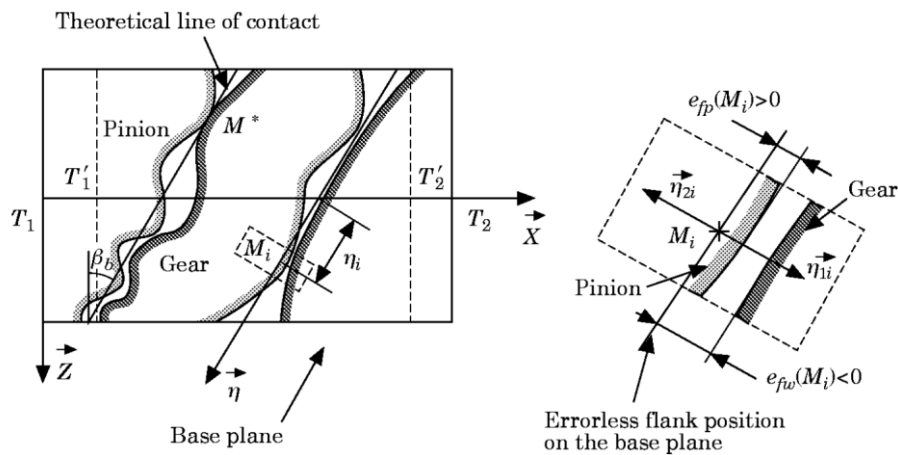


Fig. I-21: Definition of shape deviations on the base plane, acc. to Velex and Maatar [VEL96]

The latest evolutions addressed the global dynamic problem including not just the gear-shaft-bearing assembly but also the housing contributions [LIM89]. In the 1990s, Lim *et al.* [LIM90-91] coupled the housing with a gearbox interior for dynamic analysis. Rigaud *et al.* [RIG96-99] coupled a hybrid lumped parameter / finite element model of a gear-shaft-bearing

system with a finite element model of the casing. Transmission error excitations were considered and the authors concluded that any change in the elastic properties of the gearbox components modifies its dynamic behaviour, thus justifying the need for an accurate model of the global gearbox. Abbas *et al.* proposed an alternative method based on sub-structuring [ABB05-07] and developed a coupled structural-acoustic model to predict the acoustic pressure [ABB08]. Zhou *et al.* [ZHO14] used the finite element discretization to analyse the vibrations of a gearbox housing in Fig. I-22. The dynamic response was analysed independently of the housing and the corresponding dynamic bearing forces were used as excitations sources for the housing model.

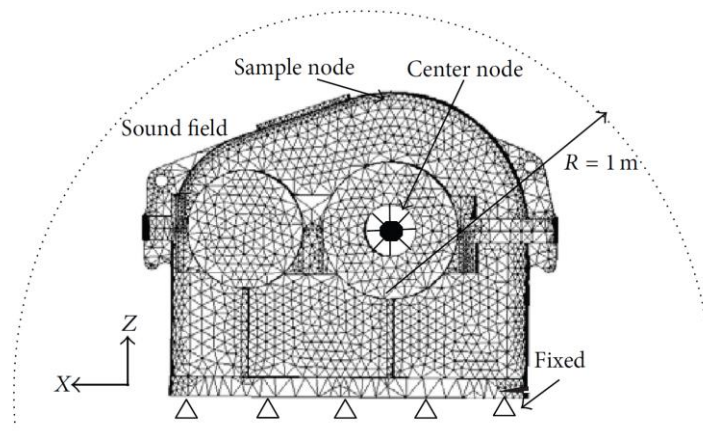


Fig. I-22: Finite element model of a realistic housing geometry, acc. to Zhou *et al.* [ZHO14]

Guo *et al.* [GUO14] introduced a complete FE / contact mechanics gearbox model with the housing. It provides a detailed analysis of gear tooth and rolling element contacts including the fluctuations of bearing stiffness due to rollers passage into the loaded zone. However, the contact models for rolling element bearings were not used in dynamic due to their enormous computational needs. To reduce computational costs and allow to cover a speed range (in speed-sweeps), the authors proposed an equivalent lumped-parameter model in which gear tooth contact is solved by discretizing contact lines into linear spring distributions.

4. Flexibility Inclusion

All these models present the same limitation as they use rigid body gears and cannot represent the full flexible behaviour of the lightweight gears that are used in aeronautical transmissions. In an attempt of giving an accurate description of the flexible gear static and dynamic behaviour, many studies have been conducted over the years on these particulars wheels.

4.1. Dynamic Hybrid Models

Parker and Vijayakar developed a bi-dimensional spur gear model which combines finite elements and an analytical contact model [PAR00.a] (Fig. I-23 & Fig. I-24) and avoids preliminary computations of mesh stiffness or static transmission error.

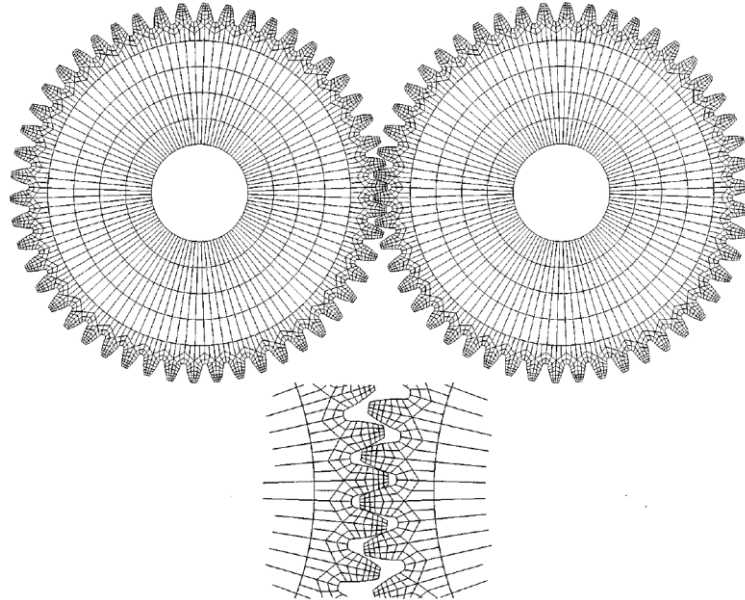


Fig. I-23: Finite element model of a spur gear pair, acc. to Parker et al. [PAR00.a]

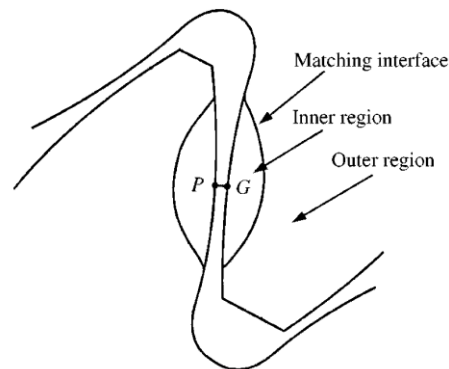


Fig. I-24: Contact zone with analytical solution for inner part and finite element solution for outer part [PAR00.a]

The methodology was then extended to planetary gears [PAR00.b], and enhanced by Vijayakar and Kahraman for the integration of gear body flexibility [KAH01-SIN08-KAH10].

In order to limit the computational times due to FE models, Eritenel and Parker [ERI12] proposed a model which accounts for the non-linearities at high speeds, such as partial and total contact losses, by introducing a full contact model and also bulk stiffness for rim deflections. Parker and Cooley [COO14-15] simulated flexible gears by introducing rotating elastic rings

resting on constant stiffness elastic foundations while keeping lumped stiffness elements for mesh elasticity.

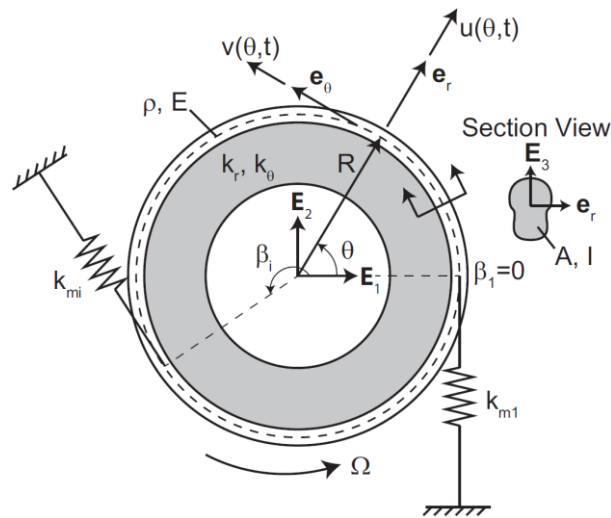


Fig. I-25: Rotating ring scheme with space-fixed discrete stiffness [COO14]

This simplified elastic ring, shown Fig. I-25, enables Parker and Cooley to develop the motion equations analytically and derive closed-form expressions for the eigenvalues in case of a rotating ring. Fig. I-26.a shows the eigenvalues for a free ring only, the Nodal Diameters are identified with a frequency split depending on speed, which is typical of axisymmetric systems in rotation [LAL90].

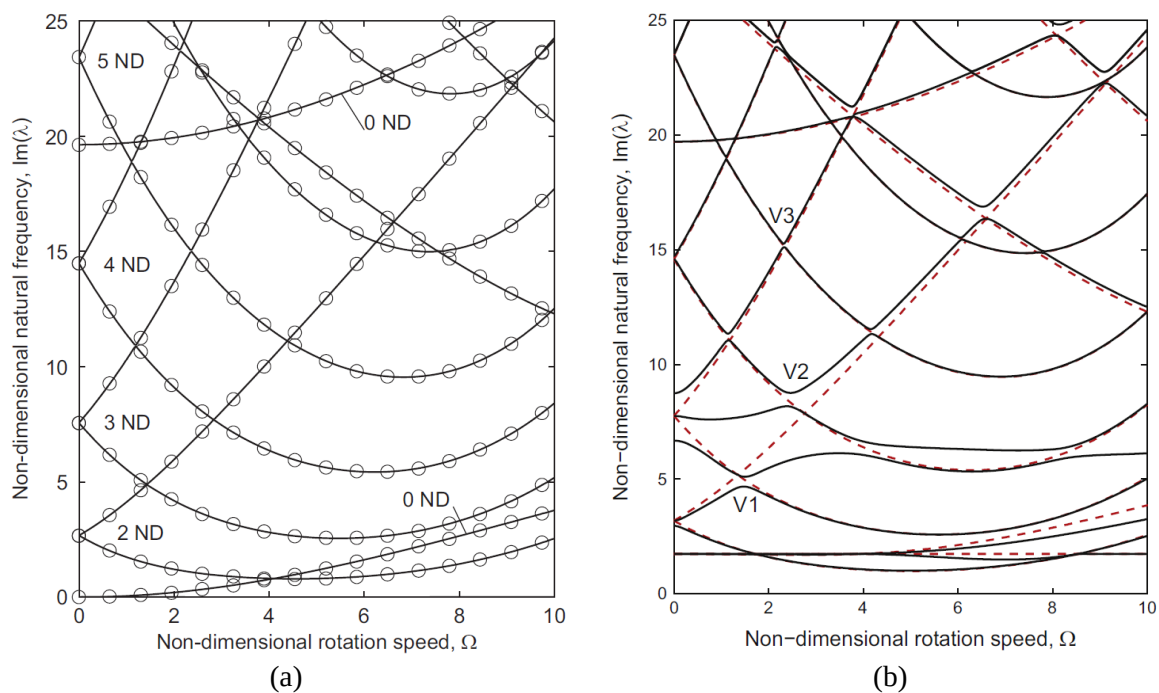


Fig. I-26: Eigenvalues of a rotating ring on elastic foundation (a) alone and (b) with a single discrete stiffness element for varying rotating speed [COO14]

Fig. I-27.b shows the same ring with the addition of mesh stiffness, the free ring solutions are represented by the dashed lines. The presence of a mesh stiffness element disrupts the axi-symmetry of the disk and as shown in [PUS11], the zero speed solutions bifurcate as speed increases. It is therefore concluded that mesh stiffness influences flexible disc dynamics and needs to be accounted for when calculating elastic ring dynamic responses. In order to represent actual gear geometries, Parker and Kahraman [KAH03] introduced a full 3D FE model. Using a different approach, Abousleiman *et al.* [ABO06-07] and Bettaieb *et al.* [BET06-07] reduced the system size by a Ritz method based on a truncated modal basis [ABO04], the corresponding state equations are solved by a time-step HHT algorithm combined with a unilateral normal contact algorithm [VEL96]. Typical results are shown in Fig. I-27 which prove that gear body compliance alters tooth dynamic loading.

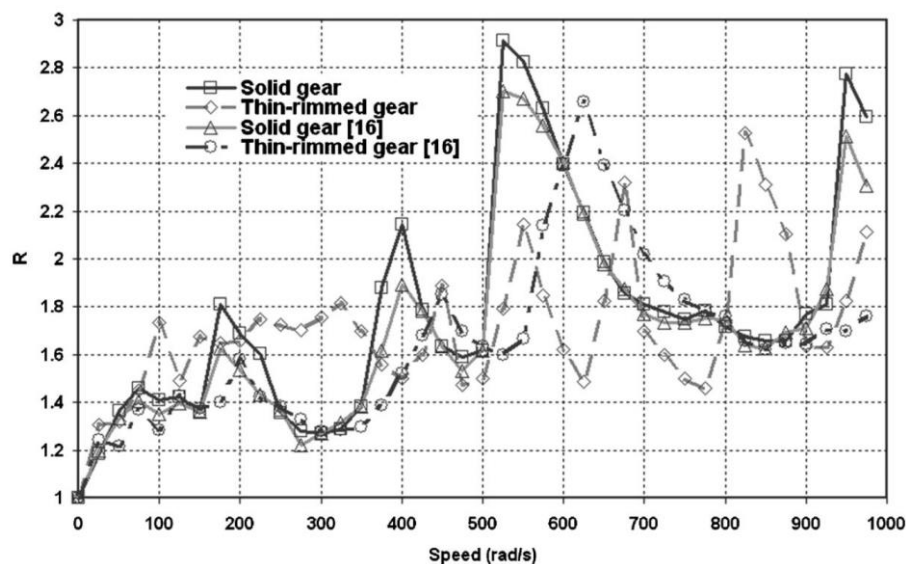


Fig. I-27: Dynamic ratio versus increasing rotation speed for both solid and thin-rimmed gears [BET07]

4.2. Full Finite Elements Models

In the context of mechanical transmissions, accurate deflection modelling was first introduced in the design of keyways [ODA84.a], solid gears with thin-rimmed web [ODA86.a-90] or planetary gears in which ring-gear deformations are crucial in the load sharing properties amongst the various planets [ODA84.b-86.b-87]. The earlier studies were carried out using 2D FEM models and experimental measurements which stress the fact that thin members required precise simulations as they influence the overall behaviour and are submitted to higher stress

levels. Mounetou *et al.* [MOU14] addressed the issue of wheel modal identification and showed examples of disc modes that can be characterised by their nodal diameters. Fig. I-28.a shows a mode extracted from the wheel first modal family (0 circle) with 8 nodal diameters and Fig. I-28.b, a mode from the second family (1 circle) with 6 diameters, the colour code represents nodal displacement amplitudes. It can be observed in Fig. I-28.a that the rim is strongly impacted and consequently that the mode under consideration is likely to influence on dynamic tooth meshing. The simulation was also validated by comparing with impact test results on an isolated gear [MOU14] as illustrated in Fig. I-29.

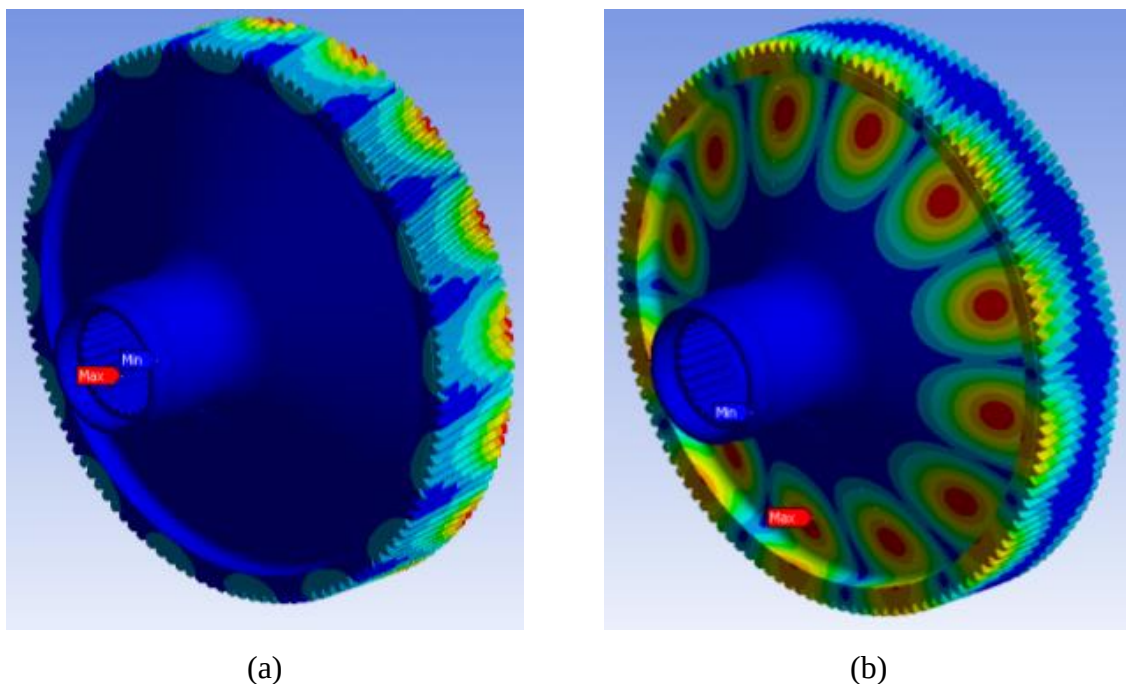


Fig. I-28: Example of mode shape for a large rim, thin-webbed wheel found by FEM [MOU14]

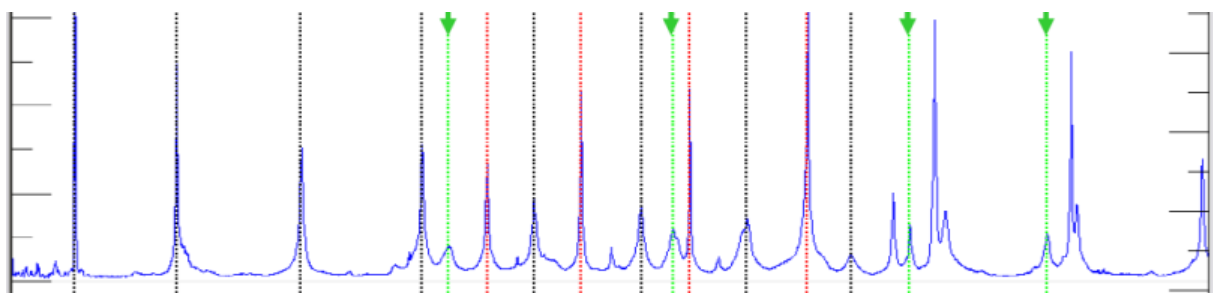


Fig. I-29: Calculated (vertical line) and measured Eigen frequencies [MOU14]

Li [LI02.a-08.a-13] used similar models to analyse tooth load patterns in light-weight thin rimmed gears submitted to nominal mesh force (Fig. I-30.a) and centrifugal forces (Fig. I-30.b) and concluded that gear body deflections cannot be ignored in the simulations of dynamic tooth load distributions.

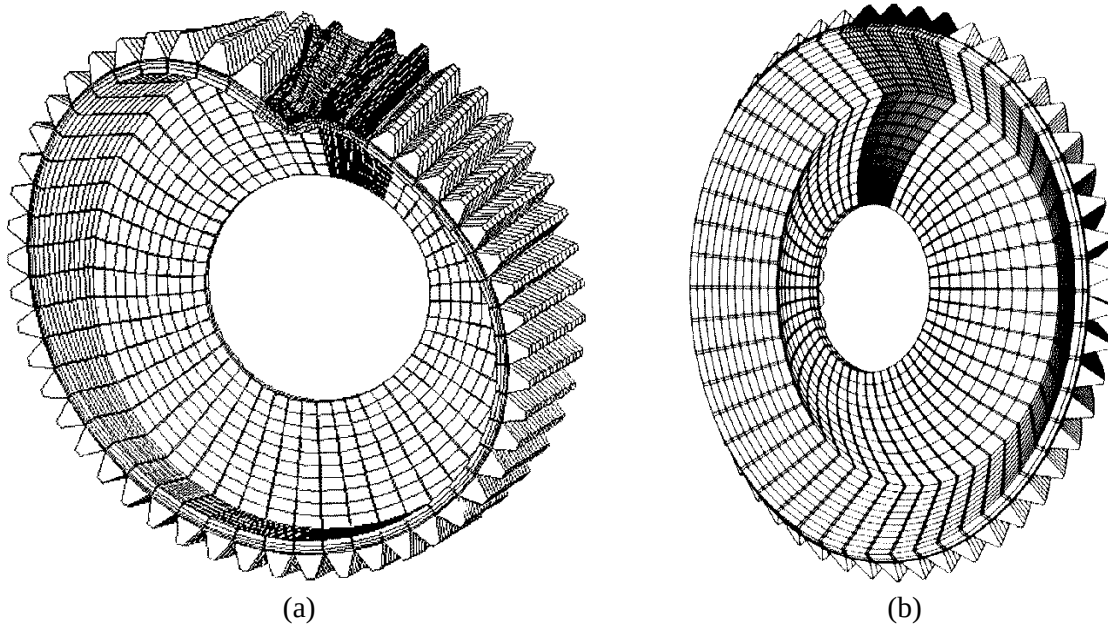


Fig. I-30: FEM model wheel for (a) mesh load and (b) centrifugal analysis [LI02.a-08.a]

Li then used his 3D FE models for analysing the influence of web position and inclination on tooth load distributions [LI08.a-13]. Fig. I-31 shows some examples of result without centrifugal effects (0 min^{-1} speed): (a) a straight centred web allows a centred contact stress pattern on tooth flank whereas, (b) an inclined web leads to uneven stress distributions with overloads at one tooth flank edge in this case.

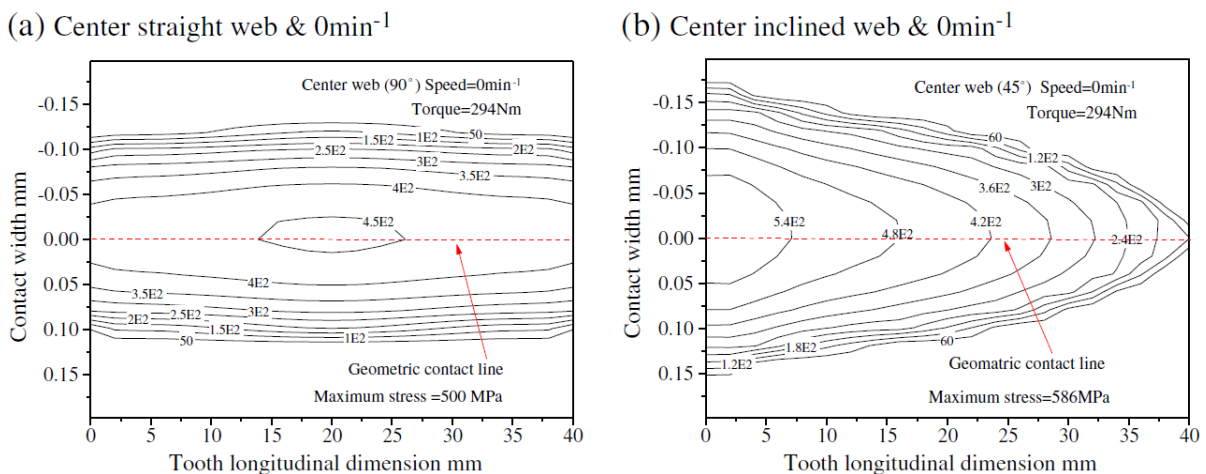


Fig. I-31: Tooth contact stresses for two types of webs at 0 min^{-1} [LI13]

Centrifugal loads were added to simulate a system in rotation while keeping a quasi-static model. The stress level curves in Fig. I-32 indicate that the contact conditions are modified and highlight the role of web flexibility on the meshing conditions.

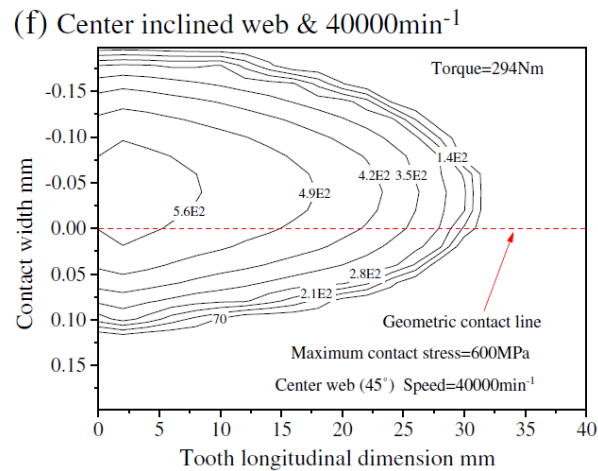


Fig. I-32: Tooth contact stresses for quasi-static analysis with centrifugal effect at 40 000 min⁻¹ [LI13]

A similar study was conducted by Heirman [HEI15] on non-axisymmetric gear geometries with hollow webs (Fig. I-33) in order to investigate the influence of holes on bulk and mesh stiffness functions. The results in Fig. I-34 point to an additional characteristic period (that of the hole passage in the meshing zone) superimpose on the classic mesh period and its harmonics, thus emphasising here too the reality of the interactions between the tooth contact conditions and the structural properties of gear bodies. Based on these observations, it can be anticipated that the dynamic behaviour is likely to be modified too hence justifying extensions of the classic lumped parameter models.

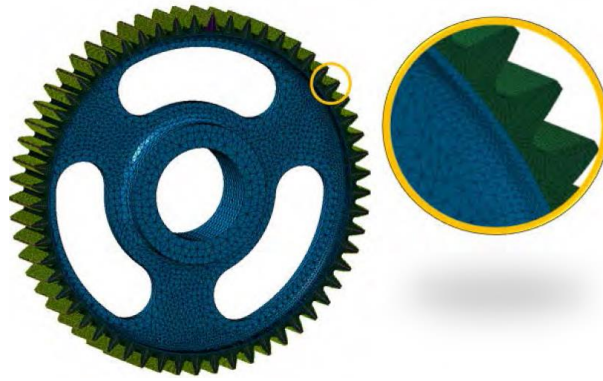


Fig. I-33: Wheel geometry for the hollow web study [HEI15]

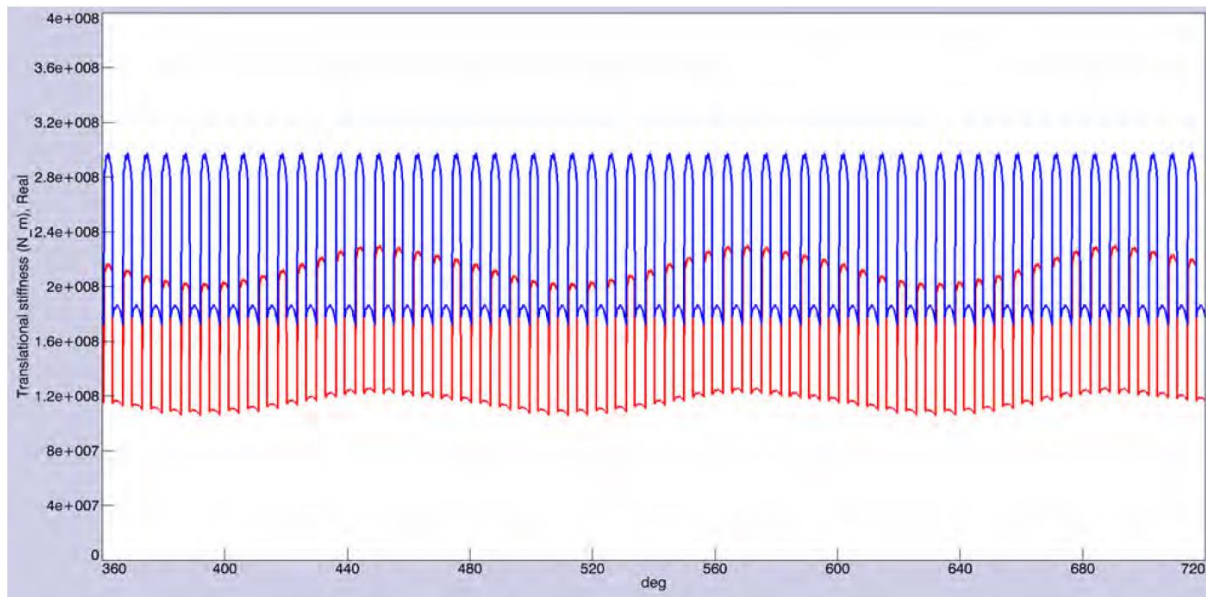


Fig. I-34: Instantaneous mesh stiffness for axisymmetric lightweight wheel (steady), and lightweight gear with holes (varying) [HEI15]

5. Thesis Objectives

In the continuation of the previous works on the integration of flexible gears, the research reported in this memoir will focus on the numerical integration of flexible components in dynamic gear models. In order to be compatible with design constraints in industry, particular attention will be given to limiting computational times so that extensive parameter studies are still possible. From a different perspective, the objective to develop models which can be used together for static and dynamic conditions will be pursued. To this end, an original mesh interface will be presented which is compatible with finite elements for structural parts and elastic foundations models as used in most gear dynamic models for contact simulations. The concept of hybrid models will be presented which makes it possible to combine continuous and discrete models based on the architecture and geometry of the gear system under consideration. By so doing, computational times remain limited and modelling precision can be brought to the parts with maximum flexibility and/or complex geometry only.

Elements of validations will be given based on comparisons with other model results but also experimental evidence from actual helicopter transmissions. Finally, some typical phenomena associated with high speed gears will be presented and discussed.

Chapter II

Numerical Model Presentation

1. Modular Gear Model Elements
2. Hybrid Model – Tooth Model Development
3. Building the Dynamic Model
4. Conclusion

This chapter is aimed at introducing the main characteristics of an original dynamic model of geared transmissions which makes it possible to account for deformable, thin-rimmed pinions and gears as encountered in lightweight helicopter transmissions.

The classic FE models rely on beam, lumped parameter elements and connection elements representing pinion-gear pairs. This gear element generally comprises two rigid cylinders with all 6 degrees of freedom each, which are connected by an elastic foundation [MAA96]. The main hypothesis is that all the contacts between the mating teeth are line contacts lying in the theoretical plane of action, tangent to the pinion and gear base circles so that tooth elasticity is transferred to the base plane and leads to a time-varying, possibly non-linear mesh stiffness matrix. This matrix is determined by slicing all the contact lines into individual cells which are all attributed an individual stiffness k_{ij} .

In the new approach, the rigid pinion or/and gear can be replaced by a flexible body, modelled by Finite Elements and condensed at some master nodes located at the rim and bearing interfaces. This combination leads to a fully modular model while keeping the same mesh stiffness and forcing term modelling. However, the discrete elastic foundations and the FE continuous models are not directly compatible and can generate numerical artefacts when directly connected. In order to solve this compatibility issue, a mortar based interface has been developed which makes it possible to correctly relate the discretised tooth flanks and the gear/pinion FE models.

The elements of theory needed for the development of this enhanced modelling strategy are presented in this chapter along with some technical elements associated with the solution of the dynamic equations and the introduction of centrifugal effects which need to be incorporated in high-speed transmissions.

1. Modular Gear Model Elements

1.1. Classical Gear Model Elements

a. Gear Support Elements – Shaft, Bearing and Housing

The initial gear model is a lumped parameter model based on the developments of Velez and Maatar [VEL96] which comprises standard Timoshenko 2-node shaft elements with 6 degrees of freedom per node [TIM55] (Fig. II-1).

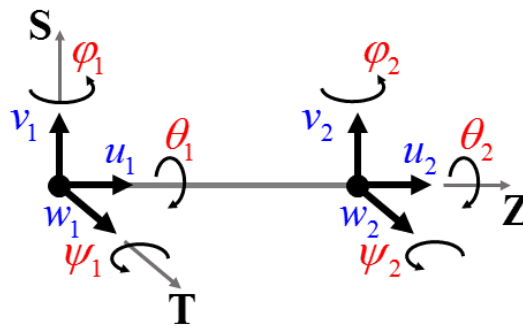


Fig. II-1: Shaft element

The different motions are uncoupled and lead to a total stiffness matrix as the sum of the individual contributions for axial, bending and torsional displacements (eq. 2.1).

$$\mathbf{K}_{shaft} = \mathbf{K}_{tc} + \mathbf{K}_{Tor} + \mathbf{K}_{Bs} + \mathbf{K}_{Bt} \quad (2.1)$$

$$\mathbf{M}_{shaft} = \mathbf{M}_{tc} + \mathbf{M}_{Tor} + \mathbf{M}_{Bs} + \mathbf{M}_{Bt}$$

With indexes *tc* : traction, *Tor* : torsion, *Bs* and *Bt* bending effect (defined in annex 1.)

Bearings and housing are represented by additional lumped stiffness elements at the designated node of the supported shaft elements described above.

b. Gear Body

For many applications with solid gears, it can be approximated as fully rigid or by using beam elements for wide-faced gears for which pinion bending and torsion cannot be neglected.

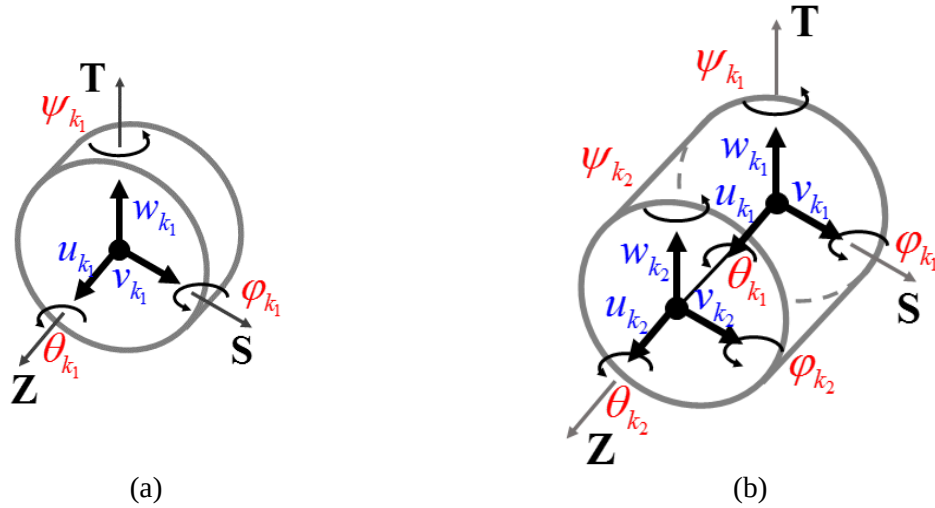


Fig. II-2: Gear body for (a) rigid gear with single node and (b) beam type gear body, with $k = 1, 2$ depending on pinion or wheel

Fig. II-2.a shows the case of a rigid pinion or gear assimilated to a rigid cylinder with a single node at its centre with 6 DOFs, 3 infinitesimal translations and 3 infinitesimal rotations representing the generalised displacements of traction (axial displacements: u_{k_1}), bending (translations in the perpendicular centre directions: v_{k_1}, w_{k_1} and rotations accounting for misalignment angles: $(\varphi_{k_1}, \psi_{k_1})$ and torsion (small angles θ_{k_1} superimposed on large rigid-body rotations). The DOFs being infinitesimal generalised displacements, they can be expressed as screws of coordinates:

$$\begin{Bmatrix} \mathbf{u}_k(O_k) \\ \boldsymbol{\omega}_k \end{Bmatrix} = \begin{Bmatrix} v_{k_1} \mathbf{S} + w_{k_1} \mathbf{T} + u_{k_1} \mathbf{Z} \\ \varphi_{k_1} \mathbf{S} + \psi_{k_1} \mathbf{T} + \theta_{k_1} \mathbf{Z} \end{Bmatrix} \quad (2.2)$$

With O_k centre of pinion or wheel, $k = 1, 2$ depending on pinion of wheel (Fig. II-2).

For the cases of beam-like deformable bodies, two nodes (hence 12 DOFs) are introduced which are connected by a Timoshenko beam element in order to simulate gear body distortions (mainly the torsion and bending of wide-faced pinions) and their influence on tooth load distributions.

1.2. Flexible Body Integration – FE Condensation

For real full flexible gear body, the beam-like model presented above is not sufficient anymore, especially for lightweight webbed wheels with complex body geometries and 3D finite elements models are preferred [MOU14].

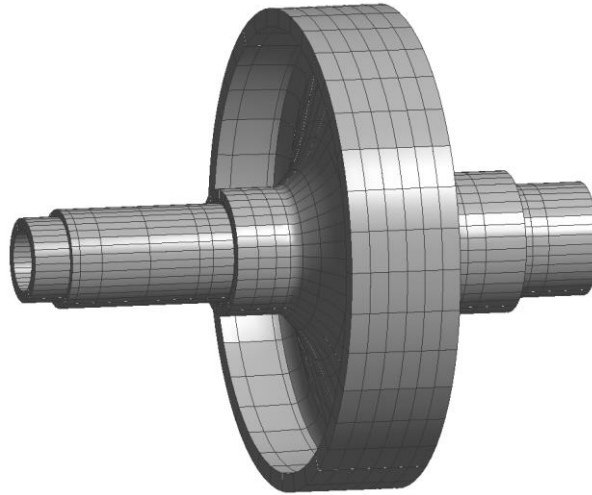
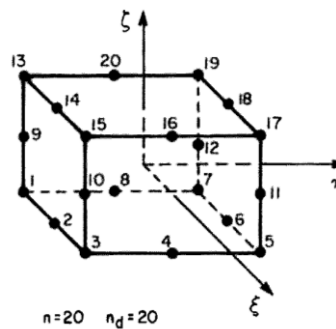


Fig. II-3: Finite Element model of a gear flexible wheel

This method allows the numerical discretisation of any complex geometry into a finite number of simpler elements governed by their shape functions [DHA81]. For instance, Fig. II-3 shows a wheel modelled by using brick Finite Elements (Fig. II-4). Its mechanical analysis is made through a finite number of equations proportional to the number of nodes present in the system.



$$\langle P \rangle = \langle 1 \quad \xi \quad \eta \quad \zeta; \quad \xi^2 \quad \xi\eta \quad \eta^2 \quad \eta\zeta \quad \zeta^2 \quad \xi\zeta; \\ \xi^2 \eta \quad \xi\eta^2 \quad \eta^2 \zeta \quad \eta\zeta^2 \quad \xi\zeta^2 \quad \xi^2 \zeta \quad \xi\eta\zeta; \quad \xi^2 \eta\zeta \quad \xi\eta^2 \zeta \quad \xi\eta\zeta^2 \rangle$$

Fig. II-4: Dhatt's brick Finite Elements [DHA81]

In the present case, the webbed body can have a particular geometry that requires a large number of elements leading to millions of degrees-of-freedom which, in practice, prevents from the direct use of finite element models. A classic method of model reduction is the condensation of FE models, also referred to as Component Mode Synthesis (CMS) which can simulate the static and modal behaviour of a complex FE structure by using a reduced number of interface nodes. This approach has two main advantages:

- The use of interface nodes only considerably reduces the system size and computational cost.
- The possibility of creating modular models by connecting a variety of substructures linked by their respective interface nodes.

In order to keep the interface nodes only, the set of nodes of the complete model is divided into two subsets: a) the boundary and, b) the interior nodes leading to the following partitioned DOF vector \mathbf{X}_{ss} , mass and stiffness ($\mathbf{M}_{ss}, \mathbf{K}_{ss}$) matrices:

$$\mathbf{X}_{ss} = \begin{Bmatrix} \mathbf{X}_b \\ \mathbf{X}_i \end{Bmatrix} \quad (2.3)$$

$$\mathbf{M}_{ss} = \begin{bmatrix} \mathbf{M}_{bb} & \mathbf{M}_{bi} \\ \mathbf{M}_{ib} & \mathbf{M}_{ii} \end{bmatrix}, \mathbf{K}_{ss} = \begin{bmatrix} \mathbf{K}_{bb} & \mathbf{K}_{bi} \\ \mathbf{K}_{ib} & \mathbf{K}_{ii} \end{bmatrix}$$

With : b and i respectively standing for boundary and interior DOFs

From this choice of interior and boundary nodes, numerous technics of condensation are possible which are usually separated into a) fixed-interface condensations and, b) free-interface condensations. Both methodologies rely on shape functions of static and dynamic modes. For the sake of illustrating these notions, the simplified example proposed in [WEN98] is developed below. Fig. II-5 shows a simple beam model composed of two beam elements and a single interface node with two DOFs (x_b, φ_b) at its centre (Fig. II-5).

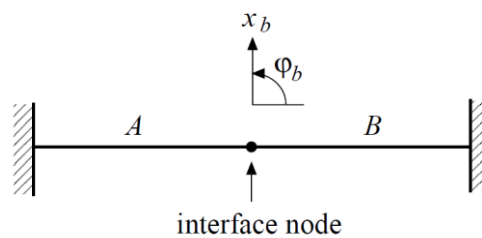


Fig. II-5: Simple example of a beam with a single interface node [WEN98]

a. Fixed-Interface Method

Starting with the widely used fixed-interface method as designated by Craig and Bampton [CRA68], the static modes are obtained by imposing a unit displacement (x_b or φ_b) at the interface node while all the others are blocked thus leading to the static mode shapes in Fig. II-6.



Fig. II-6: First ($x_b = 1, \varphi_b = 0$) and second ($x_b = 0, \varphi_b = 1$) constraint (static) modes [WEN98]

On the other ends, the dynamic modes are the first n modes of the sub-structure determined with the interface node held fixed (for example, the first mode is shown Fig. II-7).

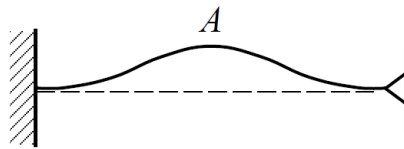


Fig. II-7: First dynamic mode [WEN98]

b. Free-Interface Method

Several free-interface methods have been developed over the years which use the static modes found when applying a single load at one interface DOF of the structure while the others remain free of load (Fig. II-8). Such modes are called flexibility modes.

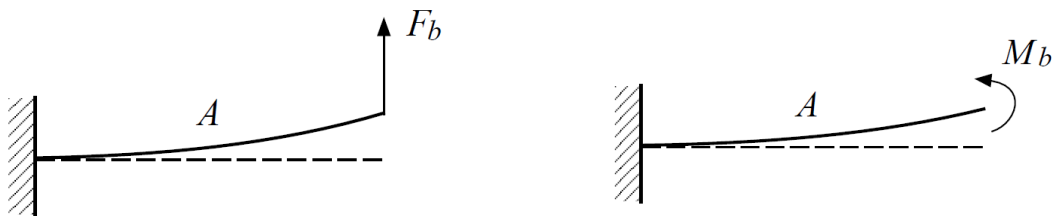


Fig. II-8: First ($F_b = 1$) and 2nd ($M_b = 1$) flexibility modes [WEN98]

The dynamic modes are the n modes obtained on the sub-structure while the interface nodes remain free (first mode in Fig. II-9).

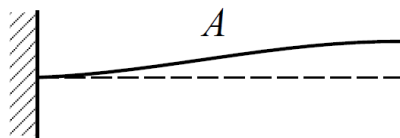


Fig. II-9: First Dynamic mode [WEN98]

The main problems of this type of condensation techniques come from the possible presence of rigid-body modes with a free interface. Herting [HER85] includes these rigid-body modes by temporarily imposing a boundary condition on their displacement so that the system is in equilibrium between the load on the free interface DOFs and the inertial load arising from rigid-body accelerations [TRA15].

The choice between these two techniques mainly depends on the load distribution on the whole structure [HER85]. A system with heavy components, where most of the interface points are constrained, will be better condensed by using the fixed-interface method. A lighter structure, comprising lots of interface nodes that could remain free after the link to the other part of the model will be better condensed with the free-interface method. Besides, the fixed-interface method, easier to implement, is more suited when low frequencies are concerned whereas the free-interface method is more precise for higher frequencies.

Considering the particular case of interest in this memoir, i.e. high-speed light-weight gears connected to the rest of the system by a few nodes only, the Herting free-interface method has been retained, for which the resulting DOF vectors are expressed in terms of the full DOFs system as:

$$\{\mathbf{u}\} = \begin{Bmatrix} \mathbf{u}_b \\ \mathbf{u}_i \end{Bmatrix} = [\mathbf{H}_{gh}] \{\mathbf{u}_h\} + \begin{Bmatrix} \mathbf{0} \\ \delta\mathbf{u}_i \end{Bmatrix} \quad (2.4)$$

With:

$\mathbf{u}_b, \mathbf{u}_i$ and \mathbf{u}_h respectively the boundary, interior and full structure DOFs

$$[\mathbf{H}_{gh}] = \begin{bmatrix} \mathbf{I} & \mathbf{0} & \mathbf{0} \\ \mathbf{G}_{ib} & \mathbf{H}_{i0} & \phi_i - \mathbf{G}_{ib}\phi_b \end{bmatrix} \text{ transfer matrix defined according to [HER85]}$$

$\delta\mathbf{u}_i$ relative function calculated [HER85]

This relation between the interior and boundary DOFs makes it possible to keep the boundary nodes only thus enabling direct DOF couplings in modular systems comprising several sub-structures. The resulting condensed matrices can then be expressed in terms of the boundary static and modal DOFs as:

$$[\mathbf{M}_s] = \begin{bmatrix} \mathbf{M}_{bb} & \mathbf{M}_{bn} \\ \mathbf{M}_{nb} & \mathbf{M}_{nn} \end{bmatrix} \quad [\mathbf{K}_s] = \begin{bmatrix} \mathbf{K}_{bb} & \mathbf{0} \\ \mathbf{0} & \mathbf{K}_{nn} \end{bmatrix} \quad (2.5)$$

With b and n respectively boundary and modal DOFs.

It is also interesting to note that in this particular free-interface formulation, the boundary and modal DOFs are statically uncoupled [HER85].

Following [BET06-COO15-NOG09-BOG12], the gear teeth are discarded from the substructure representing the wheel (Fig. II-3) and the interface nodes are those lying on the gear body rim and one node located at the centres of the bearing supporting the gear shaft as illustrated in Fig. II-10.

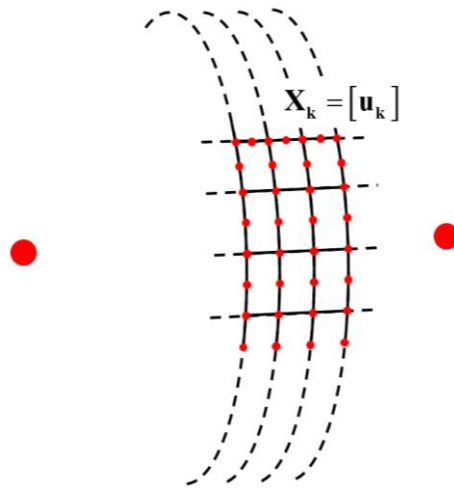


Fig. II-10: Sub-structure master nodes ($k = 1, 2$ depending on pinion or wheel)

Because of the nature of the brick Finite Elements [DHA81], the interface rim nodes to be connected to the gear mesh each have 3 DOFs (three infinitesimal translations) while the master nodes defined at the bearing locations have 6 DOFs (three infinitesimal translations and three infinitesimal rotations) allowing a direct link to bearing stiffness matrices.

1.3. Gear Element Presentation – Modular Model

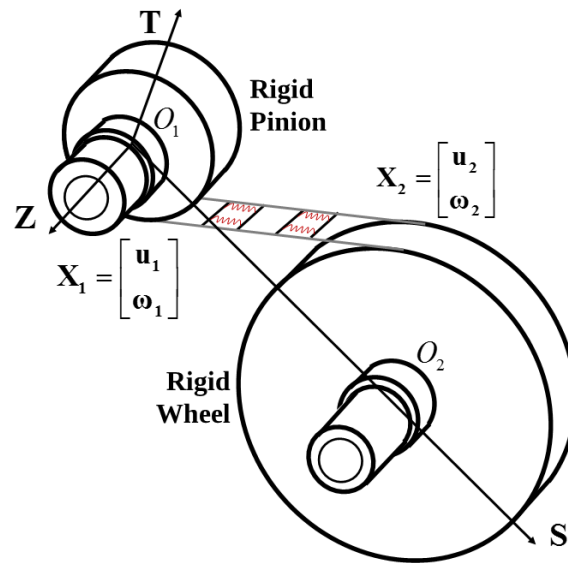


Fig. II-11: Initial gear element with rigid body approach

The initial gear model is based on the developments of Maatar and Vexex [VEL96] illustrated in Fig. II-11 and described in section 1.1. The hypothesis of displacements is used throughout and it is assumed that geometry is not affected by deflections. It is assumed that all the contact points lie on the lines of contact in the theoretical base plane which are discretized into equal-length elementary cells as shown in Fig. II-12.

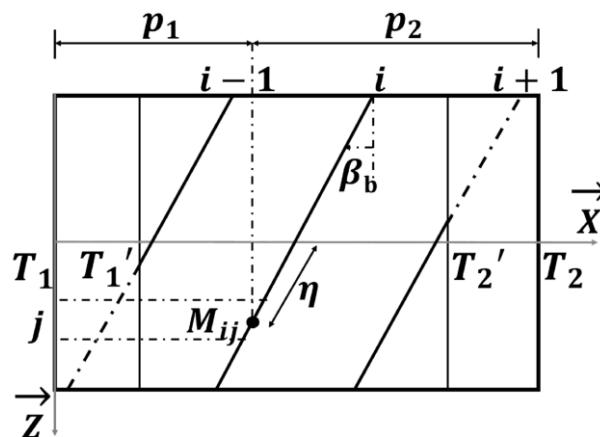


Fig. II-12: Discretised base plane of the gear

A local mesh stiffness k_{ij} and a composite normal deviation, which accounts for errors and tooth shape modifications on the pinion and gears tooth flanks, are associated with every cell j of line i centred at M_{ij} . Depending on the contacting cells at time t , the corresponding

instant contact length and mesh stiffness functions are derived, which leads to the time-varying mesh stiffness $[\mathbf{K}_{12}(t)]$.

The normal deflection $\Delta(M_{ij})$ at any cell of the base plane can be expressed as:

$$\Delta(M_{ij}) = \delta(M_{ij}) - \delta_0(M_{ij}) \quad (2.6)$$

With δ_0 and δ , respectively the initial tooth separation and normal approach.

The normal approach with respect to rigid-body positions in the normal direction reads (eq. 2.7).

$$\delta(M_{ij}) = \mathbf{u}_1(M_{ij}) \cdot \mathbf{n}_1 + \mathbf{u}_2(M_{ij}) \cdot \mathbf{n}_2 \quad (2.7)$$

With $\mathbf{n}_1, \mathbf{n}_2$ the unit outer normal vector to the pinion and gear tooth flanks respectively.

The initial tooth gap [VEL11] includes the sum of the normal deviations on both pinion and wheel flanks denoted $e(M_{ij})$ which, conventionally, is positive when material is added to the theoretical flank surfaces and negative when material is removed (profile or lead modifications etc.) (Fig. II-13).

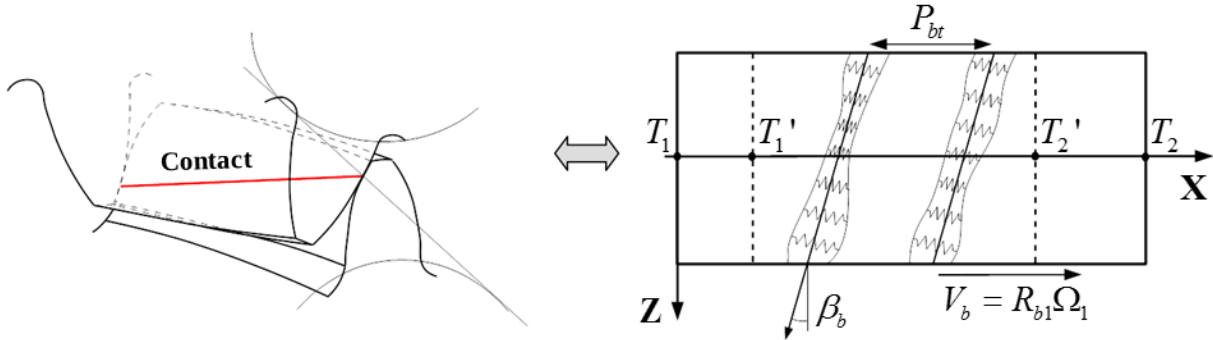


Fig. II-13: Base plane with initial tooth gap distribution on contact lines [VEL11]

Under no-load conditions, contacts occur where $e(M_{ij})$ is maximum so that the initial normal separation between the pinion and gear tooth flanks is derived as:

$$\delta_0(M_{ij}) = \max_M (e(M_{ij})) - e(M_{ij}) \quad (2.8)$$

With $\max_M (e(M_{ij}))$ maximum of $e(M_{ij})$ over all potential contact points M_{ij}

Considering rigid pinion and gear bodies with one central node each, the normal deflection can be expressed in terms of the degrees of freedom at the central node O_1 and O_2 as:

$$\Delta(M_{ij}) = \begin{bmatrix} \mathbf{n}_1 \\ \mathbf{n}_1 \times \mathbf{M}_{ij} \mathbf{O}_1 \\ \mathbf{n}_2 \\ \mathbf{n}_2 \times \mathbf{M}_{ij} \mathbf{O}_2 \end{bmatrix}^T \begin{bmatrix} \mathbf{u}_1(O_1) \\ \boldsymbol{\omega}_1 \\ \mathbf{u}_2(O_2) \\ \boldsymbol{\omega}_2 \end{bmatrix} - \delta_0(M_{ij}) \quad (2.9)$$

With $\mathbf{X} = \{\mathbf{u}_1(O_1) \quad \boldsymbol{\omega}_1 \quad \mathbf{u}_2(O_2) \quad \boldsymbol{\omega}_2\}^T$ DOFs at the pinion and gear centres.

The proposed approach consists in replacing one or two rigid cylinders by a deformable body simulated by using finite elements as schematically represented in Fig. II-14. Conceptually, this is equivalent to the substitution of the central node O_k of one of the members by condensed mass and stiffness matrices expressed at the interface nodes with the mesh elastic foundation [GUI18-in prep.].

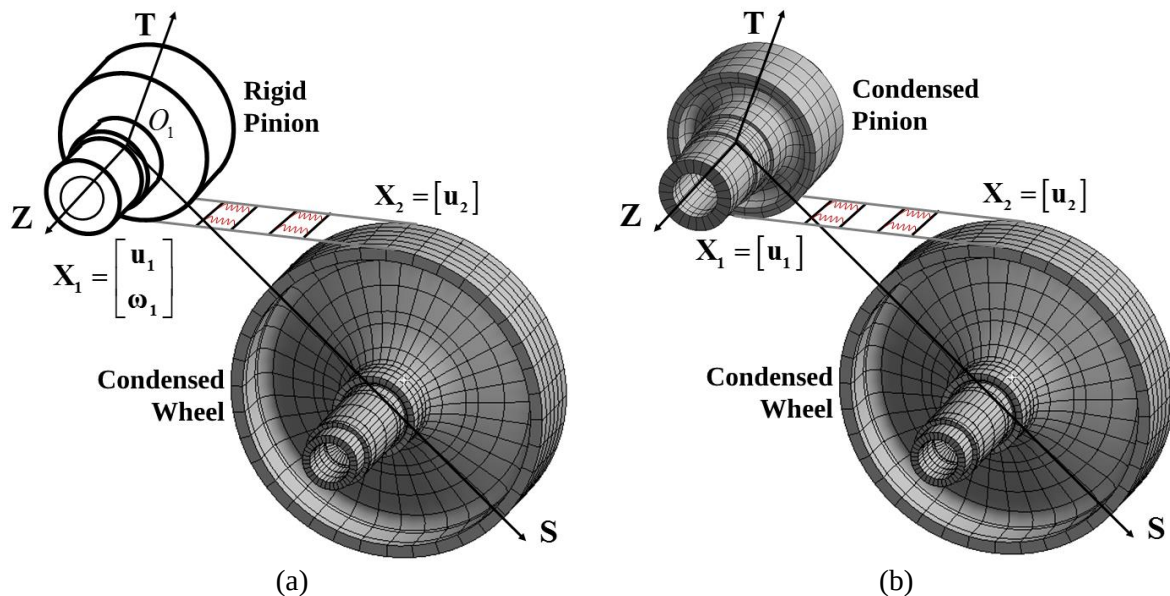


Fig. II-14: Modular model with (a) only flexible gear and (b) flexible pinion and gear

The normal deflection at any potential point of contact takes a different form as it involves different degrees of freedom at different points i.e. at the rim of the condensed sub-structure. Considering the hybrid model combining a rigid pinion and a flexible gear (Fig. II-14.a example case), one obtains:

$$\Delta(M_{ij}) = \begin{bmatrix} \mathbf{n}_1 \\ \mathbf{n}_1 \times \mathbf{M}_{ij} \mathbf{O}_1 \\ \mathbf{n}_2 \\ \mathbf{n}_2 \times \mathbf{M}_{ij} \mathbf{M}_{p_{ij}} \end{bmatrix}^T \begin{bmatrix} \mathbf{u}_1(O_1) \\ \boldsymbol{\omega}_1 \\ \mathbf{u}_2(M_{p_{ij}}) \\ \boldsymbol{\omega}_2 \end{bmatrix} - \delta_0(M_{ij}) \quad (2.10)$$

With $\mathbf{n}_2 = -\mathbf{n}_1$ and $\mathbf{X} = \{\mathbf{u}_1(O_1) \quad \boldsymbol{\omega}_1 \quad \mathbf{u}_2(M_{p_{ij}}) \quad \boldsymbol{\omega}_2\}^T$ DOFs vector expressed at the pinion centre O_1 and the tooth root $M_{p_{ij}}$ of the gear for each cell ij of the discretised base plane.

As for the classic model, the DOF vector associated with the pinion at any potential point of contact can be readily deduced from that at its centre by using the shifting property of screws. On the other hand, the degrees of freedom of interest for the flexible gear model comprise only translational displacements and no rotations (brick elements) and are not defined at the position corresponding to the points of contact on tooth flanks but at the root of these teeth. In these conditions, a specific tooth model needs to be developed to connect the root and flank DOFs.

2. Hybrid Model – Tooth Model Development

2.1. Introduction

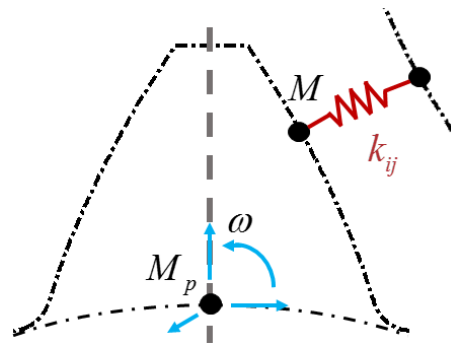


Fig. II-15: Rigid plate tooth model

Each tooth is decomposed into a number of very thin slices and, in order to remain consistent with the mesh models previously employed, every slice is assimilated to a rigid plate with translational and rotational degrees of freedom. Because of symmetry, it is interesting to introduce the point M_p at the intersection of the slice neutral fibre and the root cylinder. In agreement with the developments of Weber [WEB53], Sainsot *et al.* [SAI04] for determining the contributions of elastic gear body to tooth deflections, only the rotation with respect to the \mathbf{Z} axis is conserved thus leading for every slice to a screw of infinitesimal displacements of the form (Fig. II-15):

$$\begin{cases} \mathbf{u}(M_p) \\ \omega \mathbf{Z} \end{cases} \quad (2.11)$$

By so doing, the displacement at any point of contact M on the side of this slice can be determined using the shifting property of the moment fields of screws. The situation is therefore similar to that of the classic model with the difference that far more degrees of freedom are involved (those of all the slices in contact) as opposed to the 6 degrees-of-freedom at the centre of the pinion or the gear.

The main difficulty at this stage comes from the way to connect every slice to the deformable body (gear and/or pinion) model and the two following issues will be successively addressed:

- The definition of the angular degree of freedom $\omega_{\mathbf{Z}}$ knowing that the FE model uses brick elements with translational DOFs only.
- The problem of compatibility between a discrete Winkler foundation with independent stiffness elements (mesh elastic model) and a continuous FE model.

2.2. Two-point Connection

The link between every thin slice and a deformable body can conceptually be viewed as a two-point connection, i.e. two points M_{p_1} and M_{p_2} situated on the root circle arc of a slice at the same distance from M_p are supposed to be rigidly fixed to the finite element grid surface at the rim (Fig. II-16). Such a methodology makes it possible to transfer both translations and rotations (limited to that around \mathbf{Z} here) between the tooth and gear body models.

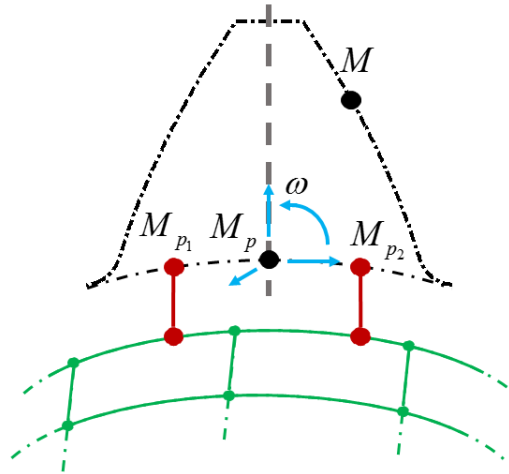


Fig. II-16: Tooth rotation inclusion on a thin slice for tooth root displacement

Let us introduce the following vectors:

- \mathbf{u}_1 and \mathbf{u}_2 , the ‘exact’ displacements at points M_{p_1} and M_{p_2} respectively which here correspond to the displacements given by the finite element model,
- $\tilde{\mathbf{u}}_1$ and $\tilde{\mathbf{u}}_2$, the approximate displacements at points M_{p_1} and M_{p_2} respectively which are obtained by supposing that M_{p_1} and M_{p_2} are two points of the rigid slice so that they can be expressed in terms of the DOFs at the central point M_p as:

$$\begin{aligned}\tilde{\mathbf{u}}(M_{p_1}) &= \mathbf{u}(M_p) + \mathbf{M}_{p_1} \mathbf{M}_p \times \omega \mathbf{Z} \\ \tilde{\mathbf{u}}(M_{p_2}) &= \mathbf{u}(M_p) + \mathbf{M}_{p_2} \mathbf{M}_p \times \omega \mathbf{Z}\end{aligned}\quad (2.12)$$

In theory these two vector fields must be identical but the connection is not fully compatible (since the circle arc can be distorted and $\|\mathbf{M}_{p_1} \mathbf{M}_{p_2}\|$ is not necessarily constant). However, an approximate formulation is employed which relies on the minimization of the difference between the exact and approximate displacements. The following functional is introduced:

$$J(u, v, w, \omega) = \frac{1}{2} \left[(\tilde{\mathbf{u}}_1 - \mathbf{u}_1)^2 + (\tilde{\mathbf{u}}_2 - \mathbf{u}_2)^2 \right] \quad (2.13)$$

where u, v and w are the three components of $\mathbf{u}(M_p)$

$$\begin{aligned}\frac{\partial J}{\partial u} = 0, \quad \frac{\partial J}{\partial v} = 0, \quad \frac{\partial J}{\partial w} = 0 \\ \frac{\partial J}{\partial \omega} = 0\end{aligned}\quad (2.14)$$

After developing and rearranging the first three equations, one obtains:

$$2\mathbf{u}(M_p) - \mathbf{u}_1 - \mathbf{u}_2 + \omega(\mathbf{M}_{p_1} \mathbf{M}_p + \mathbf{M}_{p_2} \mathbf{M}_p) \times \mathbf{Z} = \mathbf{0} \quad (2.15)$$

Noticing that $(\mathbf{M}_{p_1} \mathbf{M}_p + \mathbf{M}_{p_2} \mathbf{M}_p)$ is a small quantity (which would be nil if the curvature between P_1 and P_2 were neglected), a first order approximation leads to:

$$\mathbf{u}(M_p) \approx \frac{1}{2}(\mathbf{u}_1 + \mathbf{u}_2) \quad (2.16)$$

The minimisation with respect to ω (eq. 2.17) combined with the approximate result above (eq. 2.16) finally gives the expression of the angular degree of freedom associated with the thin slice:

$$\begin{aligned}(\mathbf{M}_{p_1} \mathbf{M}_p \times \mathbf{Z}) \cdot (\mathbf{u} + \mathbf{M}_{p_1} \mathbf{M}_p \times \omega \mathbf{Z} - \mathbf{u}_1) \\ + (\mathbf{M}_{p_2} \mathbf{M}_p \times \mathbf{Z}) \cdot (\mathbf{u} + \mathbf{M}_{p_2} \mathbf{M}_p \times \omega \mathbf{Z} - \mathbf{u}_2) = 0\end{aligned}\quad (2.17)$$

$$\omega \approx \frac{1}{2 \left(\|\mathbf{M}_{p_1} \mathbf{M}_p\|^2 + \|\mathbf{M}_{p_2} \mathbf{M}_p\|^2 \right)} \left[(\mathbf{u}_1 - \mathbf{u}_2) \cdot (\mathbf{M}_{p_1} \mathbf{M}_{p_2} \times \mathbf{Z}) \right] \quad (2.18)$$

Based on these results the displacement at the point of contact M of the gear in the normal direction of the slice can be derived by using the shifting property of the moment field of screws as:

$$\mathbf{u}(M) \cdot \mathbf{n}_2 = \mathbf{u}(M_p) \cdot \mathbf{n}_2 + (\mathbf{M}\mathbf{M}_p \times \omega \mathbf{Z}) \cdot \mathbf{n}_2 \quad (2.19)$$

NB: similar developments can apply for the pinion but, for the sake of simplicity, only the case of a rigid pinion body and a flexible gear is considered in this section.

The new normal deflection at M_p point is then be upgraded for both pinion and wheel sides with the same procedure for each tooth slice ij (eq. 2.10). This leads to an expression that separates the tooth flank line of contact, into two lines lying on rim mesh (Fig. II-17).

$$\Delta(M) = [\mathbf{n}_1, \mathbf{n}_1 \times \mathbf{M}\mathbf{O}_1, \frac{1}{2} \mathbf{n}_2^T + \lambda_p(M) \boldsymbol{\kappa}_p, \frac{1}{2} \mathbf{n}_2^T - \lambda_p(M) \boldsymbol{\kappa}_p]^T \begin{bmatrix} \mathbf{u}(O_1) \\ \boldsymbol{\omega}_1 \\ \mathbf{u}_1 \\ \mathbf{u}_2 \end{bmatrix} - \delta_0(M) \quad (2.20)$$

With:

$$\lambda_p(M) = \mathbf{Z} \cdot (\mathbf{M}_p \mathbf{M} \times \mathbf{n}_2)$$

$$\boldsymbol{\kappa}_p = \frac{\mathbf{M}_{p_1} \mathbf{M}_{p_2} \times \mathbf{Z}}{2 \left(\|\mathbf{M}_{p_1} \mathbf{M}_p\|^2 + \|\mathbf{M}_{p_2} \mathbf{M}_p\|^2 \right)}$$

$$\mathbf{n}_2 = -\mathbf{n}_1$$

2.3. Mortar Based Interface for Virtual Compatibility

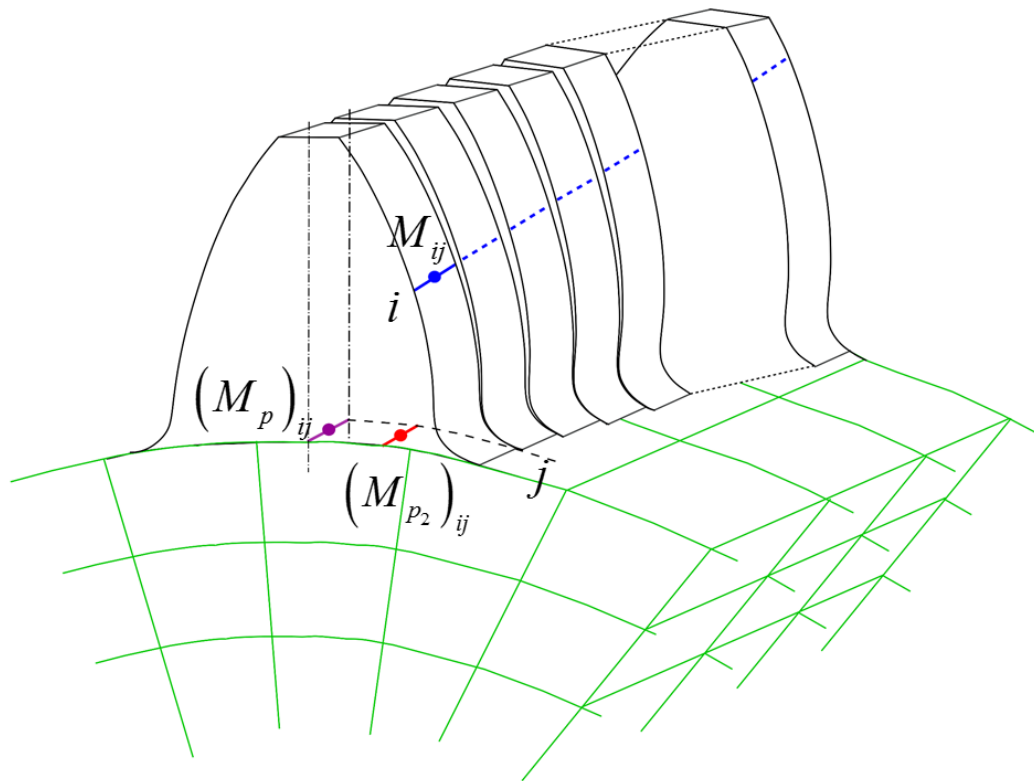


Fig. II-17: Two-point connection for tooth width (only point $(M_{p_2})_{ij}$ is displayed for simplicity sake)

With the objective of calculating not only global dynamic mesh forces but also instant dynamic tooth load distributions on tooth flanks, the contact lines transferred on the two-point connection (Fig. II-17) and the 3D finite element model need to be compatible in order to avoid local load spikes generated by mismatched grids. In this context of coupling 3D and 1D models, the methods of domain decomposition [BER94-LAC97-CHA07] and mortar [BEL97] have been proved effective whereas the Arlequin [DHI05] and Latin [DUR03] techniques appear as more adapted to multimodel and multi-physics 3D coupling.

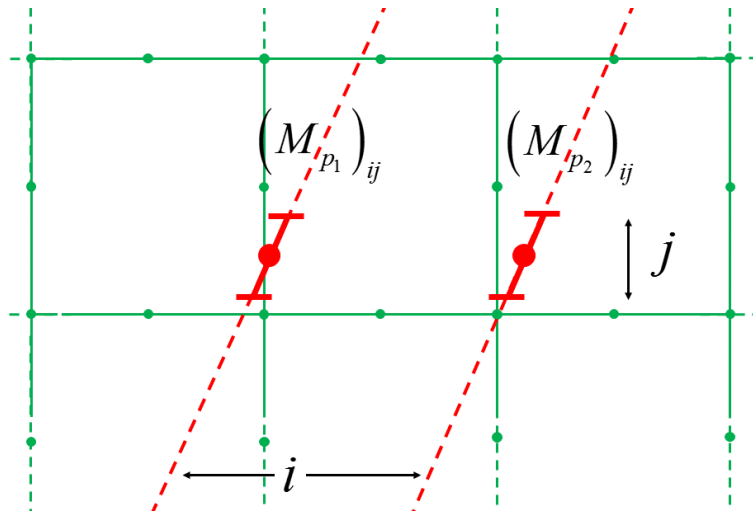


Fig. II-18: Projection of discretised segment on FE mesh

The purpose of the proposed mortar-based interface applied to the lines of contact is to introduce an intermediate line discretisation with nodes not just at the centre (as is the original model in Fig. II-17 and Fig. II-18) but also nodes at the extremities, leading to a quadratic continuous representation compatible with the rim FE model (Fig. II-19).

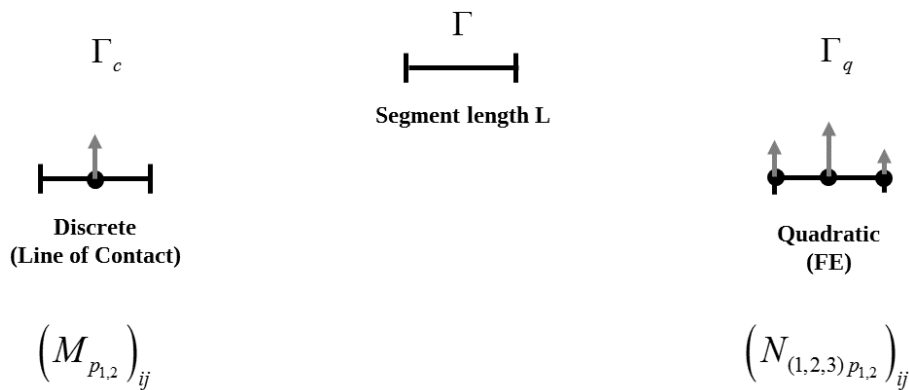


Fig. II-19: Different discretisation for the segment, from c for discrete line of contact to q for the quadrating FE matching segment

The segment of reference Γ of length L , independent of the discretisation, represents a real segment of contact submitted to a continuous force field \mathbf{f} and characterised by a resulting continuous displacement field \mathbf{q} . As the discretisation shift is identical in all directions, the theory is developed in one direction only and scalar displacement and force fields q and f are employed in what follows.

Γ_c is an initial stepwise segment of length L which stems for the discrete contact lines and is associated with the two-point connection model each segment centred at points (nodes) $M_{p_{1,2}}$ on the surface of the rim finite element model (Fig. II-17). It is characterised by a uniform force per unit of contact length F_c and a constant displacement Q_c .

Γ_q is a segment with quadratic approximation (length L) for both displacement and force fields which can be linked with the finite element and ensures continuity between adjacent segments. The three nodes are denoted $N_{(1)P_{1,2}}$, $N_{(2)P_{1,2}}$ and $N_{(3)P_{1,2}}$. The corresponding force per unit of contact length at the three nodes of the segment is denoted \mathbf{F}_q whereas the displacements at the same nodes are embodied in vector \mathbf{Q}_q .

The objective is formulated as to find the relation between the displacements of the stepwise and quadratic segments based on the works generated on the two grids. The work associated with the stepwise discretisation is simply:

$$W_c = F_c Q_c L \quad (2.21)$$

whereas, for the quadratic approximation, it reads:

$$W_q = \int_{\Gamma} (\mathbf{N}_q^T \mathbf{F}_q)^T (\mathbf{N}_q^T \mathbf{Q}_q) d\Gamma \quad (2.22)$$

where \mathbf{N}_q includes the quadratic shape functions for a line element [DHA81] such that:

$$\mathbf{N}_q^T = \left[\frac{\xi}{L} \left(\frac{2}{L} \xi - 1 \right) \quad -\frac{4}{L} \left(\frac{L}{2} - \xi \right) \left(\frac{L}{2} + \xi \right) \quad \frac{\xi}{L} \left(1 + \frac{2}{L} \xi \right) \right] \quad (2.23)$$

With ξ coordinate on the segment, $\xi \in \left[-\frac{L}{2} \quad \frac{L}{2} \right]$ and L segment length

Using a mortar technique, the force and displacement fields for two different approximations are combined so that the following approximate equation is obtained:

$$F_c Q_c L \approx \int_{\Gamma} F_c (\mathbf{N}_q^T \mathbf{Q}_q) d\Gamma \quad (2.24)$$

hence,

$$Q_c \approx \frac{1}{L} \left[\int_{\Gamma} \mathbf{N}_q^T d\Gamma \right] \mathbf{Q}_q \quad (2.25)$$

which, after integration, finally gives:

$$Q_c \approx \frac{1}{30} [5 \quad 20 \quad 5] \mathbf{Q}_q \quad (2.26)$$

The demonstration so far was limited to a single DOF per node but can be readily extended to nodes with 3 translational degrees-of-freedom as is the case for the brick finite elements. on the discretised line of contact, for all three u, v, w , Q_c is extended to the vector $\mathbf{u}(M_{p_{1,2}})_{ij}$, and the vector \mathbf{Q}_q is extended from 3 to 9 DOFs (3 nodes of 3 DOFs each) to the vector $\mathbf{u}(N_{(1,2,3)p_{1,2}})_{ij}$.

The shape function matrices are duplicated for all directions, and the resulting displacement field is written from eq. 2.25, leading to visualisation Fig. II-20.

$$\mathbf{u}(M_{p_{1,2}})_{ij} = [\mathbf{N}] \mathbf{u}(N_{(1,2,3)p_{1,2}})_{ij} \quad (2.27)$$

with $[\mathbf{N}] = \begin{bmatrix} 5 & 20 & 5 & 0 & 0 & 0 & 0 & 0 & 0 \\ 0 & 0 & 0 & 5 & 20 & 5 & 0 & 0 & 0 \\ 0 & 0 & 0 & 0 & 0 & 0 & 5 & 20 & 5 \end{bmatrix}$

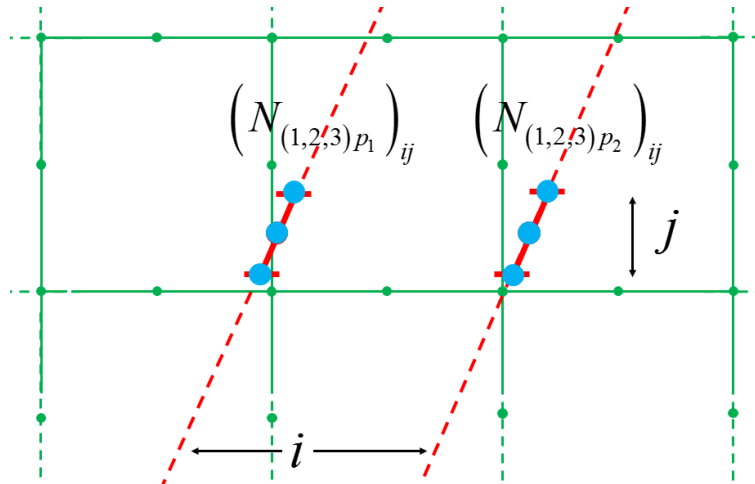


Fig. II-20: New node place on mesh after mortar

The interest and accuracy of the mortar-based formulation in equation (2.26) is illustrated by considering the 2D patch test represented in Fig. II-21. A discrete line model (discrete elements) is pressed by a uniform line force distribution \mathbf{f}_d against a 2D finite element

grid with different node distributions at the contact interface. Fig. II-22 shows the discretised solutions obtained by direct collocation and using the mortar gluing technique described above. The exact solution consists in a uniform displacement field and it can be observed that direct collocation induces unrealistic load spikes whereas (2.26) leads to the exact solution thus proving that the proposed methodology is sound.

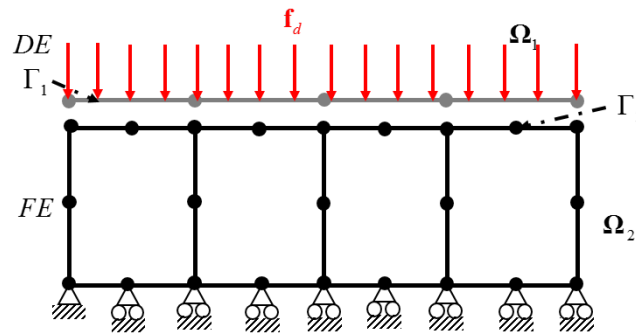


Fig. II-21: Patch test problem with discrete elements (DE) and finite element (FE)

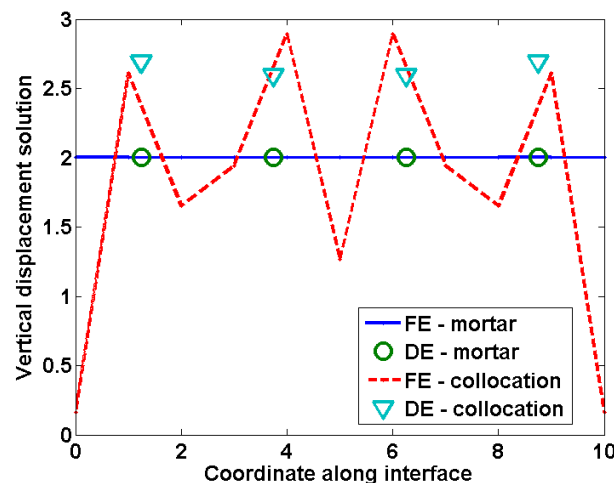


Fig. II-22: Displacement along the interface for collocation and mortar interface

2.4. Shape Functions for Node Coincidence – Final Link

The last phase of the procedure is aimed at linking the displacement at $\left(N_{(1,2,3)p_{1,2}}\right)_{ij}$, every node of the discretised line to the far fewer rim FE model nodes lying underneath Fig. II-20. Each point $\left(N_{(1,2,3)p_{1,2}}\right)_{ij}$ can lie anywhere on the surface of the 20-node brick elements of

the rim model which, as far as displacement approximation is concerned, can be restricted to 8 node elements since surface displacements only are needed (Fig. II-20).

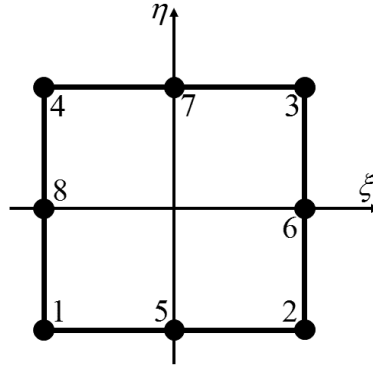


Fig. II-23: Node repartition for brick element surface

The linkage point lies on the surface of this 8 node element (Fig. II-17). The shape functions P_i associated are calculated with the natural coordinates of each point $\left(N_{(1,2,3)p_{1,2}}\right)_{ij}$ determined into the parent element coordinate system η, ξ .

$$\begin{aligned}
 P_1 &= -\frac{1}{4}(1-\xi)(1-\eta)(1+\xi+\eta) & P_5 &= \frac{1}{2}(1-\xi^2)(1-\eta) \\
 P_2 &= \frac{1}{4}(1+\xi)(1-\eta)(\xi-\eta-1) & P_6 &= \frac{1}{2}(1+\xi)(1-\eta^2) \\
 P_3 &= \frac{1}{4}(1+\xi)(1+\eta)(\xi+\eta-1) & P_7 &= \frac{1}{2}(1-\xi^2)(1+\eta) \\
 P_4 &= \frac{1}{4}(1-\xi)(1+\eta)(\eta-\xi-1) & P_8 &= \frac{1}{2}(1-\xi)(1-\eta^2)
 \end{aligned} \tag{2.28}$$

Their contribution to the displacement \mathbf{u}_3 of discretisation Γ_q of the contact line can therefore be written in the form:

$$\mathbf{u}_3 \left(N_{(1,2,3)p_{1,2}} \right)_{ij} = \mathbf{P} \left(N_{(1,2,3)p_{1,2}} \right)_{ij} \mathbf{X}_2 \tag{2.29}$$

With $\left[\mathbf{P} \left(N_{(1,2,3)p_{1,2}} \right) \right]_{ij}$ matrix of the shape functions at point $\left(N_{(1,2,3)p_{1,2}} \right)_{ij}$ at the surface of the element and \mathbf{X}_2 sub-structure displacements.

The full virtual interface, composed of the two-point connection, mortar interface and FE model function can be seen as a patch between the discrete model mesh and condensed sub-structure as illustrated in Fig. II-24.

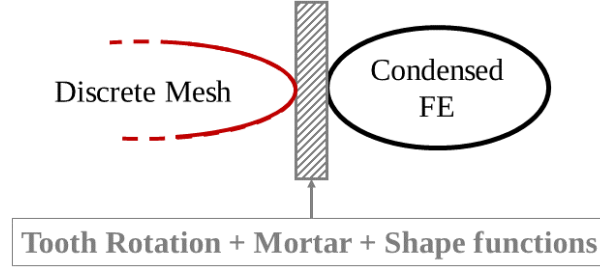


Fig. II-24: Scheme of interface summary

This new model is introduced in the normal deflection expression (eq. 2.9) linking the discrete mesh model points M_{ij} to the condensed FE model rim nodes. The normal deflection can thus be written again:

$$\Delta(M_{ij}) = \mathbf{V}^*(M)^T \mathbf{X}_m - \delta_0(M_{ij}) \quad (2.30)$$

With:

$$\mathbf{V}^*(M)^T = \left[\left\{ \mathbf{n}_1^T \quad (\mathbf{n}_1 \times \mathbf{M}\mathbf{O}_1)^T \right\} \right. \\ \left. \left\{ \left(\frac{1}{2} \mathbf{n}_2^T + \lambda_p(M) \boldsymbol{\kappa}_p \right) \mathbf{I}_{\text{int}}^T \quad \left(\frac{1}{2} \mathbf{n}_2^T - \lambda_p(M) \boldsymbol{\kappa}_p \right) \mathbf{I}_{\text{int}}^T \right\} \right]$$

$$\lambda_p(M) = \mathbf{Z} \cdot (\mathbf{M}_{p_1} \mathbf{M} \times \mathbf{n}_2)$$

$$\boldsymbol{\kappa}_p = \frac{\mathbf{M}_{p_1} \mathbf{M}_{p_2} \times \mathbf{Z}}{2 \left(\|\mathbf{M}_{p_1} \mathbf{M}_p\|^2 + \|\mathbf{M}_{p_2} \mathbf{M}_p\|^2 \right)}$$

M , M_{p_1} and M_{p_2} standing for M_{ij} , M_{ij,p_1} and M_{ij,p_2} for each tooth slice

$\mathbf{X}_m = \{ \mathbf{u}_1(O_1) \quad \boldsymbol{\omega}_1 \quad \mathbf{X}_2 \}^T$ new DOF vector with \mathbf{X}_2 sub-structure master node DOFs

$\mathbf{I}_{\text{int}} = \frac{1}{L} \mathbf{NP} \left(N_{(1,2,3)p_{1,2}} \right)_{ij}$ mortar interface terms for each $\left(N_{(1,2,3)p_{1,2}} \right)_{ij}$ new root point after

mortar interface

3. Building the Dynamic Model

3.1. Equation of motions – Introduction of Damping

a. Dynamic Equations

The global mesh stiffness matrix and forcing term vector can then be written in terms of the structural vector obtained with the new modular approach.

$$\begin{aligned} [\mathbf{K}_{12}(t)] &= \sum_i \sum_j k_{ij} \mathbf{V}^*(M_{ij}) \mathbf{V}^*(M_{ij})^T \\ \mathbf{F}_{12}(t) &= \sum_i \sum_j k_{ij} \delta_0(t) \mathbf{V}^*(M_{ij}) \end{aligned} \quad (2.31)$$

with k_{ij} local stiffness at each contact cell of the base plane, calculated from Weber and Banaschek analytical model of contact and tooth flexion stiffness [WEB53], removing the foundation stiffness which is directly included in the tooth model developed in section 2.

Still considering a hybrid model with a rigid pinion body and a sub-structured gear, the global equations of motion are:

$$\begin{aligned} &\begin{bmatrix} [\mathbf{M}_1] & 0 \\ 0 & \begin{bmatrix} \mathbf{M}_b & \mathbf{M}_{bn} \\ \mathbf{M}_{nb} & \mathbf{M}_{nn} \end{bmatrix}_2 \end{bmatrix} \begin{bmatrix} \ddot{\mathbf{X}}_1 \\ \ddot{\mathbf{X}}_b \\ \ddot{\phi}_n \end{bmatrix}_2 \\ &+ \begin{bmatrix} [\mathbf{K}_1] & [\mathbf{K}_{12}(t)] \\ [\mathbf{K}_{21}(t)] & \begin{bmatrix} \mathbf{K}_{bb} & \mathbf{0} \\ \mathbf{0} & \mathbf{K}_{nn} \end{bmatrix}_2 \end{bmatrix} \begin{bmatrix} \mathbf{X}_1 \\ \mathbf{X}_b \\ \phi_n \end{bmatrix}_2 = \begin{bmatrix} \mathbf{F}_1 \\ \mathbf{F}_b \\ \mathbf{F}_\phi \end{bmatrix}_2 + \mathbf{F}_{12}(t) \end{aligned} \quad (2.32)$$

With:

\mathbf{X} , physical and ϕ_n modal DOFs of the system

subscripts 1,2 respectively referring to the pinion and gear members

subscripts b and n respectively referring to the interface physical and modal DOFs of the condensed structure.

Similar equations are derived when combining sub-structured pinion and gear members which take the form:

$$\begin{aligned}
 & \begin{bmatrix} \begin{bmatrix} \mathbf{M}_b & \mathbf{M}_{bn} \\ \mathbf{M}_{nb} & \mathbf{M}_{nn} \end{bmatrix}_1 & 0 \\ 0 & \begin{bmatrix} \mathbf{M}_b & \mathbf{M}_{bn} \\ \mathbf{M}_{nb} & \mathbf{M}_{nn} \end{bmatrix}_2 \end{bmatrix} \begin{bmatrix} \begin{bmatrix} \ddot{\mathbf{X}}_b \\ \ddot{\phi}_n \end{bmatrix}_1 \\ \begin{bmatrix} \ddot{\mathbf{X}}_b \\ \ddot{\phi}_n \end{bmatrix}_2 \end{bmatrix} \\
 & + \begin{bmatrix} \begin{bmatrix} \mathbf{K}_{bb} & \mathbf{0} \\ \mathbf{0} & \mathbf{K}_{nn} \end{bmatrix}_1 & \begin{bmatrix} \mathbf{K}_{12}(t) \\ \mathbf{K}_{21}(t) \end{bmatrix} \\ \begin{bmatrix} \mathbf{K}_{12}(t) \\ \mathbf{K}_{21}(t) \end{bmatrix} & \begin{bmatrix} \mathbf{K}_{bb} & \mathbf{0} \\ \mathbf{0} & \mathbf{K}_{nn} \end{bmatrix}_2 \end{bmatrix} \begin{bmatrix} \begin{bmatrix} \mathbf{X}_b \\ \phi_n \end{bmatrix}_1 \\ \begin{bmatrix} \mathbf{X}_b \\ \phi_n \end{bmatrix}_2 \end{bmatrix} = \begin{bmatrix} \begin{bmatrix} \mathbf{F}_b \\ \mathbf{F}_\phi \end{bmatrix}_1 \\ \begin{bmatrix} \mathbf{F}_b \\ \mathbf{F}_\phi \end{bmatrix}_2 \end{bmatrix} + \mathbf{F}_{12}(t)
 \end{aligned} \tag{2.33}$$

b. Damping

The simplest form that can be used is Rayleigh damping [CHO03] which leads to a viscous damping matrix \mathbf{C} expressed as:

$$\mathbf{C} = a_R \mathbf{M} + b_R \mathbf{K} \tag{2.34}$$

with $a_R (s^{-1})$ typically between 10^1 and 10^2 and $b_R (s)$ between 10^{-6} and 10^{-5} for webbed gear applications (\mathbf{M} and \mathbf{K} being the global mass and averaged stiffness matrices).

Modal damping can also be used supposing that there is no energy transfer between different modes thus assuming that, for each mode i , a damping coefficient c_i can be defined in terms of the modal mass and stiffness coefficient (m_i, k_i) as:

$$c_i = 2\xi_i \sqrt{k_i m_i} \tag{2.35}$$

with ξ_i modal damping factor, typically between 0.01 and 0.1.

In the particular case of gears, a composite formula can be used based on the works of Umezawa [UME85] and Ankouni [ANK14-16]. Umezawa experimentally found that a damping factor around 0.07 was representative of the dissipation at the gear mesh whereas structural modes were characterised by lower damping factors around 0.01. It is therefore proposed to employ a weighted average of the two characteristic amplitudes using the percentages of modal strain energy in the gear mesh e_i such that:

$$\xi_i = 0.07e_i + 0.01(1 - e_i) \tag{2.36}$$

3.2. Centrifugal Effects

For high rotational speeds, flexible bodies are submitted to centrifugal effects which might have a direct impact on rim dynamic behaviour and therefore need to be taken into account in the dynamic model. A number of preliminary simulations have been conducted on full 3D FE models of pinions and gears and the following conclusions have been drawn:

- The influence of centrifugal deformations on gear geometry key parameters, such as pressure angle, plane of action discretisation is negligible. A maximum variation of 1% change has been observed for the most flexible test case at its maximum speed (this point will be examined in the validation part).
- Changes are reported on thin-rimmed, thin-webbed applications only and a rigid-body approach is still valid for solid gears,
- Considering the amplitudes of the deformed shapes caused by centrifugal forces, the hypothesis of small deflections remains sound and the meshing equations can be developed using the non-deformed gear geometries. From these hypothesis, the gear geometry parameters are considered constant for any speed [GUO01- LI08.a-13].

The centrifugal effects are extracted from the FE model and condensed along with classical mass and stiffness matrices. This way of extraction allows the system to include the centrifugal nodal displacement [GER84] which is the very dominant component of the studied flexible wheels [MOU14]. It is included into the damped system equation of motions (eq. 2.32 and 2.33) re-written according to equation 2.37 [LAL90].

$$[\mathbf{M}]\ddot{\mathbf{X}} + [\mathbf{C}]\dot{\mathbf{X}} + [\mathbf{K}(t)]\mathbf{X} = [\mathbf{F}(t) + \mathbf{F}_c] \quad (2.37)$$

With

\mathbf{F}_c centrifugal load of webbed parts,

$$\mathbf{F}_c = \left\{ \begin{array}{c} 0 \\ \left\{ \mathbf{F}_b \right\} \\ \left\{ \mathbf{F}_n \right\}_2 \end{array} \right\} \text{ for rigid pinion, flexible wheel and } \mathbf{F}_c = \left\{ \begin{array}{c} \left\{ \mathbf{F}_b \right\} \\ \left\{ \mathbf{F}_n \right\}_1 \\ \left\{ \mathbf{F}_b \right\} \\ \left\{ \mathbf{F}_n \right\}_2 \end{array} \right\} \text{ for full flexible case}$$

3.3. Algorithm

The system obtained eq. (2.37) can exhibit nonlinearities associated with momentary partial or total losses followed by shocks between the mating teeth arising from large vibration amplitudes. The solving solution has first been introduced by Vexex and Maatar [VEL96-MAA97], it relies on the combination of a Newmark time step integration (annex 2.) and a contact algorithm illustrated Fig. II-25.

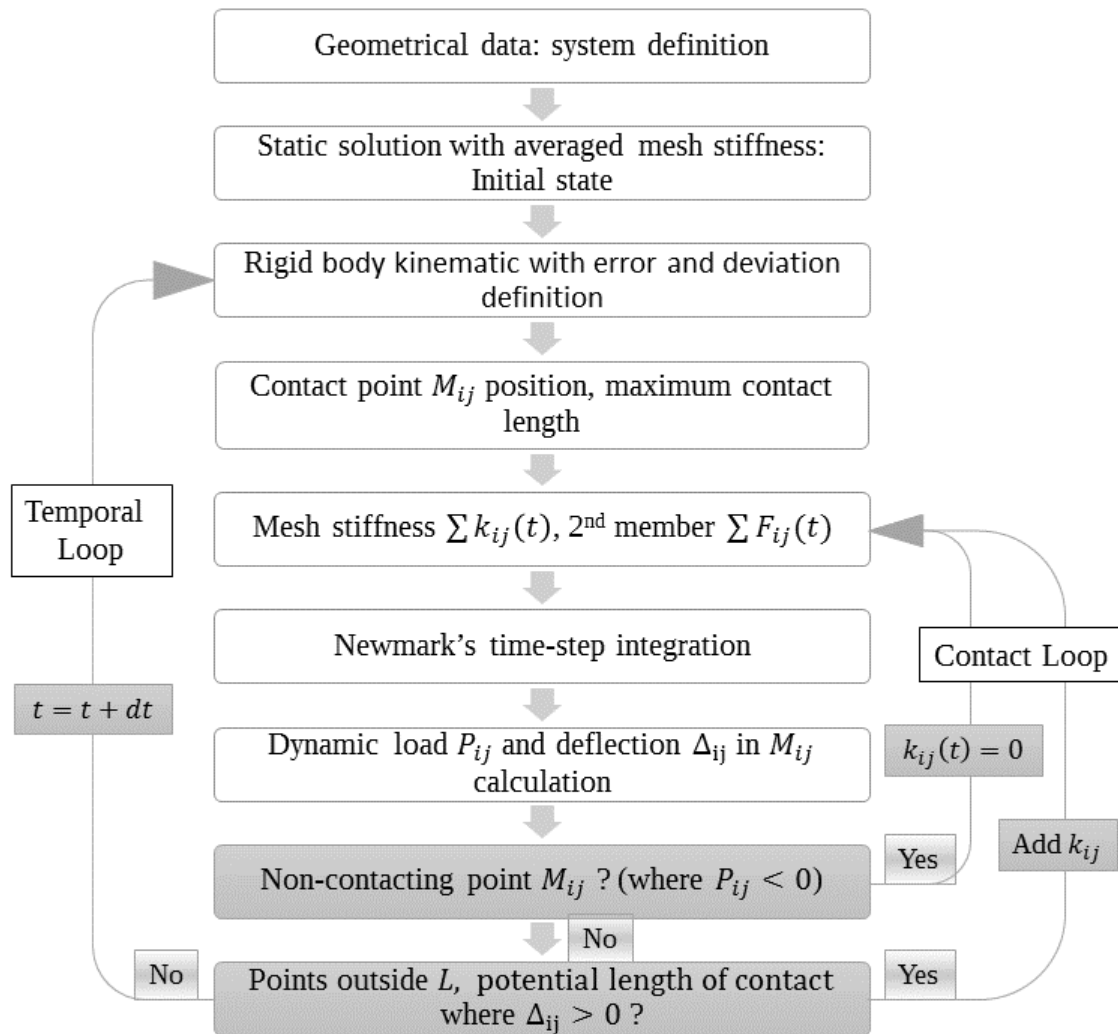


Fig. II-25: Simulation algorithm [VEL96]

The complementary time and contact loop makes it possible to evaluate the instant contact length and uses the instant mesh stiffness and forcing term to proceed to the time-step integration. At each time step, the first loop verifies that the contact load P_{ij} at each segment of the line is compressive and if not, remove the contribution of the segment to the instant mesh stiffness ($k_{ij}(t) = 0$) and forcing term. The second loop controls that there is no interference outside the contact length L determined at the end of the first loop.

4. Conclusion

In this chapter, the theoretical foundations of a new gear model have been presented which can connect classic lumped parameter and continuous finite element models which are required when it comes to thin structural elements. Such a modelling strategy leads to so-called hybrid models which can present increasing degrees of precision depending on the gear architecture specificities. More refined models can be introduced where static and dynamic elastic deflections are likely to be prominent whereas simpler (but faster) simulations can be kept for solid members. One of the interests of the methodology is that mesh elasticity and shape deviations are still accounted for by using a classic time-varying, non-linear Winkler foundation model which does not introduce additional degrees of freedom and makes it possible to still use the contact algorithm together with the integration Newmark scheme proposed by Velex *et al.* [VEL96].

In order to limit the number of unknowns, the finite elements models are reduced by using a condensation method which combines static and dynamic modes. A free-interface modal synthesis technique has been preferred.

One key point is the connection between incompatible models since Winkler foundations rely on discrete stepwise segments which do not naturally connect with 3D 20-node finite elements. A 3-step methodology is proposed: a) a two-point connection between every thin-slice of the Winkler foundation (thin or elemental tooth) and the rim finite element grid, b) a mortar based technique to introduce continuity and spread the displacement field between the segments of one contact line and, c) the shape functions of reduced 8-node elements to calculate the displacements anywhere at the surface of the finite element grid and relate them to nodal displacements.

Another improvement on the previous model is the introduction of centrifugal effects in the state equations which are shown to be influential in high-speed thin members such as those in helicopter transmissions.

Chapter III

Elements of Validation

1. Accessory Gear – Numerical Validation
2. Power Transmission – Numerical Validation
3. Industrial Power Transmission
4. Conclusion

This chapter is aimed at presenting elements of validation of the dynamic model presented in chapter II based on numerical simulations of helicopter transmissions, namely accessory gears and power transmissions. Academic examples of accessory gearbox and power transmission will be considered along with an actual industrial two-stage helicopter power transmission. For confidentiality reasons, the data and results related to the industrial case study have been normalised and dimensionless parameters will be used. The following three modelling configurations will be employed:

- rigid pinion / flexible condensed gear, (further referred to as ‘Hybrid 1: **H1**’)
- sub-structured pinion and gear, (‘Hybrid 2: **H2**’)

and finally the previously developed rigid pinion and gear model which has already been largely validated by comparison by experimental evidence [BAU02-VEL96], further referred to as **initial**.

The proposed modular model will be first applied to the academic test cases for which the flexible parts have been rigidified by using a very high Young’s modulus ($E = 4.10^{14} N / m^2$) in order to directly compare with the results provided by the classic rigid-body model (providing that the gear body mass and inertia are adjusted). Comparisons will then be extended by simulating the contributions of a deformable gear body (with standard Young’s modulus for steel) in order to appraise the static and dynamic influence of gear body compliance.

Numerical analyses have been performed for each reduction stage of the industrial reduction considered separately and a full FE model of the pinions and gears in contact has been set up and run under quasi-static conditions in order to determine bearing loads and the contact pressure distributions on the mating teeth. On the other hand, experimental measurements were conducted on the entire two-stage system by using displacement probes to estimate gear web dynamic deflections over a range of speeds close to the nominal speed. It is shown that the experimental evidence compare well with the model results thus proving that the proposed numerical simulation is sound and can effectively be used on actual helicopter transmissions.

All the dimensional results are presented in the reference frame of the gear element and FE lumped parameters model represented in Fig. III-1.

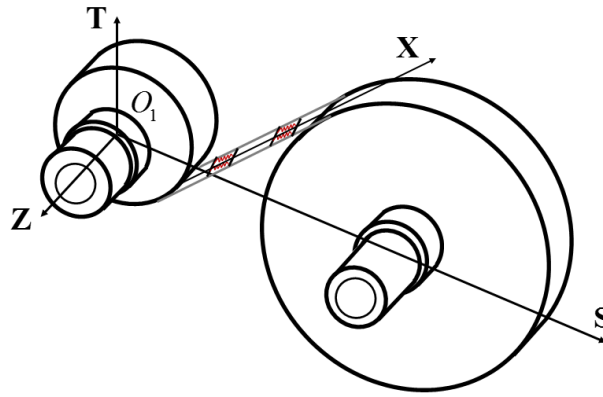


Fig. III-1: Gear element coordinate system

1. Accessory Gear – Numerical Validation

1.1. Straight Webbed Spur Gear – Quasi-Static Validation

1.1.1. Spur Gear Presentation

Accessory gears convey a fraction of the total power from the turboshaft to the starter, generator and pumps. The academic test case retained here is a classic spur gear example whose data are listed in Tab. III-1; the pinion torque is $T_n \approx 80Nm$.

	Pinion	Gear
Module m (mm)	1.5	
Number of teeth	45	86
Pressure Angle ($^\circ$)	25.	
Helix Angle ($^\circ$)	0	
Addendum coefficient	0.9447	
Dedendum coefficient	1.1933	
Profile shift coefficient	0.341	0.481
Fillet Radius / module	0.25	
Rim width b (mm)	11.5	9.5

Tab. III-1: Accessory gear train: tooth geometry data

The corresponding gear body geometry is described in Fig. III-2. The pinion is a solid gear mounted on a hollow shaft whereas the gear body is thin-rimmed in order to reduce its mass as shown in Fig. III-2.b. For the two drawings below, the bearings are schematically represented by their central points (dots) on the geometrical axis.

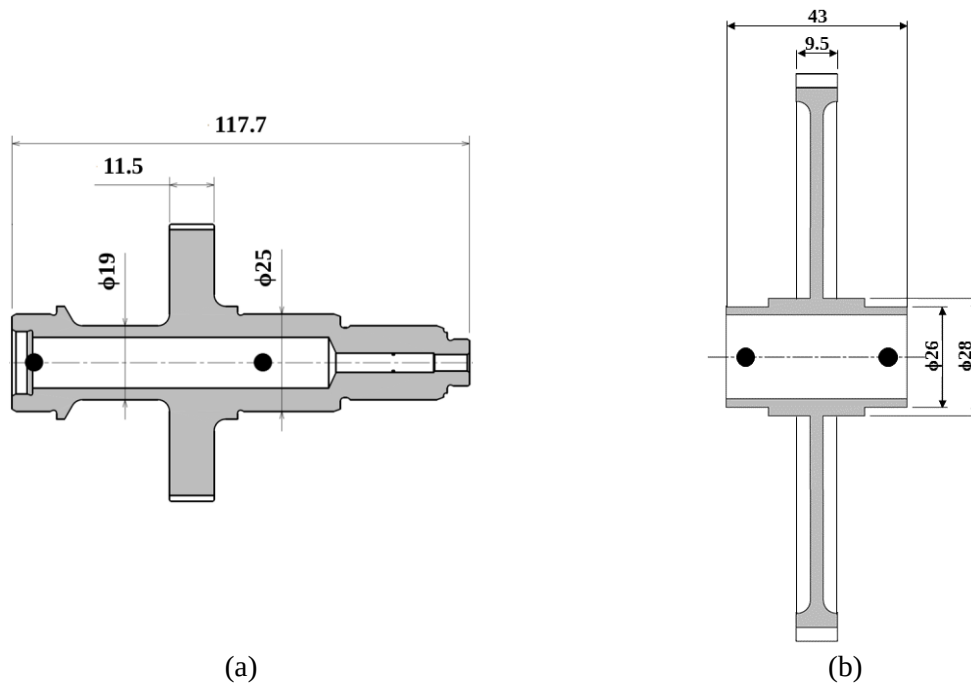


Fig. III-2: Geometry for (a) pinion and (b) wheel of the spur test case

Given the simple geometry of the web, this accessory gear is well adapted to better apprehend the effect of gear body flexibility.

1.1.2. Static/Quasi-Static Numerical Validation

Bearing displacements have been calculated in static conditions for the three models described above using a time-averaged mesh stiffness function and unmodified tooth shapes. The results for bearings 1 and 2 on the pinion and gear shafts (labelled B1 and B2) in Tab. III-2 and Tab. III-3 show that all the configurations give very similar radial and tangential displacement amplitudes although some slight deviations (<5%) are reported on the gear bearings when a condensed 3D model is used.

It is also noted that the transmission is lightly loaded in relation to bearing stiffness since the maximum displacement does not exceed 1.6 μm .

Bearing	B1			B2		
Displacement	Initial	H1	H2	Initial	H1	H2
S (μm)	-0.35	-0.35	-0.34	-0.77	-0.77	-0.76
T (μm)	-0.70	-0.70	-0.67	-1.55	-1.55	-1.50

Tab. III-2: Pinion bearing displacements in static conditions for $k_b = 1 \times 10^9 \text{ N/m}$ bearing radial stiffness

Bearing	B1			B2		
Displacement	Initial	H1	H2	Initial	H1	H2
S (μm)	0.55	0.56	0.54	0.57	0.58	0.56
T (μm)	1.11	1.11	1.06	1.15	1.15	1.10

Tab. III-3: Gear bearing displacements under static load

Comparisons have been extended to quasi-static load distributions on tooth flanks by considering a very low rotational speed ($\Omega_p = 0.01 \text{ rad/s}$ on the pinion). Fig. III-3.a shows the tooth load distribution in N/mm over the face width b , for a tooth passing in the base plane as given by the hybrid model H1. The usual sharp variation in the line of action direction for spur gears is observed which corresponds to the transition between two tooth pairs and one single one. It can be noticed that, because of the bearing asymmetry on the pinion shaft, the load distribution across the face width is uneven. All the models give similar results as illustrated in Fig. III-3.b where slight load oscillations are observed when using finite elements. The maximum difference between the maximum tooth load distributions is around 3.5% and the full finite element based model appears as slightly more flexible with more pronounced axial asymmetry.

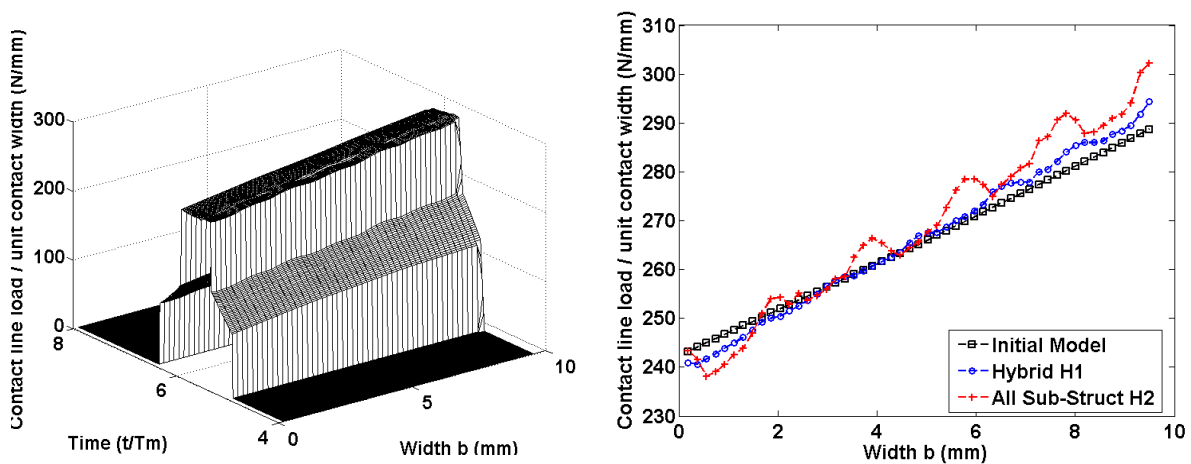


Fig. III-3: (a) Local load on contact line and (b) maximum local load for different modular models in case of rigid gear

These observations are amplified when considering a flexible gear body (Fig. III-4), tooth load oscillations are found across the face width in relation to the finite element discrete grid. Compared with the rigid case, pinion and gear body compliances modify axial tooth load distributions even for centred rims suggesting that cautions must be taken in the design of thin rim and web assemblies. However, here again, for this spur gear example, the differences remain limited.

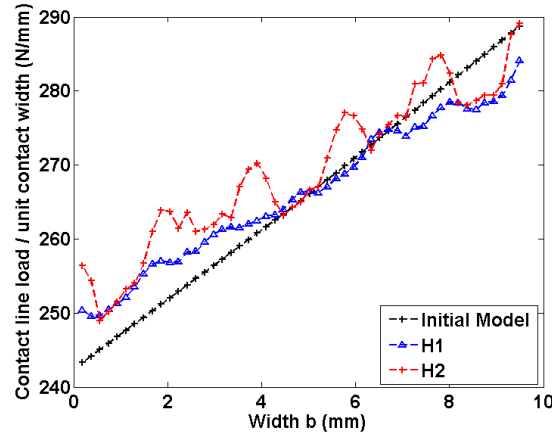


Fig. III-4: Local load maximum for hybrid models webbed wheel

1.2. Model for Gear Optimisation

1.2.1. Profile Modification Definition

Tooth flank modifications are widely used to avoid corner contacts at engagement [MAA97] improve transmission error and limit contact pressures on tooth flanks [MAA97-VEL16]. Profile modifications correspond to material removal near tooth tips and/or at the root of the teeth (Fig. III-5) which, when considering linear relief, can be parametrized by an extent or length of modification L_c and a depth of modification E .

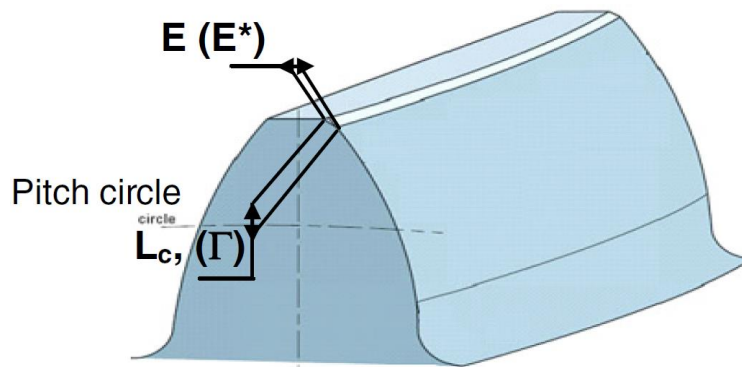


Fig. III-5: Profile relief parameter on tooth [GHR13]

The extent of modification is frequently expressed as a distance in the base plane and can therefore be normalised with respect to the theoretical length of contact, leading to the non-dimensional parameter Γ defined as:

$$\Gamma = \frac{L_c}{\varepsilon_\alpha P_{bt}} \quad (3.1)$$

With ε_a profile contact ratio and P_{bt} base plane step.

Fig. III-6 shows the geometrical deviation at point M ($e_{00}(M)$) (cf. chapter II) which stems from a symmetric linear profile modification (same profile modification on the pinion and gear tooth tips) for which two parameters only E and Γ are required.

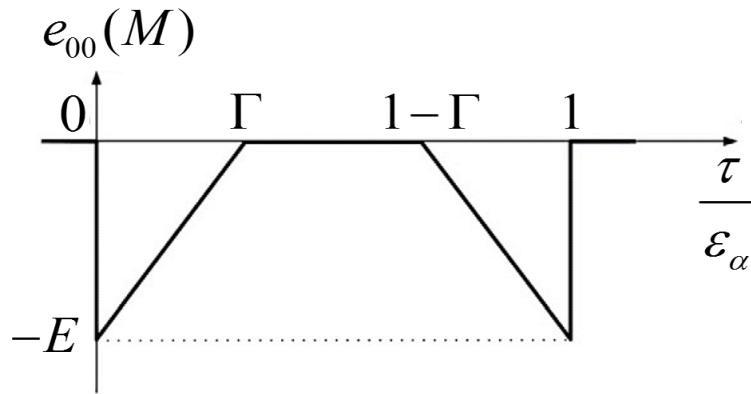


Fig. III-6: Profile relief parameters in the profile direction (or line of action direction) [BRU14]

This influence of profile relief has been extensively studied by Bruyère *et al.* [BRU13-15-VEL11] who introduced the concept of Master Curve in the (Γ, E) plane (black dashed line in Fig. III-7) which defines a family of interesting profile modifications with regard to transmission error time variations and consequently vibration and noise [MUN89-AJM05]. Interestingly, similar Master Curves have been obtained for internal gears and multi-mesh transmissions such as planetary gears [VEL16].

The initial model [VEL96] has been used for the calculation of the RMS of quasi-static transmission error (TEs) while systematically sweeping over realistic ranges of profile modification parameters. Fig. III-7 shows an example of such massive run by Ghribi *et al.* [GHR12] where the modifications with minimum TEs are actually in the vicinity of the analytical Master Curve. Optimisation by using a genetic algorithm (GA) leads to similar results thus proving the robustness of the concept of Master Curve.

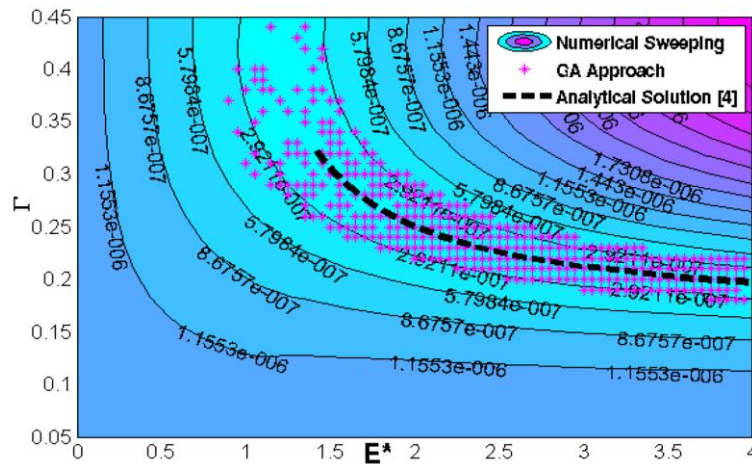


Fig. III-7: Analytical MasterCurve comparison with numerical sweep from the initial model [VEL96] and genetic algorithm [GHR12]

1.2.2. MasterCurve Fitting

Systematic quasi-static simulations ($\Omega_p = 0.01 \text{ rad/s}$) have been performed using the initial and hybrid models. Examples of quasi-static transmission error (TEs) time signals are shown in Fig. III-8 for both the initial and hybrid models with condensed rigid and flexible gear bodies. For all three cases, similar curves, typical of spur gears, are found which, however, exhibit different mean values (from 19 to 41 μm) and RMS illustrating the difference in overall flexibility between the different modelling strategies.

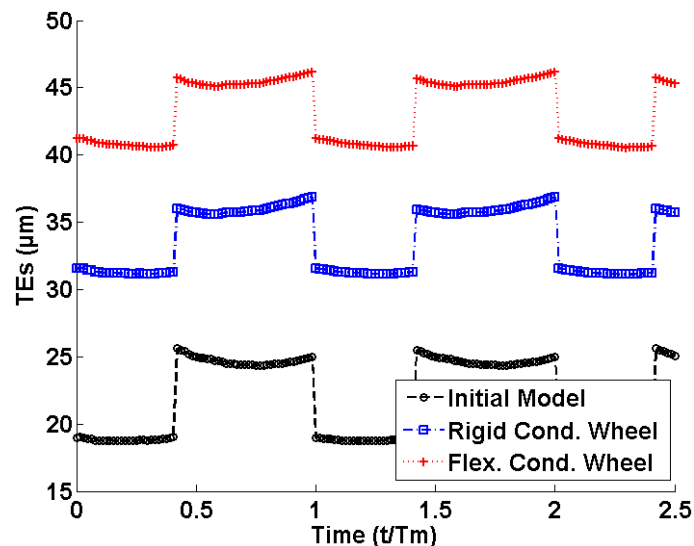


Fig. III-8: Quasi-static transmission error depending on wheel flexibility (rigid and flexible condensed wheel with model H1: one node pinion and condensed wheel)

Using full FE gear models, Rigaud [RIG99] came to the conclusion that both the elastic couplings between adjacent teeth and gear body compliance were influential on the mean value

and shape of TEs curves. The results in Fig. III-8 confirm these findings since the interactions between neighbouring teeth included in the FE condensed gear body increase the mean value of TEs and change its shape. The same conclusions are drawn using a more flexible wheel for which the mean value is increased and the time variation amplitudes are altered as illustrated in Tab. III-4 which gives the RMS of transmission error for all the models tested.

	Initial Model	Hybrid Model 1: H1		Hybrid Model 2: H2	
Wheel	Rigid	Rigid	Flexible	Rigid	Flexible
RMS (μm)	2.92	2.36	2.33	1.79	1.80

Tab. III-4: RMS value of quasi-static transmission error comparison for all models

However, the contour plots of the RMS of TEs in Fig. III-9 suggest that, in spite of the differences highlighted above, the concept of Master Curve, i.e. the definition of optimum profile relief, remains relevant for this example of spur gear with centred straight thin rim even if the theory was initially developed for solid gears.

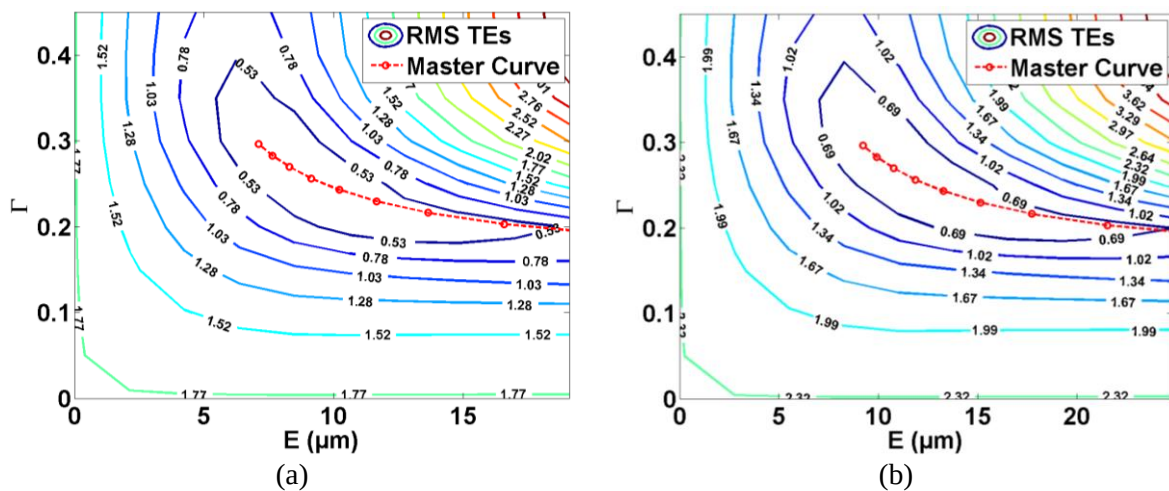


Fig. III-9: Comparison with rigid body Master Curve for (a) 2nd hybrid model H2 with rigid bodies and (b) 1st hybrid model H1 with flexible wheel

1.3. Dynamic Study

1.3.1. Numerical Validation of the Spur Gear

Dynamic calculations have been performed first by using a rigidified gear body (wheel). Modal damping factors have been introduced whose amplitudes are calculated as the weighted average of a) a damping factor of 0.07 typical of mesh damping according to Umezawa *et al.* [UME85] and, b) a structural damping factor of 0.02. The coefficients used in the weighted average are based on the percentages of modal strain energy stored in the mesh in order to

distinguish the structural contributions (lightly damped) from those associated with the tooth contacts (usually with higher damping levels [ANK14-16]). The speed range up to $\Omega_p = 3000 \text{ rad/s}$ on the pinion is investigated. In order to reduce the numerical start-up transient regime, for each speed, the time-step integration scheme is initialized by using the solution in terms of displacements and speeds obtained at the end of the iterations for the previous speed. The resulting dynamic ratio is plotted versus pinion speed in Fig. III-10 for the two hybrid models and compared with the results from the initial model. Tooth critical speeds correspond to dynamic ratios significantly larger than one in this figure.

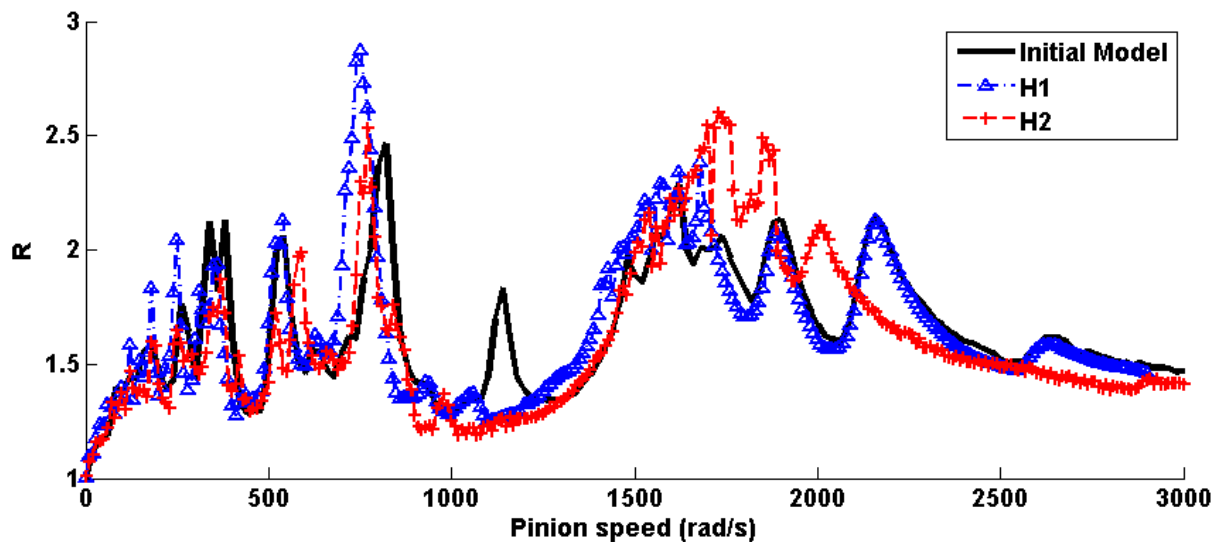


Fig. III-10: Comparison with modal dependent damping – Rigidified gear body

Although, some slight difference can be found, all the simulation results are in good agreement thus proving the consistency of the various approaches in this case of rigidified gear body. The initial model response curve exhibits a peak near 1150 rad/s not observed for the hybrid models which, based on modal energy distributions, is related to the gear shaft and bearings whose models are different for the H1 and H2 simulations (3D FE based). Some discrepancies can also be noticed between 1500 and 2000 rad/s which are attributed to amplitude jumps and the difficulty to obtain stabilized time responses in this speed range. In order to investigate this point further, higher and different damping has been considered (Fig. III-11). The results confirm that the nature and amplitude of damping reduce the deviations noted above thus confirming the role of dissipation.

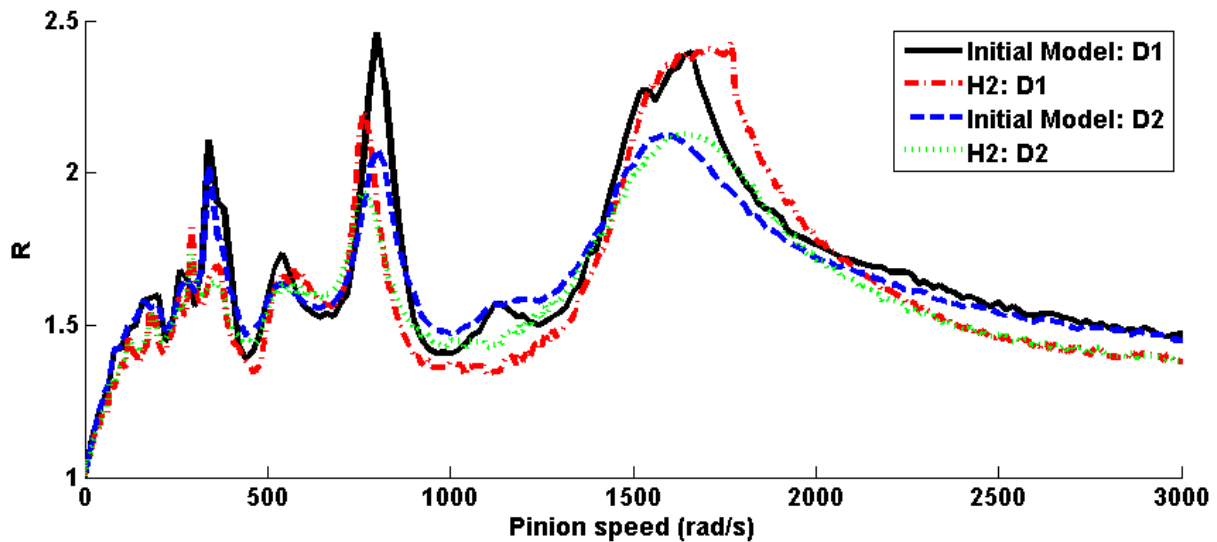


Fig. III-11: 2nd hybrid model H2 comparison to initial depending on Rayleigh damping definition with (a) D1: $a_R = 25.0 \text{ s}^{-1}$, $b_R = 2.5 \times 10^{-6} \text{ s}$ and D2: $a_R = 40.0 \text{ s}^{-1}$, $b_R = 4.0 \times 10^{-6} \text{ s}$

1.3.2. Introduction of a Flexible Gear

The rigidified web is now replaced by the actual one and dynamic simulations were performed by using modal and Rayleigh damping. The corresponding response curves in Fig. III-12 show that:

- The two hybrid models give very similar dynamic factors
- The purely rigid model leads to higher tooth critical speeds suggesting that web compliance is actually influential on dynamic tooth loading.
- No additional response peaks are introduced by the flexible gear suggesting in this example that the major contribution of gear body compliance on dynamic tooth loading comes from the static contribution rather than the modal contents.

The latter has been confirmed by examining the influence of the modal basis kept in the sub-structuring method. Fig. III-13 shows the dynamic factor curves over a broad speed range (0-3000 rad/s) obtained for 10, 50 and 100 modes and proves that most of the response curve is obtained even when using a limited number of modes thus confirming the major contribution of the static deflection. In the rest of this chapter, 50 modes have been kept in order to limit the computational cost while keeping a good precision on dynamic factors.

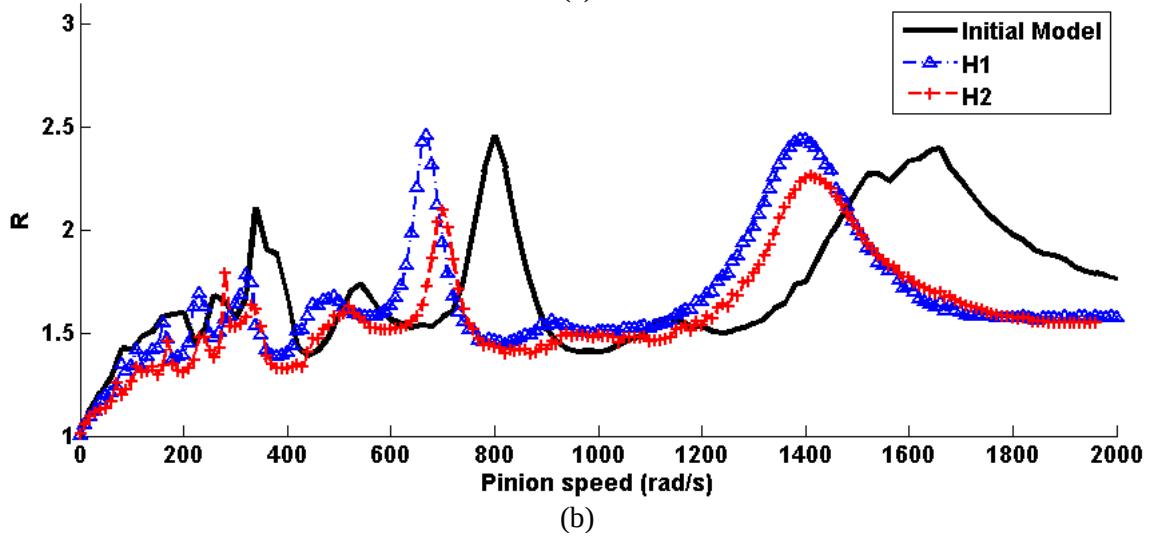
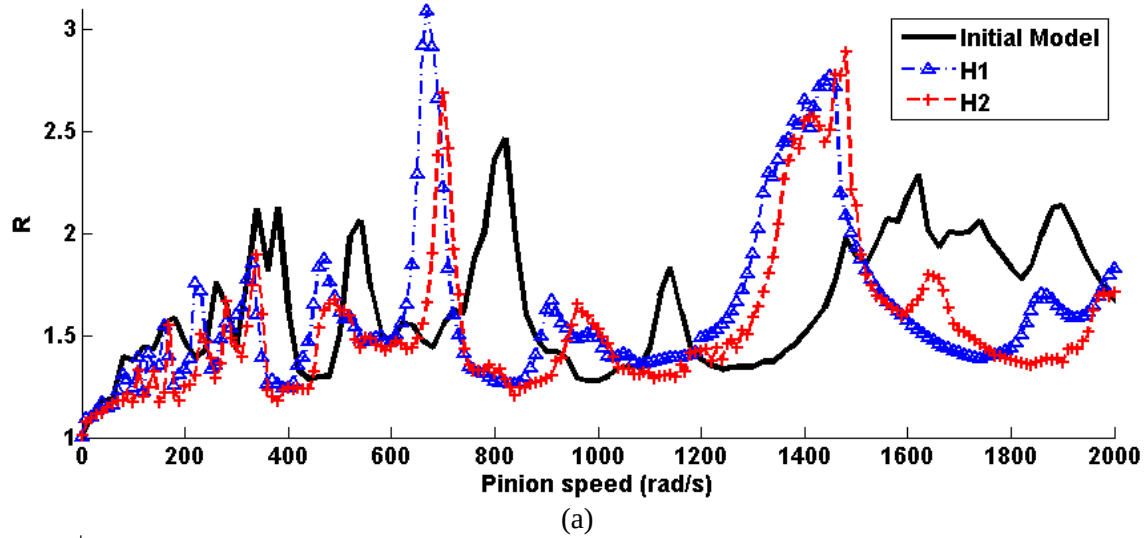


Fig. III-12: Comparison between model with flexible wheel in both hybrid models for (a) modal dependant damping and (b) Rayleigh damping $D1$ with $a_R = 25.0 \text{ s}^{-1}$, $b_R = 2.5 \times 10^{-6} \text{ s}$

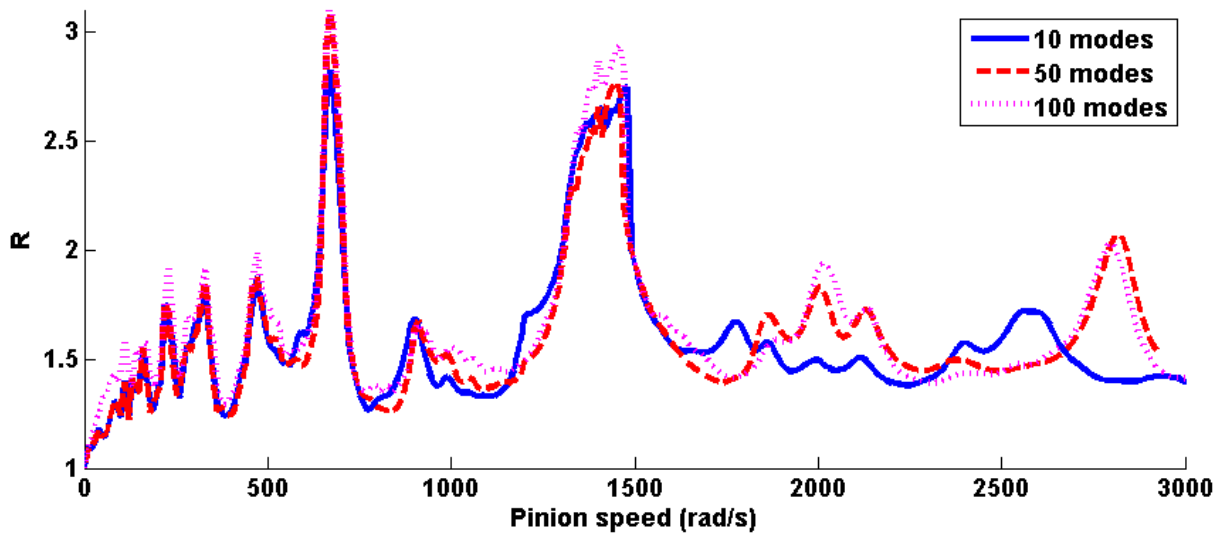


Fig. III-13: Number of mode choice in the condensed wheel influence on the dynamic ratio

2. Power Transmission – Numerical Validation

2.1. Validation for Rigid Body Gears

2.1.1. Helical Gear Data

In helicopters, turboshafts are connected to the main transmission gearbox via power transmission gears which transfer higher powers and loads than the accessory gearboxes studied in the previous section ($T_n \approx 310 \text{ Nm}$ is a typical order of magnitude on the pinion). Their design is therefore different since helical gears are preferred and thicker rims / tooth face widths are employed (Tab. III-5).

	Pinion	Wheel
Module m (mm)		2.5
Number of teeth	35	68
Pressure Angle ($^\circ$)		25.
Helix Angle ($^\circ$)		12.
Addendum coefficient	0.976	0.970
Dedendum coefficient	1.262	1.268
Profile shift coefficient	0.275	0.317
Fillet Radius / module		0.25
Rim width b (mm)		~40

Tab. III-5: Helical gear geometry

These constraints associated with the larger powers to be transmitted and the fact that mass reduction remains crucial, imply that material needs to be removed from gear bodies leading to thin web geometries. For instance, Fig. III-14 shows an academic example based on a former SAFRAN HE gear (wheel) design which will be used for validation purposes in this section. The gear shaft rests on three bearings materialized as dots in the figure and labelled B1, B2 and B3 from left to right in what follows. The pinion (input) associated with this gear is solid and is mounted on a symmetric shaft so that it can be modelled as a rigid cylinder on beam and lumped parameter elements.

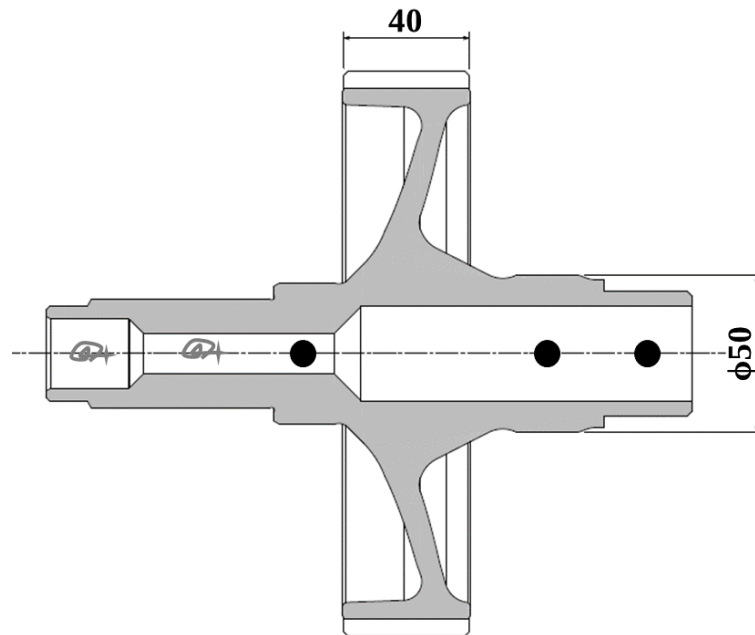


Fig. III-14: Power transmission wheel geometry, including the web

2.1.2. Quasi-Static Load

The various models are first run for quasi-static conditions ($\Omega_p = 0.01 \text{ rad} / \text{s}$) in order to determine the bearing mean loads. The pinion bearing loads (Tab. III-6) are very similar for the initial model and model H1 (sub-structured gear) whereas some differences appear when a sub-structured deformable pinion is considered (model H2).

Bearing	B1			B2		
	Initial	H1	H2	Initial	H1	H2
S (N)	-2008	-2007	-2015	-1436	-1438	-1510
T (N)	-3406	-3402	-3374	-3423	-3427	-3449

Tab. III-6: Load Comparison on Pinion Bearings

The gear bearing loads are more sensitive to the presence of deformable gear bodies and substantial deviations can be reported in Tab. III-7 suggesting that gear body deflections interact with load bearing distribution for this example of hyper-static system. From a physical viewpoint, these deviations are probably generated by the uneven tooth load patterns which induce distortions and change the bearing force distributions.

Bearing	B1			B2			B3		
	Initial	H1	H2	Initial	H1	H2	Initial	H1	H2
S (N)	723	798	886	1482	1611	1248	1240	1095	1366
T (N)	4216	4243	4304	1847	1931	1689	767	656	831

Tab. III-7: Load Comparison for the Wheel Bearings

2.1.3. *Dynamic Effects*

Simulations are extended to dynamic conditions and the dynamic factor has been calculated over a broad range of speeds. As before, the integration scheme at one given speed is initialized by using the steady-state solution obtained at the previous speed (for speed sweep). Modal and Rayleigh damping models are employed and comparisons in dynamics will be limited to the so-called initial and H2 (fully sub-structured) models. The 1st hybrid model, H1 has been validated the same way but, for the sake of concision, its results will not be presented here.

Fig. III-15 presents the response curves obtained by the two models (initial and H2 with rigidified pinion and gear) when using a) modal damping factors and b) Rayleigh's damping. It can be observed that the critical speeds are globally at the same speeds with some slight frequency shifts. The amplitudes are comparable and the majority of the differences are attributed to the chosen damping model. However, some peaks emerge in the low-medium speed range which can be attributed to the flexible shafts modelling, i.e., beam elements as opposed to 3D finite elements thus suggesting some degree of interaction between shaft vibrations and dynamic tooth loading.

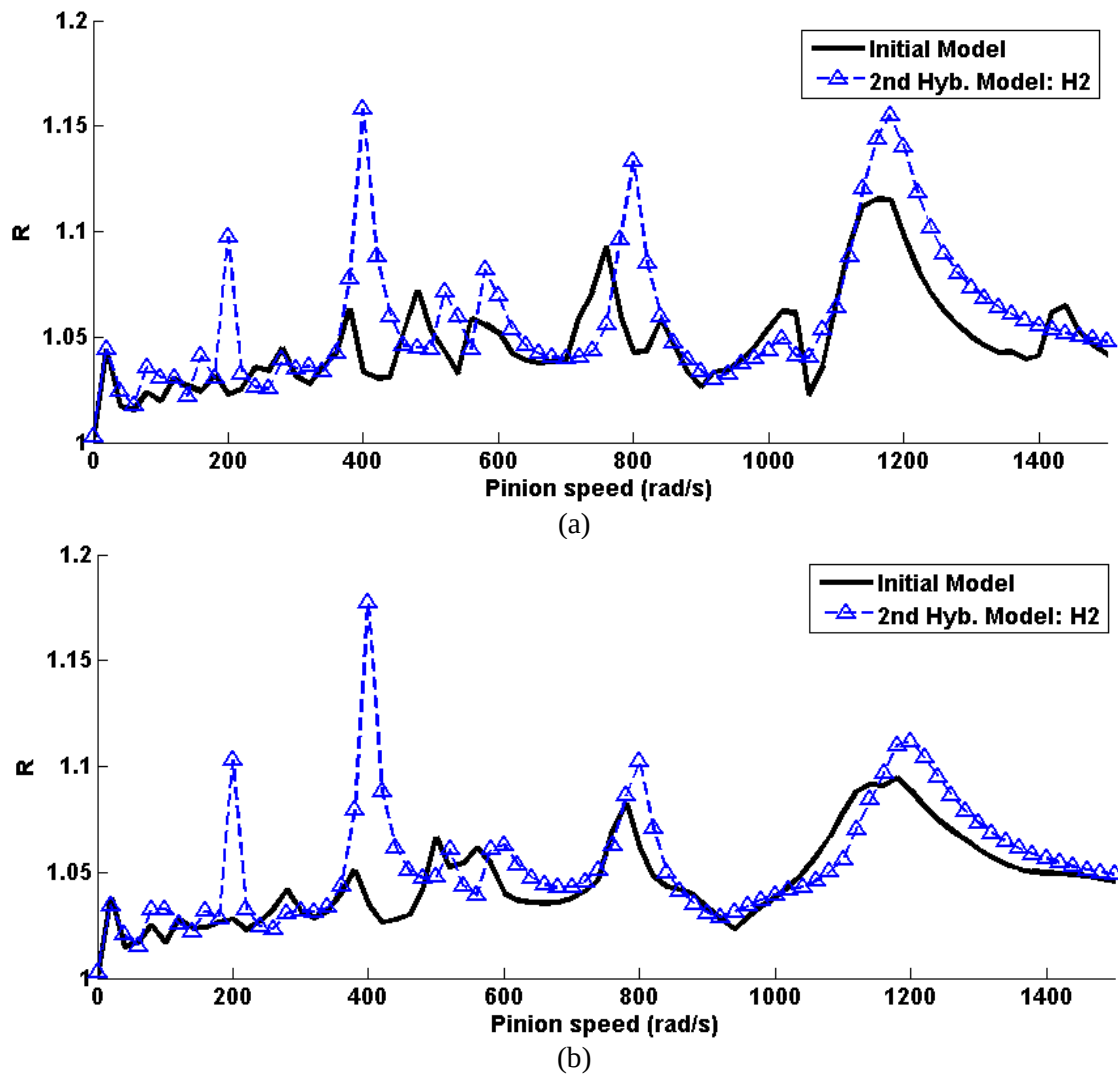


Fig. III-15: Dynamic ratio comparison for (a) modal dependent damping and (b) Rayleigh damping

2.2. Flexible Web Influence

The Young's modulus of the pinion and gear webs is set to the standard value for steel and the influence of deformable gear bodies is now investigated. Here again, only the initial and H2 (sub-structured pinion and gear) models are compared.

2.2.1. Effect of wheel static deformation

Tab. III-8 shows (in red) the gear bearing loads under quasi-static conditions and proves that gear and pinion deflections influence static bearing load distribution to a large extent

particularly on bearings 2 and 3. It can be noticed that the bearing closer to the web is more loaded while the end of the shaft is unloaded. It is concluded that, in this case, web and rim compliance need to be considered in any realistic load simulation.

Bearing	B1			B2			B3		
Load	Initial	Rig	Flex	Initial	Rig	Flex	Initial	Rig	Flex
S (N)	723	798	756	1482	1611	1832	1240	1095	915
T (N)	4216	4243	4210	1847	1931	2173	767	656	446

Tab. III-8: Wheel bearing load for flexible web for H1 model

Li has shown [LI02] that the gear and rim flexibility has also a local impact. Fig. III-16 shows the load distribution on both lines of action for a central web and an offset one for quasi-static analysis.

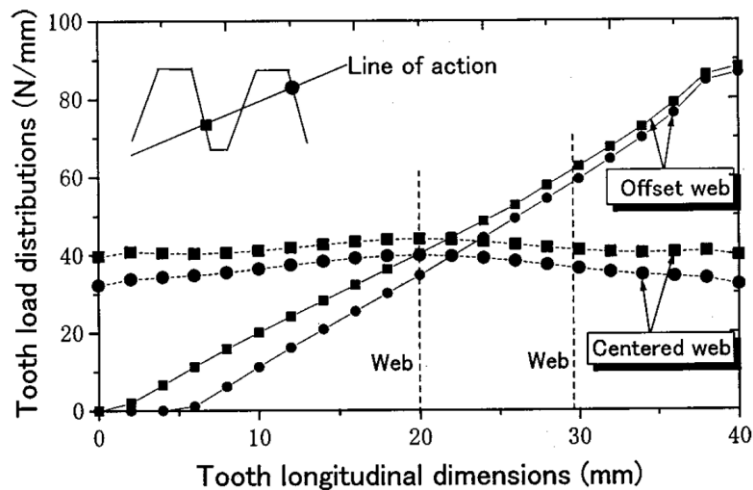


Fig. III-16: Local load over a tooth for various web arrangements [LI02.b]

The same analysis has been made for the power gear. Fig. III-17.a shows the line of contact load distribution over a passing into the mesh contact for the flexible wheel (H1). The global shape is the one that can be expected for a helical gear, even if it is more in a triangular shape than what is usual for rigid gears.

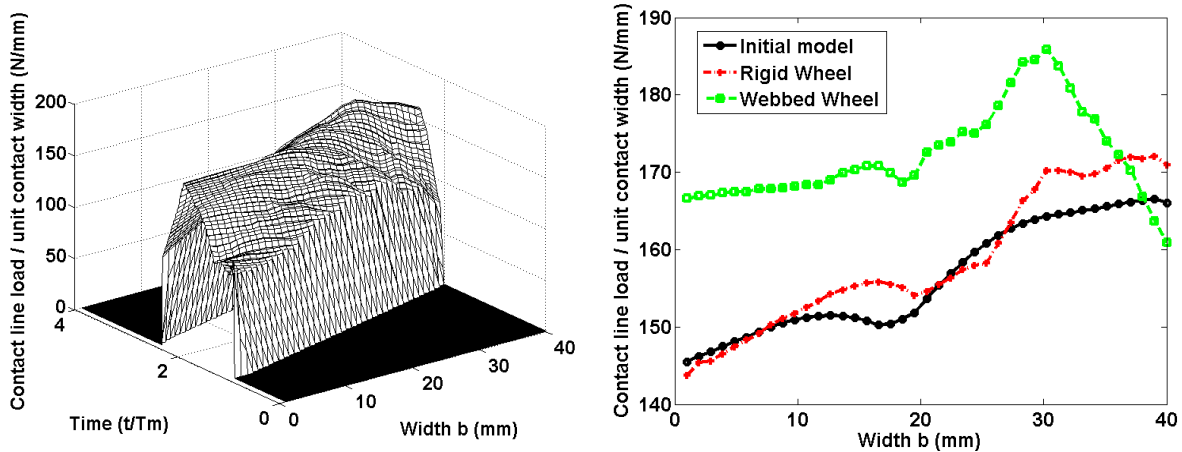


Fig. III-17: Load distribution for (a) flexible web and (b) when compared to rigid and initial model maximum contact line load when passing through the base plane

Fig. III-17.b shows the maximum contact load comparison for rigid and flexible gear. The two curves corresponding to the rigid model are almost the same, therefore the slight slope can be attributed to the common flexible parts such as shafts. The flexible gear load presents a different shape, as well as a higher maximum amplitude. When compared to the wheel geometry (Fig. III-14), it is noticeable that the position of the maximum load is just above the web-rim connection in agreement with Li's conclusions (Fig. III-16). The axial slope is also modified compared with the rigid body case and it can be confirmed that web flexibility may have a major effect on local mesh load distribution.

2.2.2. Modal Inclusion of the Condensed Wheel

Based on the results from the literature [COO14], mesh stiffness has a limited influence on gear body modal behaviour which presents similarities with that of discs. The mode shapes are usually classified in terms of nodal circles and diameters forming so-called families of mode shapes (Fig. III-18) [MOU14]. In order to illustrate this phenomenon, the modes calculated for an isolated gear (no shaft) are compared with those obtained when considering fully sub-structured pinion and gear in mesh.

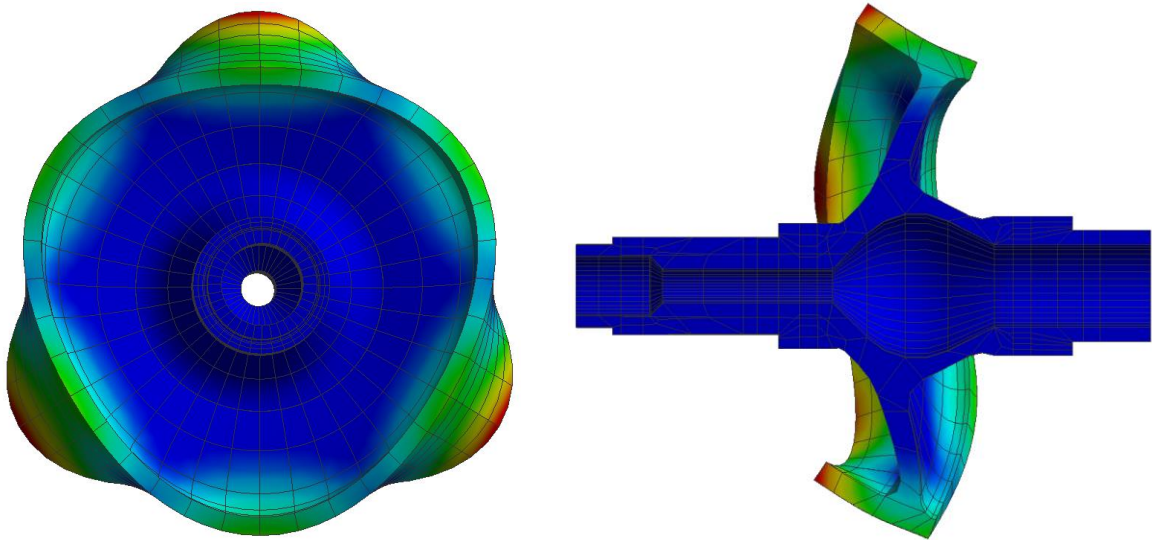


Fig. III-18: Typical web flexion mode, characterised as 0 nodal circle and 3 nodal diameters (displayed on wheel + shaft)

Fig. III-19 shows the modal comparisons between the isolated wheel and the pinion-gear systems in contact (the horizontal line corresponds to the mesh frequency at the maximum pinion speed around 3000 rad/s). Based on the modal displacements at the master nodes distributed along a circle on the gear body, it is possible to identify the n-diameter mode shapes which are confronted with those obtained using the full 3D finite element model of the isolated gear.

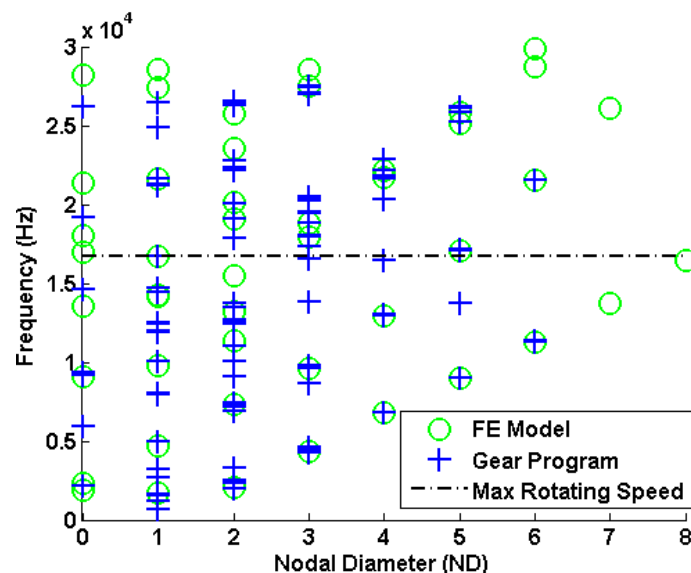


Fig. III-19: Modal comparison between the gear analysis (H1) and full FE model of wheel alone

The results in Fig. III-19 are in line with the conclusions in [MOU14] and the n -diameter modes for one flexible gear or for the entire reduction unit correspond well. However, it can be noticed that the simulation of the complete reduction stage (pinion + gear) leads to more mode shapes than the wheel alone, which is consistent with the fact that adding the pinion shaft should generate additional vibration modes. It is also noticed that, depending on the nodal diameter, the agreement is variable and modes with zero or one nodal diameter tend to exhibit more deviation as opposed to the modes with more diameters.

This supports the observations of Blevins [BLE79] and Schmiechen [SCH97] who studied the patterns of circular plate modal behaviour. The good correspondence between such patterns and thin webbed gears is illustrated Fig. III-20 in which ND is the number of nodal diameters and NC, the number of nodal circles.

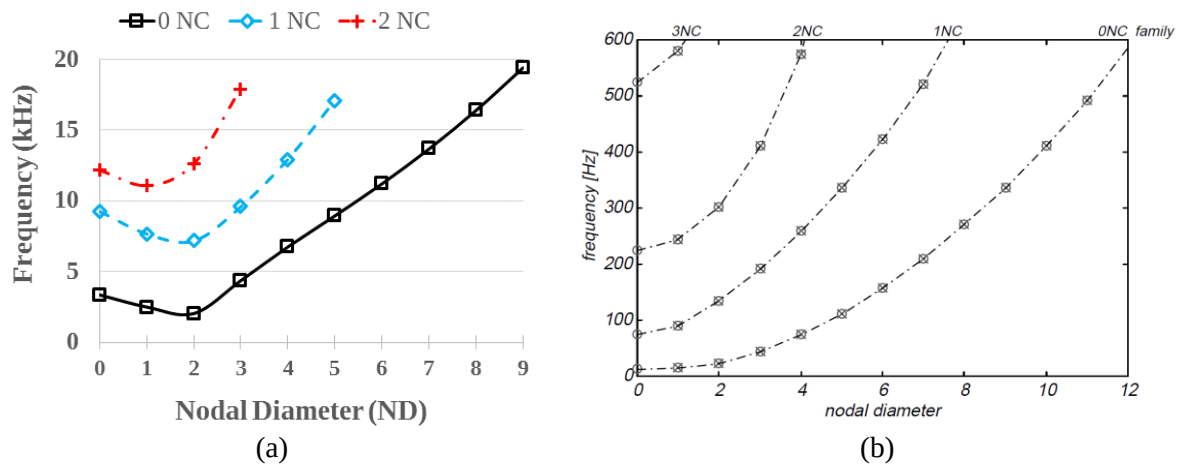


Fig. III-20: Modes distribution for (a) FE wheel studied (b) plain circular disc [SCH97]

Analytically, the dynamic displacements in circular plates can be described using Fourier series as:

$$\delta_t = \sum_{n=0}^{\infty} (\delta_c^n \cos(n\theta) + \delta_s^n \sin(n\theta)) \quad (3.2)$$

with δ_t , total displacement, δ_c^n , δ_s^n Fast Fourier Transform components and n the nodal diameter number as illustrated in Fig. III-21 for the theoretical 3 nodal diameter mode.

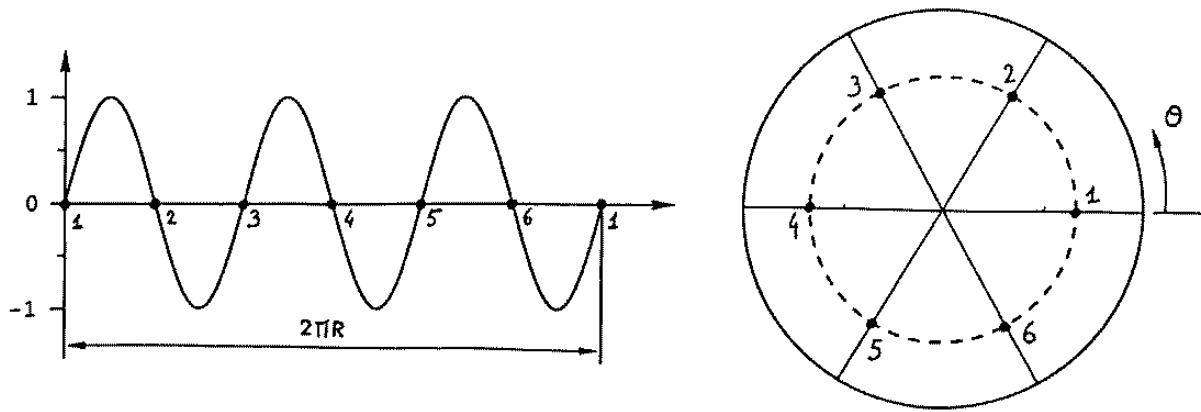


Fig. III-21: Example of 3rd nodal diameter theoretical shape for $\cos(3\theta)$ [JAC97]

Based on this decomposition, modes with zero and one diameter such as those schematically represented in Fig. III-22 will induce axial forces or moments at their centres, i.e. at their connections with their supporting shafts thus rendering these modes more sensitive to the shafts. This reasoning probably explains why the agreement between an isolated gear and the full system is poorer when it comes to zero and one diameter modes. On the other hand, 3 nodal diameter modes are self-balanced and they are consequently far less sensitive to the boundary conditions at the gear-shaft interface.

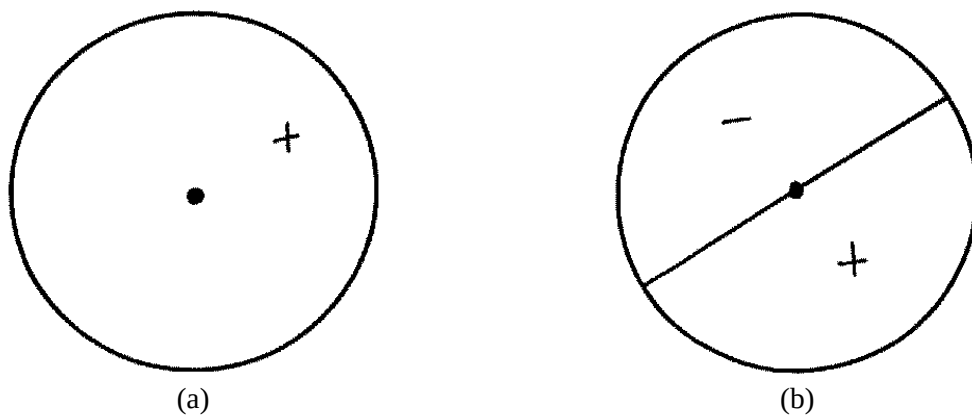


Fig. III-22: Circular plate mode shape for (a) no and (b) 1 nodal diameter mode [JAC97]

2.2.3. High Speed Investigations

Turning to dynamic responses, Fig. III-23 presents the dynamic mesh force ratio delivered by the 2nd hybrid model (H2) with the introduction of a flexible gear web and the corresponding outcome from the initial dynamic model. The main resonance peaks are clearly moved towards the lower speeds thus proving the contribution of more flexible gear webs on dynamic tooth loads.

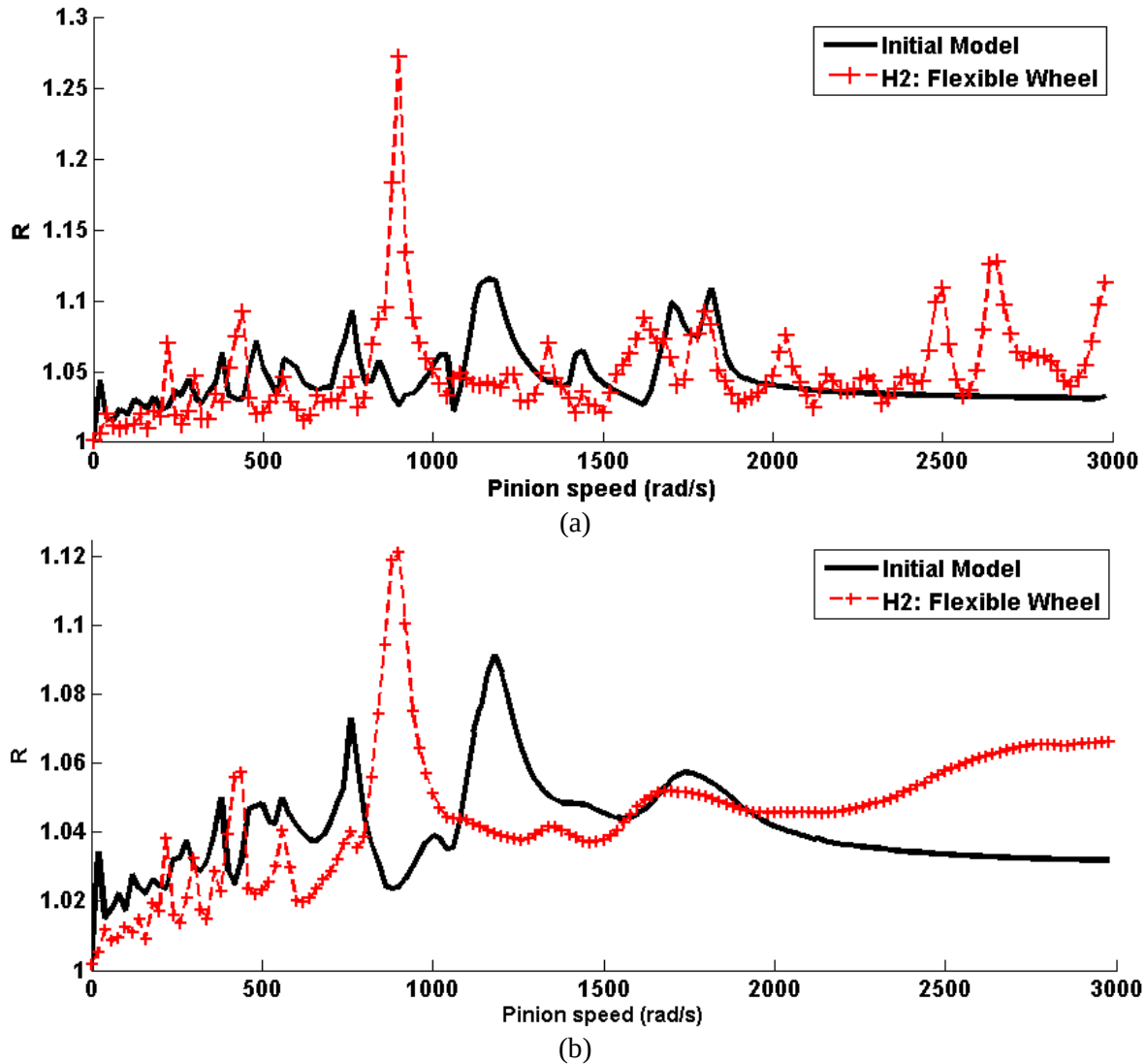


Fig. III-23: Dynamic ratio in case of the flexible wheel for (a) modal dependant damping and (b) Rayleigh damping

Another difference can be pointed out at high speeds where the tooth dynamic loading increases continuously for the H2 model. This phenomenon is caused by the centrifugal effects which are included in the deformable sub-structures and not considered when dealing with rigid

pinions and gears. This explanation is confirmed by the response curves in Fig. III-24 which shows the dynamic factors obtained for the H2 model with and without centrifugal components.

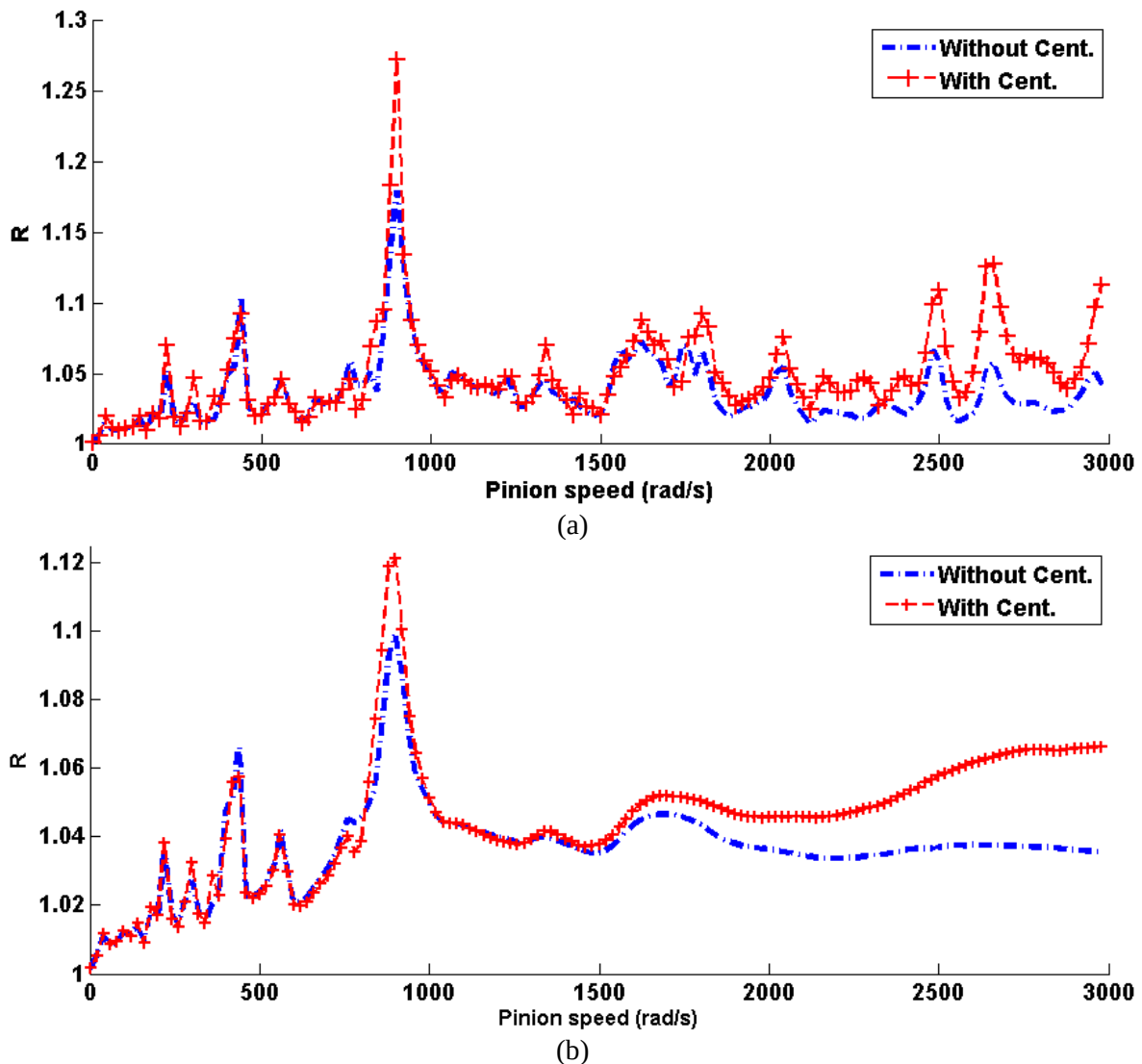


Fig. III-24: Comparison for centrifugal effect influence with (a) modal dependant damping and (b) Rayleigh damping for clarity

The importance of the centrifugal effects is also apparent on the dynamic tooth load distributions on the tooth flanks are shown in Fig. III-25. Two different tooth load patterns are represented for the same pinion speed of 3000 rad/s: a) without and, b) with centrifugal terms. The tooth distribution in the absence of centrifugal effects resembles that for quasi-static conditions (as 3000 rad/s is far from any tooth critical speed) whereas the situation is dramatically changed when the centrifugal effects are introduced. For the latter, the contact force pattern is not symmetric and one side is clearly overloaded on the cantilevered side according to Fig. III-14.

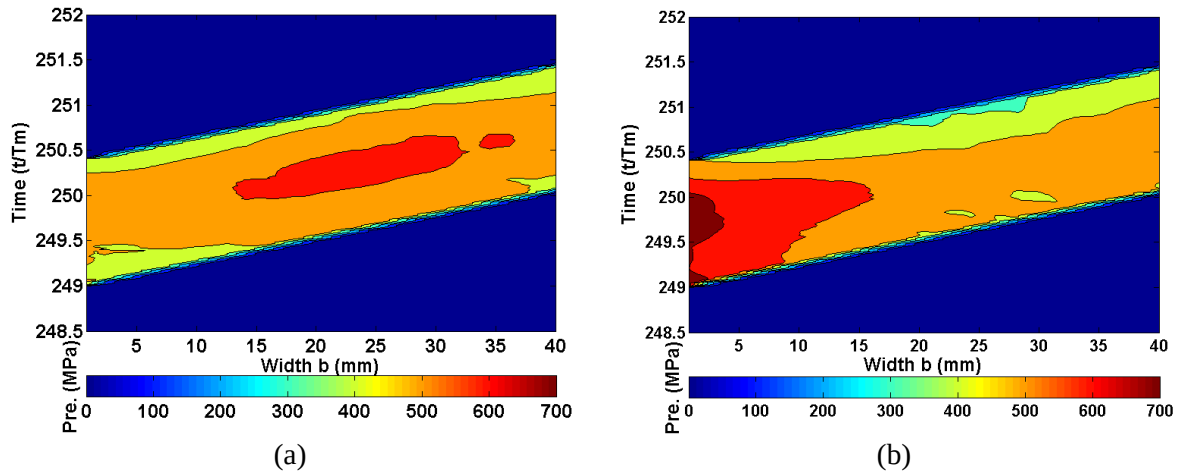


Fig. III-25: Rim pressure (a) without and (b) with centrifugal effects (id. for both hybrid model)

Fig. III-26 illustrates the origin of this problem as it shows the deformed shape of the flexible thin-webbed gear under the sole influence of the centrifugal components at 3000 rad/s on the pinion. It can be observed that the side of the face width, opposite to the web/rim connection, deforms more in the radial direction thus leading to uneven tooth load distributions across the face width.

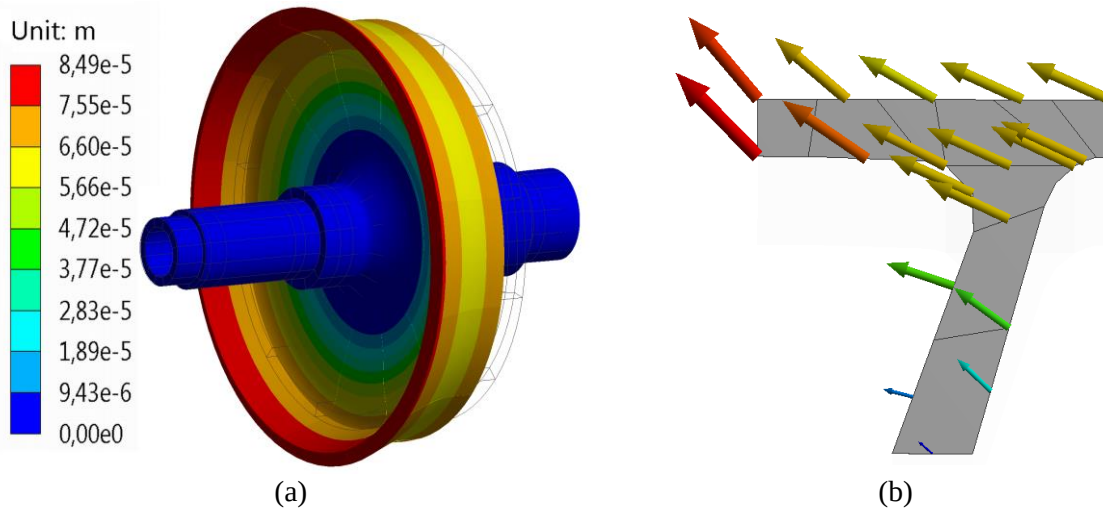


Fig. III-26: FE wheel model deformation (norm and direction) or (a) full wheel and (b) rim cut

Because of the changes in outer dimensions of the gear body, the actual meshing parameters such base radius and pressure angle are modified to some extent. Considering the maximum radial displacement (around 80 μm in this case), it is found that the base radius variation because of the centrifugal effects is approximately 0.1% leading to a 0.5% variation in pressure angle (Fig. III-27) using the following equality:

$$\alpha'_t = \cos^{-1}\left(\frac{R'_{b2}}{R_2}\right) = \cos^{-1}\left(\frac{R_{b2} + \Delta}{R_2}\right) \quad (3.3)$$

With $R_{b2} = R_2 \cos(\alpha_t)$.

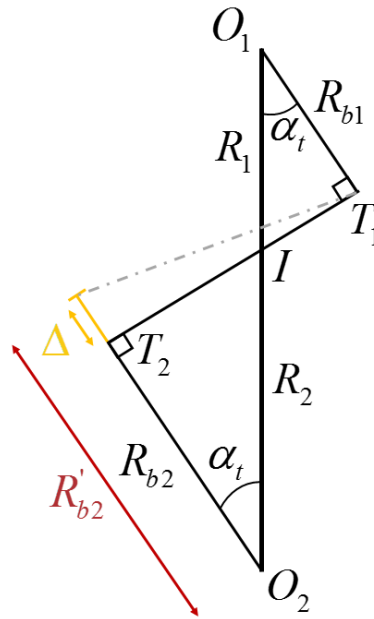


Fig. III-27: Scheme of rim expansion effect on gear key parameters

It can therefore be concluded that the influence of centrifugal effects on mesh global parameters is of secondary importance compared with their contributions to the local contact conditions associated with tooth shape modifications.

3. Industrial Power Transmission

3.1. Model Presentation – Numerical Validation

3.1.1. Gearbox Presentation

The gearbox under consideration is the two-stage power helical transmission presented in Fig. III-28. It is composed of the High Speed Train (HST), including the drive and intermediate gears, and the Low Speed Train (LST) comprising the pinion on the intermediate gear and the output gear. Comparisons will be performed on the HST.

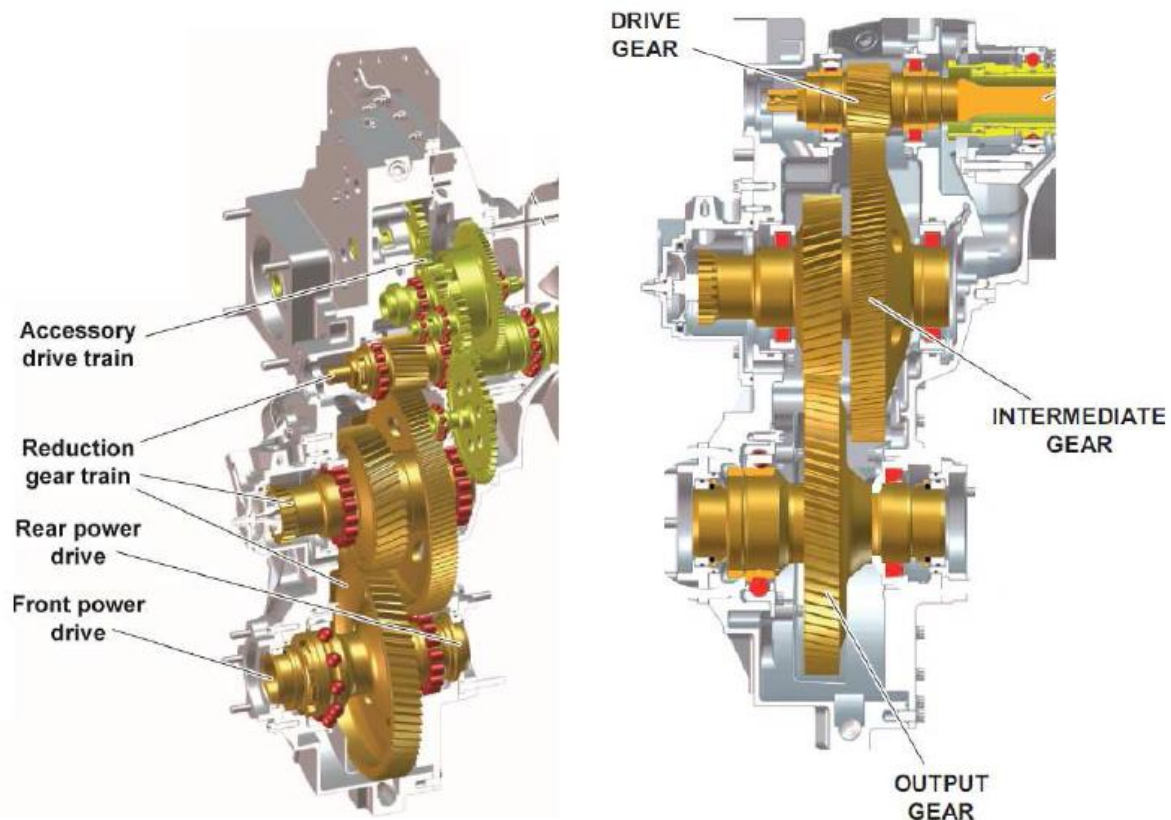


Fig. III-28: Test Transmission Architecture (Interest: drive and intermediate gear)

Tab. III-9 presents the geometrical data of the HST gear set. It is a small module helical gear with a large speed reduction (around 4.5) and a relatively large rim (above 25 mm) which corresponds to a very specific design and is detailed below.

	Pinion	Wheel
Module m (mm)		1.5
Number of teeth	28	127
Pressure Angle ($^{\circ}$)		25
Helix Angle ($^{\circ}$)		>0
Rim Width b (mm)		>25

Tab. III-9: Industrial case geometry

The driving part is composed of a hollow shaft resulting in a large tubular pinion body whereas the driven gear is mounted on the intermediate shaft along with the pinion of the next reduction stage as illustrated in Fig. III-29. In order to reduce the mass of this rather large member while keeping sufficient rigidity and acceptable contact pressure, a conical thin web with holes combined with relatively wide rim has been designed.

a. Hybrid Model

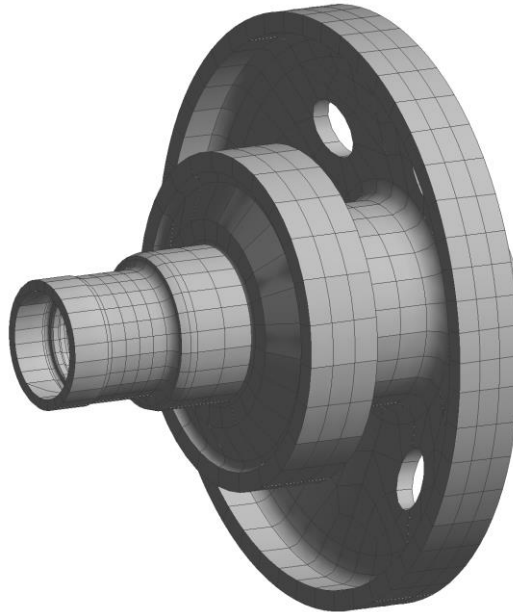


Fig. III-29: FE intermediate train (HST wheel + LST pinion) prepared for condensation process

To integrate these characteristics in the modular model, the condensation procedure as described in Chapter II is applied to the whole intermediate train shown in Fig. III-29. Due to its tubular shape, the driving pinion has been first modelled using a two-node shaft element as described in Chapter II-1.1. The influence of the pinion model will be further analysed in the final section of this chapter. In these conditions, the resulting gear element is composed of a 2-node pinion and a sub-structured gear connected by a non-linear, time-varying Winkler foundation with mortar interfaces. External forces and couples are introduced in order to account for the downstream reduction stage and lumped parameter elements are added to simulate the bearings and the housing.

b. Industrial FE Model

A full 3D finite element model has been developed by SAFRAN HE which incorporates the complete pinion and gear shafts, contact elements between the teeth and validated boundary conditions at the bearings (Fig. III-30). The static interactions with the low-speed transmission are introduced by setting to zero the normal displacement at one node on a tooth flank in the meshing zone (Fig. III-31).

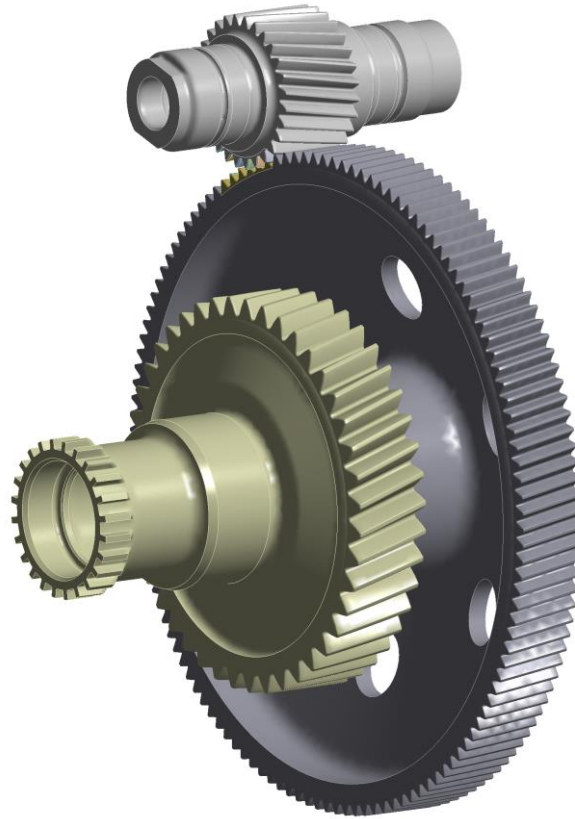


Fig. III-30: Industrial FE model of the HST

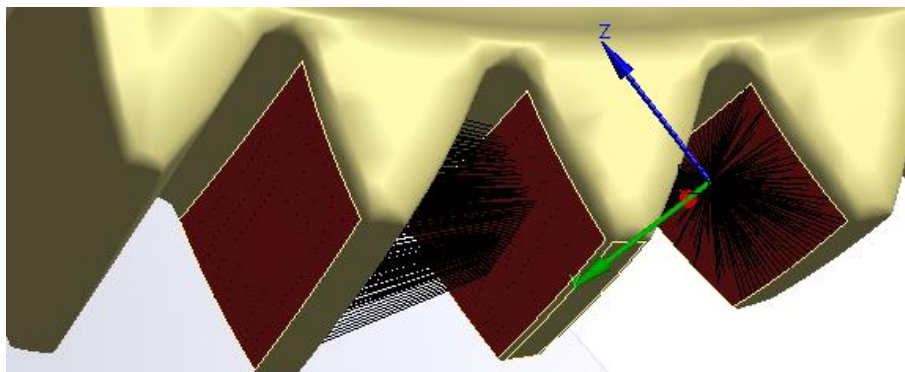


Fig. III-31: Intermediate pinion tooth boundary condition

3.1.2. Numerical Validation with Respect to FE Industrial Model

Starting with the results obtained by the full 3D industrial FE model, Fig. III-32 represents the quasi-static pressure pattern on a tooth flank (using dimensionless values) when considering the centrifugal effects at 8820 rpm on the intermediate shaft. The contour plots have been obtained from successive static calculations for a range of kinematic positions from engagement to the end of recess.

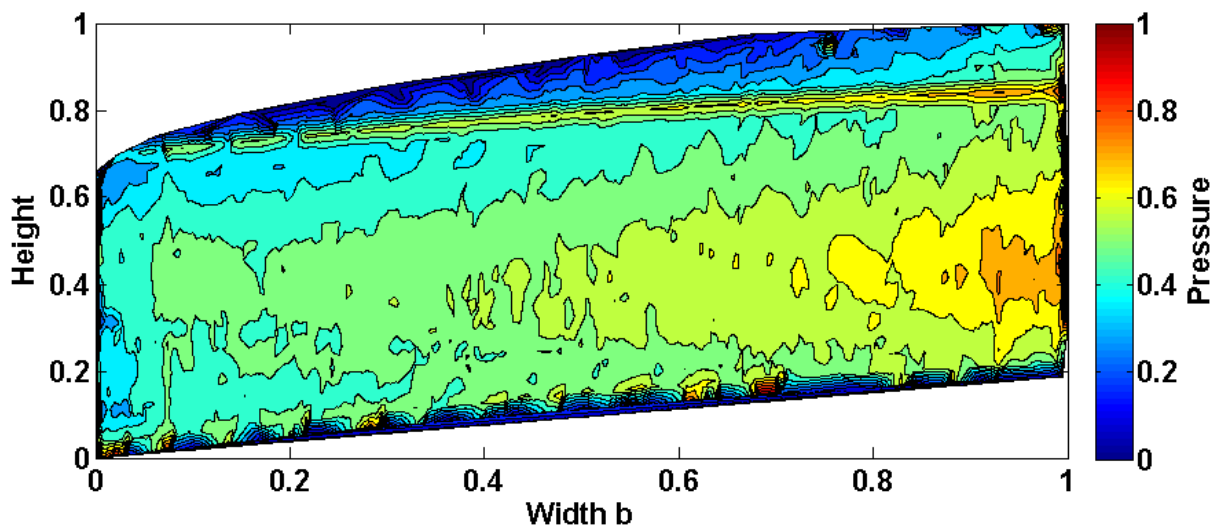


Fig. III-32: Tooth Flank analysis with quasi-static FE model (centrifugal load for $\Omega_w = 8820 \text{ rpm}$)

Considering now the hybrid dynamic model, a quasi-static analysis was performed (with a wheel speed of 1 rad/s) in order to compare with the previous static pressure distribution. It is to be noted that the scaling for all the pressure plots throughout this chapter is the same so that direct comparisons are possible.

Centrifugal effects (centrifugal load) were artificially superimposed in order to meet the conditions in the static simulations above. The corresponding dimensionless pressure distribution shown in Fig. III-33 agrees well with the outcome of the full 3D FE model with similar asymmetric pressure patterns with one side being overloaded whereas the opposite side is almost free from loading. Slight localised differences can be observed however, in particular the full FE model leads to pressure peaks near the tooth tip which are not reproduced by the hybrid model. The use of FE/contact elements can simulate off-line of action contacts (premature engagements between non conjugate tooth profiles caused by gear compliances) which can generate localised overloads if the tooth profiles are unmodified (as is the case here). On the other hand, one of the basic hypothesis of the hybrid model is that all tooth contacts lie

in the base plane thus making it impossible to simulate these pressure peaks at engagement. However, the influence remains very local and it is believed that the hybrid dynamic model can also provide relevant quasi-static pressure distributions.

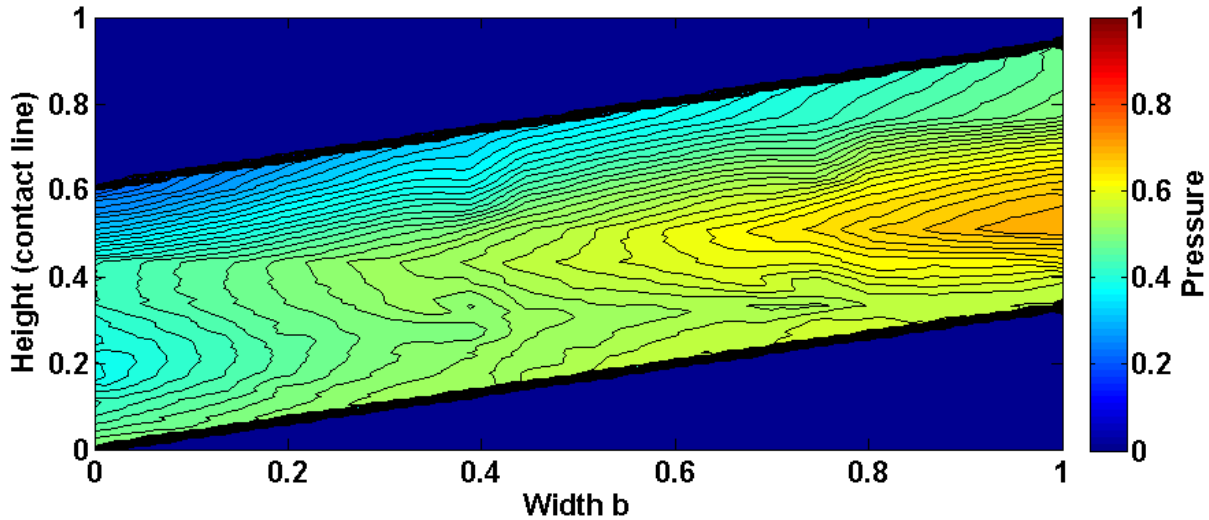


Fig. III-33: Line of contact pressure on base plane

Further simulations for dynamic conditions have been performed using the hybrid model in order to assess the possible modifications brought by dynamic effects on tooth loading. Fig. III-34.a shows the resulting pressure distribution obtained at the nominal speed (same scale as in Fig. III-33). The dynamic pressures are similar to what was found in quasi-static conditions but more evenly distributed over the tooth flank. Fig. III-34.b corresponds to the results obtained for a tooth above one of the holes in the gear web and proves that there is no real influence of the holes on tooth loading. Based on these results, it can be concluded that tooth loads and pressures are dependent on centrifugal effects via the web deflections but far less sensitive to vibrations (dynamic behaviour) and the presence of holes (which is certainly not desirable).

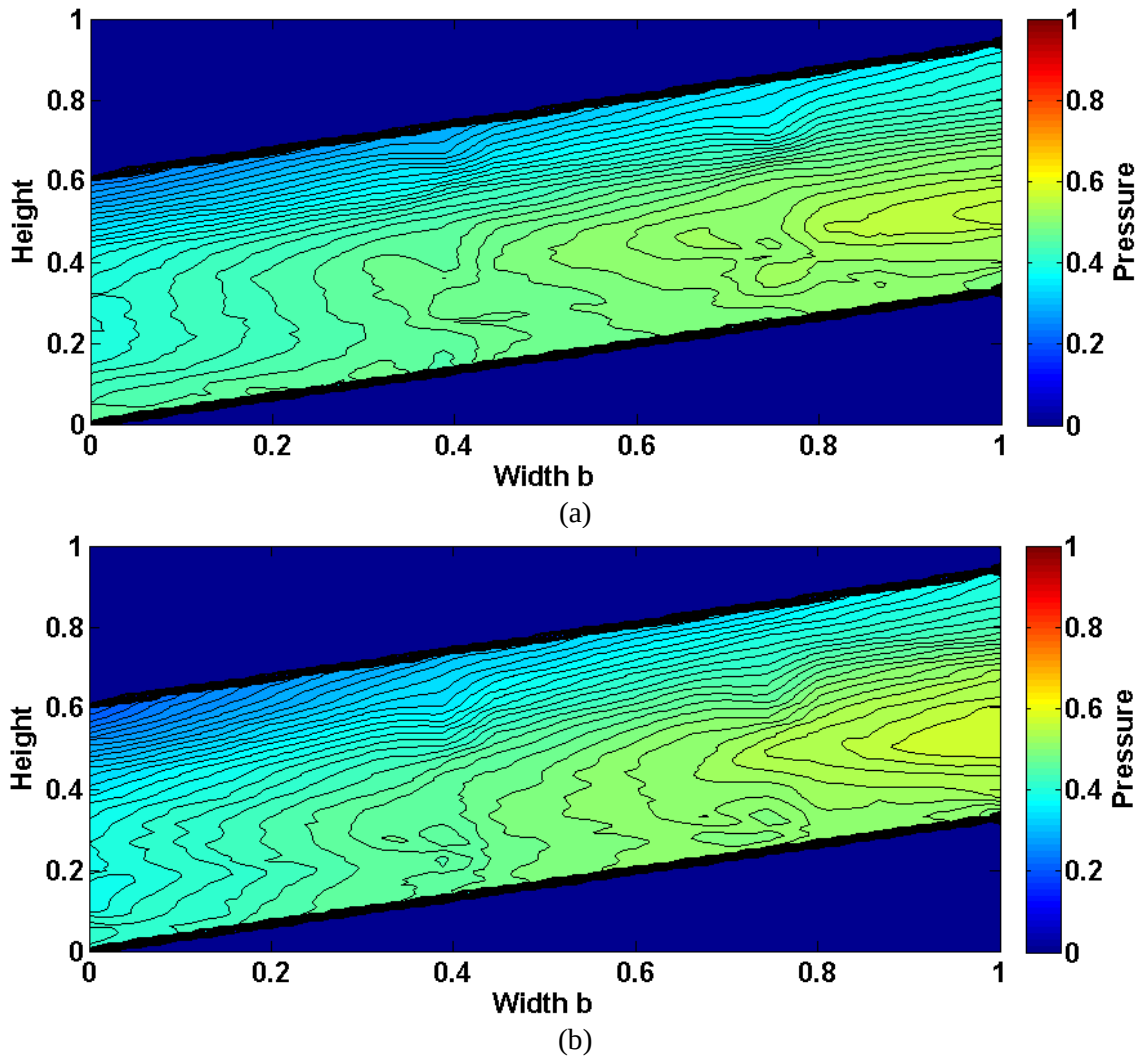


Fig. III-34: Meshing pressure of the hybrid model H1 on dynamic run for (a) above material and (b) above a hole meshing conditions

Comparisons between the full 3D and hybrid models are extended to bearing loads. Tab. III-10 gives the corresponding deviations (in %) for all the bearings in the directions **S**, **T**, **Z** (2 perpendicular radial + axial directions) as defined in Chapter II.

Direction	Pinion			Wheel		
	Av	Ar	Ax	Av	Ar	Ax
Z (%)	0	0	0.1	0	0	11.1
S (%)	3.5	9.8	0	3.7	13.5	0
T (%)	1.4	2.3	0	3.1	7.4	0

Tab. III-10: Bearing load comparison with FE model with wrench inclusion for LST influence

The results in Tab. III-10 are satisfactory with a maximum difference around 13% which prove that the modelling of the bearing and the additional forces and couples generated by LST is realistic.

3.1.3. Modal Behaviour

Prior to running extensive dynamic simulations with the hybrid model, the modes of the substructure shown in Fig. III-29 are compared with the experimental results obtained on the real system by interferometry [MOU14]. Fig. III-35 displays the percentages of deviation between the calculated and measured frequencies on the real system for several identified mode shapes in terms of nodal circles (NC) on the gear web and pinion body (both on the intermediate shaft). The vertical blue lines represent the limits of the operating mesh frequency on stage 1 which will be used further in the comparisons between experimental and simulated displacements.

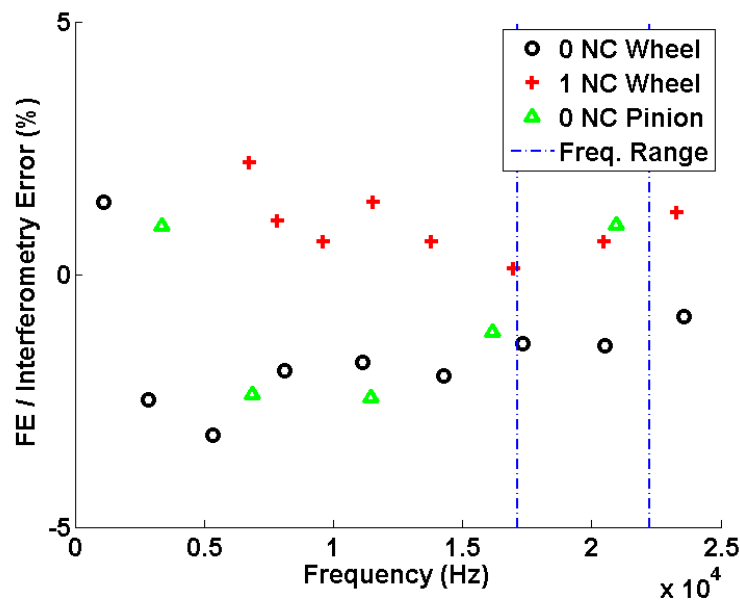


Fig. III-35: FE wheel modal comparison to interferometry test (starting to the 2nd nodal diameter (ND) mode for each circle family (NC))

Generally speaking, a very good correspondence is observed with maximum deviations below 3%. The agreement is better for the frequencies near the operating conditions (between the two blue vertical dotted lines). Fig. III-36 shows the shape of one of the principal mode within the frequency limits of interest (blue vertical lines) which indicates that the rim contributes significantly to this 9-diameter mode shape (no nodal circle). It can therefore be inferred that dynamic couplings between the meshing and gear body are likely to exist at this particular frequency and that mesh excitations may be critical for this mode as reported by Oda [ODA85-86.c].

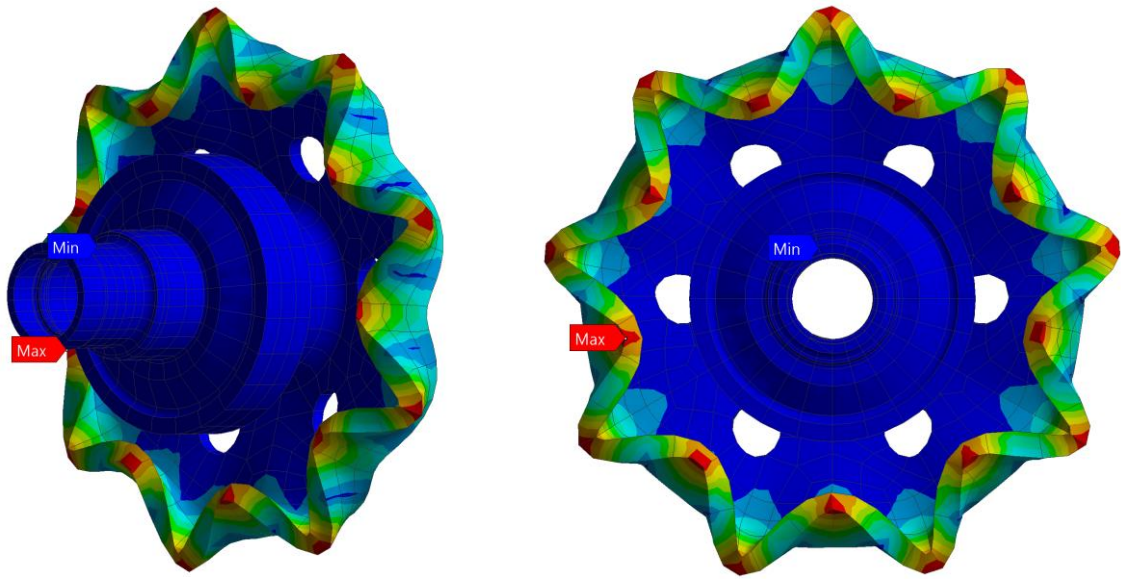


Fig. III-36: 9th diameter mode as example: Rim mode of interest

It has been proved [MEH91-SCH97] that, for rotating flexible bodies, apparent frequencies are affected by the observer coordinate system (Doppler Effect). The phenomenon can be illustrated in this case of rotary members using the simple example developed in section 2.2 of Chapter III. Considering a disc with free boundary conditions vibrating at one of its bending natural frequencies, its resulting deformed mode shapes in the direction \mathbf{n} , normal to the disc surface, can be expressed in the rotating coordinate system attached to the disc under the form:

$$\delta_R(\theta) = \sum_{n=0}^{\infty} (\delta_c^n \cos(n\theta) + \delta_s^n \sin(n\theta)) = \sum_{n=0}^{\infty} \delta^n \cos(n\theta + \varphi_0) \quad (3.4)$$

with δ_R , displacement viewed from the rotating frame, n the nodal diameter number, θ angular coordinate and φ_0 phase angle.

Neglecting damping and focusing on one mode n of natural frequency $\omega_n = \omega_0$, the displacement in the coordinate system attached to the disc can be expressed, as long as interactions between adjacent natural frequencies can be discarded, as:

$$\delta_R(t, \theta) = \delta^n \cos(n\theta + \varphi_0) \sin(\omega_0 t) \quad (3.5)$$

with ω_0 , natural pulsation of the studied mode.

re-written as:

$$\delta_R(t, \theta) = \frac{\delta^n}{2} (\sin(\omega_0 t + n\theta + \varphi_0) + \sin(\omega_0 t - n\theta - \varphi_0)) \quad (3.6)$$

When the observer is attached to the fixed frame, the wheel/disc rotational speed is Ω and, from the fixed frame perspective, the angular coordinate θ of the stationary wave on the wheel becomes:

$$\theta = \Omega t + \theta_0 \quad (3.7)$$

with θ_0 an arbitrary initial angular coordinate on the disk.

Equation 3.6 in the rotating frame leads to the following expression in the fixed frame.

$$\delta_f(t) = \frac{\delta^n}{2} \left(\sin((\omega_0 + n\Omega)t + \theta_0 + \varphi_0) + \sin((\omega_0 - n\Omega)t - \theta_0 - \varphi_0) \right) \quad (3.8)$$

With δ_f total displacement expressed from a fixed frame observer

Each mode exhibits therefore two apparent frequencies for an observer attached to the fixed frame, depending on its natural frequency and its spatial distribution, i.e. its nodal diameter number n .

In case of forced response, a mode is amplified when the excitation frequency coincides with its natural frequency. For conventional gears (with the exception of planetary gears with rotating planet carriers), mesh excitation are attached to the fixed frame and act on a small fraction of the disc periphery. The corresponding fundamental excitation frequency is $Z\Omega t$ with respect to the fixed frame for a gear (simulated as a disc) with Z teeth so that, depending on the coordinate system of the observer, resonances will occur when:

$$\begin{cases} Z\Omega = \omega_0 \pm n\Omega & \text{in fixed frame} \\ \omega_0 = (Z \pm n)\Omega & \text{in rotating frame} \end{cases} \quad (3.9)$$

This qualitative demonstration can be easily reversed to find the meshing frequency of excitation as viewed from the rotating frame attached to the disc. In this case, for a known rotational speed, the excitation cannot be separated from the mode spatial repartition, i.e. its diameter number n and it will also lead to two response frequencies in the rotating frame. For each coordinate system, the evolution of the response frequencies for one given mode are plotted as Campbell diagrams (Fig. III-37).

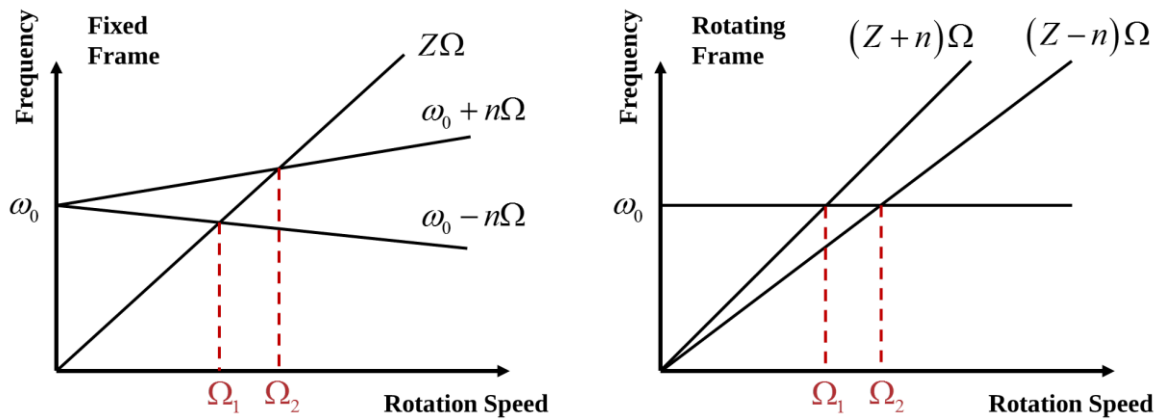


Fig. III-37: Campbell diagrams depending on the chosen frame of expression

This figure illustrates how two critical rotational speeds Ω_1 and Ω_2 , independent of the coordinate system of reference, can be identified which conventionally represent the backward and forward whirl at frequency ω_0 respectively. It can be noticed that points attached to the wheel (disc) do not respond with a frequency equal to the excitation frequency and that the change from stationary to rotary coordinate systems must be included in the analysis.

For the industrial case treated here, the frequency of excitation in the fixed frame is the gear mesh frequency $Z\Omega_2 = 127\Omega_2$ and the conversion for each gear body nodal diameter order of resonance in the rotary coordinate system is given in Tab. III-11.

ND (n)	5	6	7	8	9	10	11
Backward	132	133	134	135	136	137	138
Forward	122	121	120	119	118	117	116

Tab. III-11: Rotating frame frequency order ($Z_2 = 127$) for the wheel flexion modes

In what follows, backward modes will be identified as $-nND$ whereas forward modes will be referred to as $+nND$ where n is the nodal diameter number (Tab. III-11).

3.2. Data Acquisition Process

3.2.1. Experimental Device

The full power transmission (Fig. III-28) was tested over the frequency range corresponding to the operating conditions (defined by the two vertical blue lines in Fig. III-35) and emphasis was placed on the mode shapes with significant rim deformations as they are likely to interfere with the meshing conditions.

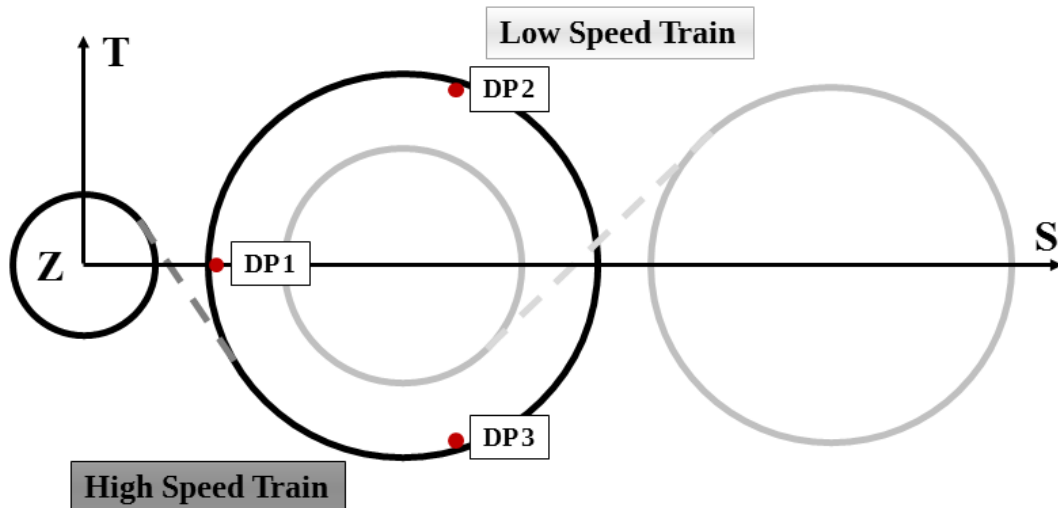


Fig. III-38: Angular position of Displacement Probes (DP) for Numerical model / Experiment comparison

Focusing on the high speed stage, in bold black in Fig. III-38, the instrumentation comprises three displacement probes evenly distributed along a wheel circumference with the objective of identifying the potentially critical web vibrations excited by the meshing. The probes, embedded in the transmission housing (fixed coordinate system), are used to measure the radial displacements of the rim as schematically represented in Fig. III-39.

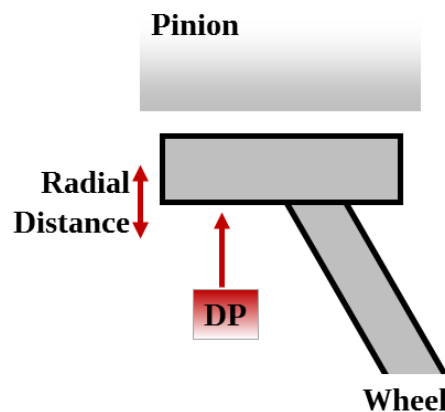


Fig. III-39: Radial and axial position of Displacement Probes (DP) devices for rim radial displacement measure

Data are recorded during speed up tests and, for each constant speed increment, Fast Fourier Transform (FFT) are performed. The fundamental mesh frequency response for each sensor is isolated and displayed in terms of RMS vibration amplitude versus speed as shown in Fig. III-40.

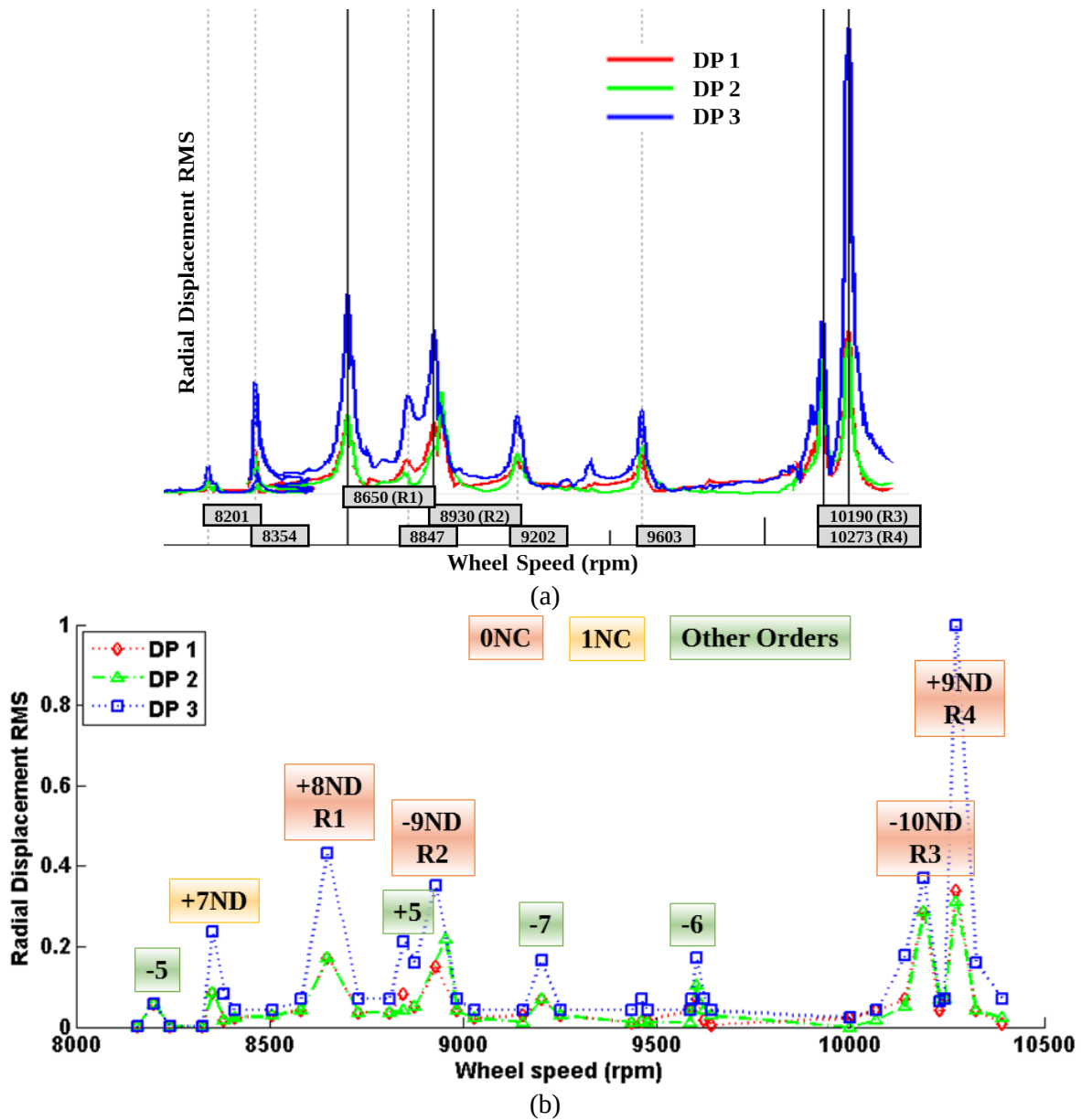


Fig. III-40: (a) Experimental results and (b) extracted scheme for each DP

Fig. III-40.a shows the raw data as extracted from the frequency analyses. All three displacement probe plots exhibit the same response peaks, even if the corresponding RMS amplitudes differ. The main resonances are labelled R1 to R4. The rotating structure theory of displacement analysis in the moving and fixed frame developed in [LAL90] makes it possible to identify the resonant frequencies and mode shapes using the displacement measurements over the speed range of interest.

Identification		Speed of Apparition (rpm)	Importance
Nodal Diameter (ND)	Nodal Circle (NC)	Rotation speed (rpm)	Resonance of Importance
- 5 th order of rotation		8201	
+7	1	8354	
+8	0	8650	R1
+5 th order of rotation		8847	
-9	0	8930	R2
-7 th order of rotation		9202	
-6 th order of rotation		9603	
-10	0	10190	R3
+9	0	10273	R4

Tab. III-12: Speed for each mode apparition

The first frequency (R1) can be identified as the forward 8th nodal diameter mode, +8ND of the first family (no nodal circle). The second one, R2 corresponds to the backward 9th nodal diameter mode (-9ND) of the same family whereas R3 is identified as -10ND and R4, +9ND. It is observed that the frequency shift by the rotational speed has placed these two separate modes very close to each other in the nominal speed range, thus justifying the careful analysis of the wheel dynamic behaviour.

Fig. III-40.b is a dimensionless variant of the previous graph which is introduced for comparisons purposes with simulation results and will be used in the rest of this chapter. The vertical scale has been defined by setting the maximum value to 1.0.

In the simulation, modal damping factors α_i are introduced and estimated from the experimental response peaks using the bandwidth method [LAL84]:

$$\frac{\Delta\Omega_i}{\omega_i} = \frac{\Delta f_i}{f_i} \approx 2\alpha_i = \frac{1}{Q_i} \quad (3.10)$$

with $\Delta f_i = f_{2i} - f_{1i}$, bandwidth and Q_i , system amplification factor for mode i .

A damping matrix can be derived by using a Rayleigh damping as

$$[\mathbf{C}] = a_R [\mathbf{M}] + b_R [\mathbf{K}] \quad (3.11)$$

With a_R and b_R Rayleigh coefficients; $[\mathbf{K}]$, the averaged overall stiffness matrix.

For one mode i , one obtains [LIU95], [CHO03]:

$$\alpha_i = \frac{a_R}{2\omega_i} + \frac{b_R \omega_i}{2} \quad (3.12)$$

With ω_i frequency of the modes i .

(3.12) is plotted in Fig. III-41, in order to separate the contribution of a_R and b_R depending on the frequency range.

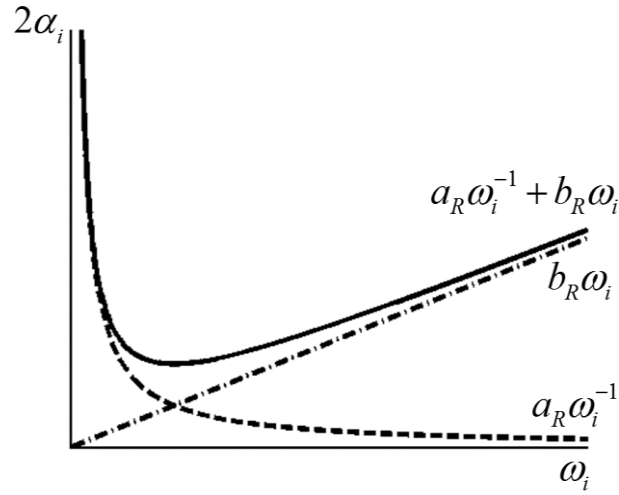


Fig. III-41: Contribution of Rayleigh damping parameters depending on frequency ω_i

It can be observed that, for high frequencies, i.e. high rotational speeds as is the case for the systems under consideration, parameter a_R can be ignored so that:

$$\alpha_i = \frac{b_R \omega_i}{2} \Leftrightarrow b_R = \frac{2\alpha_i}{\omega_i} \quad (3.13)$$

The damping matrix can therefore be taken as proportional to the average global stiffness matrix such that:

$$[\mathbf{C}] = b_R [\mathbf{K}] \quad (3.14)$$

3.2.2. Dynamic Model

The numerical model which was described in section 1 is limited to the High Speed Train (HST) with the drive pinion and the intermediate gear only. A rim master node is placed at the same axial and radial locations as the displacement probe (Fig. III-42) and an example of radial displacement for a wheel revolution is shown in Fig. III-43 for $\Omega_w = 8420 \text{ rpm}$.

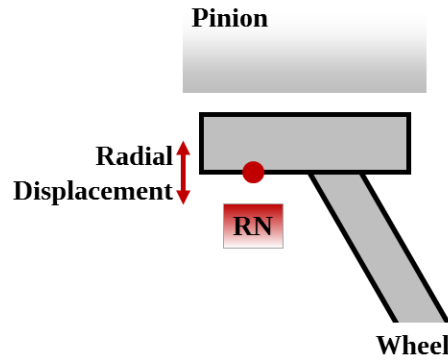


Fig. III-42: Numerical data gathering scheme: Rim Node (RN)

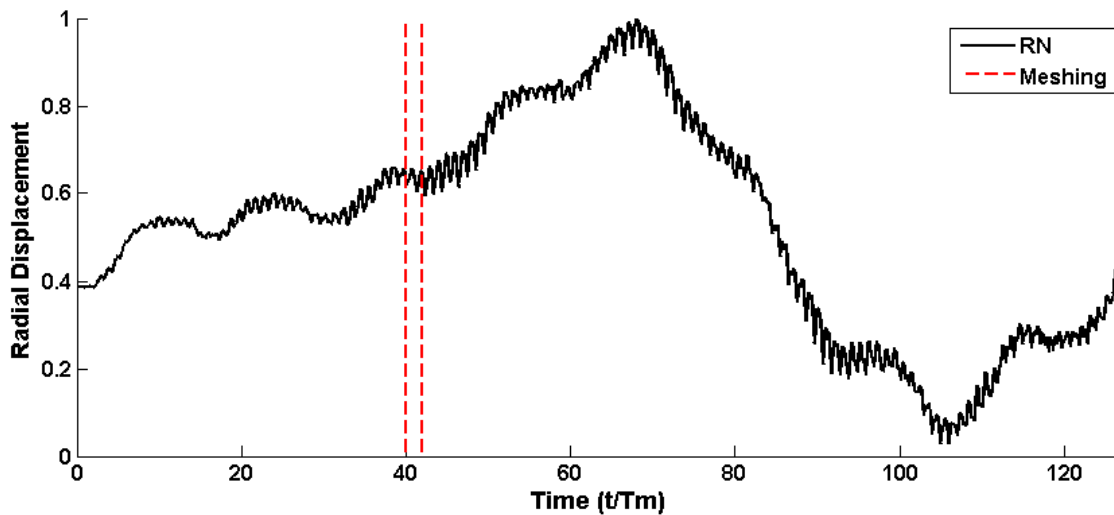


Fig. III-43: Rim Node response over a full wheel revolution

Note that, for confidentiality reasons, the displacement amplitudes have been normalised with respect to the maximum displacement amplitude. The results clearly show that the response is dominated by low frequency components associated with the rotation of the parts whereas higher mesh-related frequencies exhibit smaller amplitudes. The time limits corresponding to the passage of the master node under the meshing area are indicated by the dashed red vertical lines. Fig. III-44 shows the corresponding dimensionless spectrum around the mesh order (127) whose vertical scale is the same as in Fig. III-43 for comparison purposes.

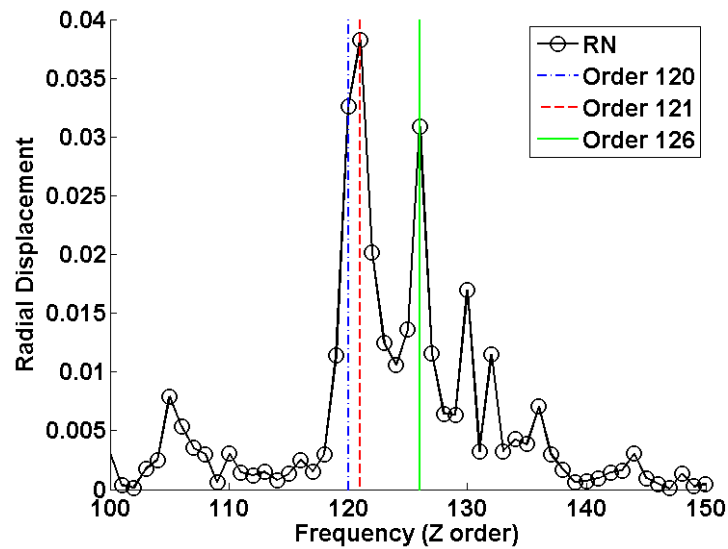


Fig. III-44: Fast Fourier Transform of the Rim Node response over a full revolution versus tooth number (127 being meshing order)

According to the theory, the mesh frequency (order 127) does not emerge in the response Fourier Transform and, based on the references in Tab. III-11, the peaks in Fig. III-44 are those associated with the 6th and 7th nodal diameter backward modes as well as the first nodal diameter forward mode. The latter can also be another type of mode such as a bearing or shaft mode, whose frequency is modulated by the rotational speed.

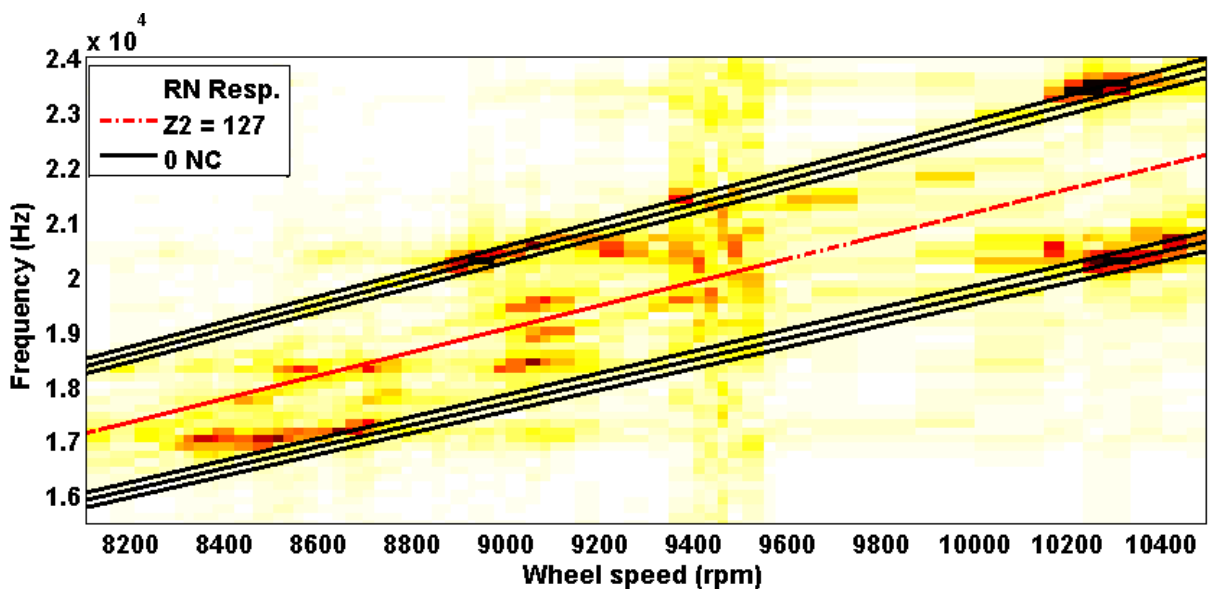


Fig. III-45: Campbell diagram drawn with the RN, (0 NC corresponding to the 8th, 9th and 10th nodal diameters of the family)

Fig. III-45 shows a Campbell diagram derived from simulation results over a range of speeds. The 8th, 9th and 10th nodal diameter orders that can be seen in the experimental data have been superimposed. The figure is typical of what is obtained for a rotary system (Fig. III-37) and the significant amplitudes are never associated with the mesh frequency (127th order) but are sidebands as expected.

3.3. Validation – Experimental Comparison

3.3.1. Results Analysis at Significant Speed Steps

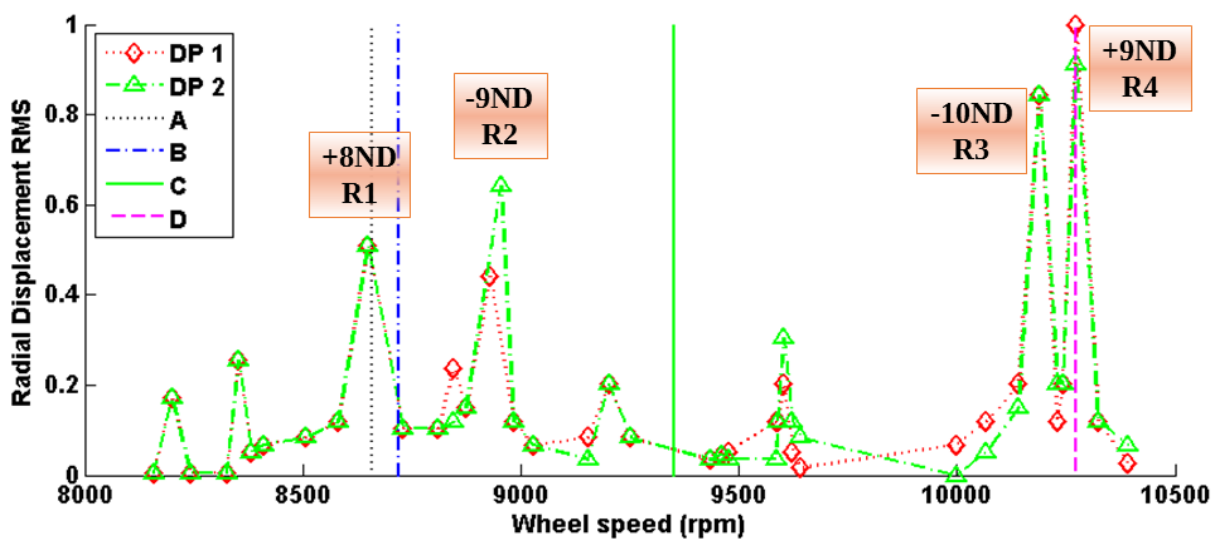


Fig. III-46: Identification of the speeds of interest

Several speeds have been used in order to compare the simulation and measured results (sensed in different coordinate systems) which are visualised in Fig. III-46 by vertical lines and labelled A, B, C and D. Test cases A and D correspond to two resonance peaks (+8thND and +9thND respectively) (R1, R4) whereas cases B and C are situated between resonances where no identified peaks emerge.

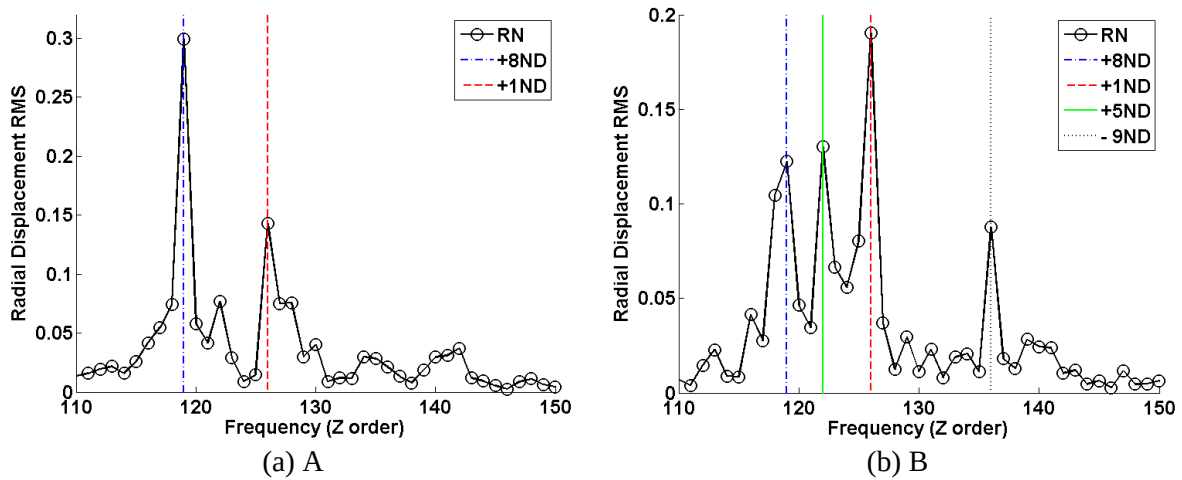


Fig. III-47: Full frequency analysis with FFT for case A and B

The spectra of the simulated response in the vicinity of the mesh order are displayed in Fig. III-47 for cases A and B. For case a), the 119 order response corresponding to the +8thND (R1) is clearly visible in agreement with the identification of the +8thND critical speed (Fig. III-46). It is also interesting to note that a modulation on 1 of the Z_2 order is present, as well as numerous lower amplitude responses. Fig. III-47.b, shows peaks at the +8thND and -9thND frequencies but there is also a peak at the first modulation of the Z_2 order, as well as a peak which would coincide with a +5thND mode. Moreover, a number of lower frequency peaks are also present. These results confirm that resonance peaks can clearly be identified by their order but also that between two close resonances of the wheel, both contributions appear in response spectra.

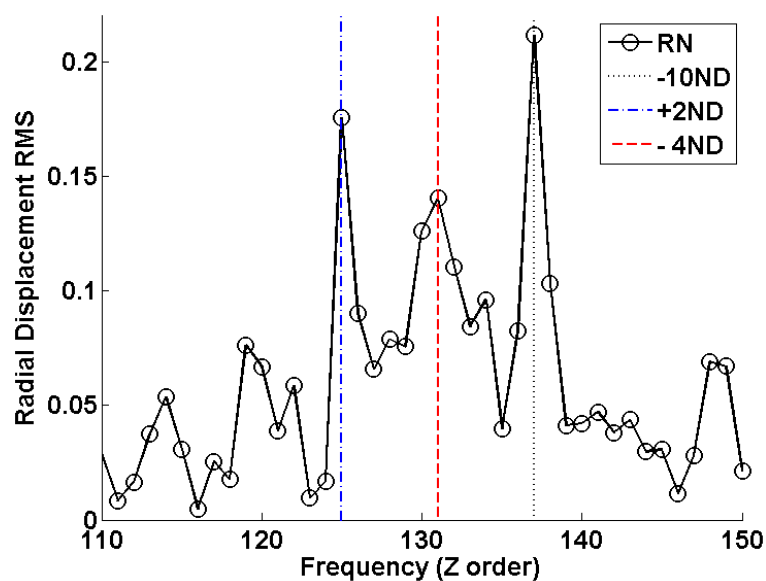


Fig. III-48: Frequency analysis for the case C

Fig. III-48 presents the frequency analysis (FFT) of case C, corresponding to a non-resonant situation. A peak at order 137 emerges clearly which is associated with the +10thND mode situated at higher speed. Here again, outside a resonance zone, the contribution of various modes to the signal is identified.

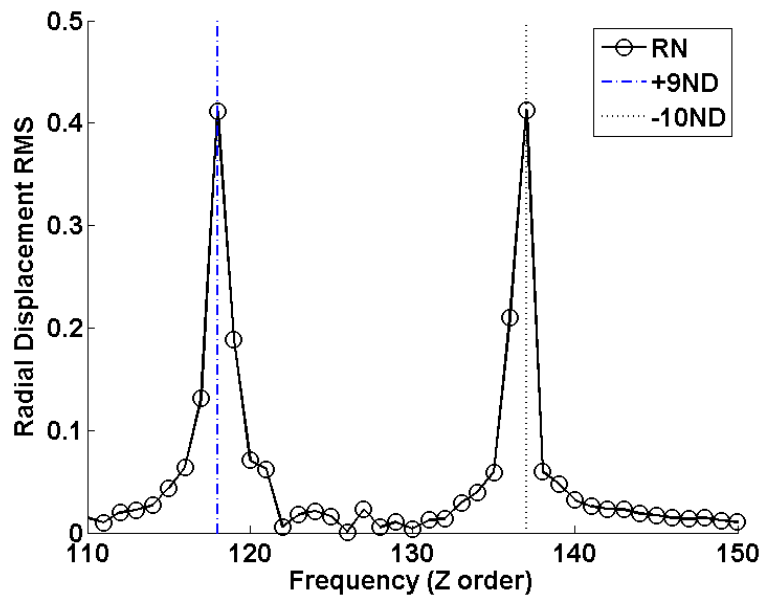


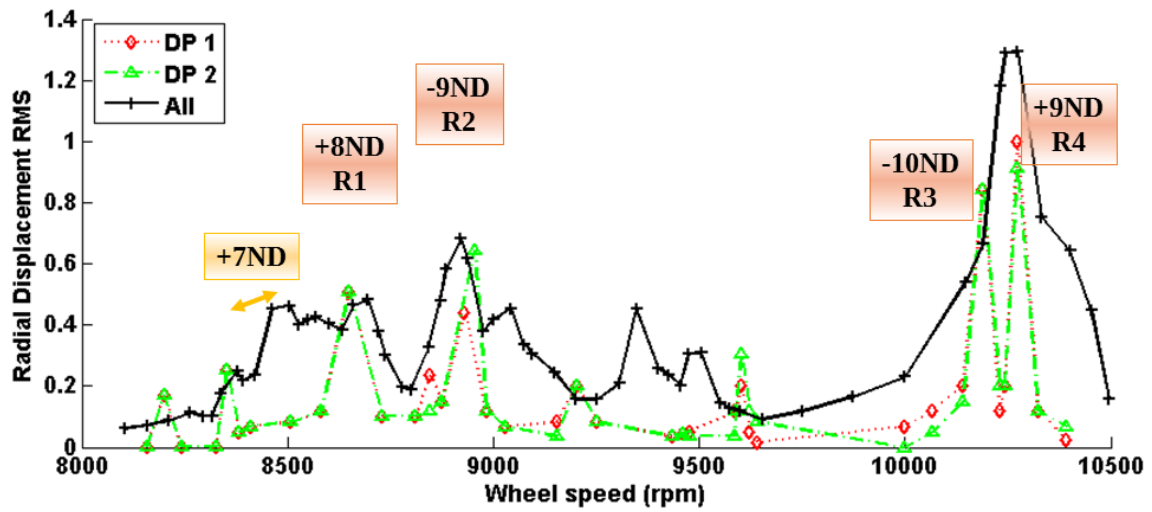
Fig. III-49: Frequency analysis for the case D

Two resonance peaks are clearly noticeable in Fig. III-49 for case D which correspond to the experimentally identified +9thND and -10th ND modes.

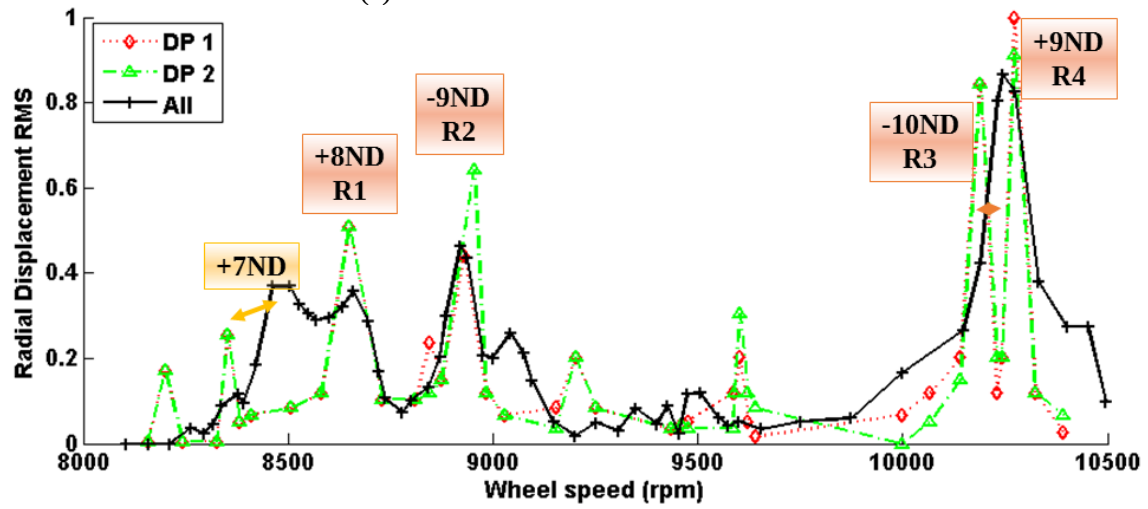
3.3.2. Validation – Experimental Comparison

The summation of the amplitudes at all the orders has been performed to be able to compare the numerical simulation results with the experimental displacement probe responses over the range of speeds under consideration Fig. III-50. Two graphs are presented: a) the first one corresponds to the direct summation of the spectrum amplitudes and, b) to the summation of filtered spectra in order to eliminate some of the numerical noise produced by the simulation process. To this end, the contributions in the non-resonant areas have been eliminated before summations were performed.

It can be noticed that the overall agreement is reasonable thus proving that the simulation and model put in place are sound.



(a) Raw curve drawn without noise filter



(b) Curve treated with signal filter

Fig. III-50: Sum of all nodal diameter signals

4. Conclusion

This chapter is dedicated to the validation of the new hybrid model whose main lines are presented in chapter II. To this end, three test cases have been used. The first one is a part of an academic accessory gearbox with a spur gear over a thin straight web. The second case is an academic helical gear unit corresponding to one reduction stage in a power transmission. The gear is also a webbed wheel but its shape is more complex with an inclined and sided web under a large rim. Finally, an actual helicopter two-stage power transmission has been analysed and both experimental and numerical results have been presented and compared.

Several variants of hybrid models have been considered which combine rigid-body and finite element models of the pinion and/or the gear. A number of comparisons for quasi-static conditions are presented which all prove the validity of the modelling principles and simulation techniques. In particular, it is shown that the bearing displacements and loads found by all the models agree well and that the tooth load distribution given by the hybrid model is very similar to that obtained when using a full 3D finite element model with contact elements.

Comparisons have been extended to dynamic results and, here again, all the models are consistent and their results agree very well providing that the damping levels and modelling are comparable. It has also been demonstrated that centrifugal effects can strongly influence tooth load patterns in the presence of a thin web/rim.

Finally, the numerical results have been confronted with the experimental measurements from displacement probes attached to the ground over a range of speeds. By taking into account the frequency shift induced by the rotation of the wheel, it is possible to reconstruct the amplitudes at a given frequency and compare data obtained in the fixed and rotary coordinate systems. By so doing, a fairly good agreement between the predictions and measurements is observed which, to a large extent, validate the theoretical developments in the previous chapter.

The signal analysis at several main speed shows that the model successfully place the main critical speeds in frequency. The resulting curve confirms the results coherence. It also points out the issues of the signal frequency analysis detail and the noise which is present between resonances, both due to limitation in the simulation precision for time calculations reason. Despite these imprecisions, it is demonstrated that the model validation can be done with success.

Chapter IV

Influence of Gear Flexibility on Transmission Design

1. Static Deflection Influence – Accessory Gearbox
2. Dynamic Contributions of Rotating Webs – Power Transmission Gears
3. Flexibility for Fully Webbed Power Transmission Case
4. Conclusion

It has been shown in the previous chapters that the proposed hybrid modelling technique was effective and led to results on load distributions, dynamic factors and transmission errors which agree well with other simulation results and experimental findings. This chapter is aimed at illustrating the potential of the models by specifically analysing the influence of flexible members on the design of high-speed gears.

Three examples are successively examined:

- a) a gear from an accessory gearbox whose body deflections are significant and which is considered with the objective of optimising transmission error under load.
- b) dynamic effects in terms of modal behaviour or high speed phenomena are investigated on a helicopter power transmission with one gear exhibiting several web modes in the operating speed range.
- c) finally, the coupling between the pinion and gear flexibility is studied by considering a thin webbed pinion introduced in the power transmission and its impact on its modal and high speed behaviour.

The examples treated in this chapter prove the versatility of the modelling strategy and show that the proposed modular approach makes it possible to integrate most of the components in light-weight high-speed transmissions.

1. Static Deflection Influence – Accessory Gearbox

1.1. Gear Design – Tooth Optimisation

1.1.1. Helix Angle Inclusion Effect – Web Adequacy

The accessory gear described in chapter III is a thin-rim spur gear mounted on a centred thin-web. The initial validation of the hybrid models H1 and H2 was performed by considering a rigid pinion and wheel (simulated by using a condensed sub-structure with a very large Young's modulus: $E = 4.10^{14} \text{ N/m}^2$). It has been shown that the wheel flexibility mainly increases static compliance because of the straight web whose deflections under load are analysed further in the following section. In what follows, the web/shaft assembly is similar to that in chapter III but the spur gear is replaced by a helical gear.

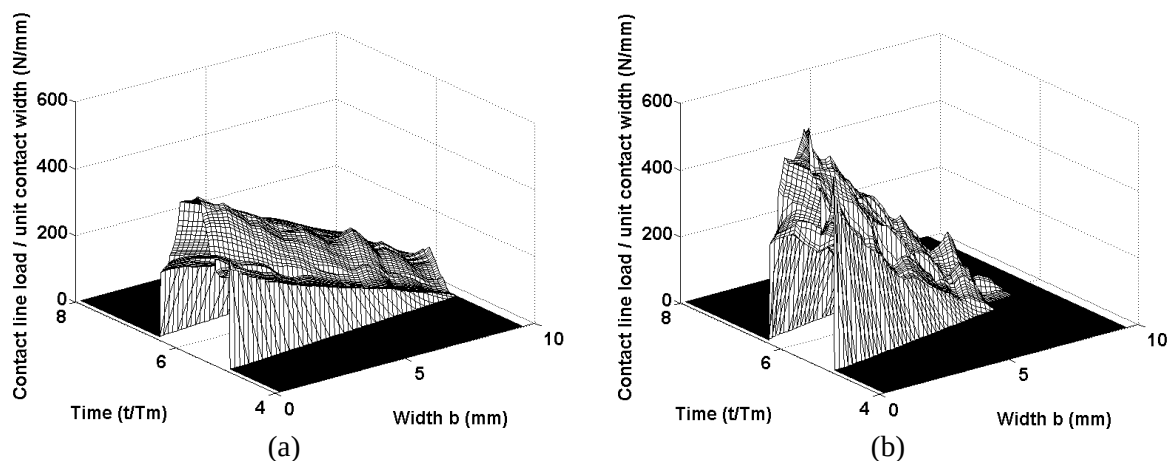


Fig. IV-1: Load at contact for (a) $\beta_b = 10^\circ$ and (b) $\beta_b = 20^\circ$ helix angle

Fig. IV-1 shows two examples of quasi-static load distributions on tooth flanks for a helix angle of 10 and 20° respectively. Although helical gears often have straight webs, it can be observed that the load distribution across the face width is not satisfactory. Because of the axial thrust generated by the helix angle, the web is deformed and tooth contacts are misaligned under load, the effect is more marked as the helix angle increases and can possibly lead to severe overloads at one edge of the face width whereas the opposite one can be unloaded. This effect is correctly captured by the proposed model and proves that it can be used at the early design stage and help define adapted geometries for a given load and type of gear.

1.1.2. Quasi-Static Optimisation of Transmission Error

Fig. IV-2 shows the level curves of transmission error for the same two examples of helical gear in the presence of symmetric linear profile modifications (the depth at tooth tip is E and the extent in the profile direction is characterised as a percentage of the active line of action Γ). The Master Curves as defined by Bruyère *et al.* [BRU13-15] are superimposed which correspond to the family of optimal relief in the case of solid gears. It can be noticed that, in the case of helical gears, the web flexibility is influential as it moves the optimum relief area towards the deeper profile modifications and needs to be accounted for in the definition of tooth micro-geometry. It can also be observed that, for a deformable web, the performance in terms of transmission error time variations is downgraded for a larger helix angle as opposed to what is often encountered with solid gears.

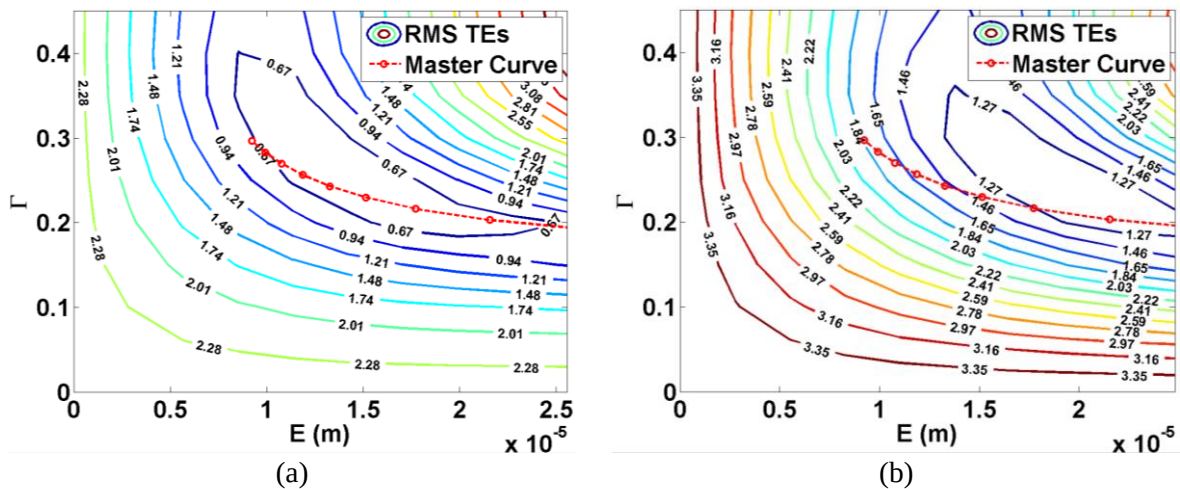


Fig. IV-2: Optimisation with regards to the Master Curve for (a) $\beta_b = 10^\circ$ and (b) $\beta_b = 20^\circ$

Turning back to spur gears, the modifications on the Master Curves appear as still relevant as illustrated in Fig. IV-3. The quasi-static tooth load distribution is significantly improved by choosing a symmetric relief on the Master Curves in Fig. IV-2 with $E = 15 \mu\text{m}$ (depth) and $\Gamma = 0.25$ of the active profile and the dynamic simulation results in Fig. IV-4 reveal that the dynamic factor is largely improved too. Two different damping models (modal and Rayleigh) have been tested and, in spite of some differences in the amplifications at critical speeds, they both confirm the interest of the chosen profile modification in terms of dynamic mesh forces over a broad range of speeds (0-2000 rad/s on the pinion).

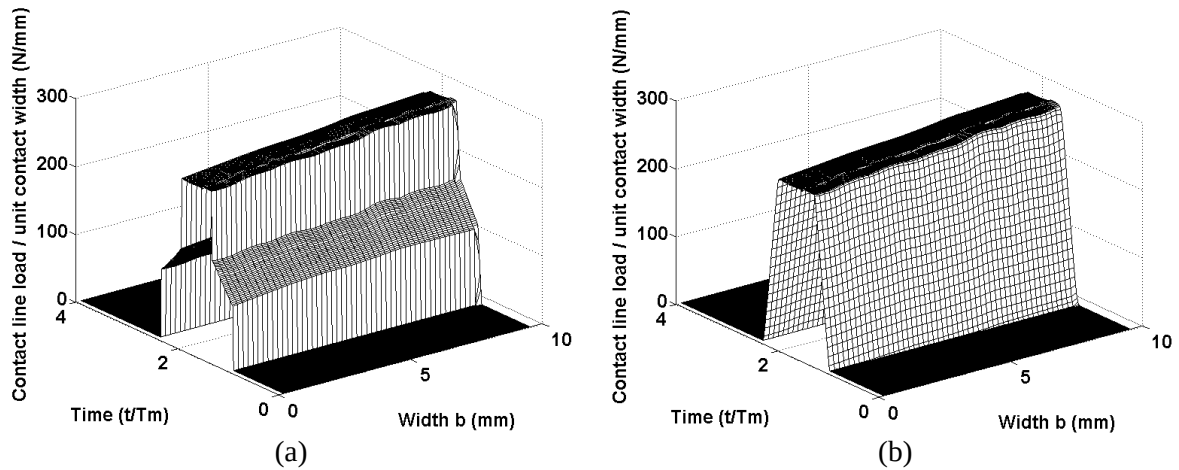


Fig. IV-3: Quasi-static load distribution on contact line for (a) original gear (b) gear modified with tip relief thanks to the Master Curve

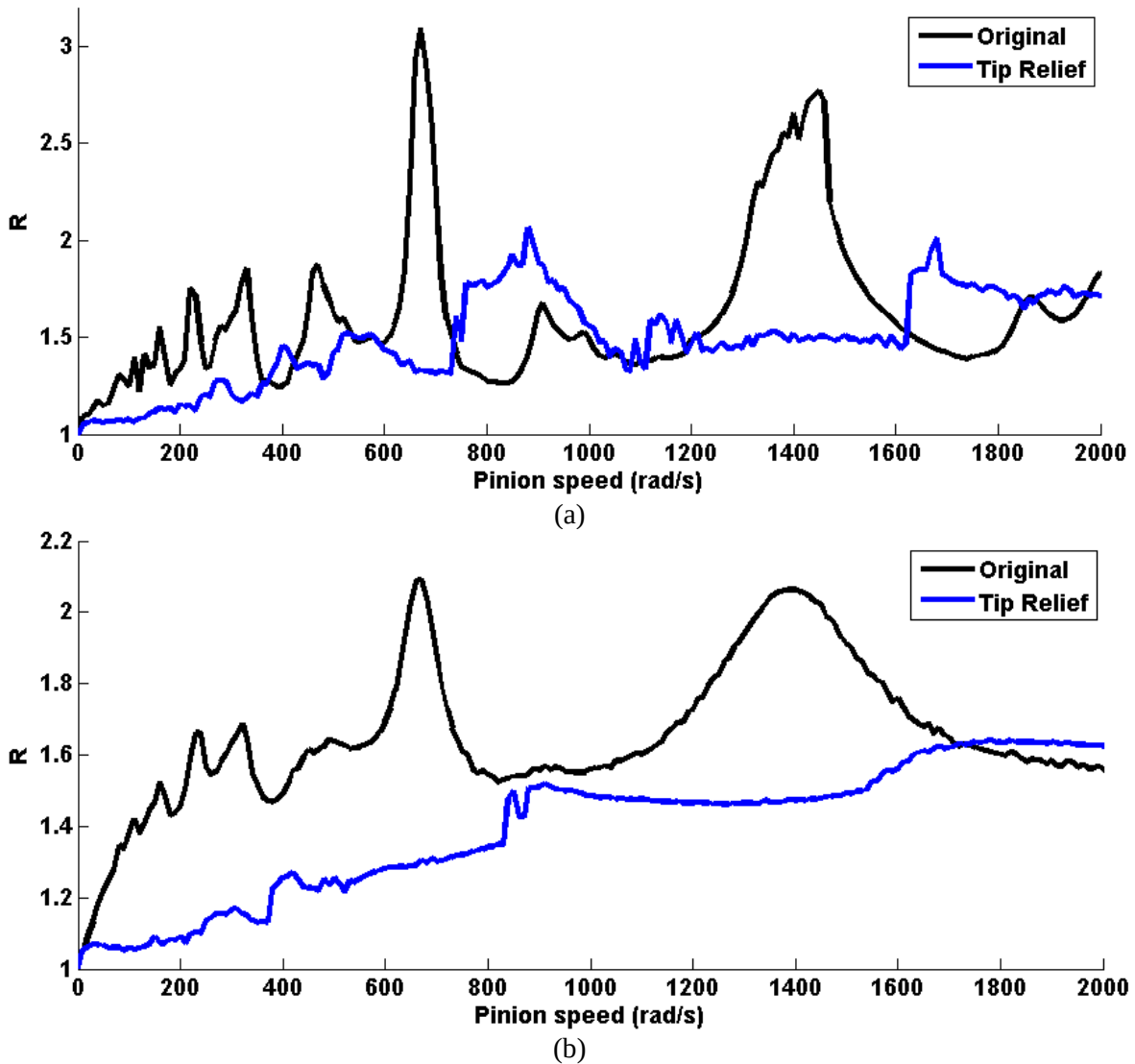


Fig. IV-4: Tip Relief impact on dynamic ratio for (a) modal dependant damping and (b) Rayleigh damping

1.2. Case of Actual Gears – Tooth Profile Deviations

1.2.1. Definition - Local Effects

The previous analyses were conducted using an academic gear example (ideal geometry) and it seems interesting to focus on the influence of tooth shape deviations which, for the most part, cannot be avoided in actual geared transmissions.

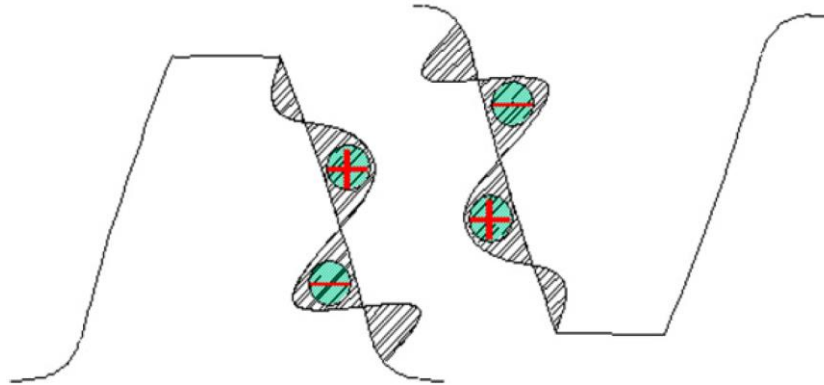


Fig. IV-5: Definition of machining deviations of gears [LI07]

Tooth flank deviations are simulated as material addition or removal with respect to the theoretical tooth flank (Chapter I) which can be approximated by position-varying functions along the tooth profile as schematically represented in Fig. IV-5. The normal deviations on the pinion and wheel tooth flanks are cumulated to define composite errors $e(M_{ij})$ and initial normal separations $\delta_0(M_{ij})$ in the expression of the normal deflections $\Delta(M_{ij})$ (Chapter II).

Accessory gears are usually manufactured with an ISO quality grade of 5/6 and, in order to simulate realistic gears, the profile errors shown in Fig. IV-6, have been superimposed on the linear profile relief trace. Two different defect amplitudes (8 μm and 13 μm peak-to-peak) corresponding to ISO 5 and 7 quality grades have been considered and it is assumed that there is no variation in the tooth face width direction.

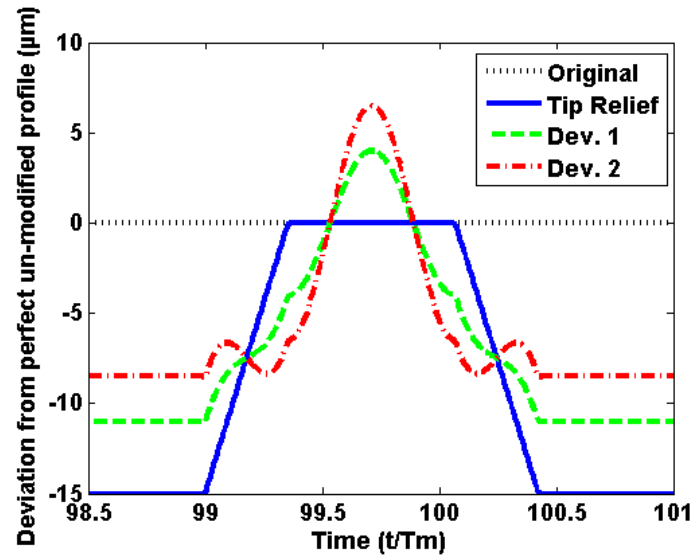


Fig. IV-6: Profile deviation $e(M_{ij})$ for a line of contact through the base plane

Fig. IV-7 shows the quasi-static load distributions for the two deviations and it can be observed that the largest profile deviation tend to almost cancel the smoothing effect brought by tip relief.

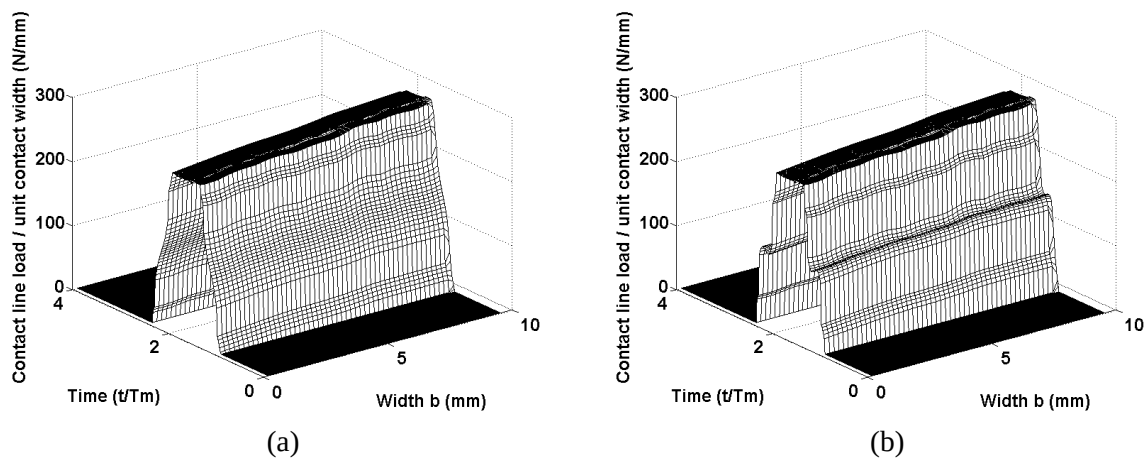
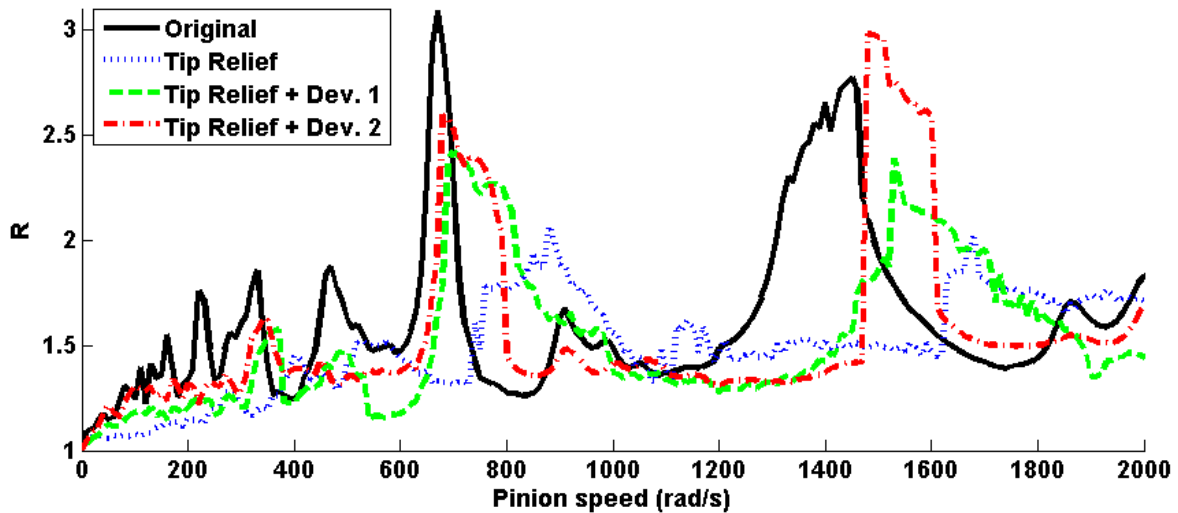
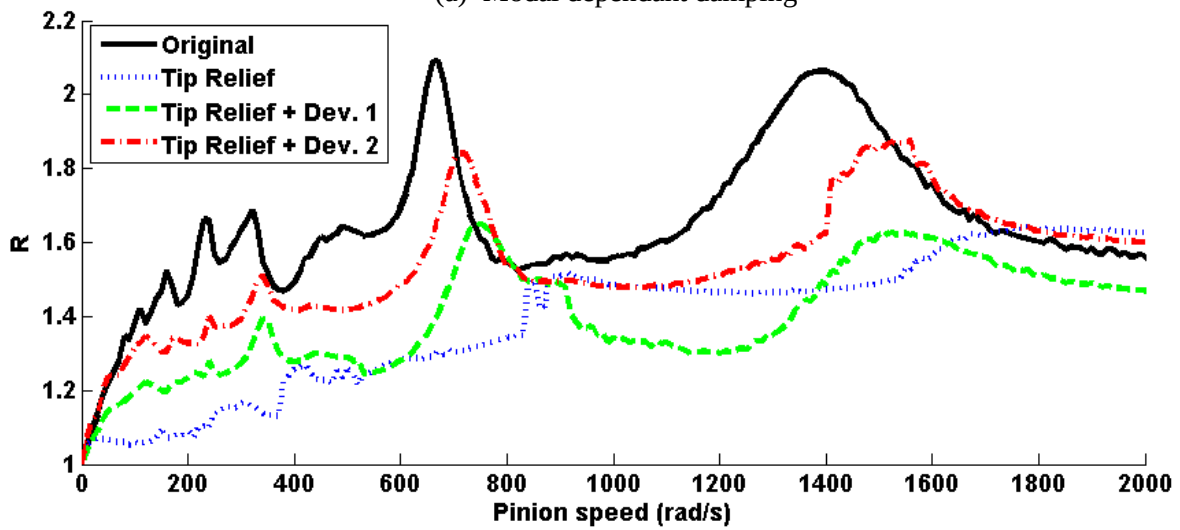


Fig. IV-7: Contact line load for (a) Aeronautic ISO standard and (b) lower quality gear

Similar trends are reported in the dynamic response curves in Fig. IV-8 where it is clearly visible that the improvement on dynamic tooth forces by using tip relief is no longer observed in the presence of profile errors. Here again, two different damping models have been used which both lead to similar conclusions re the influence of profile deviations. As expected, the most severe dynamic response is found for the largest profile error. From a technical viewpoint, it is to be noted that the stabilization of the time response at every speed has been checked over the entire range of speeds



(a) Modal dependant damping



(b) Rayleigh damping

Fig. IV-8: Dynamic ratio comparison for deviated gears

1.2.2. Influence of Modifications

To further investigate the model ability to take various tooth shapes into account, parabolic tip relief are introduced (Fig. IV-9) in place of the classical linear relief previously used. The parameters E and Γ are the same as before, and the profile modification is once again applied with the same definition as before: $E = 15 \mu\text{m}$ and $\Gamma = 0.25$.

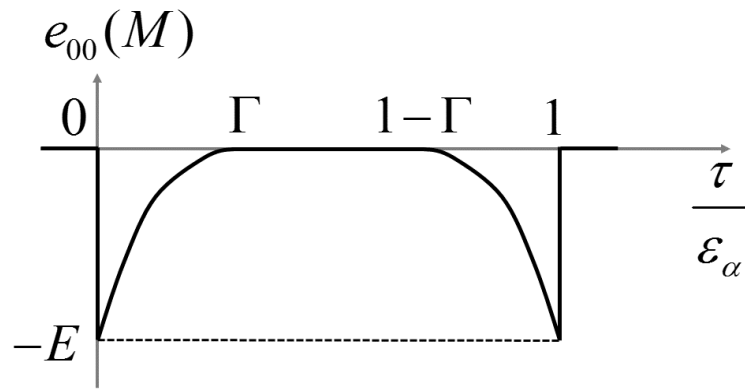


Fig. IV-9: Parabolic profile modification definition

The same deviations are also applied on the modified gear, using ISO 5/6 and 7 quality grades (Fig. IV-10).

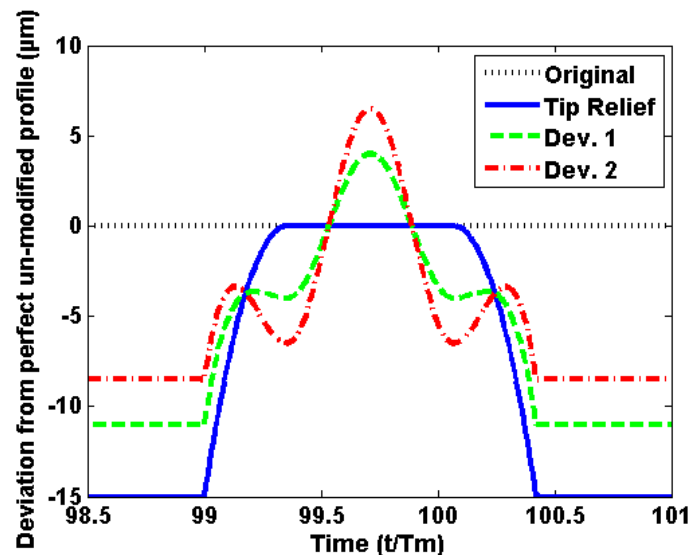


Fig. IV-10: Profile modification and deviation definition

Fig. IV-11 shows that the new tip relief definition has almost no effect on the quasi-static load distribution with profile deviation. Here again, the aeronautic quality gear (a) has a smooth load pattern while the lower quality gear (b) leads to a tooth load distribution closer to that for unmodified tooth profiles.

Fig. IV-12 shows the dynamic ratio of modified gears for both modal dependent (a) and (b) Rayleigh damping models. The response curves are globally close to those calculated with linear tip relief; however, the amplitudes jumps previously observed when profile defects were introduced have almost disappear showing that parabolic modifications can be superior to linear relief re dynamic mesh forces.

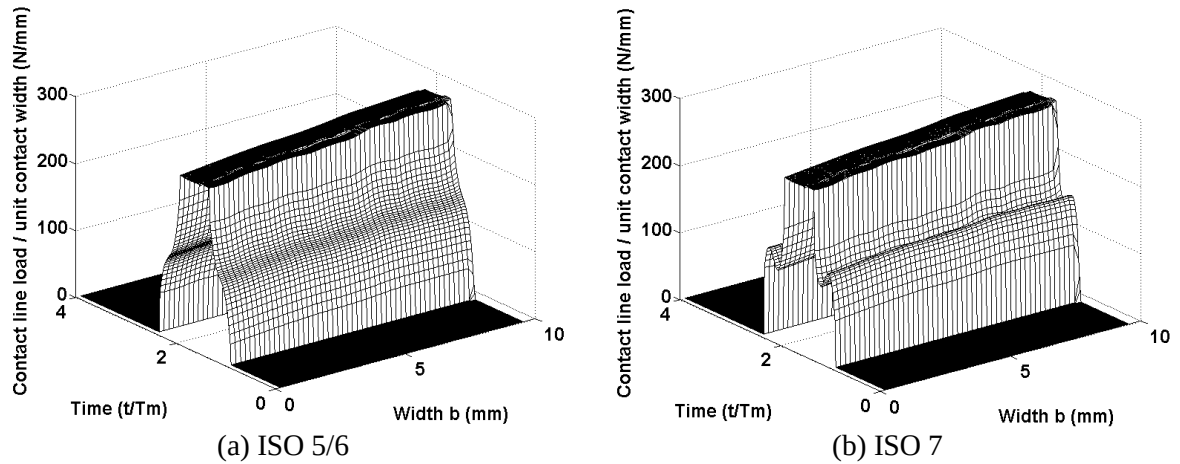


Fig. IV-11: Quasi-static load distribution with parabolic modifications and profile deviations

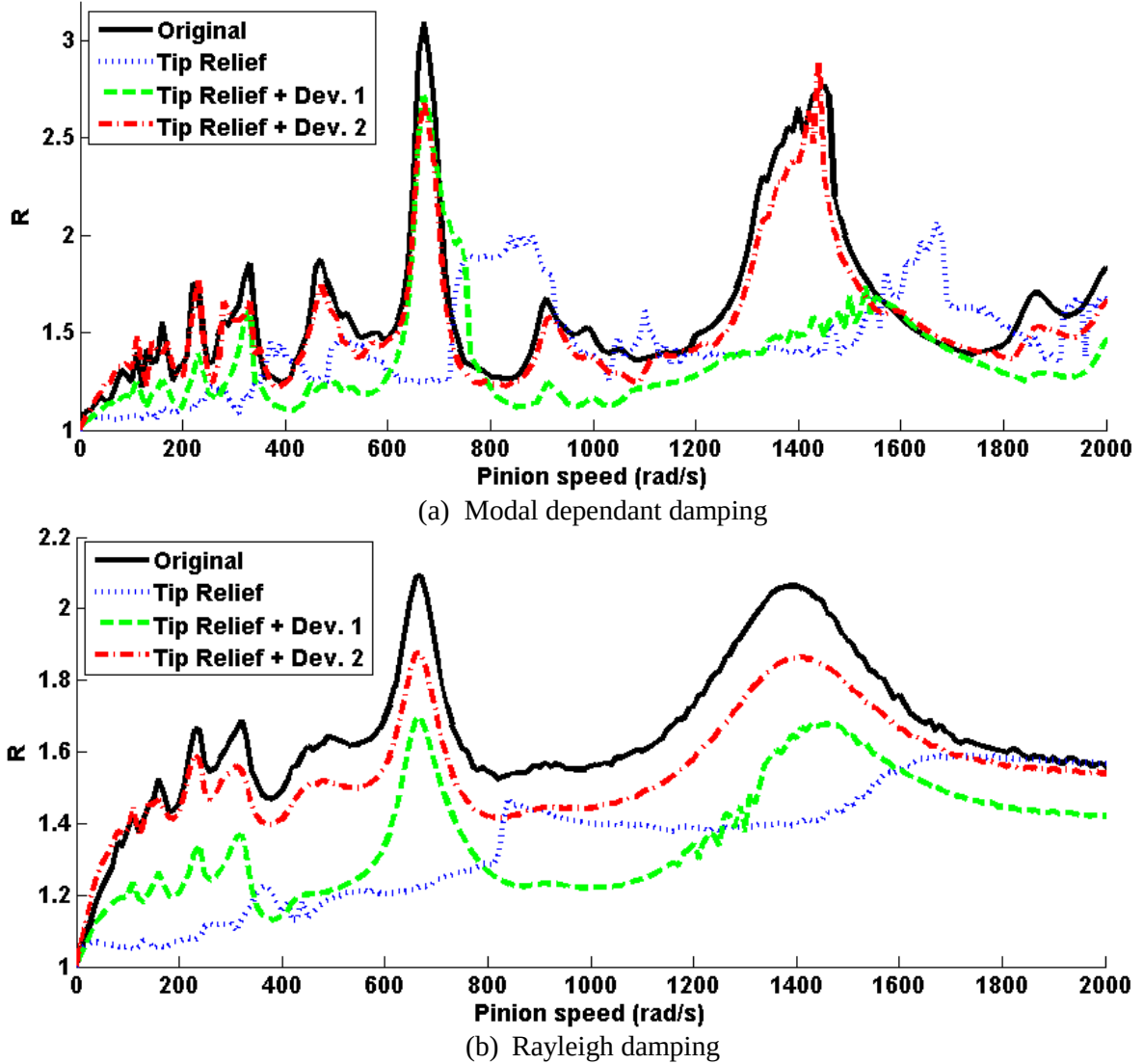


Fig. IV-12: Profile deviation influence on dynamic ratio

1.3. Webbed Pinion

To further investigate the effect of gear body flexibility, a webbed pinion whose geometry is close to that of the wheel, is introduced and simulated using the modular H2 model, i.e. comprising both a sub-structured pinion and wheel. The global geometry is unchanged and the only difference comes from the pinion body (Fig. IV-13) with a straight central web.

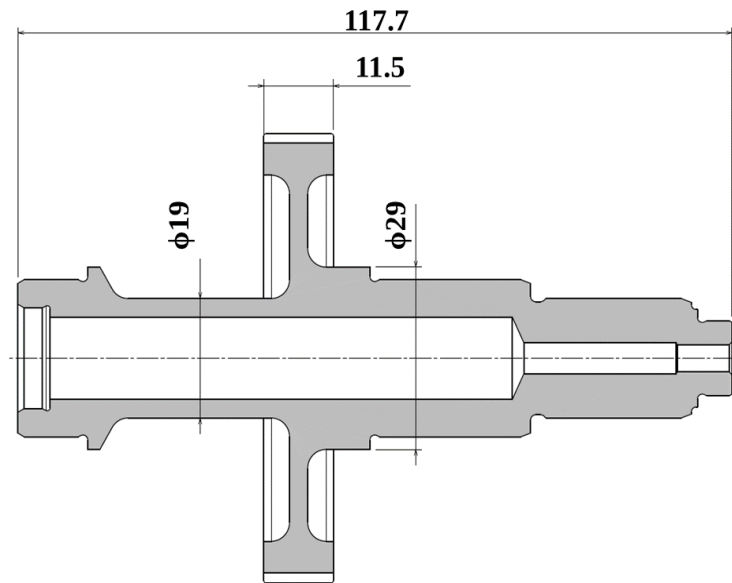


Fig. IV-13: Webbed pinion geometry

The corresponding dynamic mesh force factor versus pinion speed curves are shown in Fig. IV-14 below for the two damping models. The specific influence of the thin web pinion seems to be reduced to a shift in the response peaks towards the lower speeds typical of a reduction in the system global stiffness.

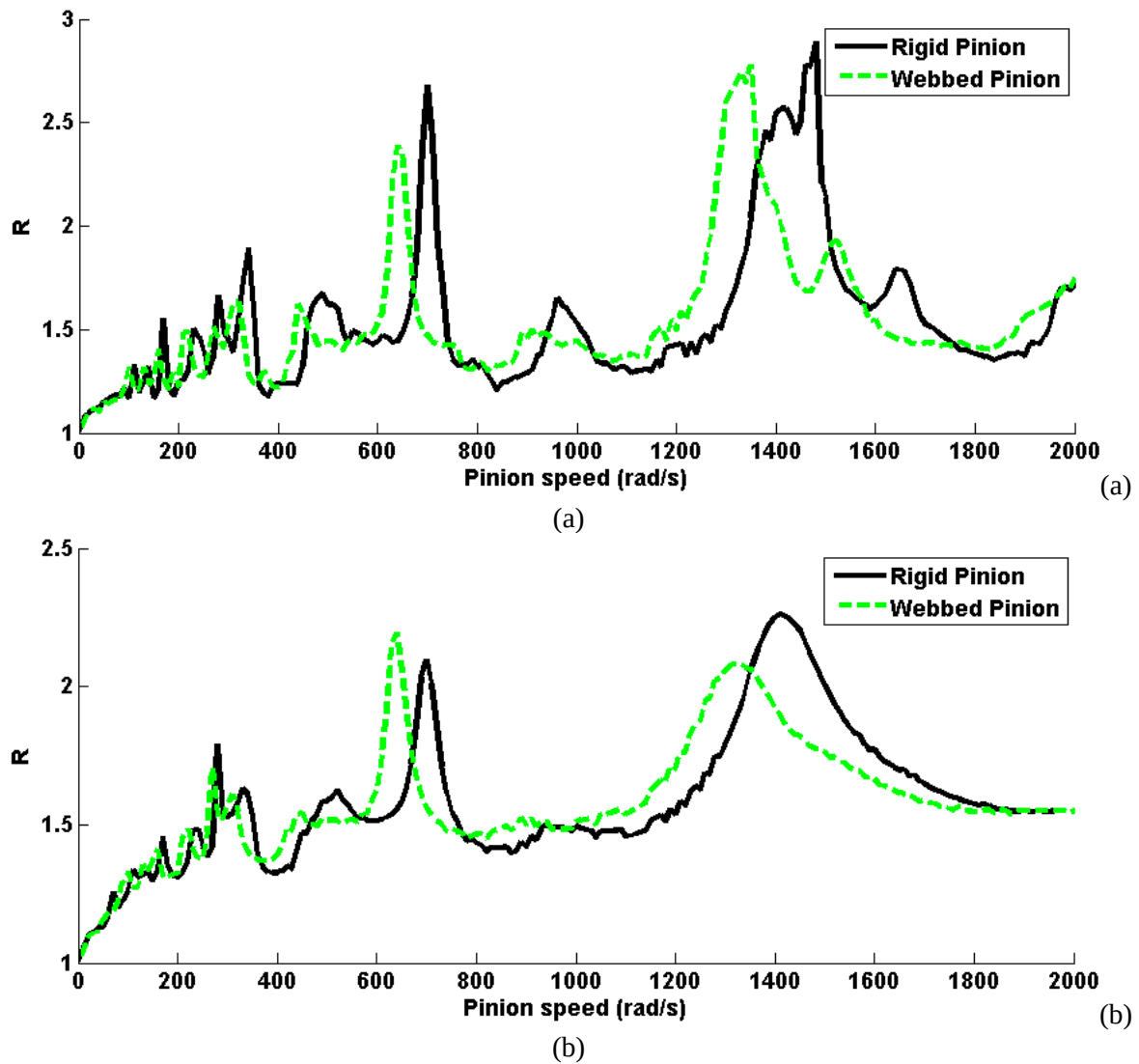


Fig. IV-14: Dynamic ratio calculation for webbed pinion influence with (a) modal dependent damping and (b) Rayleigh damping

This is confirmed by the transmission error (TEs) plots in Fig. IV-15 which shows that the average TEs significantly increases from the initial model to that with flexible gear and pinion bodies. This confirms the fact that body flexibility is highly influential on global gear deflections [RIG99].

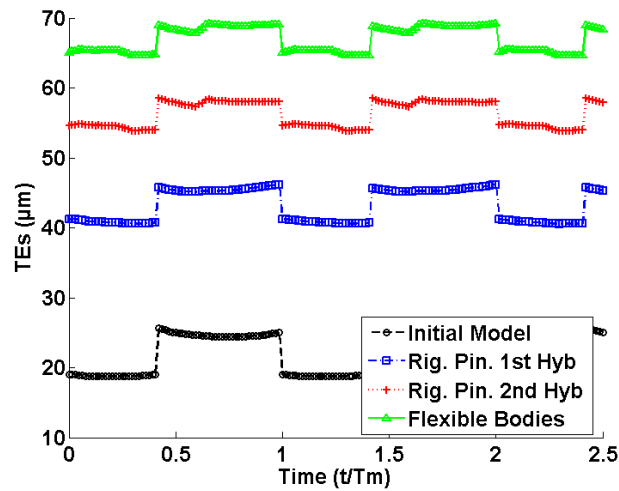


Fig. IV-15: Quasi-static transmission error depending on pinion model and rigidity

Symmetric linear profile modifications have been introduced and systematic sweeps have been run over a range of depths E and lengths of modification Γ . The results are presented under the form of transmission error level curves in Fig. IV-16 along with the Master Curve giving the position of the optimum relief for solid gears (with rigid bodies). Contrary to what was reported for a rigid pinion/flexible spur gear set (whose behaviour was similar to that of rigid gears with respect to TEs variations), the presence of the flexible pinion body (spur gear) moves the optimum relief area as is the case for helical gears. The reason of this unexpected influence is very likely related to the asymmetry of the pinion shaft which leads to uneven tooth load distributions across the face width (not shown).

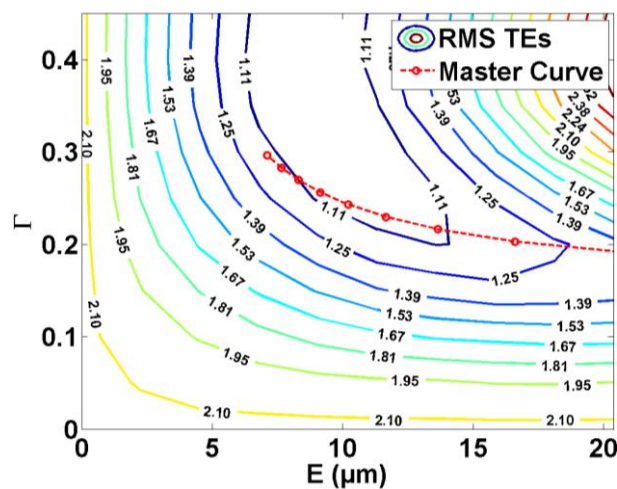


Fig. IV-16: Profile optimisation for model with flexible bodies

2. Dynamic Contributions of Rotating Webs – Power Transmission Gears

The dynamic participation of rotating webs is studied in this part for a total of 6 rotational speeds listed in Tab. IV-1.

	Ω_1	Ω_2	Ω_3	Ω_4	Ω_5	Ω_6
Pinion Speed Ω_p (rad/s)	410	840	1100	1780	2490	3000
Resonance (R.)	R.	R.	/	R.	R.	/

Tab. IV-1: Display of the several speeds for rotational wheel analysis

2.1. Transmission Modal Behaviour – Effect of Modes

The simulations on the academic power transmission defined in Chapter III have been validated and this particular gear set is used again for the rest of this chapter. This transmission has the particularity of having a helical gear over a slightly inclined web with a large rim ($b \approx 40 \text{ mm}$).

The study of the industrial test case in Chapter III showed that wheel modes, comprising nodal circles and diameters, are excited by the meshing and that the model was able to capture them. Using the H1 hydric model (rigid pinion body and beam elements for the pinion shaft), the critical speeds Ω_1 , Ω_2 listed in Tab. IV-2 have been identified (Ω_3 is a non-resonant speed).

Studied Cases	Ω_1	Ω_2	Ω_3
Pinion Speed	410 rad/s	840 rad/s	1100 rad/s
Modes	2 250 Hz	5 020 Hz	/
Nature of mode	+/- 2D Wheel	Pinion	/

Tab. IV-2: Conditions at various speeds

Fig. IV-17 shows the dynamic ratio Fast Fourier Transform for the three speeds of interest Ω_1 , Ω_2 and Ω_3 with the frequency axis normalised with respect to the mesh frequency. The two first speeds (Ω_1, Ω_2) exhibit the highest response at the meshing frequency and its second harmonic while the non-resonant speed amplitude is far lower.

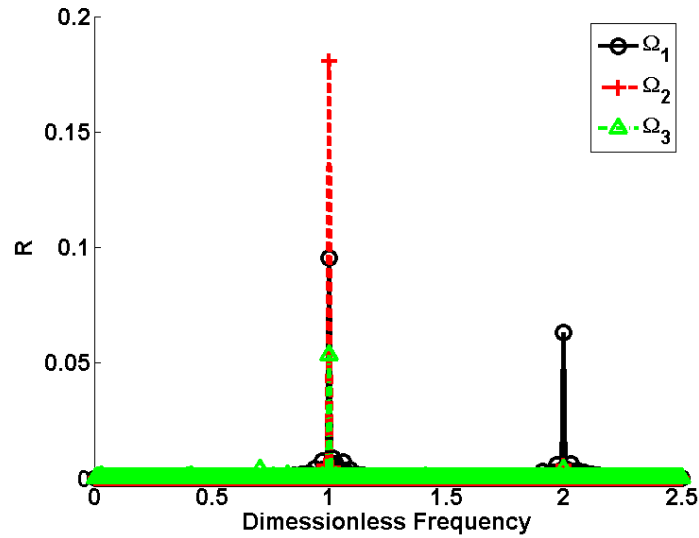


Fig. IV-17: Dynamic ratio for the three dynamic conditions

The web response is now studied for each of the characteristic speeds. The same procedure as for the industrial transmission validation is followed. A Web Node (WN) is condensed along with the other nodes (rim and bearing nodes) of the wheel sub-structure. Its displacement can therefore be extracted from the simulation and plotted in terms of radial displacements.

For confidentiality reason and avoiding full-scale comparisons with the previous non-dimensional values, this Web Node (WN) is not axially positioned at the same position as before but on the opposite part of the rim, at a web extremity (Fig. IV-18). Here again, the radial displacement of this point is measured and several nodes are distributed along the circumference for comparison purposes.

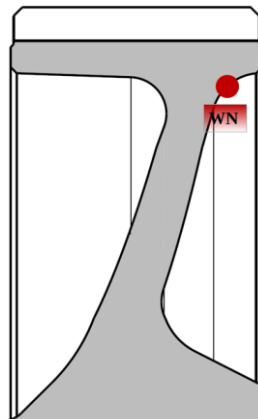


Fig. IV-18: Web node definition for web displacement

The Fast Fourier Transform of the wheel node response has been performed for the three speeds. The first graph for speed Ω_1 in Fig. IV-19 is dominated by two main peaks at the backward and forward two-diameter frequencies ($Z_2 \pm 2 = 66/70$) of different amplitudes.

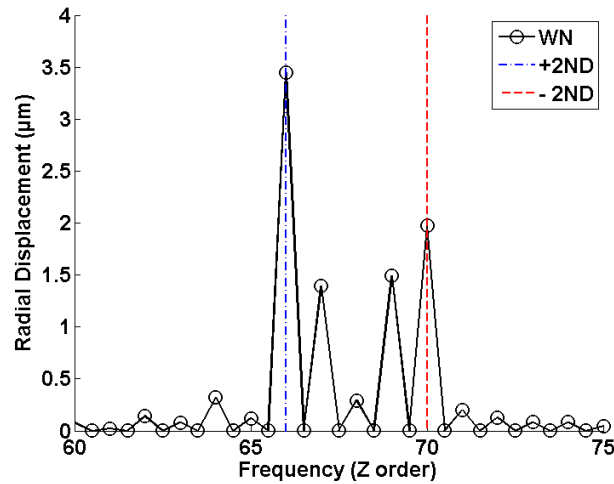


Fig. IV-19: Web node response for Ω_1 , wheel mode

The same study have been conducted for the two other speeds Ω_2 and Ω_3 (Fig. IV-20) and, for both cases, the response amplitudes are far lower. Case (a) corresponds to a pinion mode for which two small peaks are visible at orders 67 and 69, characteristic of the shaft response frequencies ($\omega_0 = Z_2 \pm 1$) when excited by the meshing. The last speed shows nearly nothing in its dynamic response spectrum.

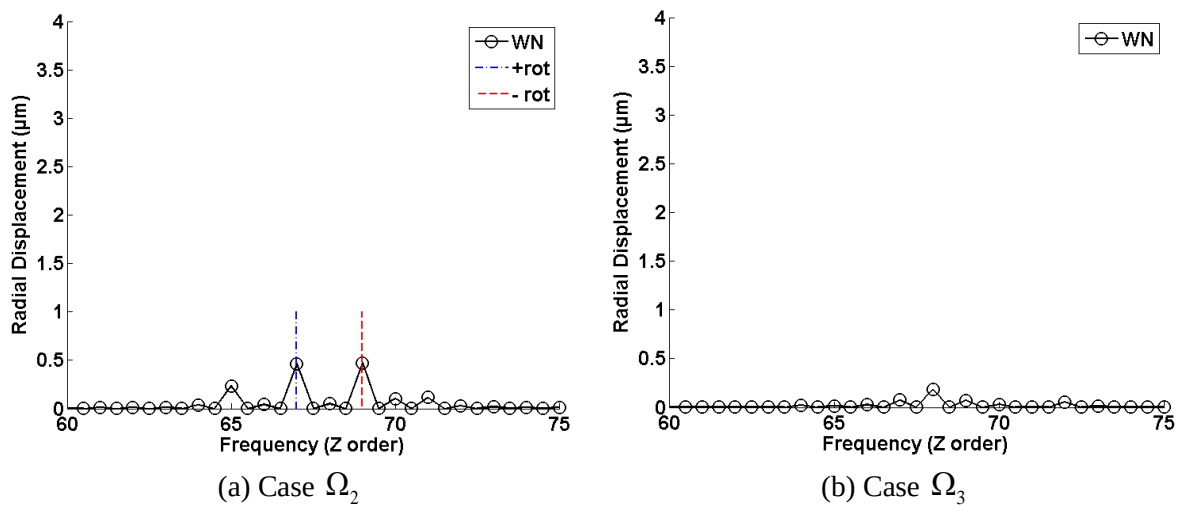


Fig. IV-20: Web node response for Ω_2 pinion mode and standard response Ω_3

The only natural frequency presenting a web mode is Ω_1 and its dynamic response can be analysed by considering three rim nodes evenly distributed along a web circumference.

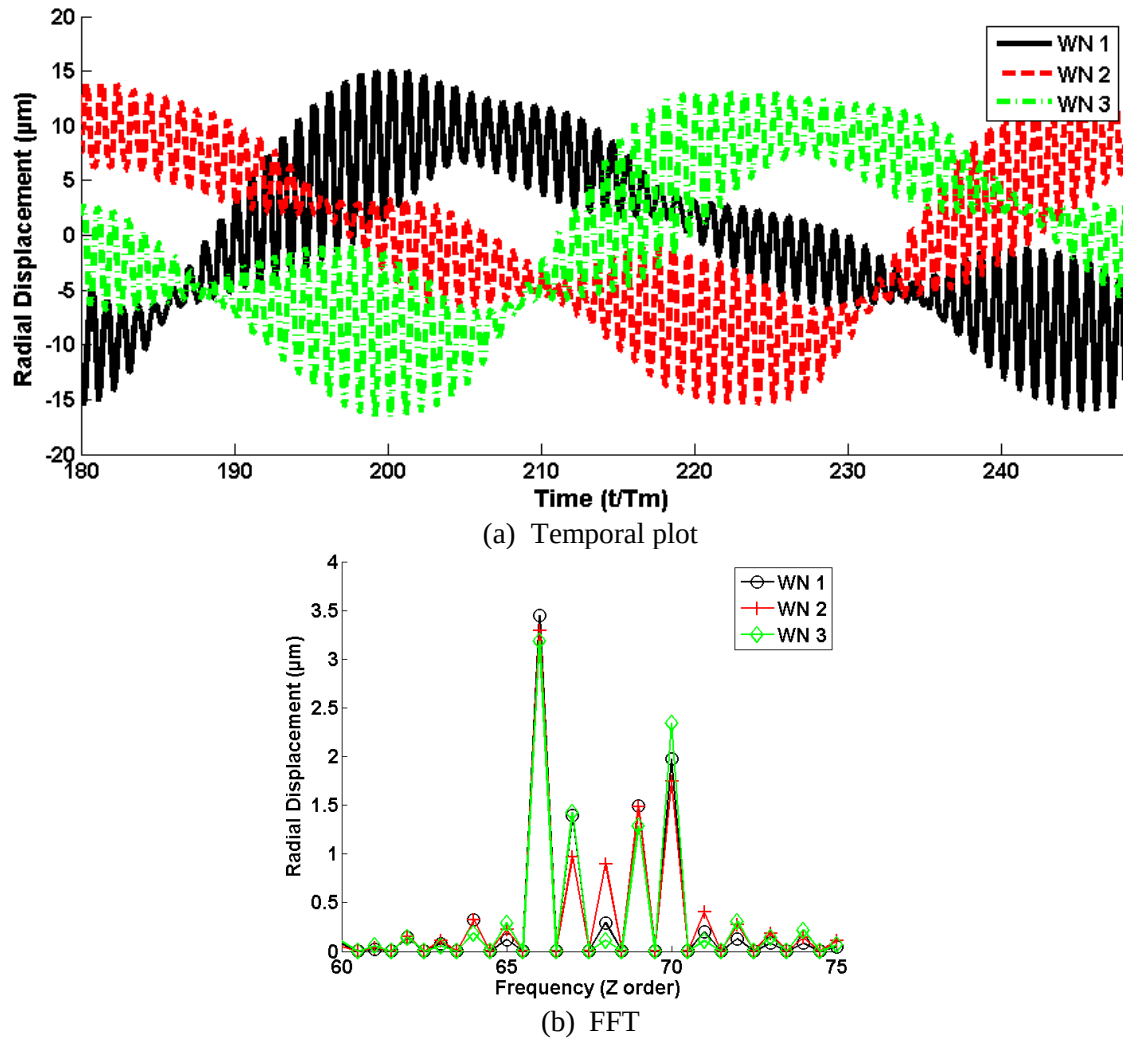


Fig. IV-21: Several Wheel Node radial response for Ω_1

Their radial displacement presents several frequency components as illustrated in Fig. IV-21 which shows the dynamic radial displacements at the three nodes. It can be noted that, as expected, the response curves are out of phase. The middle frequency seems also to be out of phase since the mode minimum displacement line does not appear at the same time for each of the nodes. In order to eliminate all the low frequency contributions arising from the rotation of the parts and focus on the modal response of the wheel, a band-stop frequency filter described in Fig. IV-22 is introduced.

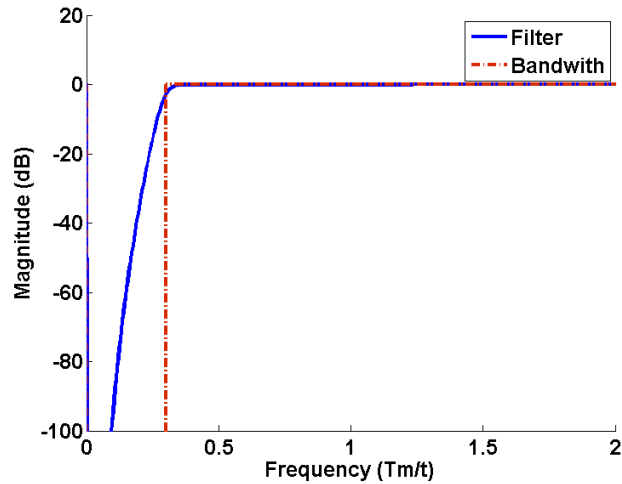


Fig. IV-22: StopBand filter to eliminate wheel rotation frequency in WN signal

Fig. IV-23 shows the time signal obtained when applying the filter on the three Wheel Nodes. This manipulation makes it possible to superimpose all the signals and check their phasing along a wheel circumference under resonance conditions. This plot clearly shows that the 3 points behave differently.

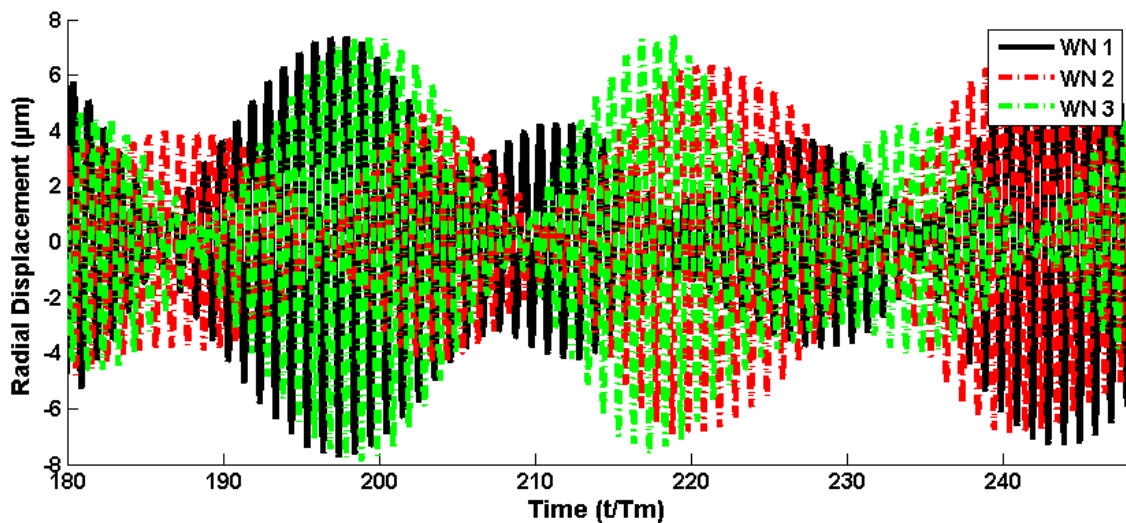


Fig. IV-23: Web response phasing after post-processing

2.2. Wheel Mode Study

	Ω_1	Ω_4	Ω_5
Pinion Speed (rad/s)	410	1780	2490
Resonance (R.)	R.	R.	R.

Tab. IV-3: Speeds for the wheel frequency modes

The study is extended to the response in the vicinity of the three speeds indicated in Tab. IV-3 which corresponds to some of the speeds with amplification of the web radial displacements. The corresponding spectra are given in Fig. IV-24 for the last two speeds. For both speeds, the displacement amplitudes are low but characteristic of web diameter modes.

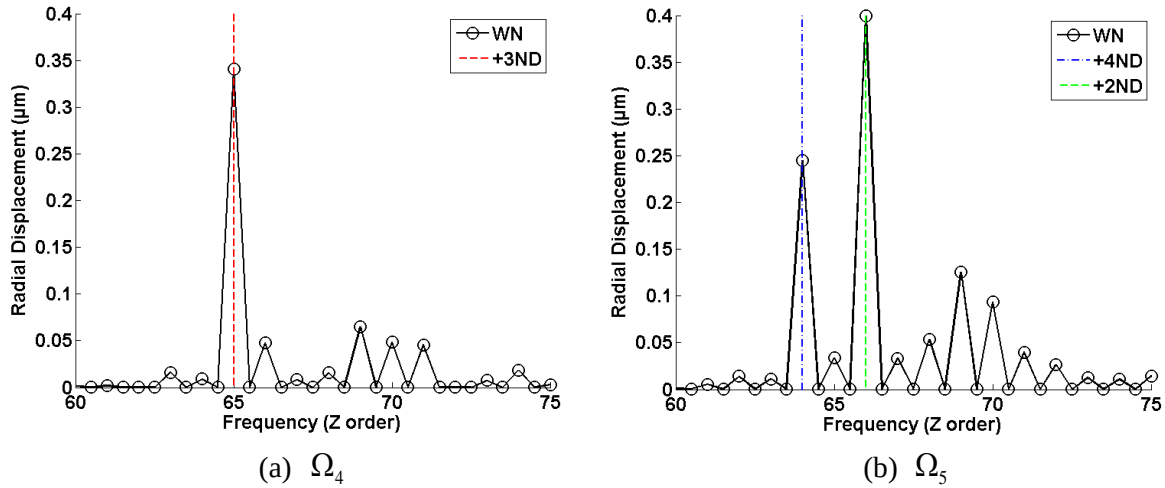


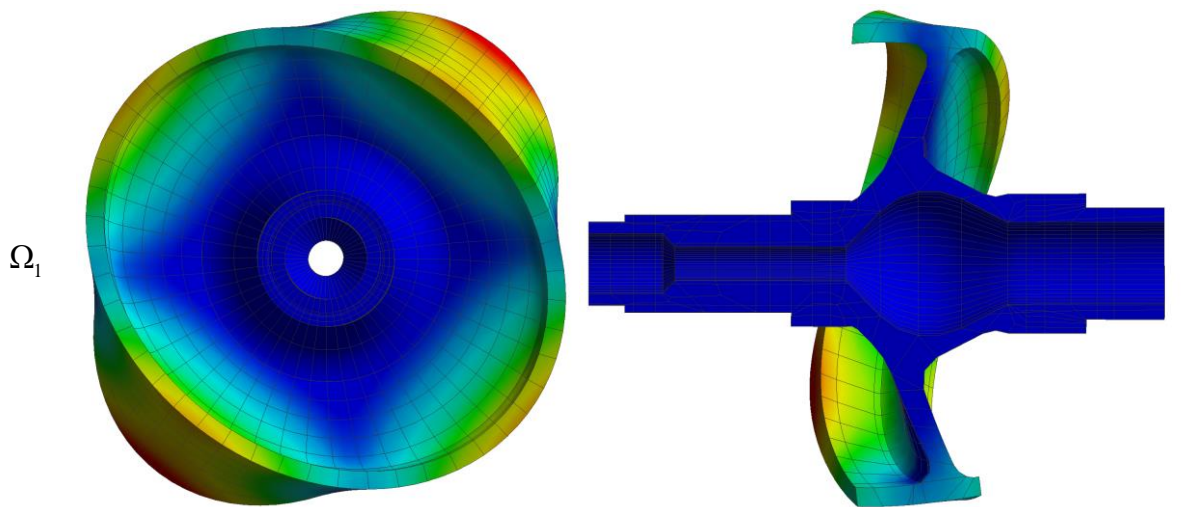
Fig. IV-24: Frequency analysis of the web displacement

In (a), a single +3ND mode is identified while (b) exhibits the possible participation of two different modal responses (+2ND and +4ND) triggered at the same speed. It is easy to calculate the frequency at zero speed with the critical speed and mode nodal diameter number from the Campbell diagram theory detailed in Chapter III which led to:

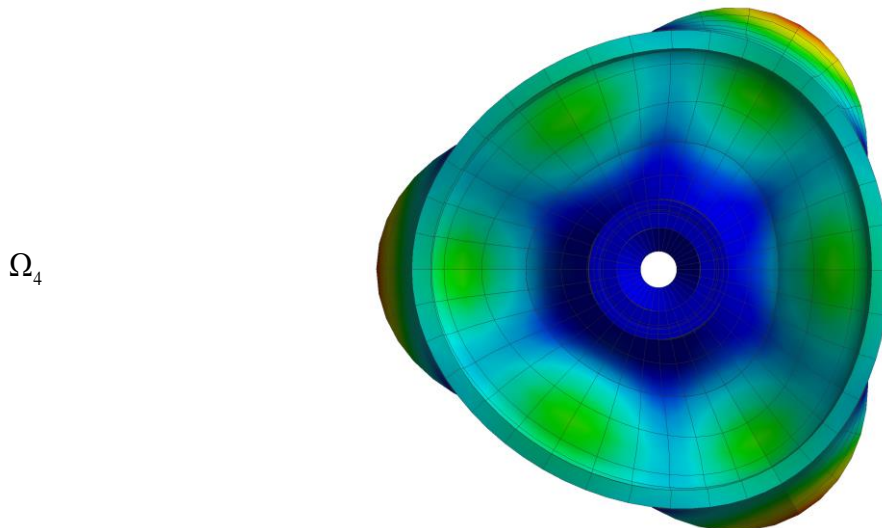
$$\omega_0 = (Z \pm n)\Omega \quad (4.1)$$

with ω_0 , frequency at zero speed, Ω , rotational speed, Z , number of wheel teeth and n , nodal diameter number.

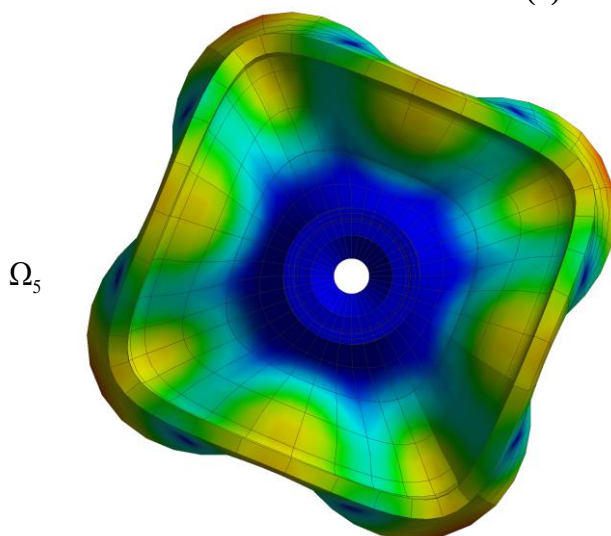
From the zero speed frequency ω_0 obtained from each mode shape, the nearest corresponding mode of the FE modal analysis is retained and drawn in Fig. IV-25. These figures show the 2ND modes for Ω_1 , 3ND for speed Ω_4 and two modes for Ω_5 which are respectively the 4ND of the family with one nodal circle and the 2ND belonging to the family with two nodal circles.



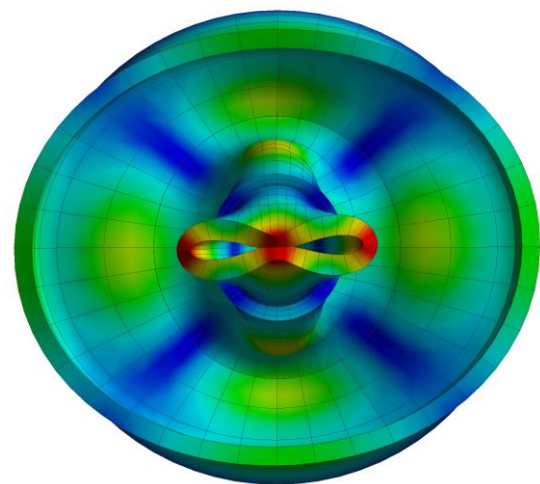
(a) +/- 2ND: 2 250 Hz



(b) + 3 ND: 9 595 Hz



(c) + 4 ND: 12 954 Hz



(d) +2 ND: 13 456 Hz

Fig. IV-25: Mode shape of full FE model modal analysis

The corresponding Campbell diagrams with the three rotational speeds under consideration are shown in Fig. IV-26 where the meshing excitation lines have been superimposed. The vertical dashed lines correspond to the identified critical speeds and it can be verified that the diagrams in the rotary and fixed frames are consistent since they point to the same critical speeds.

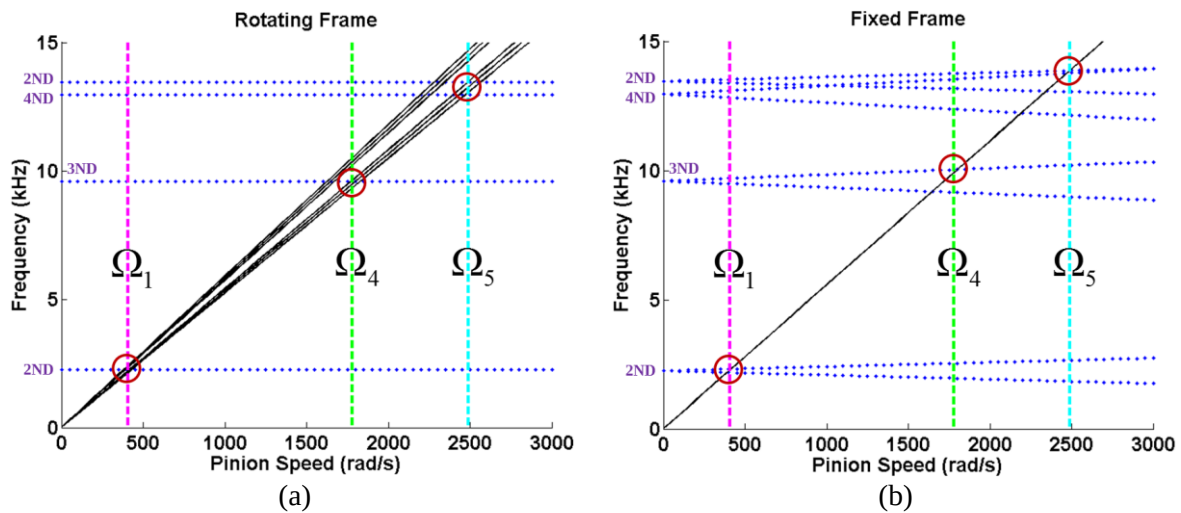


Fig. IV-26: Campbell diagram for modes present at the studied speeds (Ω_1 , Ω_4 and Ω_5)

The literature on the analysis of the deformed shape of rotating structures in operating conditions is sparse. One can cite the paper by Almeida *et al.* [ALM12-14] who studied experimentally the dynamic deformed shape of a rotating centrifugal compressor based on strain gauge measurements on the compressor.

Numerically, the displacement of the web nodes can provide a first insight into the wheel behaviour. In order to be more accurate, the FFT of the time signals performed for one Wheel Node (Fig. IV-19 and Fig. IV-24) has been extended to 48 nodes to improve precision. The frequency previously identified as the diameter mode response is isolated and the inverse FFT is determined for each frequency of interest. The resulting time signals can then be drawn in terms of the position of the wheel nodes at different time-steps, giving the full deformed shape of the wheel rim in terms of radial displacements and their time variations.

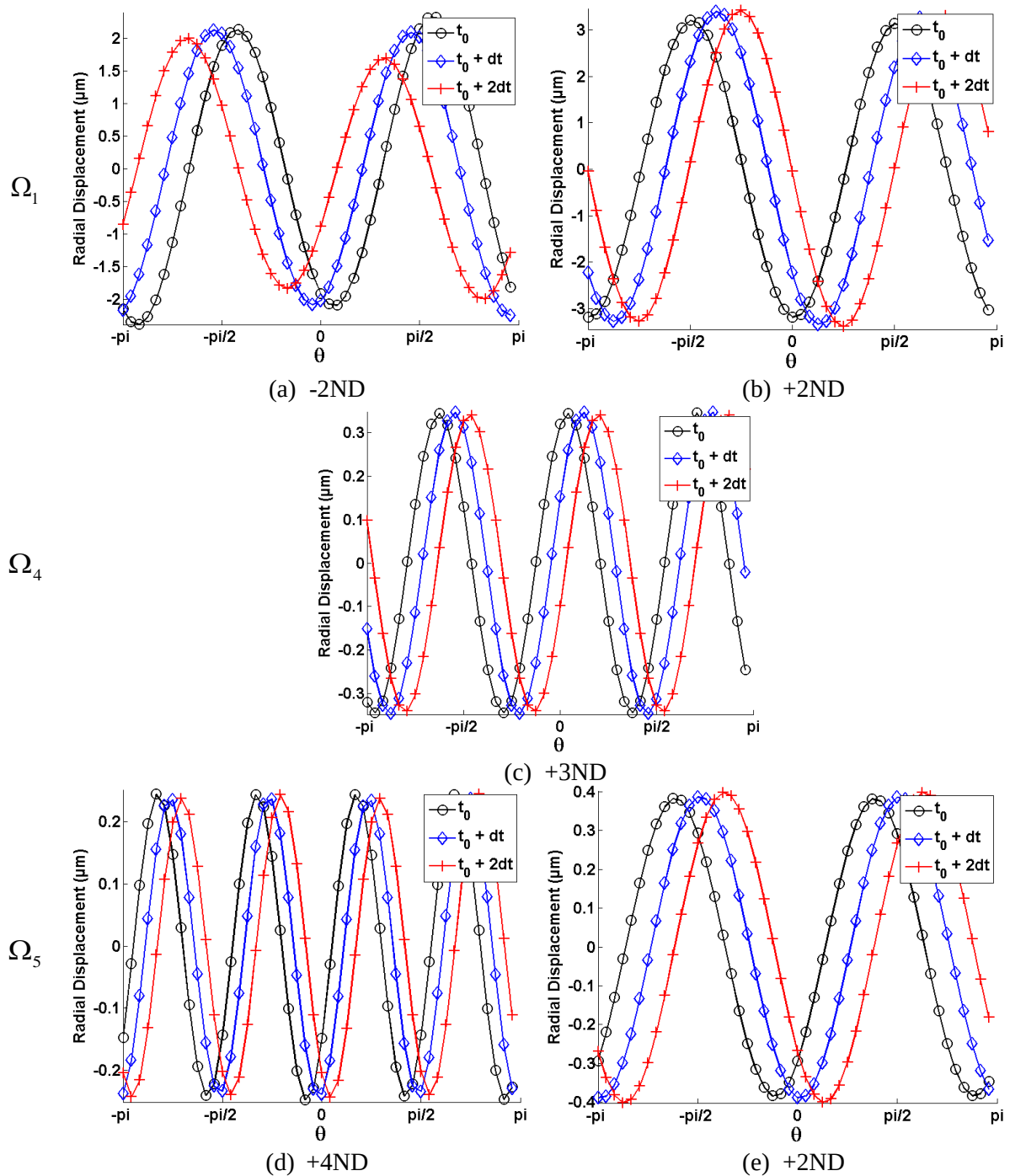


Fig. IV-27: Mode shape for spotted web modes with $dt = \frac{1}{16}T_m$

Fig. IV-27 shows the resulting plots for the three wheel resonance speeds, on their principal identified response frequencies. The direction from $-\pi \rightarrow \pi$ corresponds to the positive wheel rotation.

The number of spatial periods of each mode corresponds well with the identified mode for each graph. It is visible that all the modes are not attached to wheel points but are moving with respect to the wheel body since the modal nodes vary with time. The plots were displayed

over a very short amount of time $dt = 1/16 Tm$ and the numerical simulations were performed with 64 time-steps for one mesh period in order to ensure good space and time representations.

The direct modes identified as positive in the Campbell diagram present a shift in the wheel rotation direction whereas the only identified backward mode seems to move in the other direction. This confirms that the modes actually correspond to propagating waves whose properties have been summarized in Tab. IV-4 in terms of rotational speed and corresponding propagation speed in the material. The theoretical propagation speed of a mechanical wave is estimated from [MAR07], by considering the rim circumference as a bar submitted to bending waves as:

$$c_f = \sqrt[4]{\frac{Ea_x^2}{\rho}} \sqrt{\omega_i} \quad (4.2)$$

With: $a_x = \frac{h^2}{\sqrt{12}}$, h bar height and $\omega = 2\pi f$ with f frequency

	Ω_1		Ω_4	Ω_5	
Pinion speed	410 rad/s		1780 rad/s	2490 rad/s	
Wheel speed	211 rad/s		916 rad/s	1 282 rad/s	
Modes	-2ND	+2ND	+3ND	+4ND	+2ND
Frequency	2 250 Hz		9 595 Hz	12 954 Hz	13 456 Hz
Wave speed	- 8528 rad/s	8200 rad/s	23 738 rad/s	24 820 rad/s	49 800 rad/s
	- 596 m/s	574 m/s	1 662 m/s	1 787 m/s	3 486 m/s
Theoretical speed	+/- 505 m/s		1 044 m/s	1 213 m/s	1 236 m/s

Tab. IV-4: Wave speed

The wave velocities as determined by (4.2) and derived from Fig. IV-27 are of the same orders of magnitude though the actual wave speeds are higher and seem to depend on the mode frequency and rotational speed in a complex way. Examining the propagating speed and the wheel rotational speed, it can also be remarked that all the mode shapes are moving with respect to the two characteristic coordinate systems which are: a) the fixed frame which the mesh excitations are attached to, and b) the rotary frame linked to the rotating wheel. The 2 ND mode appears as a singularity as its wave speed is much larger than the estimated theoretical speed probably because of the complexity of its mode (Fig. IV-27.d) which cannot be represented by a simple bar submitted to bending waves.

2.3. Design Effect – Hollow Web and High Rotational Speed

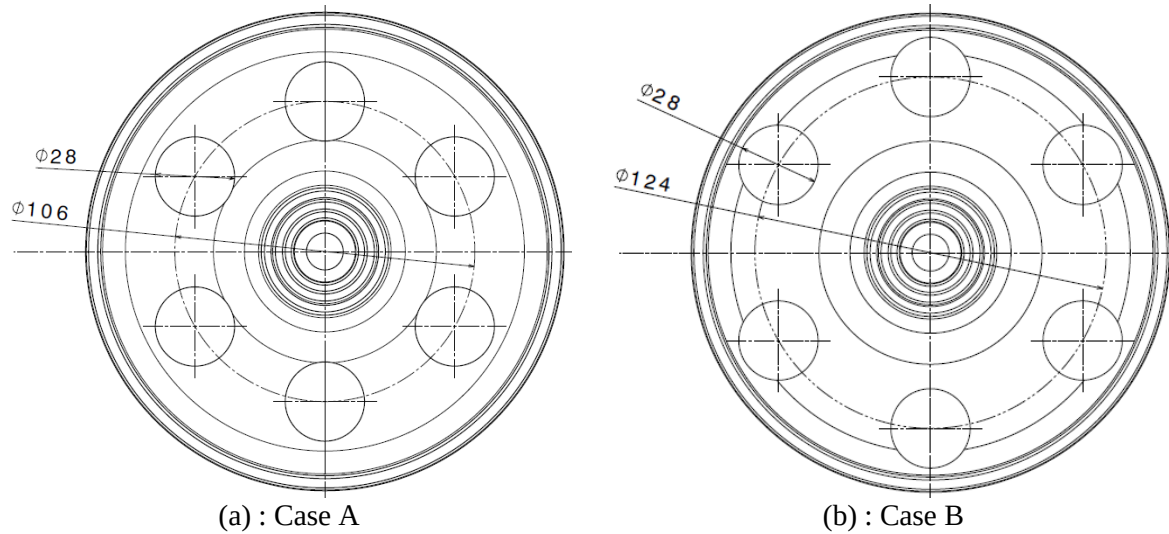


Fig. IV-28: Hollow web geometry with regard to wheel rim

Hollow webs are frequently used in power transmissions and this section is devoted to the analysis of their contributions in static and dynamic conditions. The studied cases (A and B) are presented in Fig. IV-28, both comprise 6 identical holes distributed along a web circumference whose centres are located on different radii. Test case C in Fig. IV-29 exhibits the same principal hollow web arrangement as case B (close to the rim) but an additional number of smaller holes are added which are placed on a smaller circle with staggered angular positions with respect to the larger hole distribution.

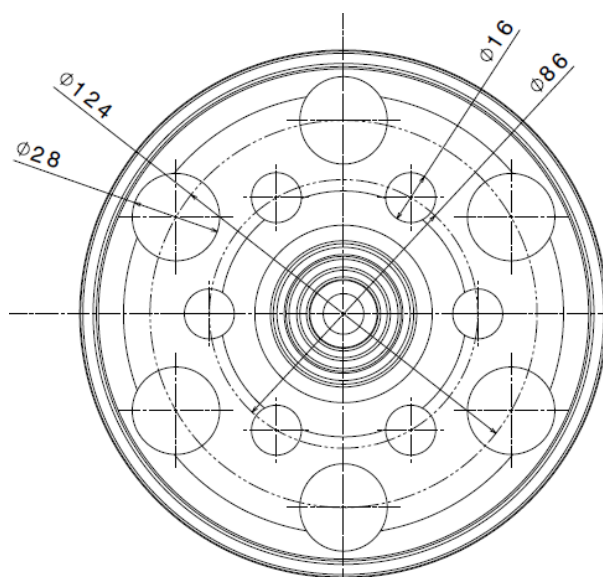


Fig. IV-29: Test Case C: Test Case B + secondary holes

Tab. IV-5 shows the mass effect of the hollow parts. Compared with the Original Case O (the axisymmetric gear used in the previous part), significant gains in mass are reported in Tab. IV-5 (cases A and B are very similar).

	Original Case O	Test Case A	Test Case B	Test Case C
Total Mass Variation (web + shaft %)	-	- 6.5	- 6	- 8.5

Tab. IV-5: Mass variation depending on hollow web disposition

Speed Ω_1 is retained for the modal analysis as it is the principal speed with wheel web response. The resonance speeds for all the cases are listed in Tab. IV-6, it can be noticed that the stiffness reduction and the mass reduction brought by the presence of holes are not in proportion thus leading to a frequency shift. On the other hand, it has been found that the introduction of holes does not modify the nodal circle and diameter distributions although the frequencies and consequently the critical speeds are altered.

Test Case	O	A	B	C
Critical speed Maximum Ω_1 (rad/s)	410	380	380	370

Tab. IV-6: modification for the test cases at Ω_1

Dynamic mesh force factors have been calculated at the critical speed for each case and the corresponding FFTs for all four cases are displayed in Fig. IV-30. It can be seen that cases A and B present quite similar response patterns but with different amplitudes while cases B and C have richer modulation sidebands and smaller amplitudes at the critical frequency.

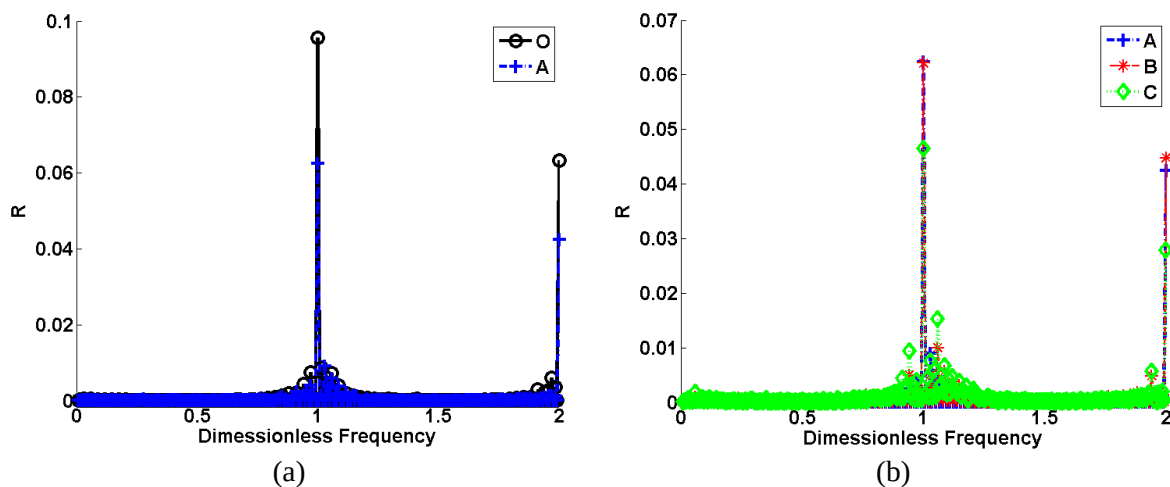


Fig. IV-30: FFT analysis of Ω_1 for the different web geometries

At this wheel critical speed, the same kind of response for all test cases is observed (same as the Original Case O) and the associated mode shapes have the same +2 ND characteristics which appear therefore as not sensitive to hollow webs.

The global frequency contents of the dynamic mesh forces for the non-resonant case Ω_3 are shown in Fig. IV-31. While the axisymmetric case (O: Fig. IV-31.a) generates a single peak at each meshing harmonic, the second test case (B) with holes exhibits a more complex spectrum. Several response peaks can be noticed at very low frequency along with modulation sidebands around the mesh frequency harmonics. The lower frequency peak is at 0.088, which corresponds to the hole passing frequency (eq. 4.3).

$$f = \frac{n_{holes}}{Z_2} = \frac{6}{68} = 0.088 \quad (4.3)$$

With: n_{holes} number of holes and Z_2 tooth number.

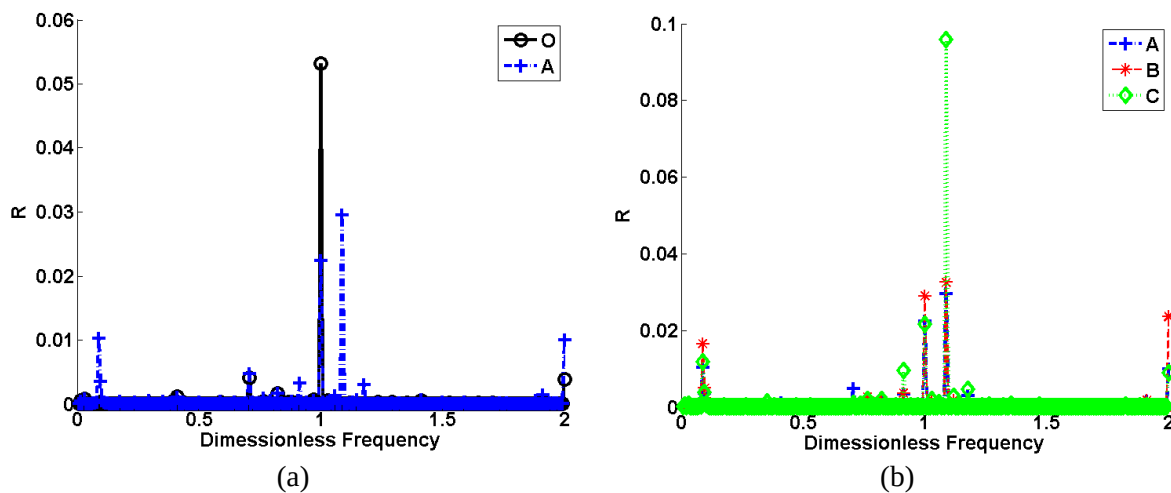


Fig. IV-31: Dynamic ratio response depending on test case for Ω_3

When comparing the response of the different test cases (Fig. IV-31.b), it can be seen that they all present the same additional peaks. Comparing case A and B; it is observed that the additional peaks are globally larger on B where the holes are closer to the rim. Test case C however seems to have a rather different dynamic response. The peaks associated with the holes are of similar amplitudes to those in case A whereas the smaller holes smooth the hole passing contribution.

2.4. Tooth Design Constraints Regarding Flexible Wheels

From a design perspective, the conclusion of the previous section is that case B is very likely the most appropriate choice as it reduces the wheel mass substantially while keeping satisfactory dynamic properties. Tab. IV-7 shows the three different speeds (non-resonant cases) which have been considered for this case. The first speed is so low that it prevents from any dynamical effects, the second one would correspond to standard operating conditions and finally, the third one is typical of high-speed applications.

Studied Cases	Ω_s	Ω_3	Ω_6
Pinion Speed	0.01 rad/s	1100 rad/s	3000 rad/s
Resonance (R.)	/	/	/

Tab. IV-7: Case study for hollow web effect

Fig. IV-32 displays the contact pressure patterns for Case B obtained at the three speeds in Tab. IV-7 for two different conditions: a) a tooth between two holes and, b) a tooth just above a hole. For Ω_s and Ω_3 , the contact pressures on teeth above a hole are slightly better distributed compared with what is found for teeth between two holes. For high speeds (Ω_6 in this example), the influence of centrifugal effects becomes prominent and the pressure distributions are asymmetric across the face width with marked peaks on one edge. Here too, the additional flexibility brought by the holes seem to be positive as it spreads more the high pressure zone thus reducing the maximum amplitudes.

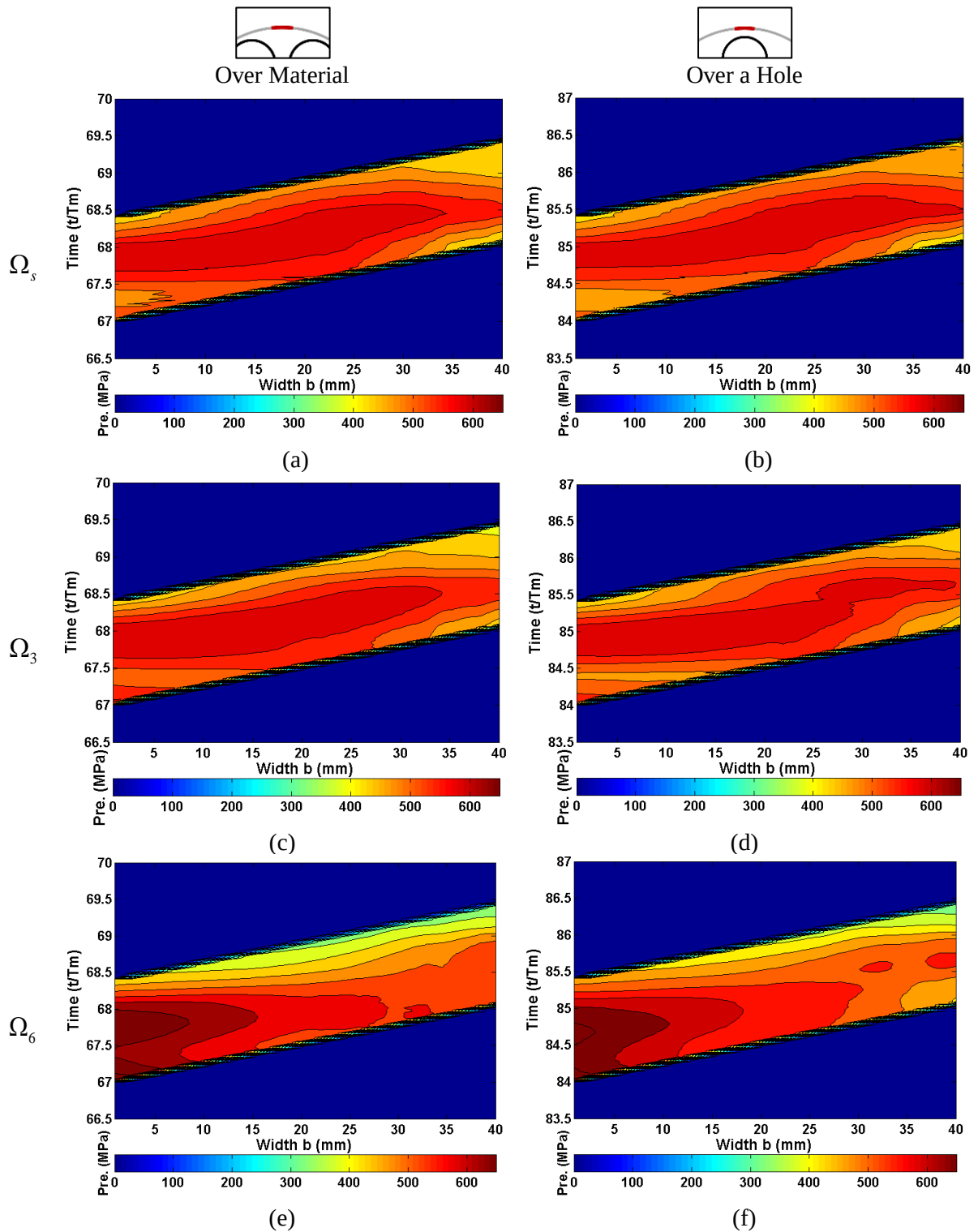


Fig. IV-32: Meshing pressure depending on speed for tooth spot over hollow web for case study B

In this context of uneven load distributions, it can be interesting to test the influence of tooth shape modifications. Linear lead modifications are introduced to prevent the early wear possibly induced by the centrifugal effects at high speeds (Fig. IV-33). It is defined solely on the left edge which corresponds to the overloaded area on the face width. The geometrical parameters are:

- a) Γ , the non-dimensional axial extent of modification defined as a fraction of the face width b which is set to 0.4 in what follows,
- b) the depth E chosen in the range 5 to 10 μm .

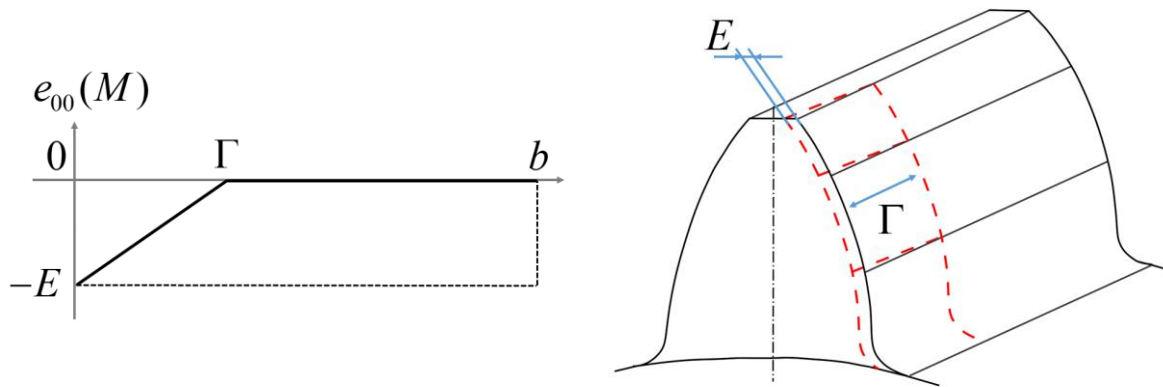


Fig. IV-33: Linear modification along lead

The Fig. IV-34 shows the corresponding results for $E = 10 \mu\text{m}$ which prove that the proposed lead modification is effective since centred pressure distributions are obtained even in the presence of centrifugal effects. It can also be noticed that the slight deviations observed depending on the position of the tooth with respect to that of holes are not visible any longer.

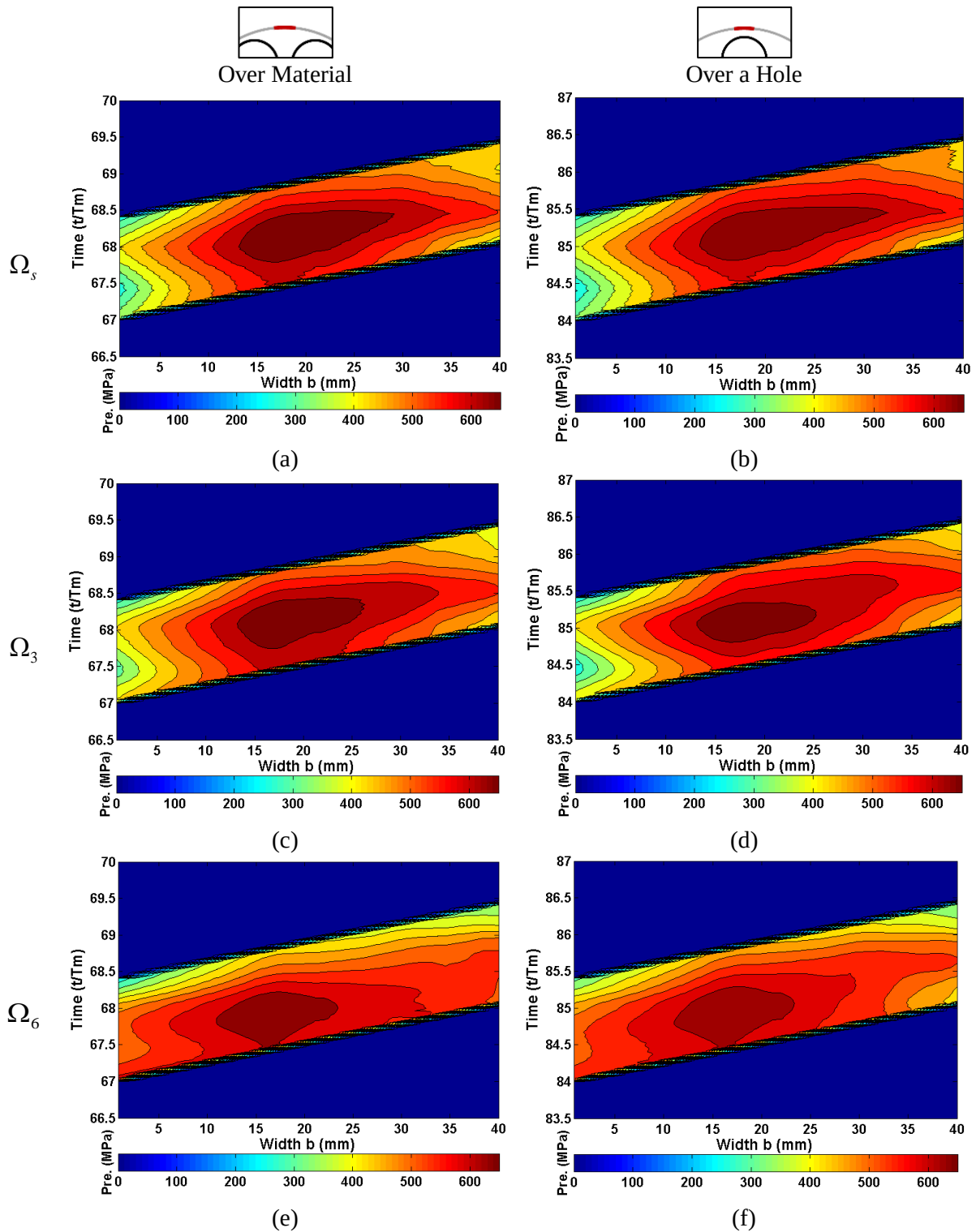


Fig. IV-34: Effect of a 10 μm linear lead modification on pressure

Higher modification depths lead to more localised pressure patterns which are still centred on the face width but whose maximum amplitudes increase. An amplitude of 10 μm appears therefore as an optimum value for the example treated beyond which it is not desirable to go as contact stresses would become too high and parts of the flanks would be unloaded.

3. Flexibility for Fully Webbed Power Transmission Case

3.1. Webbed Pinion Integration

3.1.1. Pinion Web – Influence on Meshing

In order to further reduce mass, thin-web pinions such as that shown in Fig. IV-35 can be introduced. The pinion shaft is hollow with a larger bore under the pinion and a web thickness less than half of the rim width in order to soften the contact conditions and improve tooth load distributions.

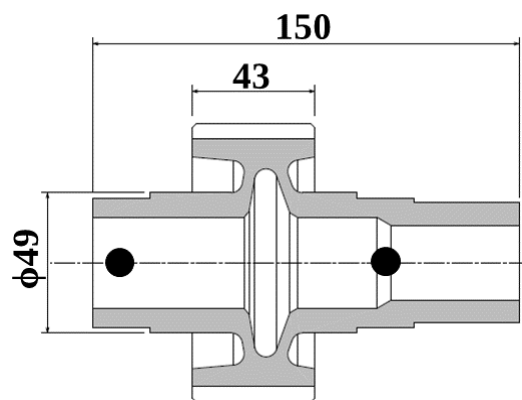


Fig. IV-35: Webbed pinion geometry

The quasi-static pressure distributions are plotted in Fig. IV-36 for both the rigid and flexible pinions. The results show that the webbed pinion tends to move the most loaded contact area to the right side of the face width and therefore have a non-negligible impact on the meshing conditions.

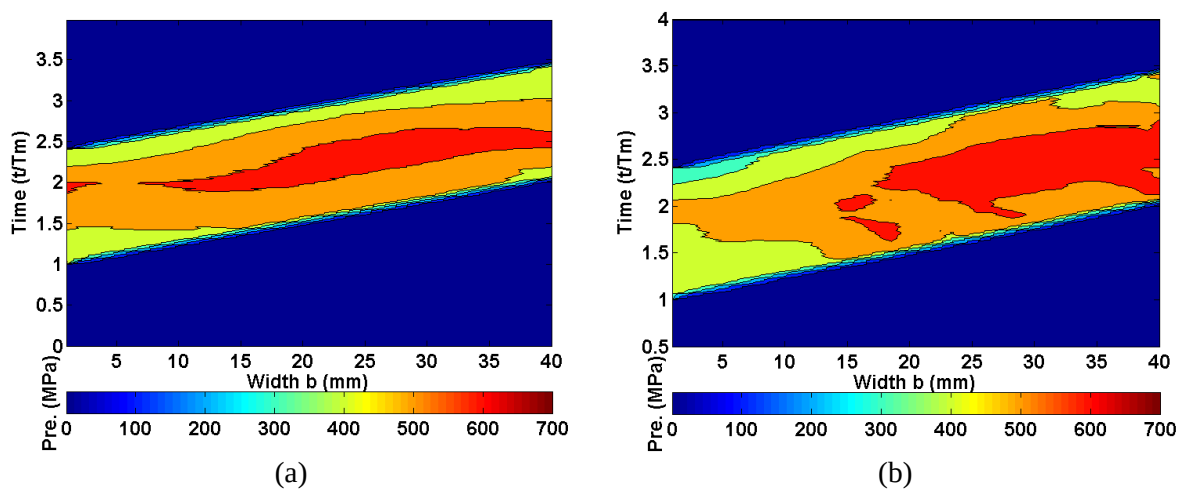


Fig. IV-36: Pressure distribution on (a) plain and (b) webbed pinion

3.1.2. Dynamic Analysis

Considering the natural frequencies and modes of the system at rest with averaged mesh stiffness, Fig. IV-37 shows the comparison between the results for a thin-webbed pinion alone and the full reduction stage over a broad frequency range. Both sets of frequencies and modes agree well but, as anticipated, the full model exhibits a richer modal content particularly at low frequencies.

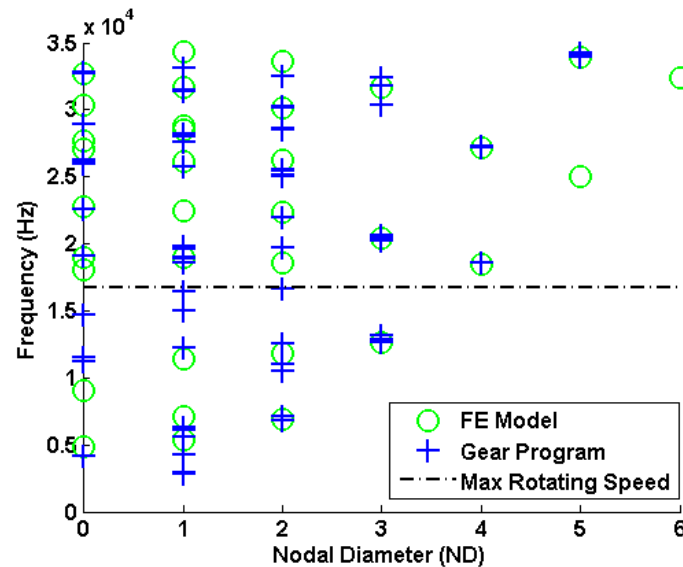


Fig. IV-37: Pinion modal data

It is also interesting to note that only a few pinion modes have a frequency below the first meshing harmonic at the maximal rotating speed so that the most part of the dynamic response is caused by the wheel body. The dynamic mesh force factor versus speed has been calculated for a solid and a thin-web pinion and the corresponding responses curves are in Fig. IV-38 below. Most of the major peaks are conserved with a slight frequency shift suggesting that mass reduction is the dominant phenomenon.

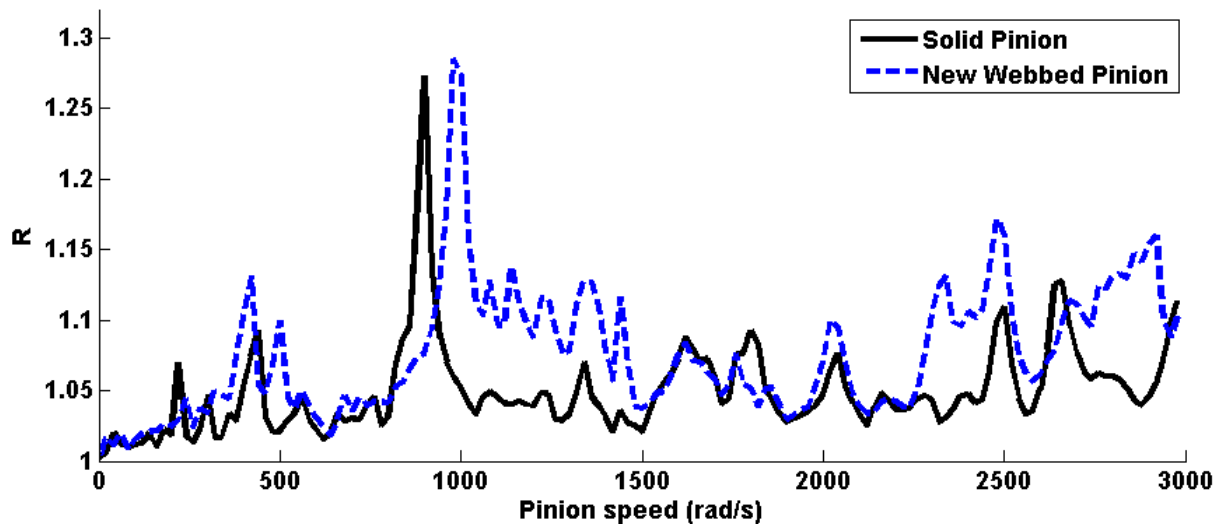


Fig. IV-38: Dynamic ratio comparison for webbed pinion inclusion

Tab. IV-8 shows the proportion (%) of strain energy stored in the gears in relation to the main critical speeds in Fig. IV-38. For the major peak between 900 and 1000 rad/s, the energy distribution appears as relatively evenly distributed between the different components. The introduction of the webbed pinion lowers the bearing contribution compared with that of the pinion. The pinion first modes are around 5500 Hz (Fig. IV-37), which coincide with the meshing first harmonic at this speed and therefore modify critical speeds.

Speed def.	Ω_1		Ω_2		Ω_{2bis}		Ω_5		Ω_{5bis}
Speed (rad/s)	410 rad/s		840 rad/s		900-1000 rad/s		2490 rad/s		2900 rad/s
Type of mode	Wheel		Pinion		Coupled		Wheel		Pinion
Energy (%)	Rig.	Web.	Rig.	Web.	Rig.	Web.	Rig.	Web.	Web.
Bearings	5	17	30	21	11	/	/	/	17.9
Pinion	/	12	38	17	38	/	/	/	82
Wheel	83	65	25	36	35	93	98	/	/
Meshing	11	6	7	26	16	2	1.6	/	/

Tab. IV-8: Energy comparison for principal response modes depending on pinion: rigid or webbed

At the lowest response peak around 410 rad/s, the pinion contribution increases between the rigid and the flexible pinion models while bearing contributions decrease. At this low speed, no pinion mode can be triggered (Fig. IV-37) so its contribution is only static. The higher critical speeds are strictly wheel and pinion modes respectively. The wheel mode, at 2490 rad/s is unchanged thus leading to a similar peak with slightly different amplitudes. The second mode at 2900 rad/s is present only for the webbed pinion case. Besides resonance shift, the dynamic

factor seems to be higher in the high-speed area for the webbed pinion case. To clarify this issue, a more precise analysis has been conducted on the newly designed gear at the maximum speed $\Omega_p = 3000 \text{ rad / s}$.

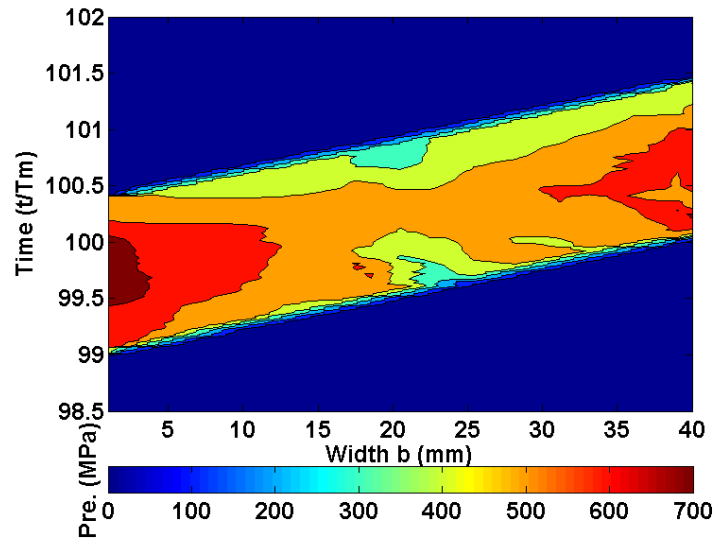


Fig. IV-39: Pressure distribution at $\Omega_p = 3000 \text{ rad / s}$ for webbed pinion

Fig. IV-39 shows the dynamic pressure distribution which reveals that overloads are found at both edges of the face width whereas the central part of the teeth is less loaded. The peak on the left part was already noticed for the solid pinion but the other one did not appear and clearly is a consequence of the thin web arrangement.

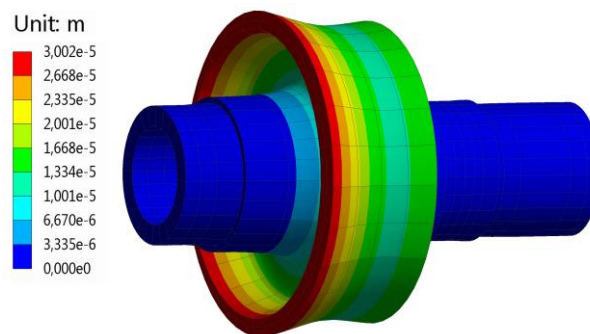


Fig. IV-40: Centrifugal effect FE calculation for $\Omega_p = 3000 \text{ rad / s}$

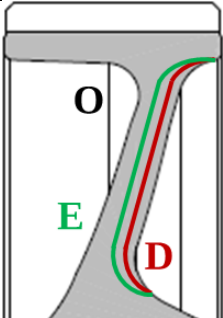
A FE analysis has been conducted on the pinion alone to determine its behaviour under centrifugal loading at high speeds, Fig. IV-40 shows the deformed shape obtained at 3000 rad/s which demonstrates that displacements as large as 30 μm are found and that both rim edges

significantly deform thus explaining the pressure pattern in Fig. IV-39. This study confirms that the centrifugal effects of the pinion and the wheel affect tooth contact conditions, and more globally, gear dynamic behaviour. Therefore, in the presence of flexible parts, all their speed components need to be taken into account for correct dynamic simulations.

3.2. Dynamic Optimisation of Lightweight Gear

3.2.1. Web Optimisation – Load Distribution

Having achieved most of the optimisation with respect to mass, web shapes can also be enhanced by refining its geometry as illustrated in Tab. IV-9, test case O standing for the original wheel that has been previously studied.

	Web thickness (%)	Total mass variation (wheel + shaft %)	
Test case O	-	-	
Test case D	- 24 %	- 6 %	
Test case E	- 48 %	- 12 %	

Tab. IV-9: Wheel web geometry thickness modification

As clear from Tab. IV-9, the material removal has consequences on both the wheel flexibility and mass. To assess the resulting impact, comparative modal tests have been conducted on three cases using the FE model of the wheel alone prior to condensation. The results in Fig. IV-41 are indexed by Nodal Circle and Diameter number and prove that the modifications have a limited impact on the wheel web modal behaviour.

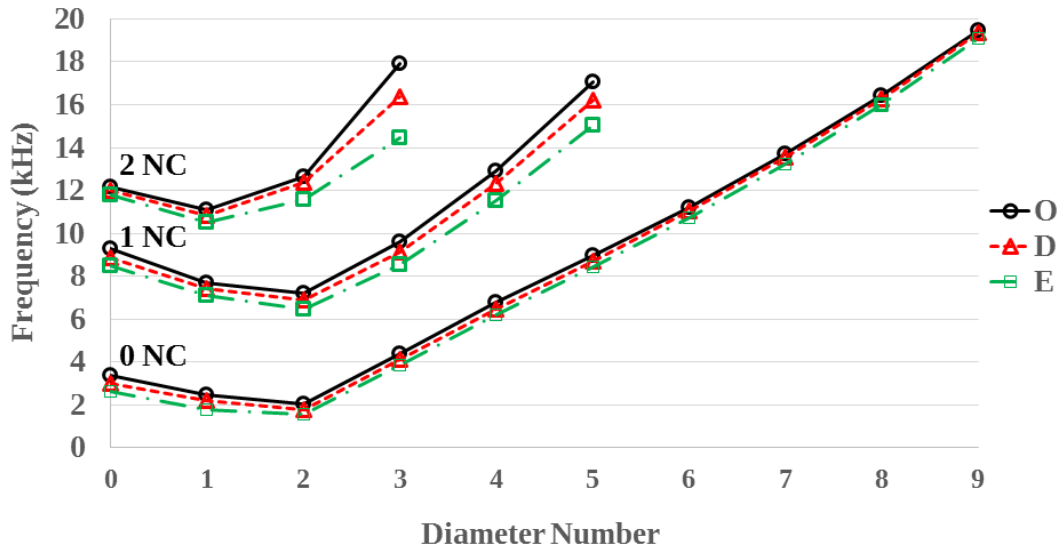


Fig. IV-41: Web thickness influence on wheel modal behaviour – FE analysis

It can be seen that the modes without any nodal circle are almost identical while deviations are more marked when it comes to higher circle and diameter numbers with a maximum difference in frequency of nearly 20% between test case O and E. The original wheel always exhibits the highest natural frequencies.

These results are in line with those of Li [LI08.b] who found that web and rim bending frequencies were increased when using thicker webs because the web/rim assembly deforms less. As an example of illustration, Fig. IV-42 displays the 2NC and 3ND mode deformed shapes for which the contribution of the rim/web part is clearly visible. However, in spite of these limited differences, it can be inferred that the web designs tested here have a limited impact of the global gear modal behaviour.

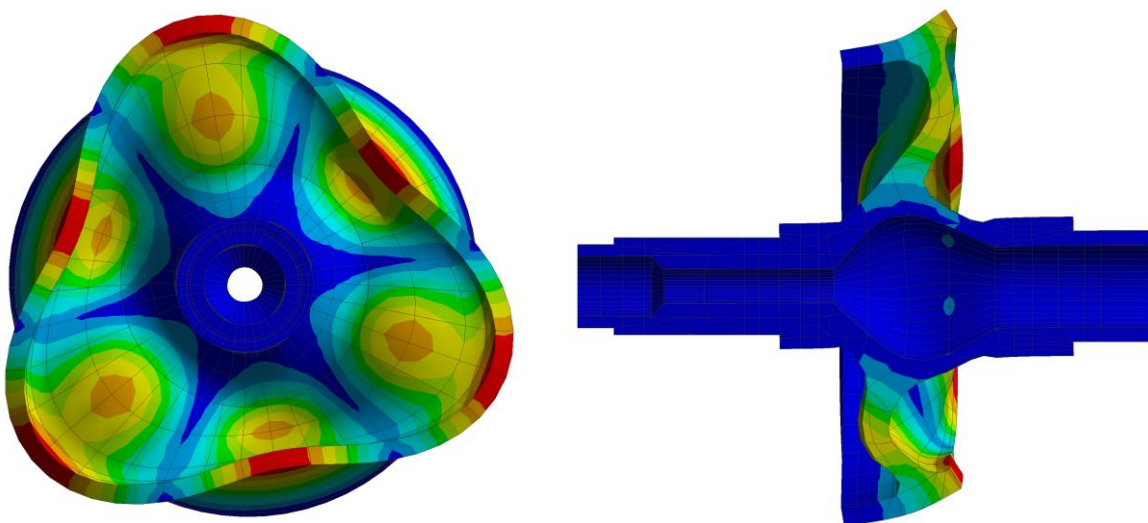


Fig. IV-42: Flexion mode example: 2 circles, 3 diameters (17 922 Hz for Case O)

Considering now the complete reduction stage, the hybrid model two (H2) is employed which was already used in section 2.2 with the original wheel case O. The impact of the new wheels (D and E) is first studied by running test cases under quasi-static conditions ($\Omega_p = 0.01 \text{ rad/s}$). The quasi-static line of contact load and tooth flank pressure comparisons are given in Fig. IV-43.

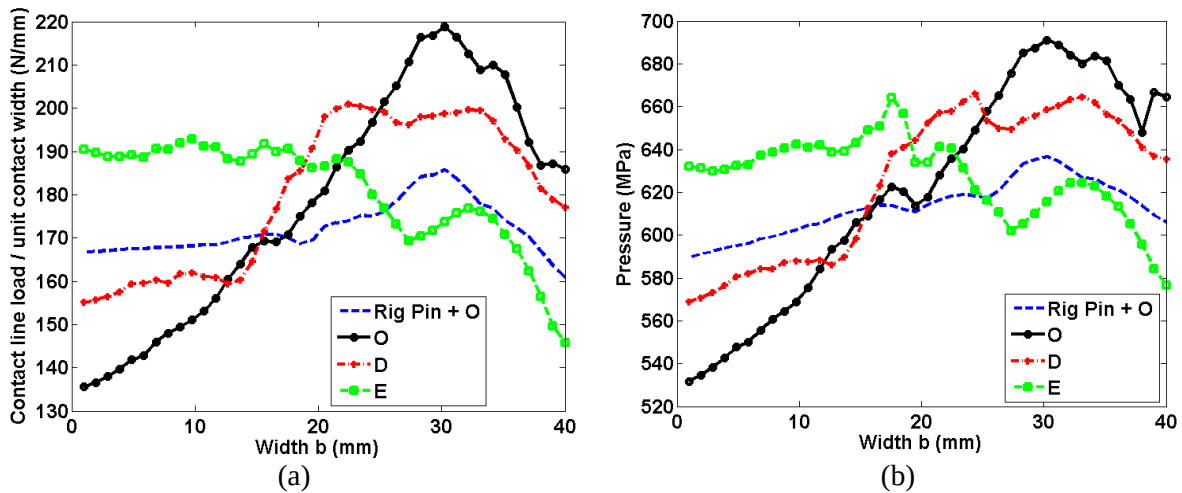


Fig. IV-43: Effect of the web on quasi-static load distribution for (a) maximum contact line load and (b) maximum pressure

The quasi-static load distributions for the two cases, with a rigid and flexible pinion, including the original wheel O (reference) are plotted. They show that, with the initial flexible pinion and wheel, the maximum load is observed at around $b = 30 \text{ mm}$ whereas it becomes more centred on the face width and the pressure is more evenly distributed as the web is made thinner. This confirms the interest of flexible components to adjust quasi-static load patterns although more vibrations could arise.

At high speed, centrifugal effects are still visible as illustrated in Fig. IV-44 which shows that pressure peaks at both face width edges emerge. Comparing with the quasi-static results in Fig. IV-43, the maximum pressure is obtained on the other side of the rim. Case E seems to deform more and be more affected by the centrifugal effects. Some secondary peaks appear near the web/rim connection which is locally stiffer. The 2D representations in Fig. IV-45 show that ‘hard spots’ near this connection are visible for case D and less so for the more flexible rim (case E) for which a better pressure distribution is observed.

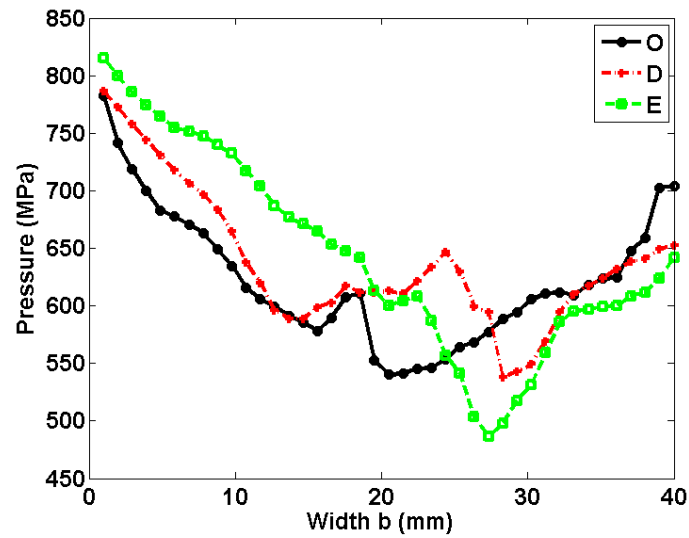


Fig. IV-44: Maximum pressure over a meshing period for the three test cases at $\Omega_p = 3000 \text{ rad} / s$

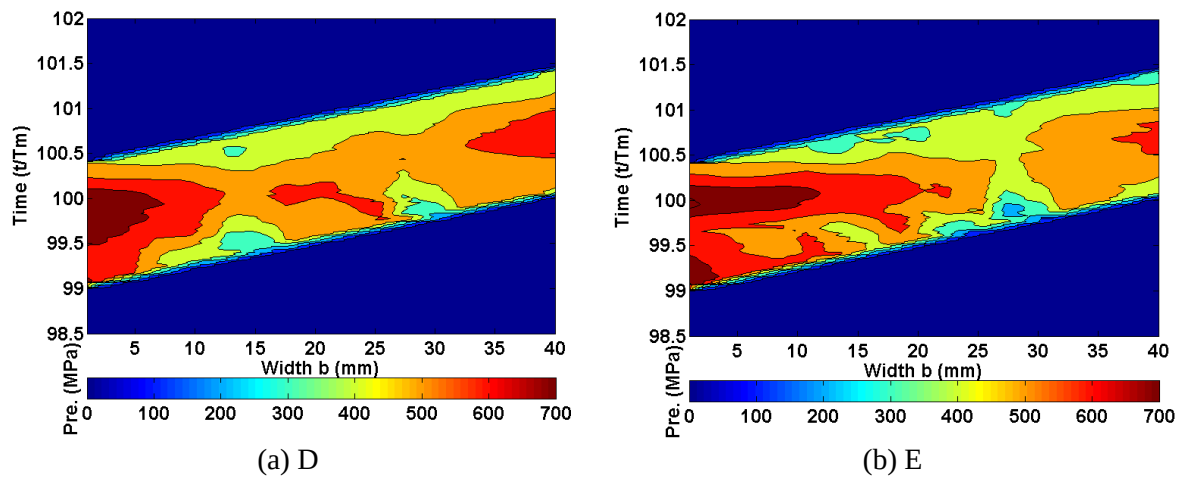


Fig. IV-45: Meshing pressure comparison for both thinner web cases at $\Omega_p = 3000 \text{ rad} / s$

3.2.2. Modification Optimisation

In order to improve the tooth contact conditions at high speeds, it seems sensible to introduce some lead crowning on the wheel or the pinion as described in Fig. IV-46 below. Based on the load distributions in Fig. IV-44 & Fig. IV-45, a parabolic axial modification of amplitude E (constant along the tooth height) seems interesting.

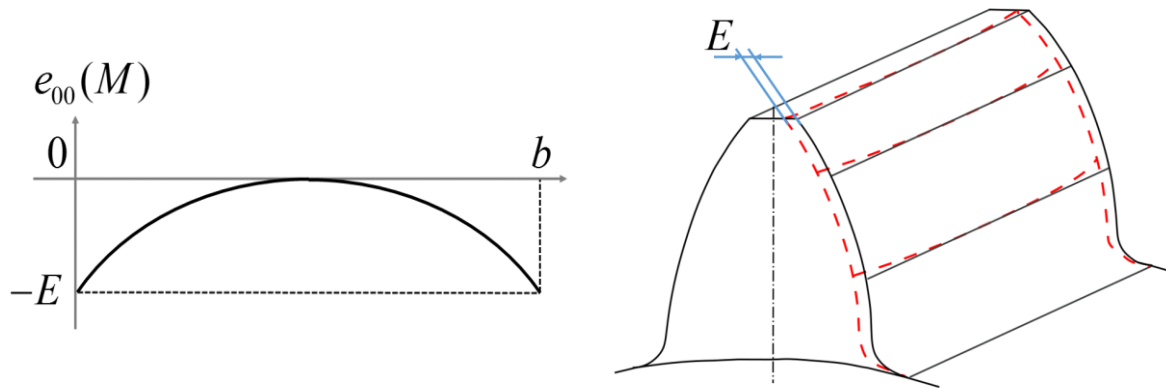


Fig. IV-46: Crowning definition in lead direction

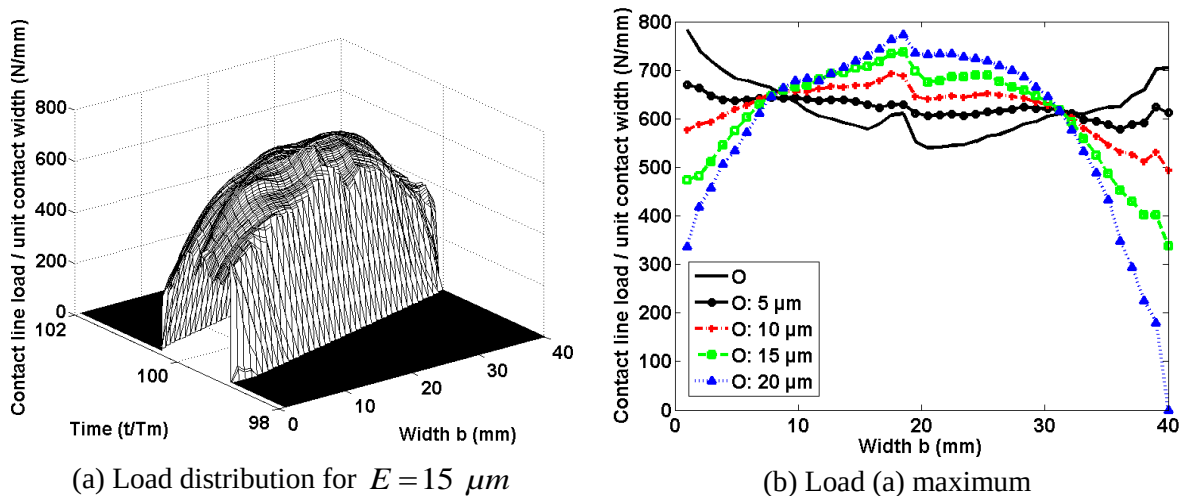


Fig. IV-47: Crowning influence on dynamic pressure distribution

Several crowning amplitudes ranging from 5 to 20 μm are first introduced on the Original test case O. The corresponding tooth load patterns in Fig. IV-47 show that an increasing value of E re-establishes more balanced distributions which are correctly centred on the tooth face width. Above 10 μm , the edges become progressively less loaded which might be interesting in practice providing that the maximum contact stress at mid-tooth span is not

too high. Finally, care needs to be taken as crowning is introduced to balance the highly speed-dependent centrifugal effects and should therefore be adjusted depending on the operating conditions.

In terms of dynamics phenomena, the dynamic factors for different crowning depths in Fig. IV-48 show that the larger the crowning, the higher the mesh force oscillations calculated at high speed (3000 rad/s). In such conditions, it can be concluded that an interesting compromise between load pattern quality and dynamic forces would be for a crowning amplitude around 10 μm .

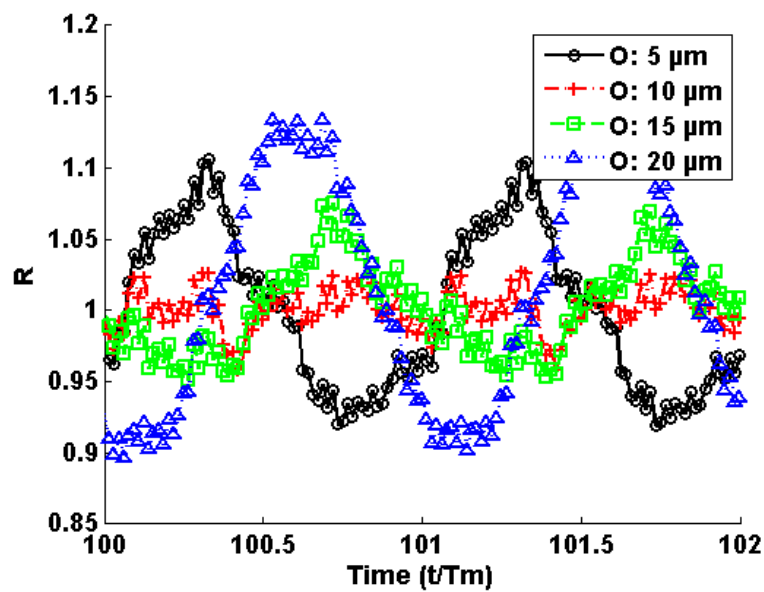


Fig. IV-48: Dynamic ratio for original gear O with various crowning at $\Omega_p = 3000 \text{ rad} / \text{s}$

This study can be repeated on the three test cases of the previous part. Fig. IV-49 shows the maximum load distribution for the three test cases for each crowning amplitude. The web thickness effect is limited except at one tooth edge for which the limit of contact loss is dependent on the web geometry. Consequently, lead modification needs to be specifically defined according to the particular web geometry and cannot be directly transposed from another design.

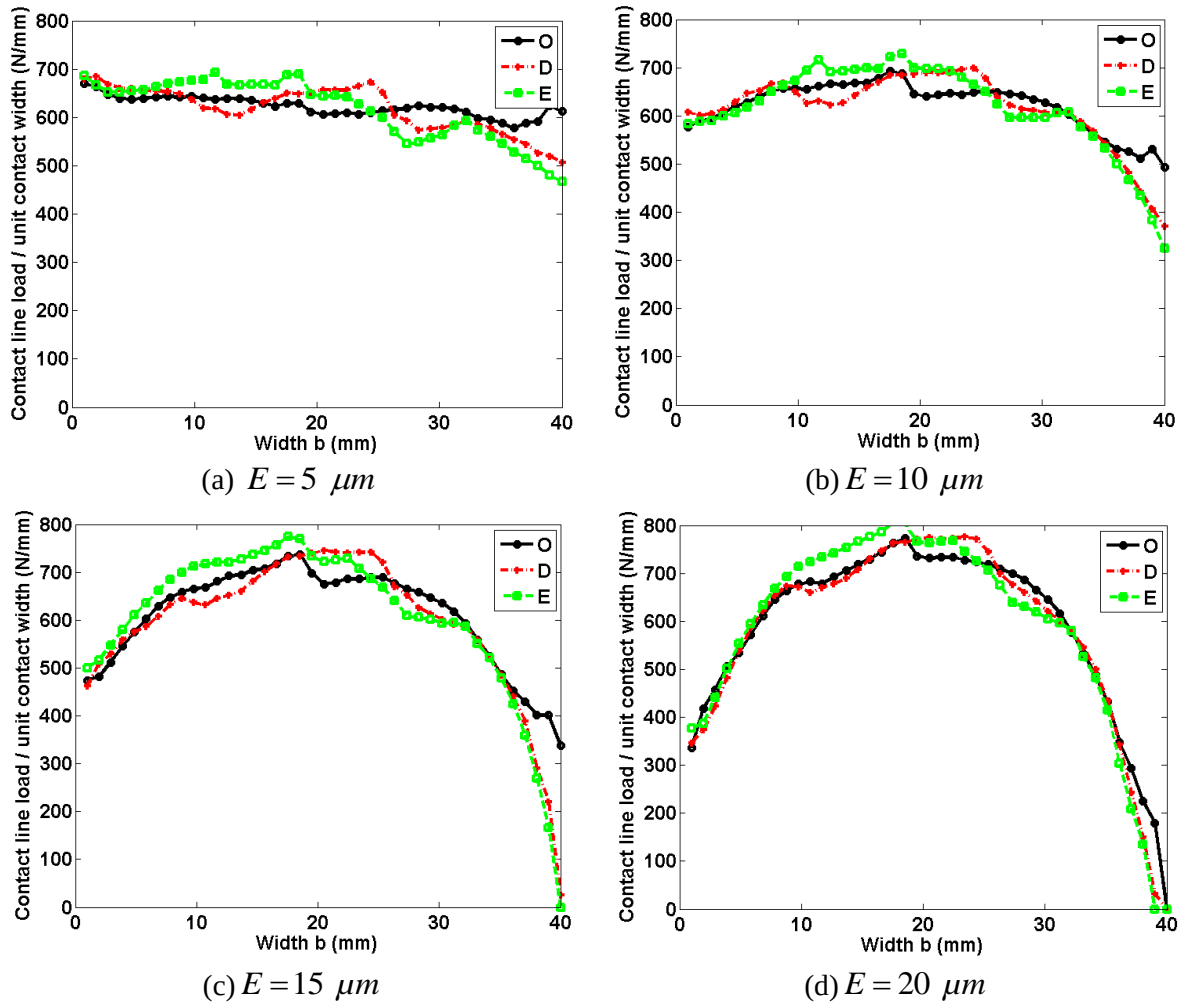


Fig. IV-49: Maximum load over a passage through the base plane comparison for various crowning values at $\Omega_p = 3000 \text{ rad} / \text{s}$

This fact is confirmed by the flank pressure distribution plotted for test case E in Fig. IV-50. The variations for an increasing crowning depth are clearly visible with a more centred pressure distribution with a significant amplification of the maximum pressure combined with pressure relief near the tooth edges. Other shapes of lead modifications such as elliptical crowning or linear + parabolic modification could have been more effective in distributing the load on the teeth more evenly and reducing overloads in the tooth central part.

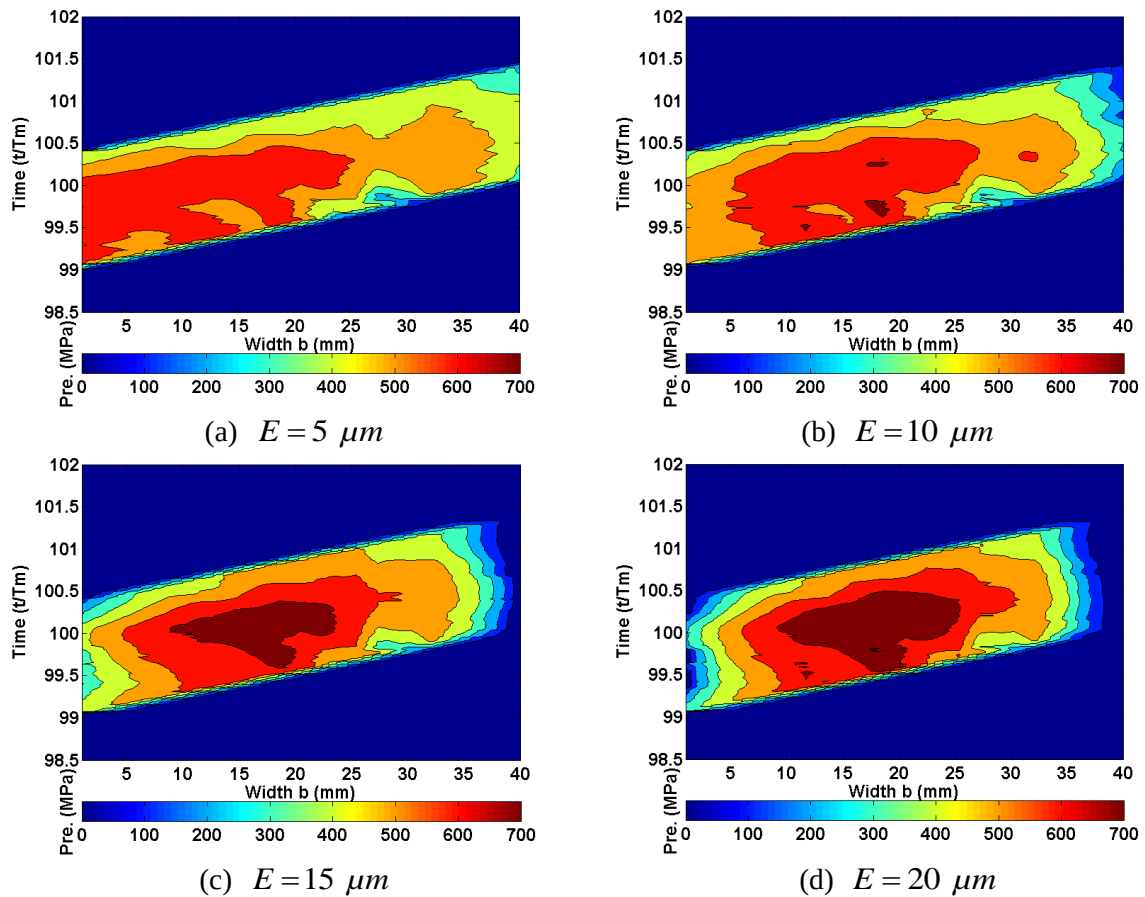


Fig. IV-50: Test Case E: meshing pressure distribution depending on crowning at $\Omega_p = 3000 \text{ rad / s}$

4. Conclusion

This chapter was aimed at analysing the influence of pinion/gear body geometry on the quasi-static and dynamic characteristics of a transmission. The first case study dealt with an accessory spur gear with a straight web which was found to be highly influential on the gear behaviour and needed to be designed accordingly. It has also been shown that profile modifications can substantially improve the meshing conditions and that web geometry and deflections have to be considered when looking for optimum profile relief. Similar conclusions have been drawn when considering a thin-webbed flexible pinion body in addition to a flexible wheel body.

In a second part, the dynamic contribution of flexible webs was investigated on the academic power transmission architecture. The dynamic mesh force curves prove that body modes have an impact on the whole gear dynamic behaviour. The response at some web nodes has been studied at several resonant and non-resonant speeds which indicate that body modes exhibit progressive wave properties. The influence of holes in webs has also been tackled and it has been demonstrated that, in certain conditions, both the static and dynamic responses can be altered when hollow webs are employed.

Finally, the design of light-weight pinions and gears in power transmissions has been examined. It has been found that the modal properties are altered compared with systems with solid pinions. One major result concerns the importance of accounting for centrifugal effects together with a precise elastic web model in high-speed gears since they can strongly modify tooth load distributions and consequently control the definition of tooth shape modifications.

General Conclusion

The major objective of this PhD was to present the developments associated with some original modular hybrid models of mechanical transmissions with thin-rimmed/webbed pinions and gears. As opposed to what can be found in the literature, a quasi-analytical model is used to describe tooth contacts in terms of elasticity and shape deviations whereas 3D finite elements are employed for all the components with linear behaviour. By so doing, the previous modelling efforts at LaMCoS re instant tooth contacts based on time-varying non-linear Winkler foundations are just adapted to a different modelling environment accounting for thin rims and webs, shafts, bearings, etc. The resulting hybrid models have therefore the capacity to combine lumped parameter + shaft element sub-models (for a pinion shaft for instance) with condensed 3D finite elements to simulate a thin-rimmed gear body and shaft. In these conditions, particular attention has been given to the connection of the lumped and finite element models via discrete elastic foundations. It has been shown that direct collocation generates artificial load spikes on tooth flanks which are caused by the incompatibility between a discrete foundation and a continuous rim model. A mortar-based approach has been developed and implemented which smoothen the numerical load oscillations mentioned above. The corresponding state equations are solved step by step in time by using a Newmark scheme and a unilateral normal contact algorithm which verifies that all contact forces between the tooth flanks are compressive and that there is no contact outside the defined contact area. Such a methodology can simulate the contributions of tooth shape deviations and errors and also capture the amplitude jumps and softening effects caused by contact losses and shocks between the teeth at the major tooth critical frequencies.

The resulting dynamic models have been largely validated by comparisons with both numerical and experimental results thus proving the versatility of the approach and its capacity to simulate actual gear sets. Further investigations concerning specifically the influence of gear body compliance and centrifugal effects have been conducted which highlight the significant contribution of centrifugal effects at high-speeds and the interest of profile and lead modifications in terms of tooth load pattern quality and vibrations. However, uncertainties remain about the simulation of damping which, as expected, is of primary importance since it controls the amplifications at critical speeds. Qualitatively, Rayleigh and modal damping models have their own limitations and quantitatively, damping amplitudes very much rely on empirical data whose range of validity should be critically assessed especially for thin members.

In terms of perspectives, the hybrid approach could be extended to incorporate casings whose flexibility certainly needs to be taken into account for determining tooth load distributions and estimating the noise radiated to the surroundings. The simulations of multi-mesh gears such as those in accessory gearboxes would also be an interesting research direction since they comprise both thin-rimmed pinions and thin casings.

References

- [ABB05] Abbes, M. S., “Gearbox vibratory analysis using carrying, coupling and slave substructures,” *International Journal of Simulation Modelling*, 4(2):67–75, 2005.
- [ABB07] Abbes, M. S., Fakhfakh, T., Haddar, M., and Maalej, A., “Effect of transmission error on the dynamic behaviour of gearbox housing,” *The International Journal of Advanced Manufacturing Technology*, 34(3–4):211–218, 2007.
- [ABB08] Abbes, M., Bouaziz, S., Chaari, F., Maatar, M., and Haddar, M., “An acoustic–structural interaction modelling for the evaluation of a gearbox-radiated noise,” *International Journal of Mechanical Sciences*, 50:569–577, 2008.
- [ABO04] Abouslieman, V., “Comportement dynamique des trains planétaires et épicycloïdaux, conditions de contact instantanées et sous-ensembles flexibles”, Ph.D., INSA Lyon, 2004.
- [ABO06] Abousleiman, V., Velex, P., “A hybrid 3D finite element/lumped parameter model for quasi-static and dynamic analysis of planetary/epicyclic gear sets”, *Mechanism and machine theory*, **41**:725-748, 2006, DOI:10.1016/j.mechmachtheory.2005.09.005.
- [ABO07] Abousleiman, V., Velex, P., Becquerelle, S., “Modelling of spur and helical gear planetary drives with flexible gears and planet carriers”, *Journal of mechanical design*, **129**(1):95-106, 2007, DOI:10.115/1.2359468.
- [AJM05] Ajmi, M., Velex, P., “A model for simulating the quasi-static and dynamic behaviour of solid wide-faced spur and helical gears”, *Mechanism and machine design*, **40**:173-190, 2005, DOI:10.1016/j.mechmachtheory.2003.06.001.
- [ALM12] Almeida, P., Leblanc., Thouverez, F., Gilbert, C., Ousty, J-P., “Experimental and numerical investigation on a rotating centrifugal compressor”, *Proceedings of ASME Turbo Expo 2012*, Copenhagen, Denmark, June 11-15, 2012.
- [ALM14] Almeida P., “Couplage thermomécanique et vibratoire d’un compresseur centrifuge lors d’un contact aube-carter”, Ph.D., Centrale Lyon, 2014.

- [AMB07] Ambarisha, V.K., Parker, R.G., “Nonlinear dynamics of planetary gears using analytical and finite element models”, *Journal of Sound and Vibration*, 302:577-595, 2007.
- [AMI98] Amini, N., Rosen, B.G., Rosen, Westberg, H., “Optimization of gear tooth surfaces”, *International Journal of Machine Tools and Manufacture*, 38(5-6):425-435, 1998.
- [ANK14] Ankouni, M., Lubrecht, A. A., Velex, P., “Numerical simulation of damping in EHL line contacts”, *International Gear Conference*, p1020-1028, vol. 2, Lyon, 26th-28th August 2014.
- [ANK16] Ankouni, M., “Modeling of damping in elastohydrodynamic lubricated contact, application to gear dynamic”, Ph.D., INSA Lyon, 2016.
- [ART11] Artoni, A., Gabiccini, M., Guiggiani, M., Kahraman, A., “Multi-objective ease-off optimization of hypoid gears for their efficiency, noise and durability performances”, *Journal of Mechanical Design, ASME*, 133(121007):1-9, 2011.
- [BAH13] Bahk, C.J., Parker, R.G., “Analytical investigation of tooth profile modification effects on planetary gear dynamics”, *Mechanism and Machine Theory*, 70:298-319, 2013.
- [BAU02] Baud, S., and Velex, P., “Static and dynamic tooth loading in spur and helical geared systems-experiments and model validation”, *Journal of Mechanical Design, ASME*, 124(2):334-346, 2002.
- [BEL97] Ben Belgacem, F. and Maday, Y., The mortar finite element method for three dimensional finite elements., *Mathematical Modelling and Numerical Analysis*, **31**:289–302, 1997.
- [BER94] Bernardi, C., Maday, Y., and Patera, A., “A new nonconforming approach to domain decomposition: The mortar element method”, *Collège de France Seminar*, pages 13–51, 1994.
- [BET06] Bettaieb, M., “Modélisation du comportement dynamique d’engrenages, couplages entre engrenements et éléments de structures flexibles”, Ph. D., INSA Lyon, 2006.

- [BET07] Bettaieb, M., Velex, P., Ajmi, M., “A static and dynamic model of geared transmission by combining substructures and elastic foundations – application on thin-rimmed gears”, *Journal of Mechanical design*, **129**:184-194, 2007, DOI:10.1115/1.2406088.
- [BLA95] Blankenship, G.W., Kahraman, A., “Steady state forced response of a mechanical oscillator with combined parametric excitation and clearance type non-linearity”, *Journal of Sound and Vibration*, 185(5):743-765, 1995.
- [BLA96] Blankenship, G.W., Kahraman, A., “Gear dynamics experiments, Part I: characterization of forced response”, *7th International Power Transmission and Gearing Conference, ASME*, **88**:373-380, 1996.
- [BLE79] Blevins, R.D., “Formula for natural frequency and mode shape”, Van Nostrand Reinhold Company, New York, 1979.
- [BOG12] Bogacz, R., Noga, S. “Free transverse vibration analysis of a toothed gear”, *Archives of Applied Mechanics*, 82:1159-1168, 2012. DOI 10.1007/s00419-012-0608-6.
- [BON08] Bonori, G., Barbieri, M., Pellicano, F., “Optimum profile modifications of spur gears by means of genetic algorithms”, *Journal of Sound and Vibration*, 313:603-616, 2008.
- [BRU13] Bruyère, J., Velex, P., “Derivation of optimum profile modifications in narrow-faced spur and helical gears using a perturbation method”, *Journal of Mechanical Design, ASME*, 135:071009-1-8, 2013.
- [BRU14] Bruyère, J., Velex, P., “A simplified multi-objective analysis of optimum profile modification in spur and helical gears”, *Mechanism and Machine Theory*, 80:70-83, 2014.
- [BRU15] Bruyère, J., Gu, X., Velex, P., “On the analytical definition of profile modifications minimising transmission error variation in narrow-faced spur helical gears”, *Mechanism and Machine Theory*, 92:257-272, 2015, DOI:10.1016/j.mechmachtheory.2015.06.001.
- [CAR11] Carbonelli, A., Perret-Liaudet, J., Rigaud, E., Le Bot, A., “Particle swarm optimization as an efficient computational method in order to minimize vibrations of multimesh gears transmission”, *Advances in Acoustics and Vibration*, 195642, 2011, doi:10.1155/2011/195642.

- [CAR13] Carbonelli, A., Perret-Liaudet, J., Rigaud, E., Pelloli, E., Barday, D., “Robust optimization of a truck timing gear cascade : numerical and experimental results”, *21^{ème} Congrès Français de Mécanique*, Bordeaux, 26th-30th August 2013.
- [CHA07] Champaney, L., and Dureisseix, D., A mixed domain decomposition approach. In Magoulès, F., editor, *Mesh Partitioning Techniques and Domain Decomposition Methods*, chapter 12, pages 293–320. Civil-Comp Press / Saxe-Coburg Publications, 2007, DOI:104203/csets.17.12.
- [CHA16] Chapron, M., Velez, P., Bruyère, J., “Optimization of profile modifications with regards to dynamic tooth loads in single and double-helical planetary gears with flexible ring-gears”, *Journal of Mechanical Design, ASME*, 138(023301):1-11, 2016.
- [CHO03] Chowdhury, I., Dasgupta, S.P., “Computation of Rayleigh damping coefficients for large systems”, *Electronic Journal of Geotechnical Engineering*, 8(0), 2003.
- [CON71] Conry, T.F., Seireg, A., “A mathematical programming method for design of elastic bodies in contact”, *Journal of Applied Mechanics, ASME*, 38(2):387-392, 1971.
- [CON73] Conry, T.F., Seireg, A., “A mathematical programming technique for the evaluation of load distribution and optimal modifications of gear systems”, *Journal of Engineering and Industry, ASME*, 95(4):1115-1122, 1973.
- [COO14] Cooley, C.G., Parker, R.G., “Vibration of high-speed rotating rings coupled to space-fixed stiffnesses”, *Journal of Sound and Vibration*, 333:2631-2648, 2014.
- [COO15] Cooley, C.G., Parker, R.G., “Limitations of an inextensible model for the vibration of high-speed rotating elastic rings with attached space-fixed discrete stiffnesses”, *European Journal of Mechanic A/Solids*, 54:187-197, 2015.
- [CRA68] Craig, R.R., Bampton, M.C.C., “Coupling of sub-structures for dynamic analysis”, *AIAA Journal*, 6(7):1313-1319, 1968.
- [DHA81] Dhatt, G., Touzot, G., Denielou, G., “Une présentation de la méthode des éléments finis”, *Maloine*, Paris, 1981.

- [DHI05] Ben Dhia, H., and Rateau, G., “The Arlequin method as a flexible engineering design tool”, *International Journal for Numerical Methods in Engineering*, 62:1442–1462, 2005, DOI:10.1002/nme.1229.
- [DIN07] Ding, H., and Kahraman, A., “Interactions between nonlinear spur gear dynamics and surface wear,” *Journal of Sound and Vibration*, 307(3–5):662–679, 2007.
- [DUR03] Dureisseix, D., Ladevèze, P., and Schrefler. B. A., “A LATIN computational strategy for multiphysics problems: Application to poroelasticity”, *International Journal for Numerical Methods in Engineering*, 56(10):1489–1510, 2003, DOI:10.1002/nme.622.
- [ERI12] Eritenel, T., and Parker, R. G., “Three-dimensional nonlinear vibration of gear pairs,” *Journal of Sound and Vibration*, 331(15):3628–3648, 2012.
- [ERI12] Eritenel; T., Parker, R.G., “Three-dimensional nonlinear vibration of gear pairs”, *Journal of Sound and Vibration*, 331(2012):3628-3648, 2012.
- [FIE85] Field, J.V., Wright, M.T., “The early history of mathematical gearing”, *Endeavour, New Series*, 9(4):0160-9327/85, 1985.
- [FUK73] Fukuma, H., Furukawa, T., and Aida, T., “Fundamental Research on Gear Noise and Vibration,” *Bulletin of the JSME*, 16:1094–1107, 1973.
- [GER84] Geradin, M., Kill, N., “A new approach to finite element modelling of flexible rotors”, *Engineering Computing*, 1:52-65, 1984.
- [GER93] Gerardin, M., Rixen, D., « Théorie des vibrations, application à la dynamique des structures », Masson, Physique Fondamentale et Appliquée, Paris, p.421, 1993.
- [GHR12] Dhafer G., Jérôme B., Philippe V., Michel O., Haddar M., “Robust Optimization of Gear Tooth Modifications Using a Genetic Algorithm”, *Condition Monitoring of Machinery in Non-Stationary Operations*. Springer, Berlin, Heidelberg, 2012.
- [GHR13] Ghribi, D., Bruyère, J., Vexex, P., Octrue, M., Haddar, M., “Multi-objective optimization of gear tooth profile modifications”, *Design and Modelling of Mechanical Systems*, p.189-197, 2013. DOI: 10.1007/978-3-642-37143-1_24

- [GOS00] Gosselin, C., Guertin, T., Remond, D., and Jeans, Y., “Simulation and experimental measurement of the transmission error of real hypoid gears under load,” *Journal of Mechanical Design*, 122:109–122, 2000.
- [GUI05] Guilbault, R., Gosseling, C., Cloutier, L., “Helical gears, effect of tooth deviations and tooth modifications on load sharing and filet stresses”, 128:444-456, 2006.
- [GUI16] Guilbert, B., Velex, P., Dureisseix, D., Cutuli, P., , “A mortar-based mesh interface for hybrid finite element/lumped parameter gear dynamic models – Applications to thin-rimmed geared systems”, *Journal of Mechanical Design*, dec. 2016.
- [GUI18-in prep.] Guilbert, B., Velex, P., Cutuli, P., “”, in-prep, 2018.
- [GUO01] Guo, D., Chu, F. L., Zhieng, Z. C., “The influence of rotation on vibration of a thick cylindrical shell”, *Journal of sound and vibration*, 242:487-505, 2001
- [GUO14] Guo, Y., Eritenel, T., Ericson, T. M., and Parker, R. G., 2014, “Vibro-acoustic propagation of gear dynamics in a gear-bearing-housing system,” *Journal of Sound and Vibration*, 333(22):5762–5785, 2014.
- [HAR58] Harris, S.L., “Dynamic loads on the teeth of spur gears”, *Proceedings of the Institution of Mechanical Engineers*, 172:87-112, 1958.
- [HEI15] Heirman, G.H.K, Toso, A., Cappellini, N., Van Wermeskerken, F.P.J, “A gear contact model to analyse the dynamics of transmissions with lightweight, flexible gears”, *International Conference on Gears*, VDI, P.1009, 2015.
- [HEN78] Henriot G., “Traité théorique et pratique des engrenages, *Tome II : Etude complète du matériel*”. 4ème édition, Paris : Dunod Technique, 608p, 1978.
- [HEN79] Henriot G., “Traité théorique et pratique des engrenages, *Tome I : Théorie et technologie*”. 6ème édition, Paris : Dunod Technique, 622p, 1979.
- [HER85] Herting, D.N., “A general purpose, multi-stage component modal synthesis method”, *Finite elements in analysis and design*, 1:153-164, 1985, DOI:10.1016/0168-874/(85)90025-3.

- [HOT08] Hotait, M., Kahraman, A., “Experiments on root stresses of helical gears with lead crown and misalignments”, *Journal of Mechanical Design, ASME*, 130(074502):1-5, 2008.
- [HOT13] Hotait, M. A., and Kahraman, A., “Experiments on the relationship between the dynamic transmission error and the dynamic stress factor of spur gear pairs,” *Mechanism and Machine Theory*, 70:116–128, 2013.
- [HOU06] Houser, D.R., Harianto, J., Talbot, D., “Gear mesh misalignment”, *Gear Solutions*, 34-43, Jun. 2006.
- [HOU94] Houser, D., Oswald, F., and Valco, M., “Comparison of transmission error predictions with noise measurements for several spur and helical gears,” *30th AIAA/ASME/SAE/ASEE Joint Propulsion Conf.*, Indianapolis, 1994.
- [ISO21771] International Organization for standardization, “ISO 21771: Gears – Cylindrical involute gears and gear pairs – Concepts and geometry”, Genève, Switzerland, 2007-09.
- [ISO6336] International Organization for standardization, “ISO 6336: Calculation of load capacity of spur and helical gears”, Part 1-5, Genève, Switzerland, 1996.
- [JAC97] Jacquet-Richardet, G., “Bladed Assemblies Vibration”, Lecture notes, INSA de Lyon, 1997.
- [JOH58] Johnson, D., “Excitation of resonant vibrations by gear teeth meshing effects,” *Proceedings of the International Conference on Gearing, Institution of Mechanical Engineers*, London, UK, pp. 18–23, 1958.
- [KAH01] Kahraman, A., Vijayakar, S., “Effect of internal gear flexibility on the quasi-static behavior of a planetary gear set”, *Journal of Mechanical Design*, 123:408-415, 2001.
- [KAH03] Kahraman, A., Kharazi, A.A, Umrani, M., “A deformable body dynamic analysis of planetary gears with thin rims”, *Journal of Sound and Vibration*, 262:752-768, 2003.
- [KAH10] Kahraman, A., Ligata, H., Singh, A., “Influence of ring gear rim thickness on planetary gear set behaviour”, *Journal of Mechanical Design, ASME*, 132(021002):1-8, 2010

- [KAH90] Kahraman A., Singh R., “Non-linear dynamics of a spur gear pair”, *Journal of Sound and Vibration*, 142(1):49-75, 1990.
- [KAH92] Kahraman, A., Ozguven, H. N., Houser, D. R., and Zakrajsek, J. ., “Dynamic Analysis of Geared Rotors by Finite Elements,” *Journal of Mechanical Design*, 114(3):507–514, 1992.
- [KAN12] Kang, M., R., Kahraman, A., “Measurement of vibratory motions of gears supported by compliant shafts”, *Mechanical Systems and Signal Processing*, 29:391-403, 2012.
- [KOH59] Kohler, H., “The mechanism and measurement of dynamic loading in spur gears,” PhD Thesis, University of Sheffield, 1959.
- [KOH70] Kohler, H., Pratt, A., and Thompson, A., “Dynamics and Noise of Parallel-axis Gearing,” *Proceedings of the Institution of Mechanical Engineers*, 184:111–121, 1970.
- [KUB72] Kubo, A., Yamada, K., Aida, T., and Sato, S., “Research on ultra high speed gear devices,” *Bulletin of the JSME*, 38:2692–2715, 1972.
- [LAC97] Lacour, C., and Maday, Y., “Two different approaches for matching non-conforming grids: The mortar element method and the FETI method”, *BIT Numerical Mathematics*, 37(3):720–738, 1997, DOI:10.1007/BF02510249.
- [LAL84] Lalanne, M., Berthier, P., Der Hagopian, J., *Mechanical Vibrations for Engineers*, John Wiley & Sons, Northern Ireland, 1984.
- [LAL90] Lalanne M., Ferraris G., “Rotordynamics”. *Prediction in Engineering*, John Wiley & Sons, New York, 1990.
- [LEW93] Lewis, M. J. T., “Gearing in the ancient world”, *Endeavour, New series*, vol. 17,1993
- [LI02.a] Li, S., “Deformation and bending stress analysis of a three-dimensional, thin-rimmed gear”, *Journal of Mechanical design, ASME*, 124 :129-135, 2002.
- [LI02.b] Li, S., “Gear contact model and loaded tooth contact analysis of a three-dimensional thin-rimmed gear”, *Journal of Mechanical design*, 124:511-517, 2002.

- [LI07] Li, S., “Finite element analyses for contact strength and bending strength for a pair of spur gears with machining errors, assembly errors and tooth modifications”, *Mechanism and Machine Theory*, 42:88-114, 2007.
- [LI08.a] Li, S., “Centrifugal load and its effects on bending strength and contact strength of high speed thin-walled spur gear with offset web”, *Mechanism and Machine Theory*, 43 :217-239, 2008.
- [LI08.b] Li, S., “Experimental investigation and FEM analysis of resonance frequency behaviour of three-dimensional, thin-walled spur gears with power-circulating test rig”, *Mechanism and Machine Theory*, 43:934-963, 2008.
- [LI11] Li, S., and Kahraman, A., “A Method to Derive Friction and Rolling Power Loss Formulae for Mixed Elastohydrodynamic Lubrication,” *Journal of Advanced Mechanical Design, Systems, and Manufacturing*, 5(4):252–263, 2011.
- [LI13] Li, S., “Effects of centrifugal load on tooth contact stresses and bending stresses of thin-rimmed spurs gears and with inclined webs”, *Mechanism and Machine Theory*, 59:34-47, 2013.
- [LIM89] Lim, T. C., and Singh, R., “A Review of Gear Housing and Acoustics Literature Dynamics,” *The Ohio State University*, 1989.
- [LIM90] Lim, T., and Singh, R., “Vibration transmission through rolling element bearings, part ii: system studies,” *Journal of sound and vibration*, 139(2):201–225, 1990.
- [LIM91] Lim, T., and Singh, R., “Vibration transmission through rolling element bearings. part iii: Geared rotor system studies,” *Journal of sound and vibration*, 151(1):31–54, 1991.
- [LIU95] Liu, M., Gorman, D.G., “Formulation of Rayleigh damping and its extensions”, *Computers & Structures*, 57(2):277-285, 1995.
- [LUN39] Lundberg, G. “Elastische Berührung zweier Halbräume”. *Forschung auf dem Gebiete des Ingenieurwesens*, 10(5):201–211, 1939.
- [MAA97] Maatar, M., Velez, P., “Quasi-static and dynamic analysis of narrow-faced helical gears with profile and lead modifications”, *Journal of Mechanical Design, ASME*, 119:474-480, 1997.

- [MAR07] Martin, V., “Elements d’acoustique générale : de quelques lieux communs de l’acoustique à une première maîtrise des champs sonores”, *Presses Polytechniques et Universitaires Romandes*, Italie, 2007.
- [MEH91] Mehdigholi, H., “Forced vibration of a rotating discs and interaction with non-rotating structures”, PhD, University of London, 1991.
- [MOU14] Mounetou, A., Talon, A., Colette, C., “Non-intrusive measurement of gear dynamic response”, *International gear conference*, p1029-1037, vol. 2, Lyon, 26th-28th August 2014.
- [MUN89] Munro R.G., “The D. C. component of gear transmission error”, Proc. 1989 *International Power Transmission and gearing conference*, p467-470, Chicago 1989.
- [MUN99] Munro, R.G., Morrish, L., Palmer, D., “Gear transmission error outside the normal path of contact due to corner and top contact”, *Proceedings of the Institution of Mechanical Engineers*, 213:389-400, 1999.
- [NOG09] Noga, S.: “Transverse vibration of a gear wheel”, *Scientific Bulletin*, XXIII(C):137-142, North University of Baia Mare Publishers, Baia Mare, 2009.
- [ODA84.a] Oda, S., Miyachika, K., “Effects of key on bending fatigue breakage of thin-rimmed spur gear”, *Bulletin of JSME*, 27(232):2279-2286, 1984.
- [ODA84.b] Oda, S., Miyachika, K., “Effects of rim thickness on root stress and bending fatigue strength of internal gear tooth”, *Bulletin of JSME*, 27(230):1759-1764, 1984.
- [ODA85] Oda, S., Koide, T., Miyachika, K., “Dynamic behaviour of thin-rimmed helical gears with various web arrangements”, *Bulletin of JSME*, 28(244):2434-2441, 1985.
- [ODA86.a] Oda, S., Miyachika, K., Sayama, T., Koide, T., Mizune, M., “Stress analysis of thin-rimmed spur gears by boundary element method”, *Bulletin of JSME*, 29(248):593-599, 1986.
- [ODA86.b] Oda, S., Miyachika, K., Sayama, T., “Effects of rim and web thicknesses on bending fatigue strength of internal gear”, *Bulletin of JSME*, 29(248):586-562, 1986.

-
- [ODA86.c] Oda, S., Miyachika, K., Koide, T., Fujii, T., “Dynamic behaviour of thin-rimmed spur gears with various web arrangements”, *Bulletin of JSME*, 29(247):241-248, 1986.
- [ODA87] Oda, S., Miyachika, K., “Root stress of thin-rimmed internal spur gear supported with pins”, *JSME International Journal*, 30(262):646-652, 1987.
- [OSM10] Osman, T., Velez, P., “Static and dynamic simulations of mild abrasive wear in wide-faced solid spur and helical gears”, *Mechanism and Machine Theory*, 45:911-924, 2010.
- [OSM12] Osman, T., Velez, P., “ A model for the simulation of the interactions between dynamic tooth loads and contact fatigue in spur gears”, *Tribology International*, 46:84-96, 2012.
- [OZG88.a] Özgüven, H.N., Houser, D.R., “Mathematical models used in gear dynamics – a review”, *Journal of Sound and Vibration*, 121(3):383-411, 1988.
- [OZG88.b] Ozgüven, H.N., Houser, D.R., “Dynamic analysis of high speed gear by using loaded static transmission error”, *Journal of Sound and Vibration*, 125(1):71-83, 1988.
- [PAR00.a] Parker, R.G., Vijayakar, S.M., Imajo, T., “Non-linear dynamic response of a spur gear pair: modelling and experimental comparisons”, *Journal of Sound and Vibration*, 237(3):435-455, 2000.
- [PAR00.b] Parker, R.G., Agashe, V., Vijayakar, S.M., “Dynamic response of a planetary gear system using a finite element/contact mechanics model”, *Journal of Mechanical Design*, ASME, 122:304-310, 2000.
- [PUS11] Pust, L. Pesek, L. “Vibration of imperfect rotating disk”, *Applied and Computational Mechanics*, 5:206-216, 2011.
- [REM98] Remond, D., “Practical performances of high-speed measurement of gear transmission error or torsional vibrations with optical encoders”, *Measurement in Science and Technology*, 9:347-353, 1998.
- [RIG96] Rigaud, E., and Sabot, J., “Effect of elasticity of shafts, bearings, casing and couplings on the critical rotational speeds of a gearbox,” *VDI Berichte*, pp. 833–845, 1996.

- [RIG99] Rigaud, E., Barday, D., “Modelling and analysis of static transmission error – effect of wheel body deformation and interaction between adjacent loaded teeth”, p.1961-1972, 1999.
- [SAI04] Sainsot, P., Velex, P., Duverger, O., “Contribution of gear body to tooth deflections- A new bidimensional analytical formula”, *Journal of Mechanical Design, ASME*, **126(4)**, 748-752, 2004.
- [SAY08] El-Sayed, A. F., “Aircraft propulsion and gas turbine engines”, Zagazig University, Egypt, CRC Press, Taylor & Francis Group, 2008, ISBN: 978-0-8493-9196-5.
- [SCH97] Schmiechen, P., “Travelling Wave Speed Coincidence”, PhD, University of London, 1997.
- [SIN08] Singh, A. Kahraman, A., Ligata, H. “Internal gear strains and load sharing in planetary transmissions: model and experiments”, *Journal of Mechanical Design, ASME*, 130(072602):1-10, 2008
- [STM17] Sainte-Marie, N., Velex, P., Roulois, G., Caillet, J., “A study on the correlation between dynamic transmission error and dynamic tooth loads in spur and helical gears”, *Journal of Vibration and Acoustics*, 139(011001):1-10, 2017.
- [SUZ86] Suzuki, T., Umezawa, K., Houjoh, H., Bagiasna, K., “Influence of misalignment on vibration of helical gears”, *Transaction of the Japan Society of Mechanical Engineers*, 52(447):1595-1600, 1986.
- [TAM07] Tamminana, V.K., Kahraman, A., Vijayakar, S., “A study of the relationship between the dynamic factors and the dynamic transmission error of spur gear pairs”, *Journal of Mechanical Design, ASME*, 129:75-84, 2007.
- [TAV86] Tavakoli, M.S., Houser, D.R., “Optimum profile modification for the minimization of static transmission errors of spur gears”, *Journal of Mechanisms, Transmissions, and Automation in Design, ASME*, 108(1):86-94, 1986.
- [TIM55] Timoshenko, S., “Strength of materials, Part I. Elementary theory and problems”, 3rd Edition, Van Nostrand, New York, p. 442, 1955.

-
- [TRA15] Tran, D.H., Réduction de modèle en dynamique des structures et des systèmes couplés aéroélastiques, HDR, INSA Lyon & Université Claude Bernard Lyon I, 2015.
- [TUP50] Tuplin, W.A., “Gear tooth stresses at high speed”, *Proceedings of the Institution of Mechanical Engineers*, 16:162-167, 1950.
- [UED17] Ueda, A., Kubo, A., Matsuoka, H., Watanabe, J., Miyazaki, M., “Explores for the origin of gears in traditional Japanese clock (Wadokei)”, *JSME International Conference on Motion and Power Transmission*, Kyoto, 28th Feb – 3rd March 2017,
- [UME85] Umezawa, K., Suzuki, T., Houjoh, H., Sato, T., “Vibration of power transmission helical gears : (the effect of contact ratio on the vibration)”, *JSME*, 238-18, 1985
- [VEL06] Velex, P., and Ajmi, M., “On the modelling of excitations in geared systems by transmission errors”, *Journal of Sound and Vibration*, 290:882-909, 2006.
- [VEL07] Velex, P., and Ajmi, M., “Dynamic tooth loads and quasi-static transmission errors in helical gears – Approximate dynamic factor formulae”, *Mechanism and Machine Theory*, 42:1512-1526, 2007.
- [VEL09] Velex, P., “On the relationship between gear dynamics and transmission errors”, *Proceedings of MPT2009-Sendai*, Matsushima Isles Resort, Japan, May 13th-15th 2009.
- [VEL11] Velex, P., Bruyère, J., Houser, D.R., “Some analytical results on transmission errors in narrow-faced spur and helical gears: Influence of profile modifications”, *Journal of Mechanical Design*, 133(031010):1-11, 2011, DOI:101115/1.4003578.
- [VEL16] Velex, P., Chapron, M., Fakhfakh, H., Bruyère, J., Becquerelle, S., “On transmission errors and profile modifications minimising dynamic tooth load in mutli-mesh gears”, *Journal of Sound and Vibration*, 379:28-52, 2016.
- [VEL16] Velex, P., Chapron, M., Fakhfakh, H., Bruyère, J., Becquerelle, S., “On transmission errors and profile modifications minimising dynamic tooth load in mutli-mesh gears”, *Journal of Sound and Vibration*, 379:28-52, 2016.
- [VEL88] Velex P. “Contribution à l’analyse du comportement dynamique de réducteurs à engrenages à axes parallèles”, Thèse de doctorat, INSA de Lyon, 1988.

- [VEL89] Vexlex, P., Berthe, D., “Dynamic tooth load on geared train”, Proceedings of the 1989 *International Power Transmission and Gearing Conference, ASME*, Chicago, Illinois, April 25-28, 1989, vol1:447-454, 1989.
- [VEL96] Vexlex, P., Maatar, M., “A mathematical model for analysing the influence of shape deviation and mounting errors on gear behaviour”, *Journal of sound and vibration*, 191:629-660, 1996, DOI:10.1006/jsvi.1996.0148.
- [WAN80] Wang, K., “Thermal elastohydrodynamic lubrication of spur gears,” PhD Thesis, Northwestern University, 1980.
- [WEB49] Weber, C., “The deformations of loaded gears and the effects on their load carrying capacity”, *British Dept. of Scientific and Industrial Research*, Sponsored Research (Germany), Report no. 3, 1949.
- [WEB53] Weber, C., Banaschek, K., “Formänderung und Profilrücknahme bei Gerad-und Schrägverzahnten Antriebstechnik”, Vieweg, Braunschweig, **11**, 1953.
- [WEI11] Wei, J., Sun, W., Wang, L., “Effect of flank deviation on load distributions for helical gear”, *Journal of Mechanical Science and Technology*, 25(7):1781—1789, 2011.
- [WEN98] Wensing J.A., On the dynamic of ball bearings, Ph.D., University of Twente, Enschede, The Netherlands, 1998.
- [WOO59] Wood, B., “Sources of vibration excitation in spur gears,” PhD Thesis, University of Leeds, 1959.
- [ZHO14] Zhou, J., Sun, W., and Tao, Q., “Gearbox Low-Noise Design Method Based on Panel Acoustic Contribution,” *Mathematical Problems in Engineering*, pp. 1–10, 2004.

Annexes

1. Shaft Element – Beam Matrices

The beam elements rely on Timoshenko beam theory [TIM55]. Each element is composed of two nodes (Figure 1) with 6 degrees-of-freedom each (three translations and three rotations).

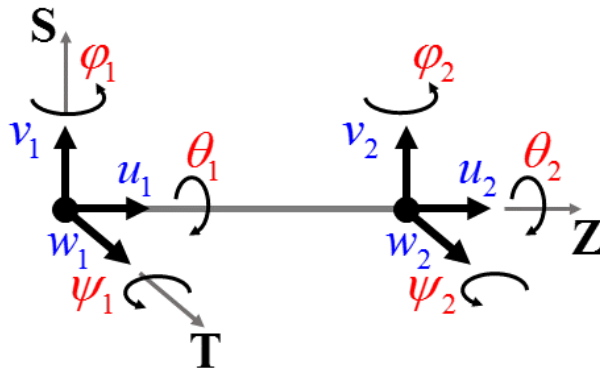


Figure 1: Shaft element - Beam definition

The element takes into account the effect of traction/compression, torsion, bending effect in both **S** and **T** direction as well as shear effect on bending (Timoshenko's beam properties). The resulting matrices are decoupled, each applying on separated DOFs of the beam, and can be super-imposed as follow:

$$\begin{aligned}\mathbf{K}_{shaft} &= \mathbf{K}_{tc} + \mathbf{K}_{Tor} + \mathbf{K}_{Bs} + \mathbf{K}_{Bt} \\ \mathbf{M}_{shaft} &= \mathbf{M}_{tc} + \mathbf{M}_{Tor} + \mathbf{M}_{Bs} + \mathbf{M}_{Bt}\end{aligned}\quad (1.1)$$

With indexes *tc* : traction, *Tor* : torsion, *Bs* and *Bt* flexure effect respectively in **S**, **T** and the resulting matrices developed bellow.

a. Traction / Compression

$$\mathbf{M}_{tc} = \frac{\rho SL}{6} \begin{bmatrix} 2 & 1 \\ 1 & 2 \end{bmatrix} \rightarrow \begin{Bmatrix} u_1 \\ u_2 \end{Bmatrix}\quad (1.2)$$

$$\mathbf{K}_{tc} = \frac{ES}{L} \begin{bmatrix} 1 & -1 \\ -1 & 1 \end{bmatrix} \rightarrow \begin{Bmatrix} u_1 \\ u_2 \end{Bmatrix}\quad (1.3)$$

With ρ density, S beam section, L beam length and E material Young modulus.

b. Torsion

$$\mathbf{M}_{Tors} = \frac{I_\theta L}{6} \begin{bmatrix} 2 & 1 \\ 1 & 2 \end{bmatrix} \rightarrow \begin{Bmatrix} \theta_1 \\ \theta_2 \end{Bmatrix} \quad (1.4)$$

With I_θ beam polar inertia.

$$\mathbf{K}_{Tors} = \frac{GJ}{L} \begin{bmatrix} 1 & -1 \\ -1 & 1 \end{bmatrix} \rightarrow \begin{Bmatrix} \theta_1 \\ \theta_2 \end{Bmatrix} \quad (1.5)$$

With

$$I_\theta = \rho L J \text{ beam polar inertia, } J = 2I, \text{ with } I = \pi \frac{D_{ext}^4 - d_{int}^4}{64}$$

$$G \text{ shear modulus : } G = \frac{E}{2(1+\nu)}.$$

c. Bending

$$\mathbf{M}_{Bs} = \frac{\rho S L}{420} \begin{bmatrix} 156 & 22L & 54 & -13L \\ & 4L^2 & 13L & -3L^2 \\ & & 156 & -22L \\ sym & & & 4L^2 \end{bmatrix} \rightarrow \begin{Bmatrix} v_1 \\ \phi_1 \\ v_2 \\ \phi_2 \end{Bmatrix} \quad (1.6)$$

$$\mathbf{M}_{Bt} = \frac{\rho S L}{420} \begin{bmatrix} 156 & 22L & 54 & -13L \\ & 4L^2 & 13L & -3L^2 \\ & & 156 & -22L \\ sym & & & 4L^2 \end{bmatrix} \rightarrow \begin{Bmatrix} w_1 \\ \psi_1 \\ w_2 \\ \psi_2 \end{Bmatrix} \quad (1.7)$$

$$\mathbf{K}_{Bs} = \frac{EI_x}{(1+\alpha)L^3} \begin{bmatrix} 12 & 6L & -12 & 6L \\ & (4+\alpha)L^2 & -6L & (2-\alpha)L^2 \\ & & 12 & -6L \\ sym & & & (4+\alpha)L^2 \end{bmatrix} \rightarrow \begin{Bmatrix} v_1 \\ \phi_1 \\ v_2 \\ \phi_2 \end{Bmatrix} \quad (1.8)$$

$$\mathbf{K}_{Bt} = \frac{EI_x}{(1+\alpha)L^3} \begin{bmatrix} 12 & 6L & -12 & 6L \\ & (4+\alpha)L^2 & -6L & (2-\alpha)L^2 \\ & & 12 & -6L \\ sym & & & (4+\alpha)L^2 \end{bmatrix} \rightarrow \begin{Bmatrix} v_1 \\ \phi_1 \\ v_2 \\ \phi_2 \end{Bmatrix} \quad (1.9)$$

With $I_x = \rho L I$ transverse beam inertia, and $\alpha = \frac{12EI_x}{GL^2 S}$ influence coefficient of shear on bending deflection.

2. Newmark Integration Scheme

Newmark time-step integration scheme is often used for system resolution in dynamics. It remains on third order Taylor development of displacement vector $\mathbf{q}_{t+\Delta t}$ at time-step $t + \Delta t$, giving the following expression for both displacement and speed vector:

$$\begin{aligned}\mathbf{q}_{t+\Delta t} &= \mathbf{q}_t + \Delta t \dot{\mathbf{q}}_t + \frac{\Delta t^2}{2} \ddot{\mathbf{q}}_t + \beta \ddot{\mathbf{q}}_t \\ \dot{\mathbf{q}}_{t+\Delta t} &= \dot{\mathbf{q}}_t + \Delta t \ddot{\mathbf{q}}_t + \gamma \ddot{\mathbf{q}}_t\end{aligned}\quad (2.1)$$

With \mathbf{q} DOF vector, t previous time-step and $t + \Delta t$ in calculation time-step.

The acceleration derived is considered linear between two time-steps:

$$\ddot{\mathbf{q}}_{t+\Delta t} = \ddot{\mathbf{q}}_t + \Delta t \ddot{\ddot{\mathbf{q}}}_t \Rightarrow \ddot{\ddot{\mathbf{q}}}_t = \frac{\ddot{\mathbf{q}}_{t+\Delta t} - \ddot{\mathbf{q}}_t}{\Delta t} \quad (2.2)$$

Giving the following equation when put back into eq. 2.1.

$$\begin{aligned}\mathbf{q}_{t+\Delta t} &= \mathbf{q}_t + \Delta t \dot{\mathbf{q}}_t + \left(\frac{1}{2} - \beta\right) \Delta t^2 \ddot{\mathbf{q}}_t + \beta \Delta t^2 \ddot{\mathbf{q}}_{t+\Delta t} \\ \dot{\mathbf{q}}_{t+\Delta t} &= \dot{\mathbf{q}}_t + (1 - \gamma) \Delta t \ddot{\mathbf{q}}_t + \gamma \Delta t \ddot{\mathbf{q}}_{t+\Delta t}\end{aligned}\quad (2.3)$$

With β and γ ponderation coefficients. They are defined for the system unconditional stability, usually $\beta = 0.25$ and $\gamma = 0.5$ are used [GER93].

Taking back the system matrices and its full definition, it can be written at $t + \Delta t$ under the following expression:

$$\mathbf{M} \ddot{\mathbf{q}}_{t+\Delta t} + \mathbf{C} \dot{\mathbf{q}}_{t+\Delta t} + \mathbf{K} \mathbf{q}_{t+\Delta t} = \mathbf{F}_{t+\Delta t} \quad (2.4)$$

With $\mathbf{M}, \mathbf{C}, \mathbf{K}$ global matrices of the system and $\mathbf{F}_{t+\Delta t}$ the time dependant 2nd member vector which is known at $t + \Delta t$.

Expressing acceleration and speed at $t + \Delta t$ by displacement by introducing eq. 2.3 into 2.4:

$$\begin{aligned}\left[\frac{1}{\beta \Delta t^2} \mathbf{M} + \frac{\gamma}{\beta \Delta t} \mathbf{C} + \mathbf{K} \right] \mathbf{q}_{t+\Delta t} &= \mathbf{F}_{t+\Delta t} \\ + \mathbf{M} \left[\left(\frac{1}{2\beta} - 1 \right) \ddot{\mathbf{q}}_t + \frac{1}{\beta \Delta t} \dot{\mathbf{q}}_t + \frac{1}{\beta \Delta t^2} \mathbf{q}_t \right] & \\ + \mathbf{C} \left[\left(\frac{\gamma}{\beta} \left(\frac{1}{2} - \beta \right) + \gamma - 1 \right) \Delta t \ddot{\mathbf{q}}_t - \left(1 - \frac{\gamma}{\beta} \right) \dot{\mathbf{q}}_t + \frac{\gamma}{\beta \Delta t} \mathbf{q}_t \right] &\end{aligned}\quad (2.5)$$

With:

$$\begin{aligned}\dot{\mathbf{q}}_{t+\Delta t} &= \frac{\gamma}{\beta} \left(\frac{\mathbf{q}_{t+\Delta t} - \mathbf{q}_t}{\Delta t} \right) + \left(1 - \frac{\gamma}{\beta} \right) \dot{\mathbf{q}}_t + \left(1 - \gamma - \frac{\gamma}{\beta} \left(\frac{1}{2} - \beta \right) \right) \Delta t \ddot{\mathbf{q}}_t \\ \ddot{\mathbf{q}}_{t+\Delta t} &= \left[(\mathbf{q}_{t+\Delta t} - \mathbf{q}_t) - \Delta t \dot{\mathbf{q}}_t - \left(\frac{1}{2} - \beta \right) \Delta t^2 \ddot{\mathbf{q}}_t \right] \cdot \frac{1}{\beta \Delta t^2}\end{aligned}\tag{2.6}$$

Practically, the calculation is achieved by calculating $\mathbf{q}_{t+\Delta t}$ by solving the equation 2.5 fully written in terms of displacement, speed and acceleration at time-step t . Then the terms of speed and acceleration are calculated thanks to eq. 2.6, leading to the full system expression ($\mathbf{q}_{t+\Delta t}, \dot{\mathbf{q}}_{t+\Delta t}, \ddot{\mathbf{q}}_{t+\Delta t}$) in $t + \Delta t$ in terms of its components at t .

Résumé Etendu en Français

This thesis has been written in English. Therefore, an extended summary, translated in French, is presented below. It describes the main work and results of the research.

Ce manuscrit de thèse a été rédigé en Anglais. Un résumé étendu contenant la description des principaux travaux et résultats est présenté ci-dessous.

1. Introduction

Les boîtes de transmission par engrenages des moteurs d'hélicoptère convoient la puissance mécanique du turbomoteur aux accessoires (pompes, démarreur) et au rotor. Leur conception dépend des nécessités des équipements embarqués, en particulier l'allègement pour réduire la consommation en carburant. Les engrenages haute-vitesse de la transmission sont allégés grâce à des enlèvements de matière dans les corps sous la denture, les voiles-minces.

La nouvelle flexibilité de ces engrenages nécessite le développement de nouveaux outils capables d'intégrer à la fois la modélisation dynamique couplée des vibrations issues du passage des dents de l'engrenage et le comportement statique et modal de ces roues à voiles-minces. Les travaux de recherche présentés dans ce manuscrit ont pour but le développement d'un modèle hybride intégrant l'ensemble des effets évoqués plus haut afin de réaliser une simulation réaliste haute-vitesse des vibrations d'une transmission d'hélicoptère.

2. Revue Bibliographique

2.1. Paramètres Principaux de Réponse des Engrenages

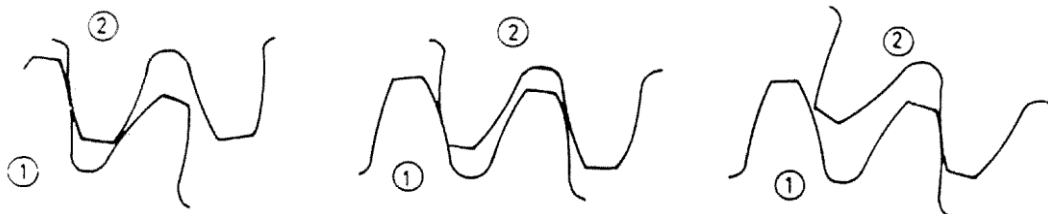


Figure 2: Engrenement, illustration du nombre de dents en prises

La principale source d'excitation de l'engrenage vient du passage des dents au contact (Figure 2). La raideur résultante varie en fonction du nombre de dents en prise à chaque instant.

Il existe plusieurs méthodes possibles pour calculer cette raideur. Elles intègrent de façon différente l'ensemble des raideurs de denture, le contact direct entre les dents, la flexion de ces dents au contact, et la fondation, résultant de la rotation de la base.

La seconde source provient des écarts de formes et de montage auxquels peuvent être soumis l'engrenage. Les premiers sont par exemple des déviations de profils ou d'hélice, pour lesquels les profils parfaits des plans de définition ont été altérés par les processus de manufacture. Les écarts de montage peuvent eux prendre la forme de désalignements. L'ensemble de ces déviations perturbent les contacts, introduisant une autre source d'excitation dans l'engrenage.

L'engrenage en fonctionnement est caractérisé par des paramètres de réponse particuliers. Le premier est l'erreur de transmission, dont la notion a été introduite par [HAR58]. Elle est définie à partir « d'une position instantanée d'une des roues, comme étant le déplacement angulaire de la dent au contact depuis la position qu'elle occuperait si les dents étaient rigides et non modifiées ». Harris a été le premier à établir que les variations de l'erreur de transmission à faible vitesse étaient responsables des vibrations de l'engrenage à un régime plus élevé.

Un autre paramètre courant est le coefficient dynamique représentant la charge à la denture normalisée par la charge statique transmise par l'engrenage. Son maximum permet généralement d'estimer les vitesses critiques de l'engrenage (Figure 3).

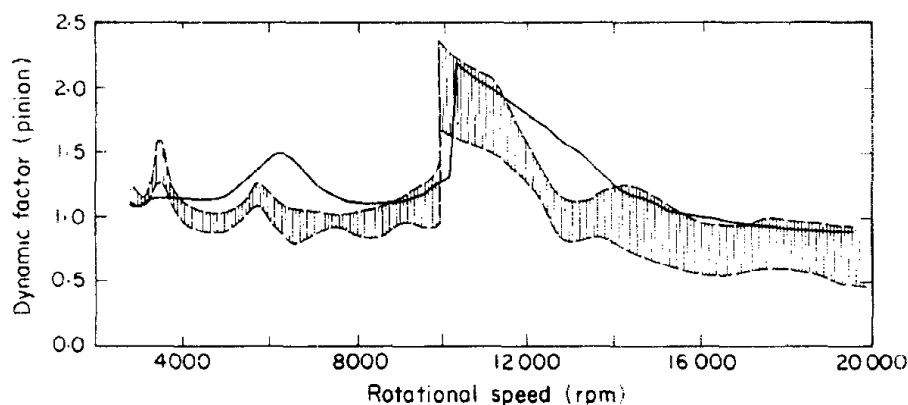


Figure 3: Comparaison des résultats expérimentaux de Kubo [KUB72] et les prédictions numériques selon [OZG88]

2.2. Modèles de Dynamique des Engrenages

L'historique et les évolutions des modèles de dynamique des engrenages au cours du temps sont très bien décrits par la revue de Ozgüven et Houser [OZG88]. Les modèles les plus simples sont limités à des représentations rigides du pignon et de la roue, connectés par la raideur d'engrènement. Les éléments secondaires étant limités, ils sont négligés ou mis sous forme de raideurs additionnelles.

Tuplin [TUP50] a mis au point le premier véritable modèle de dynamique d'engrenage, avec une raideur d'engrènement constante et des fonctions variables à la base des ressorts pour la représentation des écarts. Ce modèle était limité aux vitesses en dessous des résonances.

Ces types de modèles ont ensuite été améliorés pour la prise en compte des variations dans la raideur d'engrènement. Harris [HAR58] a développé un modèle à un seul degré de liberté qui intègre les déviations comme sources d'excitation par l'erreur de transmission. D'autres modèles ont conservé une raideur d'engrènement constante en intégrant les excitations générées par l'erreur de transmission quasi-statique comme un terme forcé dans les données d'entrée.

Puis, les comportements dynamiques des éléments adjacents ont été ajoutés. Des modèles à plusieurs degrés de liberté ont été mis au point [KOH70]. Plus tard, Velez et Berthe [VEL89], Karahaman *et al.* [KAH92] ont mis au point des modèles basés sur une discrétisation éléments finis des arbres avec une modélisation de la raideur d'engrènement constante ou variable. Velez [VEL96-BAU02-AJM05] a ensuite introduit la notion d'erreur de transmission comme un résultat du problème et non plus comme une donnée d'entrée. Pour ce faire, le problème de contact est résolu à chaque pas de temps, en discrétisant les lignes de contact avec une raideur d'engrènement élémentaire pour chaque cellule.

2.3. Cas des Engrenages à Voiles-minces

Les modèles précédents ont tous en commun l'utilisation des corps d'engrenages rigides. Ils ne sont plus suffisants pour prendre en compte les roues amincies d'aéronautique : c'est l'objet d'études récentes.

Parker et Vijayakar ont développé un modèle d'engrenage droit en 2D qui combine des éléments finis avec un modèle de contact analytique [PAR00]. Parker et Cooley [COO14-15] ont introduit un anneau flexible sur une fondation élastique pour conserver un modèle à paramètres concentrés. Il permet la visualisation des modes à diamètres, particuliers aux roues à voiles-minces en rotation.

Avec une approche différente, Abouslieman *et al.* [ABO05-07] et Bettaieb *et al.* [BET06-07] ont utilisé la méthode de Ritz de réduction modale pour diminuer de nombre de degrés de liberté de la roue EF. Cette méthode permet la résolution du système à paramètres concentrés en intégrant la flexibilité de la roue. Les résultats montrent que la flexibilité du corps de roue altère la charge dynamique. D'autres modèles offrent une description détaillée de la roue par EF: elle seule est soumise aux charges et déformations de l'engrènement. La Figure 4 en montre deux exemples.

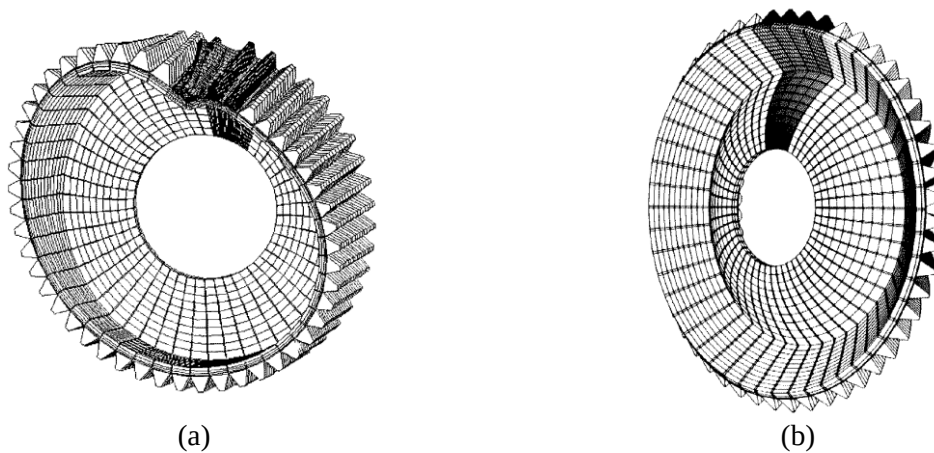


Figure 4: Modèle EF pour (a) la charge à l'engrènement et (b) effets centrifuges [LI02-08.a]

3. Présentation du Modèle Hybride d'Engrènement

3.1. Modèle de Dynamique d'Engrenage

Le modèle de dynamique d'engrenage considéré est issu du modèle de Vexel et Maatar [VEL96] pour les engrenages rigides. C'est un modèle à paramètres concentrés, avec des arbres en poutres de Timoshenko [TIM55] et des paliers et carters en raideurs additionnelles. Les engrenages à corps rigides (Figure 5.a) sont représentés chacun avec un nœud central et 6 degrés de liberté (3 translations et 3 rotations). Hypothèse est faite que tous les points de contact entre les dentures sont situés sur les lignes de contact du plan d'action. Celui-ci est discrétisé en cellules élémentaires décrites Figure 5.b. La raideur d'engrènement instantanée est calculée en affectant des raideurs élémentaires, calculées analytiquement avec le modèle de Weber et Banaschek [WEB53] à chaque cellule en contact.

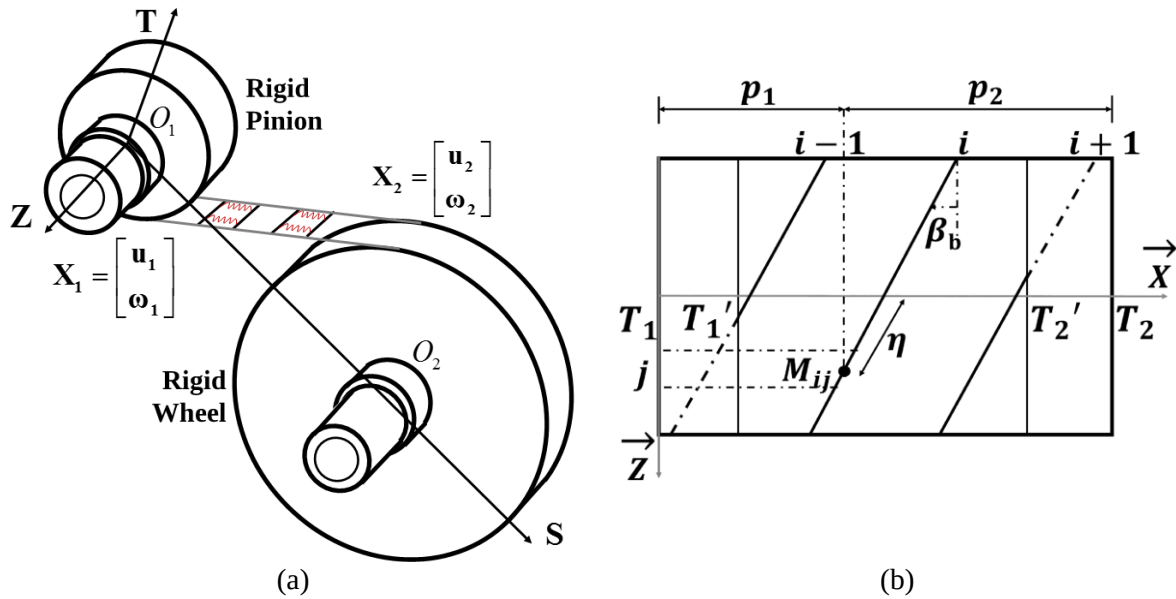


Figure 5: (a) Elément d'engrenage et (b) plan d'action discretisé associé

La déflexion normale à la denture peut être écrite pour toutes les cellules du plan d'action en fonction des degrés de liberté associés à chaque roue d'engrenage: degrés de liberté aux centres du pignon et de la roue.

$$\Delta(M_{ij}) = \begin{bmatrix} \mathbf{n}_1 \\ \mathbf{n}_1 \times \mathbf{M}_{ij} \mathbf{O}_1 \\ \mathbf{n}_2 \\ \mathbf{n}_2 \times \mathbf{M}_{ij} \mathbf{O}_2 \end{bmatrix}^T \begin{bmatrix} \mathbf{u}_1(O_1) \\ \boldsymbol{\omega}_1 \\ \mathbf{u}_2(O_2) \\ \boldsymbol{\omega}_2 \end{bmatrix} - \delta_0(M_{ij}) \quad (1)$$

Avec $\mathbf{X} = \{\mathbf{u}_1(O_1) \quad \boldsymbol{\omega}_1 \quad \mathbf{u}_2(O_2) \quad \boldsymbol{\omega}_2\}^T$ Degrés de libertés aux centres du pignon et de la roue.

Le modèle est modifié pour intégration de la roue flexible dans l'élément engrenage. Pour cela, le nœud central de la roue est remplacé par un modèle EF (Figure 6.a) condensé par la technique de sous-structuration sur les nœuds de la jante et aux paliers (Figure 6.b). La sous-structuration réduit la taille d'un modèle EF en ne conservant que les degrés de libertés choisis. Elle modélise le comportement statique et modal de la roue jusqu'à une fréquence donnée. La sous-structuration à interfaces libres de Herting [HER85] est utilisée ici.

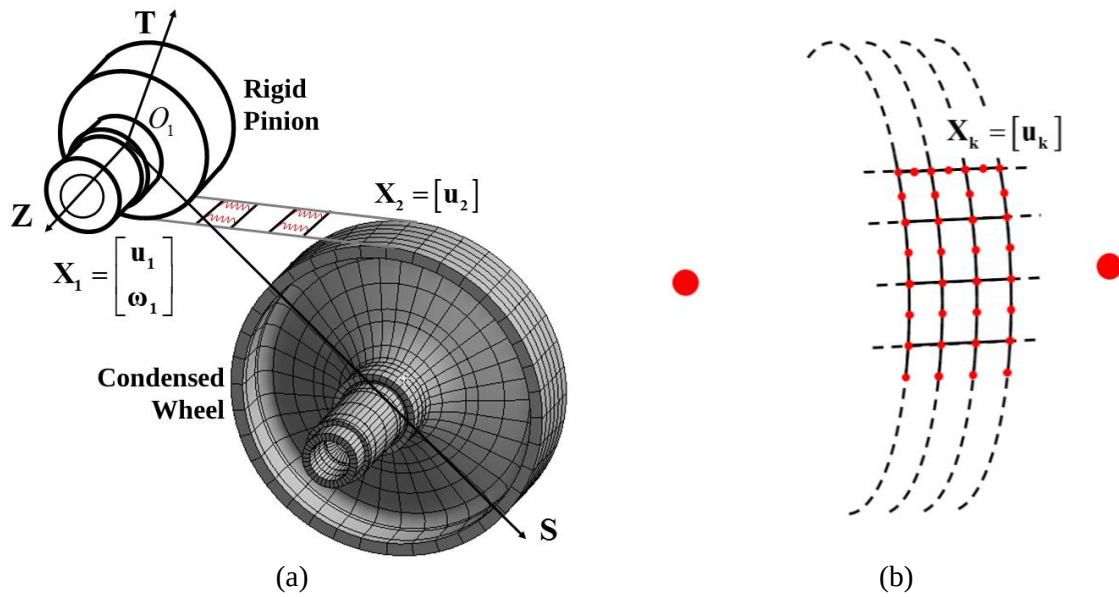


Figure 6: Modèle hybride d'engrenage avec roue flexible

Pour éviter les incompatibilités dues au passage des lignes de contact discrètes aux éléments finis continus de jante de roue, le lien entre le plan d'action et le modèle EF condensé nécessite un modèle élaboré des dents d'engrenage.

3.2. Modèle Hybride : Lien d'Interface

La dent est décomposée en tranches minces rigides suivant le plan d'action discrétisé. Chaque tranche M_{ij} est notée M dans la démonstration qui suit. Un point M_p (Figure 7.a) est introduit à l'intersection entre la fibre neutre de la dent et son rayon de pied. Les déplacements sur la ligne de contact sont transportés à ce point central et selon le modèle de tranche mince, seule la rotation en Z dans la direction axiale est conservée (notée ωZ).

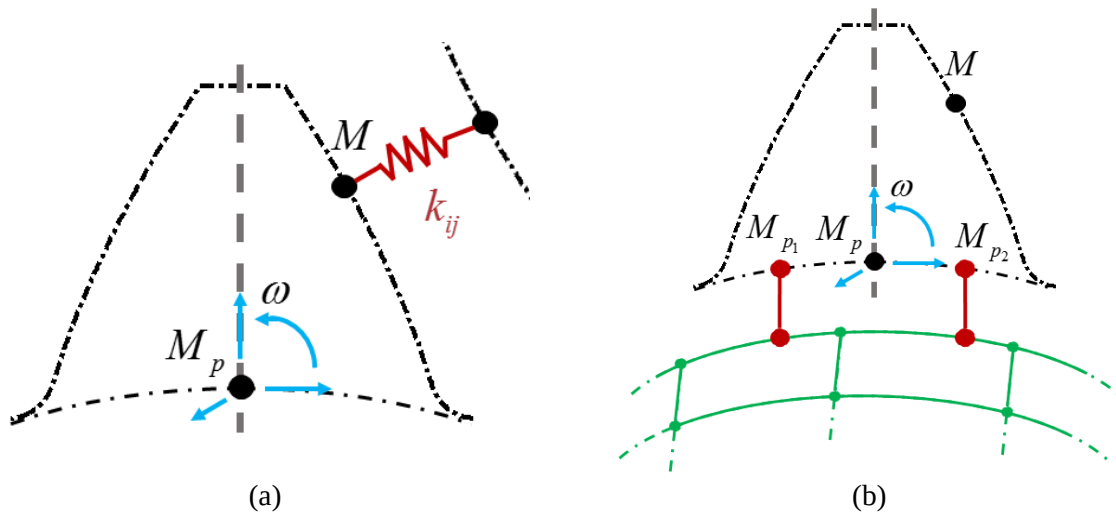


Figure 7: Schéma de la tranche mince de dent (a) seule et (b) avec les deux points pour attache à la jante EF (M_{ij} étant noté M)

Les degrés de liberté des éléments finis sous la dent (Figure 7.b) n'étant que des translations, le lien avec le point M_p ne peut pas être fait directement. La connexion est établie en deux points M_{p_1} et M_{p_2} ne possédant que des ddls de translation. La formulation approximée utilisée s'appuie sur la minimisation de la différence entre les déplacements exacts et approximatifs reliant le point M_p aux points M_{p_1} et M_{p_2} . Les déplacements de M_p s'écrivent :

$$\begin{aligned} \mathbf{u}(M_p) &\approx \frac{1}{2}(\mathbf{u}(M_{p_1}) + \mathbf{u}(M_{p_2})) \\ \omega &\approx \frac{1}{2(\|\mathbf{M}_{p_1}\mathbf{M}_p\|^2 + \|\mathbf{M}_{p_2}\mathbf{M}_p\|^2)} \left[(\mathbf{u}(M_{p_1}) - \mathbf{u}(M_{p_2})) \cdot (\mathbf{M}_{p_1}\mathbf{M}_{p_2} \times \mathbf{Z}) \right] \end{aligned} \quad (2)$$

Avec \mathbf{u} déplacements en translation et ω rotation de M_p .

La déflexion normale à la denture s'écrit avec les translations aux points M_{p_1} et M_{p_2} .

$$\Delta(M) = [\mathbf{n}_1, \mathbf{n}_1 \times \mathbf{M}\mathbf{O}_1, \frac{1}{2}\mathbf{n}_2^T + \lambda_p(M)\boldsymbol{\kappa}_p, \frac{1}{2}\mathbf{n}_2^T - \lambda_p(M)\boldsymbol{\kappa}_p]^T \begin{bmatrix} \mathbf{u}(O_1) \\ \boldsymbol{\omega}_1 \\ \mathbf{u}_1 \\ \mathbf{u}_2 \end{bmatrix} - \delta_0(M) \quad (3)$$

Avec :

$$\lambda_p(M) = \mathbf{Z} \cdot (\mathbf{M}_p \mathbf{M} \times \mathbf{n}_2), \quad \boldsymbol{\kappa}_p = \frac{\mathbf{M}_{p_1}\mathbf{M}_{p_2} \times \mathbf{Z}}{2(\|\mathbf{M}_{p_1}\mathbf{M}_p\|^2 + \|\mathbf{M}_{p_2}\mathbf{M}_p\|^2)} \quad \text{et} \quad \mathbf{n}_2 = -\mathbf{n}_1$$

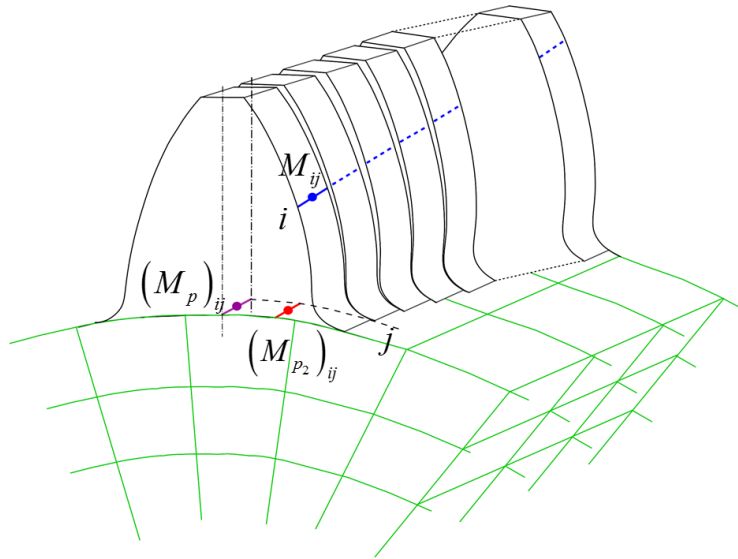


Figure 8: Modèle de dents à tranches minces pour l'ensemble de la dent et représentation sur la roue EF (en vert)

La ligne de contact discrétisée et transférée sur les deux points en pied de dent est incompatible avec les éléments finis quadratiques et continus de la jante : des pics dans la distribution de charge locale apparaissent. La technique de mortier [BEL97] est utilisée pour passer d'une modélisation discontinue de ligne de contact avec un nœud central pour chaque segment à une modélisation intermédiaire intégrant en plus de ce nœud central des nœuds aux extrémités de chaque segment : ils présentent une représentation quadratique plus continue compatible avec les EF de la jante (Figure 9).

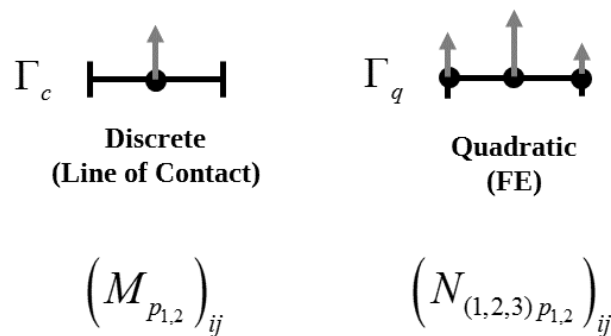


Figure 9: Evolution de la discrétisation du segment de la ligne de contact

La conservation du travail moyen sur le segment est traduite par une approximation. Les équivalences entre les différentes discrétisations sont décrites grâce aux fonctions de formes polynomiales associées à chaque discrétisation. Finalement, l'approximation entre les

déplacements sur les points des lignes en pied de dents discrétisées s'écrit en fonction des déplacements aux nœuds des éléments des lignes quadratiques :

$$\mathbf{u}(M_{p_{1,2}})_{ij} = [\mathbf{N}] \mathbf{u}(N_{(1,2,3)p_{1,2}})_{ij} \quad (4)$$

Avec $[\mathbf{N}] = \begin{bmatrix} 5 & 20 & 5 & 0 & 0 & 0 & 0 & 0 & 0 \\ 0 & 0 & 0 & 5 & 20 & 5 & 0 & 0 & 0 \\ 0 & 0 & 0 & 0 & 0 & 0 & 5 & 20 & 5 \end{bmatrix}$.

Une fois ces problèmes de compatibilité résolus, les points des lignes quadratiques sont liés aux nœuds des éléments finis de jante par les fonctions de formes des éléments finis de briques réduits à la surface de ces éléments selon Dhatt [DHA81]. Le lien entre les lignes de contact et la roue EF est ainsi complet (eq. 5).

$$\Delta(M_{ij}) = \mathbf{V}^*(M)^T \mathbf{X}_m - \delta_0(M_{ij}) \quad (5)$$

Avec:

$$\mathbf{V}^*(M)^T = \left[\left\{ \mathbf{n}_1^T \quad (\mathbf{n}_1 \times \mathbf{M}\mathbf{O}_1)^T \right\} \right. \\ \left. \left\{ \left(\frac{1}{2} \mathbf{n}_2^T + \lambda_p(M) \boldsymbol{\kappa}_p \right) \mathbf{I}_{\text{int}}^T \quad \left(\frac{1}{2} \mathbf{n}_2^T - \lambda_p(M) \boldsymbol{\kappa}_p \right) \mathbf{I}_{\text{int}}^T \right\} \right]$$

$$\lambda_p(M) = \mathbf{Z} \cdot (\mathbf{M}_p \mathbf{M} \times \mathbf{n}_2)$$

$$\boldsymbol{\kappa}_p = \frac{\mathbf{M}_{p_1} \mathbf{M}_{p_2} \times \mathbf{Z}}{2 \left(\|\mathbf{M}_{p_1} \mathbf{M}_p\|^2 + \|\mathbf{M}_{p_2} \mathbf{M}_p\|^2 \right)}$$

M , M_{p_1} et M_{p_2} pour M_{ij} , M_{ij,p_1} et M_{ij,p_2} pour chaque tranche de dent

$\mathbf{X}_m = \{ \mathbf{u}_1(O_1) \quad \boldsymbol{\omega}_1 \quad \mathbf{X}_2 \}^T$ nouveaux vecteurs des DDLs avec \mathbf{X}_2 les degrés de liberté

des nœuds maîtres de la sous-structure

$$\mathbf{I}_{\text{int}} = \frac{1}{L} \mathbf{N} \mathbf{P} \left(N_{(1,2,3)p_{1,2}} \right)_{ij} \text{ termes de l'interface de mortier pour chaque } \left(N_{(1,2,3)p_{1,2}} \right)_{ij}$$

nouveau point au pied de dent après l'interface.

Cette procédure peut aussi être faite pour le pignon par symétrie dans le cas où le pignon et la roue sont tous les deux souples et condensés.

3.3. Intégration des Effets Dynamiques

La raideur instantanée d'engrènement est ensuite calculée par intégration.

$$\begin{aligned} [\mathbf{K}_{12}(t)] &= \sum_i \sum_j k_{ij} \mathbf{V}^*(M_{ij}) \mathbf{V}^*(M_{ij})^T \\ \mathbf{F}_{12}(t) &= \sum_i \sum_j k_{ij} \delta_0(t) \mathbf{V}^*(M_{ij}) \end{aligned} \quad (6)$$

L'amortissement est ajouté sous forme d'amortissement visqueux dépendant des modes et de leur participation énergétique selon Ankouni [ANK14-16] et Umezawa [UME85] ou, sous forme d'amortissement de Rayleigh par des coefficients multipliant les matrices de raideur et masse [CHO03]. Dans les composants flexibles condensés, les effets centrifuges prennent eux la forme d'un vecteur des efforts centrifuges. Il est démontré dans la partie 4 (Validation) que ces effets sur les paramètres du système et notamment sur les données engrenages sont négligeables.

Le modèle dynamique résultant est résolu par intégration temporelle grâce à un schéma de Newmark couplé à un algorithme de contact [VEL96] qui permet de prendre en compte les potentielles pertes de contact, partielles ou totales, provenant des vibrations dynamiques de l'engrenage.

4. Eléments de Validation Numérique et Expérimentale

Les validations du modèle sont faites pour les deux versions : H1: pignon rigide et roue condensée, H2 : pignon + roue condensés. Tout d'abord, les engrenages académiques sont rigidifiés par un haut module d'Young dans la sous-structure ($E = 4.10^{14} \text{ N} / \text{m}^2$). Puis les deux modèles sont comparés au modèle numérique précédemment développé et validé au LaMCoS [BAU02]. Enfin, la flexibilité des corps d'engrenages est étudiée.

La dernière validation a été faite sur une boîte industrielle d'engrenage par comparaison de données numériques et expérimentales.

4.1. Boîte Accessoire – Validation Numérique

La première validation du modèle est réalisée sur une transmission académique de boîte accessoire, dont les données sont détaillées Table 1. Le couple moteur du pignon est $T_m \approx 80 \text{ Nm}$.

	Pignon	Roue
Module m (mm)		1.5
Nombre de dents Z	45	86
Angle de pression ($^\circ$)		25.
Angle d'hélice ($^\circ$)		0
Coefficient de saillie		0.9447
Coefficient de creux		1.1933
Déport	0.341	0.481
Rayon fond de dent / module		0.25
Largeur de jante b (mm)	11.5	9.5

Table 1: Paramètres de définition de la boîte accessoire

Le pignon (Figure 10.a) est plein et possède un arbre non-symétrique. La roue est centrée sur son arbre et sur ses roulements, elle possède un voile-mince centré sous sa jante.

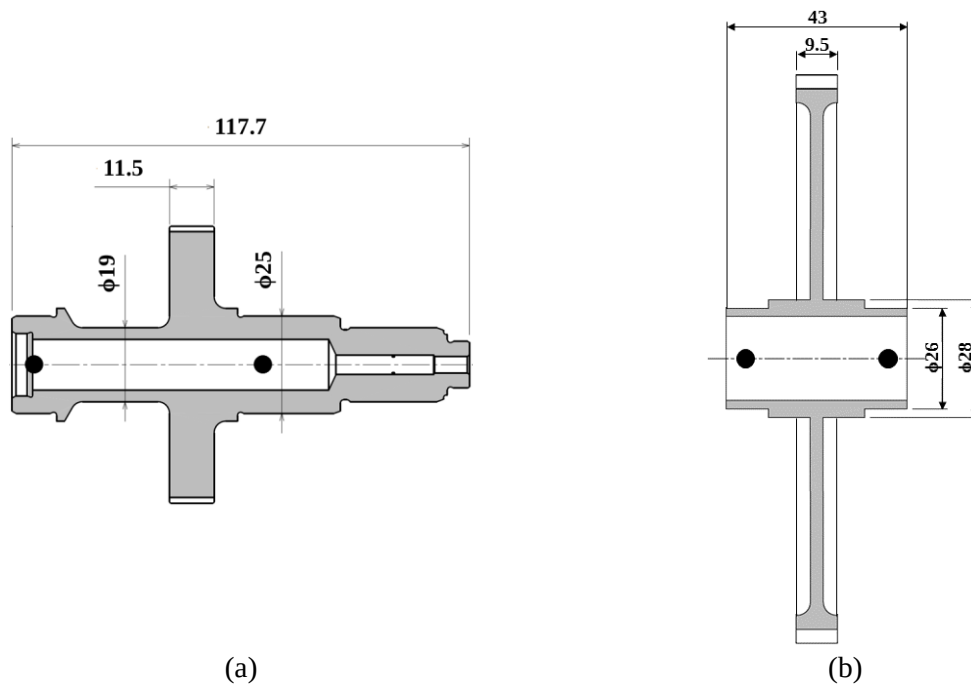


Figure 10: Plans de définition des corps d'engrenages

La première validation est faite pour la roue rigidifiée avec une comparaison au modèle à corps rigides du LaMCoS. Les premières comparaisons quasi-statiques des charges à la denture et aux paliers montrent des résultats satisfaisants.

En dynamique, le coefficient dynamique est comparé Figure 11 pour l'ensemble des modèles étudiés. Les résultats sont concluants malgré quelques différences, notamment pour le modèle H2 avec pignon et roue condensés. Ceci est probablement dû aux différences entre le pignon en poutres et celui condensé.

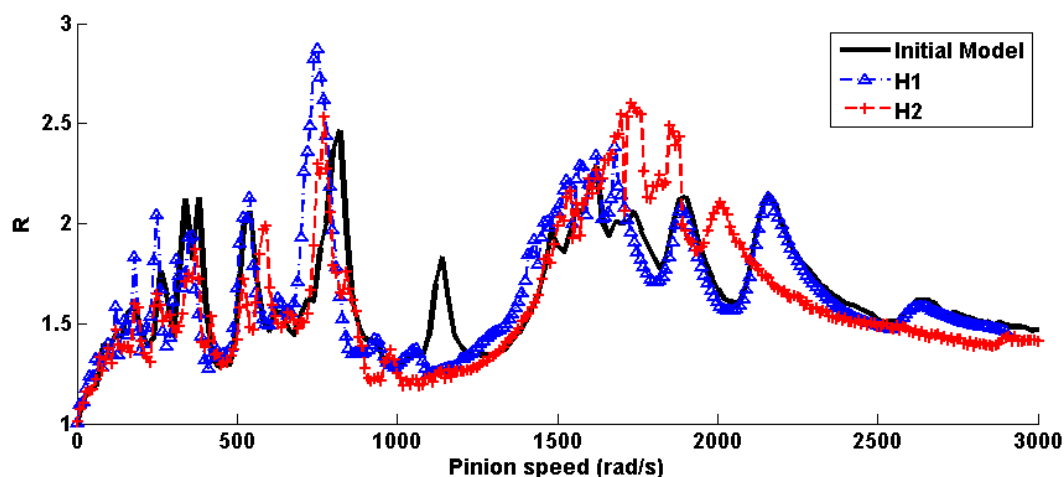


Figure 11: Comparaison des coefficients dynamiques pour les corps rigides

Le balayage en vitesse est réitéré avec la roue en acier classique. La Figure 12 montre que n'apparaissent pratiquement pas de nouveaux modes dus au comportement modal de la roue. La contribution de sa nouvelle flexibilité est principalement statique : elle diminue les fréquences des modes déjà présents.

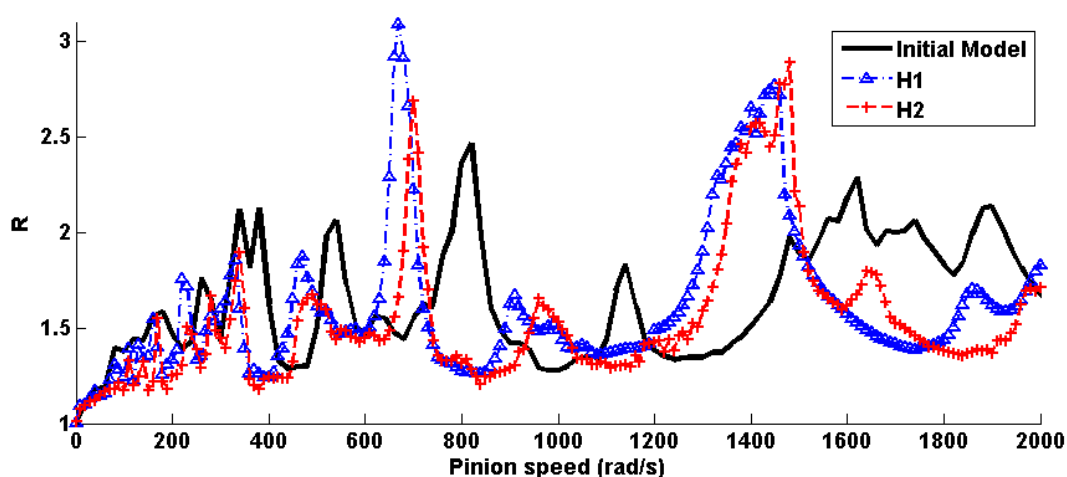


Figure 12: Coefficients dynamiques avec les corps souples pour les modèles hybrides

4.2. Transmission de Puissance – Validation Numérique

La seconde validation est faite sur un engrenage de puissance basé sur la géométrie d'une ancienne transmission de puissance de SAFRAN HE. Cet engrenage hélicoïdal a la particularité de posséder une jante large. Ses données sont détaillées Table 2.

	Pignon	Roue
Module m (mm)	2.5	
Nombre de dents Z	35	68
Angle de pression ($^{\circ}$)	25.	
Angle d'hélice ($^{\circ}$)	12.	
Coefficient de saillie	0.976	0.970
Coefficient de creux	1.262	1.268
Déport	0.275	0.317
Rayon fond de dent / module	0.25	
Largeur de jante b (mm)	~40	

Table 2: Paramètres de définition de la transmission de puissance académique

Sa jante large n'est supportée que par un voile-mince et incliné : Figure 13.

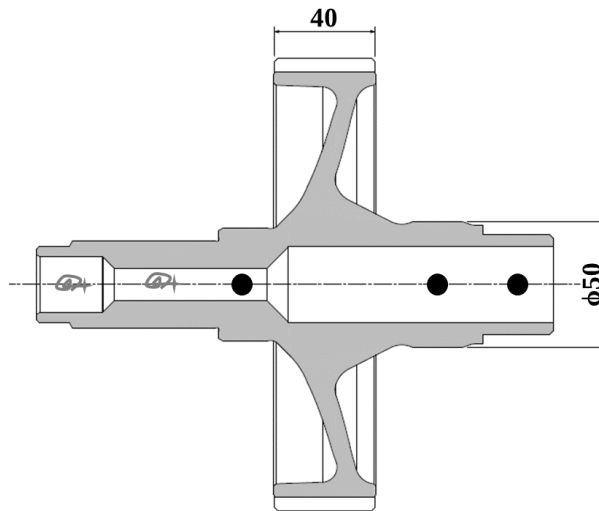


Figure 13: Plan de définition de la roue

Les validations quasi-statiques montrent des résultats concordants pour les charges aux paliers. Le balayage en vitesse donne des résultats satisfaisants sur les comparaisons du coefficient dynamique présentées ci-dessous. Ici aussi, certaines disparités, notamment des pics basse fréquence, peuvent s'expliquer par la différence de modélisations des poutres, des EF volumiques et des couplages associés.

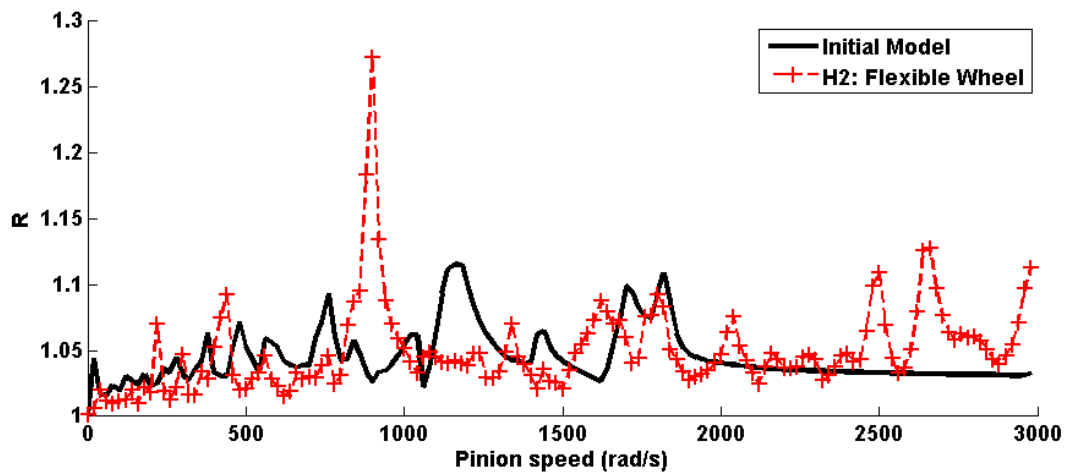


Figure 14: Comparaison du coefficient dynamique avec la roue condensée rigidifiée

La comparaison faite avec la roue flexible montre de nombreux pics attestant de la participation modale de cette roue. Les modes associés ressemblent à des modes de disques, se distinguant par des déformées comprenant des cercles et diamètres nodaux [SCH97-MOO14].

Une autre conséquence de cette nouvelle flexibilité est l'apparition des effets centrifuges : leur incidence sur la jante est visible sur le coefficient dynamique résultant (Figure 15). Par contre, il a été validé au cours des travaux que ces effets ne sont pas assez importants pour remettre en cause l'écriture des équations sur la géométrie non déformée de l'engrenage.

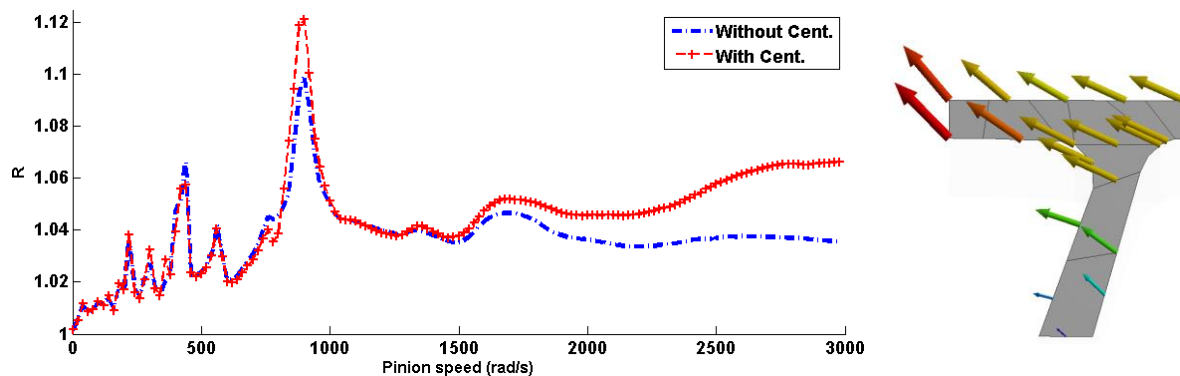


Figure 15: Influence des effets centrifuges pour (a) le coefficient dynamique et (b) les déplacements de la jante ($\Omega_p = 3000 \text{ rad / s}$)

4.3. Transmission de Puissance – Validation Expérimentale

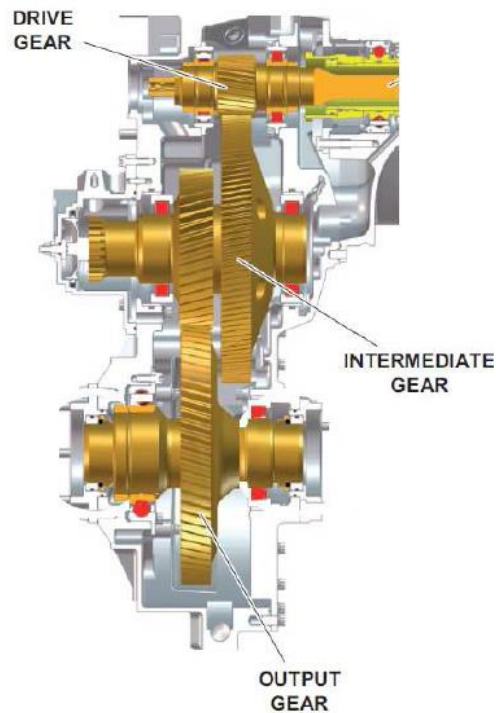


Figure 16: Transmission industrielle (étude pignon menant et roue intermédiaire)

La validation expérimentale est faite sur le train haute vitesse d'une transmission de puissance industrielle (Figure 16). Les données relatives à la transmission sont présentées Table 3. Il s'agit ici aussi d'un engrenage hélicoïdal à large jante.

	Pinion	Wheel
Module m (mm)		1.5
Nombre de dents	28	127
Angle de pression (°)		25
Angle d'hélice (°)		>0
Largeur de jante b (mm)		>25

Table 3: Données de définition de l'engrenage haute vitesse de la transmission industrielle

Les premières validations, basées sur des comparaisons au modèle EF complet, ont été réalisées en quasi-statique. Elles montrent des résultats cohérents sur les charges aux paliers et la distribution de pression à la denture.

Les validations dynamiques ont ensuite été faites grâce à des données expérimentales sur les déplacements de la jante de la roue. La roue étant en rotation par rapport à l'excitation de l'engrènement qui est fixe, un effet Doppler est visible sur les modes de la roue : la fréquence de ces modes dans le repère fixe n'est pas la même que celle dans le repère tournant. Ce changement de repère est illustré par l'équation de la déformée d'un disque dans le repère fixe en fonction de la fréquence propre du mode à l'arrêt et de la vitesse de rotation Ω de la roue :

$$\delta_F(t) = \frac{\delta^n}{2} \left(\sin((\omega_0 + n\Omega)t + \theta_0 + \varphi_0) + \sin((\omega_0 - n\Omega)t - \theta_0 - \varphi_0) \right) \quad (7)$$

Avec δ_F déformée dans la direction normale à la roue, exprimée dans le repère fixe, ω_0 fréquence propre du mode, Ω vitesse de rotation de la roue et n le nombre de diamètres nodaux du mode étudié.

Cette expression mène aux relations eq. 8 pour l'expression des fréquences de résonance : qu'elles soient étudiées dans le repère fixe ou mobile. Ces fréquences dépendent du nombre de diamètres nodaux de chaque mode, et donc de leur déformée spatiale.

$$\begin{cases} Z\Omega = \omega_0 \pm n\Omega & \text{dans le repère fixe} \\ \omega_0 = (Z \pm n)\Omega & \text{dans le repère mobile} \end{cases} \quad (8)$$

Avec $\omega_0 - n\Omega$, $(Z + n)\Omega$ et $\omega_0 + n\Omega$, $(Z - n)\Omega$ correspondants respectivement aux modes rétrograde et direct, Z étant le nombre de dents de la roue étudiée

Pour chaque vitesse de la plage étudiée, les déplacements radiaux des points du voile sont extraits en fonction du temps, puis la Transformée de Fourier du signal résultant est calculée (Figure 17). Cette figure montre une vitesse située entre pics de résonance : entre le mode direct à 8 diamètres nodaux et le mode rétrograde à 9 diamètres nodaux.

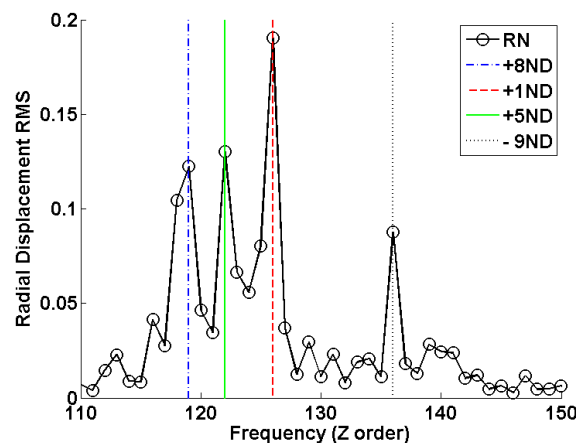


Figure 17: FFT des déplacements radiaux d'un point du voile à $\Omega_w = 8820$ rpm

Les mesures expérimentales ont été réalisées dans le repère fixe, et filtrées à la fréquence d'engrènement. Puis, pour obtenir le même signal avec les données numériques dans le repère tournant, les pics de réponse sont sommés sur les fréquences correspondant aux modes d'intérêt au voisinage des pics recherchés, les réponses loin de ces pics étant considérées comme du bruit résultant de la discrétisation numérique et des imprécisions de la FFT sur ces signaux. La Figure 18 montre qu'une bonne adéquation en fréquence et amplitude est constatée entre les signaux expérimentaux et les jauges numériques après traitement. La seule différence en fréquence visible vient du mode à 7 diamètres nodaux et 1 cercle nodal : il est établi que ce mode est dû aux simplifications faites dans la sous-structure de la roue pour son intégration et non au modèle d'engrenage lui-même.

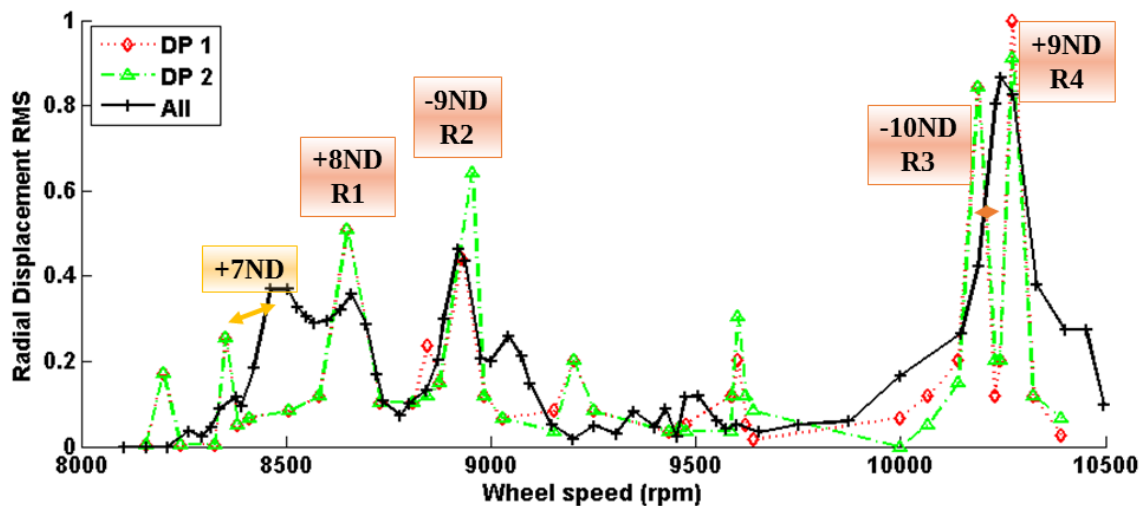


Figure 18: Validation expérimentale des déplacements du voile par comparaison des signaux

5. Résultats – Cas des Engrenages Flexibles

5.1. Influence de la Déformation Statique – Optimisation de Denture

Il a été établi que pour le voile droit de l'engrenage accessoire, l'effet de la déformation statique prédomine. Cet effet statique est visible lors de l'introduction d'un angle d'hélice. Le modèle montre que le voile ne peut supporter la charge alors induite par l'engrènement, il s'effondre : Figure 19.

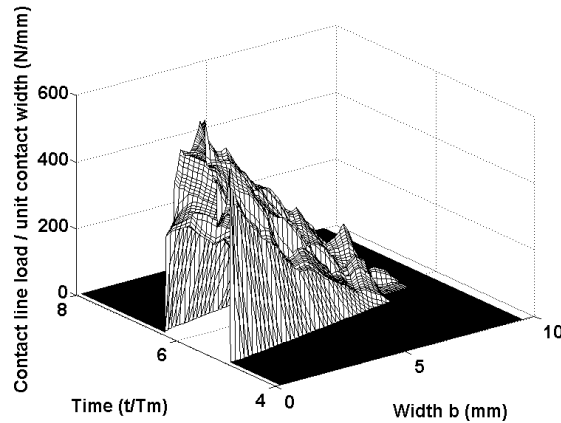


Figure 19: Charge à la denture pour $\beta = 20^\circ$

Ces constatations influent sur l'optimisation de l'engrenage. Des corrections optimales de profils linéaires et symétriques en tête de pignon et de roue ont été définies par Bruyère *et al.* [BRU15] sous la forme d'une Master Curve analytique (couple $E(\mu\text{m}), \Gamma$).

Leur utilisation a été validée pour les engrenages rigides. La Figure 20 montre que dans le cas de l'engrenage droit (a), cette Master Curve est valide, alors que dans le cas hélicoïdal, correspondant à la Figure 19, l'endroit d'application des corrections optimales doit être modifié.

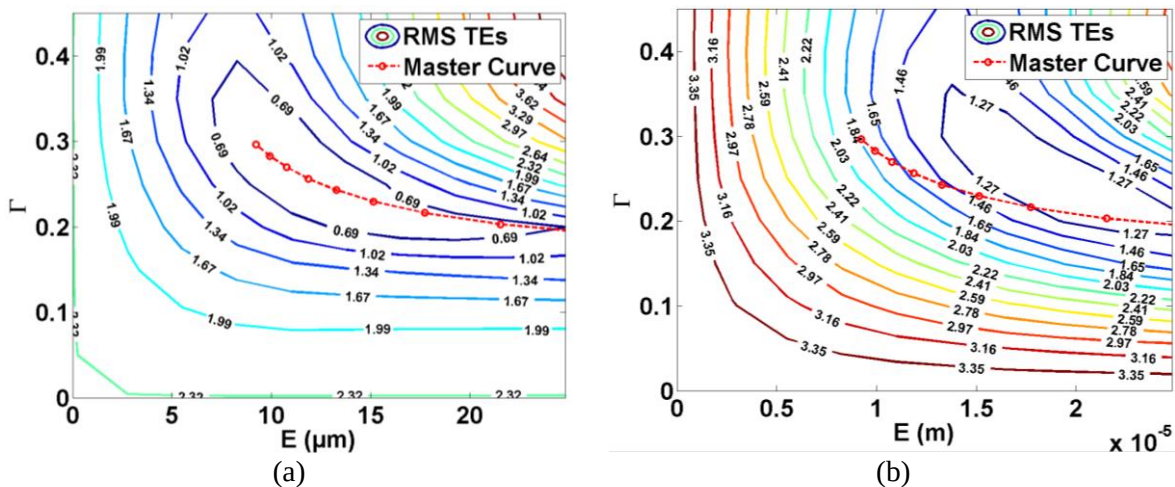


Figure 20: Corrections de profil et Master Curve [BRU15] avec (a) droit (b) $\beta = 20^\circ$

Une étude a ensuite été faite sur un ensemble de corrections optimales. Deux écarts de profils correspondant chacun à un engrenage de qualité différente ont été implémentés : un dans la norme des engrenages aéronautiques, et un de moindre qualité, qui pourrait être utilisé pour une transmission automobile. Les résultats attestent de la représentativité du modèle pour la modélisation des écarts de formes (Figure 21).

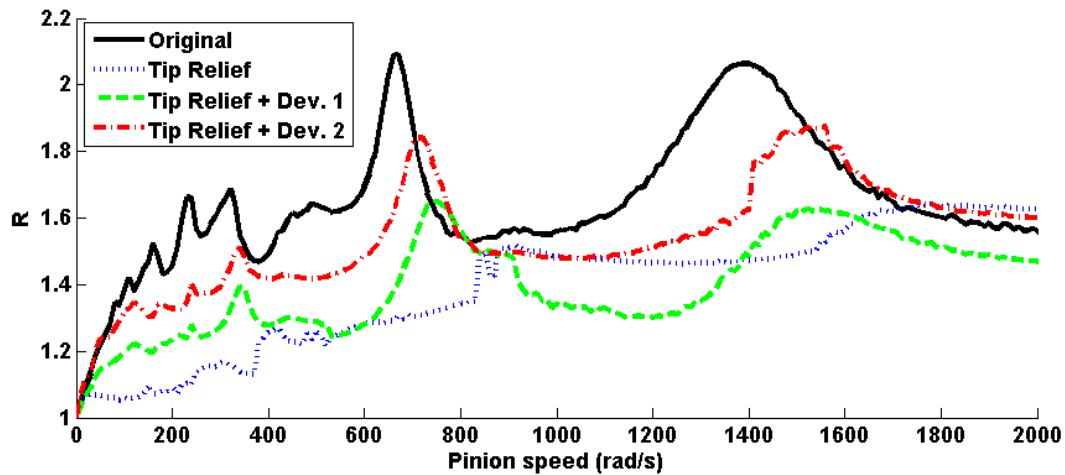


Figure 21: Comparaison avec des corrections de profils "optimales" en cas d'erreur de profil

5.2. Etude de la Dynamique de la Roue en Rotation

Les effets des différents types de modes ont été visualisés sur les déplacements de la jante de la transmission de puissance académique. Puis, un focus sur les modes de voile à diamètres a été fait. Les fréquences particulières caractérisant ces modes sont visibles sur les déplacements du voile. Le mode à deux diamètres, direct ou rétrograde s'exprime à des vitesses très proches : les deux parties sont donc visibles à une vitesse donnée (FFT Figure 22).

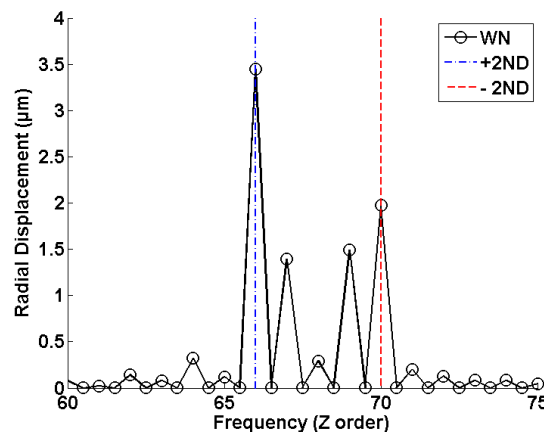


Figure 22: FFT du déplacement radial pour une résonance à $\Omega_p = 410 \text{ rad/s}$: 2 diamètres

La vitesse de rotation de résonance et la relation fréquentielle eq. 8 permettent de remonter à la fréquence du mode à l'arrêt ainsi qu'à sa déformée : Figure 23.

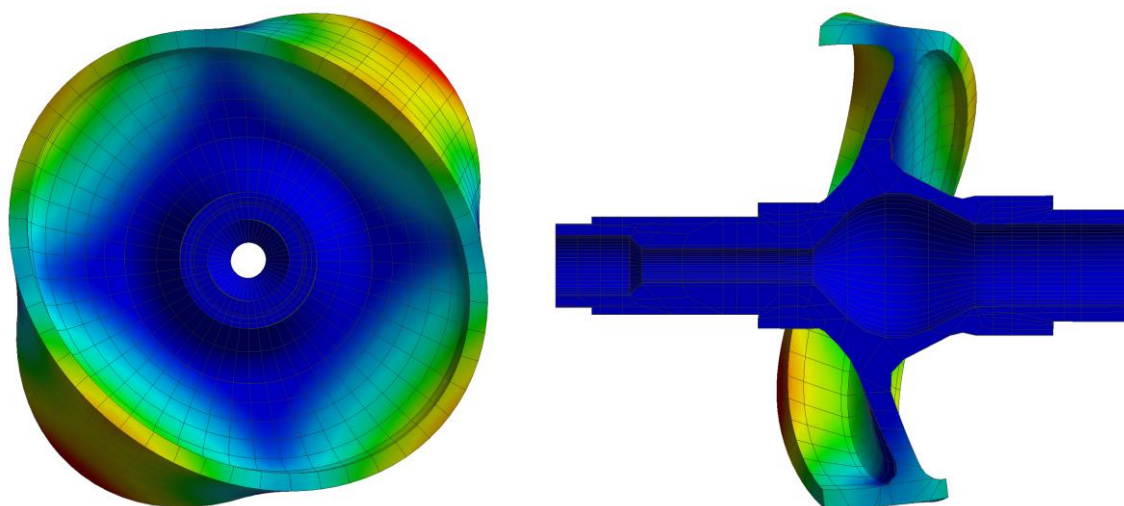


Figure 23: Déformée de la roue sur le mode étudié (2 250 Hz)

Les déformées sont ensuite étudiées directement sur la roue en rotation. Les fréquences des modes direct et rétrograde sont isolées sur la FFT (Figure 22) puis la FFT inverse permet de retrouver un signal temporel. Cette procédure est réitérée en prenant 48 points de la circonférence du voile. La déformée résultante est dessinée à plusieurs instants (Figure 24). Elle montre le caractère ondulatoire des ondes et permet de déterminer leur sens et leur vitesse.

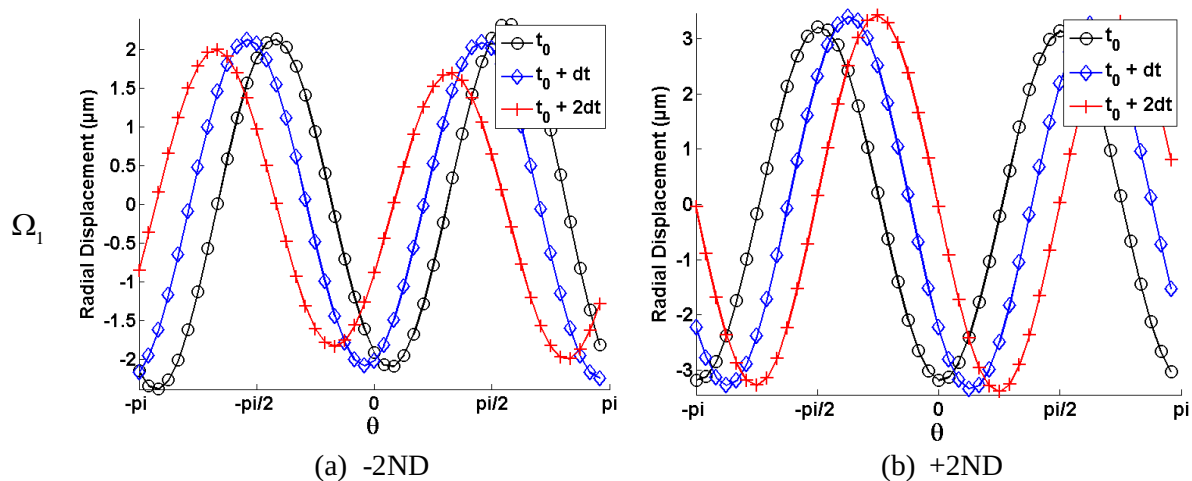


Figure 24: Analyse du déplacement de la déformée au cours du temps en filtrant la FFT sur la fréquence d'intérêt ($dt = 1/16 T_m$)

Ω_1	V. Pignon	V. Roue	Modes	Fréquence	V. Onde	V. Théorique
-2ND	410 rad/s	211 rad/s	2 250 Hz	- 8528 rad/s	- 596 m/s	+/- 505 m/s
+2ND				8200 rad/s	574 m/s	

Table 4 : Propagation des ondes dans la roue

5.3. Allègement d'une Transmission Complète

Le modèle avec le pignon et la roue condensés permet l'étude d'une transmission complètement allégée. Le pignon rigide de la transmission de puissance académique est remplacé par un pignon à voile mince lui-aussi. Les modes propres du pignon étant à haute fréquence, l'engrènement est principalement affecté par sa déformée statique. Elle change, par exemple, la répartition énergétique des modes du système. Néanmoins, les modes du voile de la roue restent découplés. L'étude menée à haute vitesse ($\Omega_p = 3000 \text{ rad/s}$) montre que la déformation du pignon sous effets centrifuges participe fortement à la distribution de pression à la denture (Figure 25).

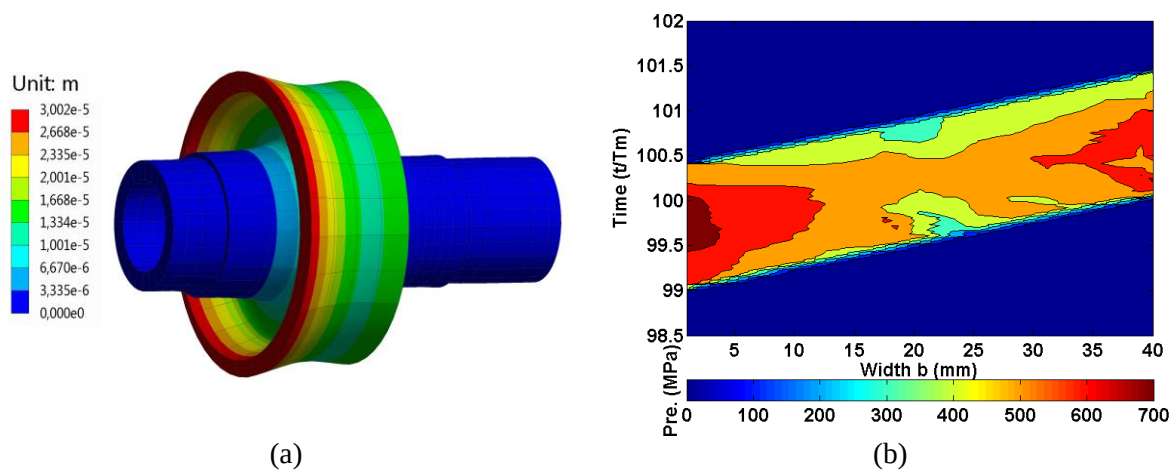


Figure 25: Effet de l'inclusion d'un pignon à voile-mince

La distribution de pression à la denture, présentée Figure 25 montre une surcharge aux extrémités. Pour pallier aux problèmes de fonctionnement et d'usure précoce qui en découleraient, un bombé selon l'hélice est introduit.

Les charges en fonction de la profondeur de correction aux bords sont données Figure 26. Il en résulte une amélioration progressive jusqu'à un positionnement de la charge maximale au centre de la largeur de contact. Pour la correction maximum ($E = 20 \mu\text{m}$), une perte de contact aux bords de l'engrènement est constatée, attestant de la trop grande correction apportée.

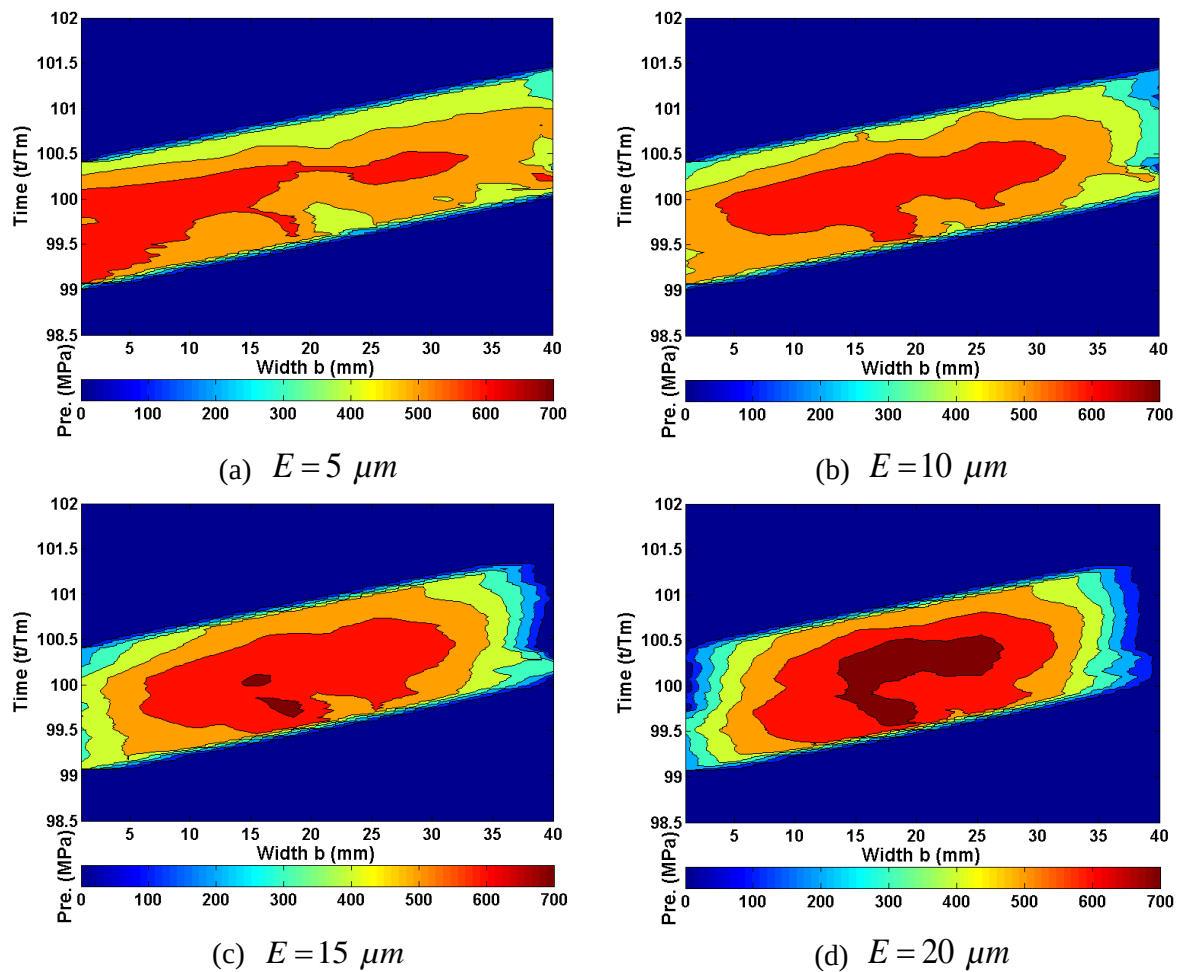


Figure 26: Amélioration de la distribution de charge à haute vitesse grâce à l'inclusion d'un bombé d'hélice

Une étude de l'influence de l'épaisseur du voile de la roue a aussi été faite. Elle montre que plus le voile est affiné, plus ses déformations modales et sous effets centrifuges peuvent être problématiques. En effet, un voile plus fin favorise l'apparition des modes dans les plages de vitesses tout en rendant la jante plus sensible aux sollicitations.

6. Conclusion

La conception des boîtes de transmission par engrenages des moteurs d'hélicoptères dépend de la nécessité des équipements embarqués, reposant principalement sur un allègement maximum pour réduire la consommation en carburant. Cet allègement est fait sur ces engrenages hautes-vitesses grâce aux enlèvements de matière dans les corps sous la denture, les voiles-minces.

Ce manuscrit a eu pour objet le développement d'un modèle hybride adapté à ces engrenages. Il s'agit à l'origine d'un modèle à paramètres concentrés, incluant des raideurs additionnelles pour les paliers et carters, des arbres en poutres ainsi qu'un pignon et une roue rigides connectés grâce à une fondation élastique calculée sur le plan d'action discrétisé. Les corps à voiles-minces sont inclus en remplaçant les éléments rigides. Le pignon ou la roue EF est condensé sur sa jante, le lien avec le plan d'action discret est fait grâce à un modèle élaboré de tranches minces de dent.

Ce modèle permet l'intégration des effets statiques et modaux de la flexibilité du pignon et/ou de la roue condensés, qu'il lie avec la dynamique de l'engrenage. Les équations de mouvement sont résolues temporellement grâce à un schéma de Newmark, couplé à un algorithme de contact prenant en compte les pertes de contact partielles ou totales qui pourraient se produire en dynamique [VEL96].

Le modèle a été validé sur trois cas testés numériquement et expérimentalement. La validation numérique d'un engrenage droit a montré des différences dues aux déformations statiques du voile. La même procédure réalisée sur un engrenage hélicoïdal à jante large a montré que le comportement modal de la roue avait une influence non négligeable et était apparenté aux modes des disques. Finalement, la validation faite expérimentalement sur un engrenage industriel a montré que le modèle est représentatif de la dynamique des roues à voiles-minces qui engrènent.

Suite à cette validation, le modèle a été utilisé sur les engrenages académiques afin d'étudier l'impact de leur flexibilité. L'engrenage droit a été optimisé. Puis le comportement de la transmission de puissance a été analysé sur une résonance de roue : la propagation des ondes a été visualisée. Enfin, un pignon avec un voile mince a remplacé le pignon rigide, ce qui a permis l'étude de son effet, notamment à haute vitesse.

Plusieurs perspectives de travail ont été envisagées. Tout d'abord, ces boîtes de vitesses, comme la transmission de puissance industrielle, sont souvent composées de plusieurs étages de réduction. Une suite des travaux consisterait à étendre le modèle aux trains multi-étages.

Ainsi, les effets transmis d'un train à l'autre : couplage de modes etc... seraient potentiellement visibles.

Enfin, les paliers et carters ne sont que peu décrits. Les carters nécessitant aussi des masses très faibles, leur conception engendre les mêmes problèmes que pour les roues d'engrenage. Leurs modes pourraient être excités par l'engrènement et leur modèle pourrait être précisé.

Scientific Contributions

Journal Publications

Guilbert, B., Velex, P., Dureisseix, D., Cutuli, P., “A mortar-based mesh interface for hybrid finite element/lumped parameter gear dynamic models – Applications to thin-rimmed geared systems”, *Journal of Mechanical Design*, 138(12):123301-123301-11. doi:10.1115/1.4034220, Dec. 2016.

Conference Publications and Oral Presentations

Guilbert, B., Velex, P., Cutuli, P., “Static and dynamic analyses of thin-rimmed gears with holes”, VDI, *International Conference on Gears*, p623-633, vol. 1, Munich, September 13-15th 2017.

Guilbert, B., Velex, P., Cutuli, P., “Optimum profile relief in thin-rimmed spur and helical gear”, *International Conference on Power Transmissions*, p425-430, vol. 1, Chongqing, 27th-30th October 2016.

Guilbert, B., Velex, P., Dureisseix, D., Cutuli, P., « Un modèle hybride du comportement statique et dynamique d’engrenages. Application aux systèmes avec voiles – minces ». *Journées Transmissions Mécaniques*, Lyon, Juillet 11-15 2016.



FOLIO ADMINISTRATIF

THESE DE L'UNIVERSITE DE LYON OPEREE AU SEIN DE L'INSA LYON

NOM : GUILBERT

DATE de SOUTENANCE : 08/12/2017

Prénoms : Bérengère Jeanne Dominique

TITRE :

Hybrid modular models for the dynamic study of high-speed thin –rimmed/-webbed gears

NATURE : Doctorat

Numéro d'ordre : 2017LYSEI127

Ecole doctorale : MEGA

Spécialité : Génie Mécanique

RESUME :

Ces travaux de thèse ont été réalisés grâce à une collaboration entre SAFRAN Helicopter Engines (anciennement Turbomeca) et le Laboratoire de Mécanique des Contacts et des Structures (LaMCoS) de l'INSA de Lyon (UMR CNRS 5259).

Les boîtes de transmissions par engrenages des moteurs d'hélicoptères convoient la puissance mécanique du turbomoteur aux accessoires (pompes, démarreur) et au rotor. Leur conception dépend des nécessités des équipements embarqués, en particulier l'allègement pour réduire la consommation en carburant. Les engrenages hautes vitesses de la transmission sont allégés grâce à des enlèvements de matière dans les corps sous la denture, les voiles-minces.

Un modèle dynamique d'engrenages a été développé pendant ce projet de recherche. Son approche modulaire permet l'inclusion conjointe des sollicitations dues aux vibrations de l'engrenage et de la nouvelle flexibilité des voiles-minces. Il dérive d'un modèle à paramètres concentrés, comprenant des arbres en poutres, des paliers et carters sous forme de raideurs additionnelles et un élément d'engrenage rigide inclus par son nœud central. Hypothèse est faite que tous les contacts sont situés sur les lignes de contact du plan d'action. Ces lignes sont discrétisées selon des tranches-minces dans les dents et la déviation normale des cellules est recalculée à chaque pas de temps selon la déflexion de la denture. Le nouveau modèle remplace l'engrenage rigide par une modélisation EF du pignon et/ou de la roue condensée sur les nœuds de jante. Une interface lie les raideurs du plan d'action discrétisé aux éléments finis du corps d'engrenage. L'élément prend donc en compte à la fois les sollicitations de l'engrenage et le comportement statique et modal des corps flexibles en dynamique.

Des comparaisons sont faites avec des données numériques et expérimentales. Elles attestent de la capacité du nouveau modèle à prédire le comportement dynamique des engrenages flexibles à hauts régimes de rotation. Ces résultats intègrent entre autres des données locales et globales en dynamique.

Finalement, le modèle est utilisé sur les deux cas académiques validés pour visualiser les effets des corps flexibles plus en détails. Un premier focus sera fait sur la déflexion statique due aux charges d'engrènement et sur l'optimisation sur le fonctionnement dynamique possible. Puis, les impacts des sollicitations de l'engrènement sur le voile en rotation seront étudiés. Enfin, le pignon et la roue seront affinés, afin de visualiser l'optimisation massique possible et son impact sur la dynamique de l'engrenage.

MOTS-CLÉS :

Dynamique d'engrenage, voile-mince, modes des ensembles flexibles, influence flexibilité, optimisation

Laboratoire (s) de recherche :

Laboratoire de Mécanique des Contacts et des Structures (LaMCoS)

Directeur de thèse:

Professeur Philippe VELEX

Président de jury

Professeur Anne TANGUY

Composition du jury :

Wim DESMET, Karsten STAHL, Roger SERRA,
Philippe CUTULI, Philippe VELEX, David DUREISSEIX